창의적 연구진흥사업
Creative Research Initiative Program

물질제조를 위한 나노 입자생성 및 제어기술연구
Nano Particle Generation and Control for Materials Processing

서울대학교

과학기술부

제 출 문

과학기술부 장관 귀하

본 보고서를 "물질제조를 위한 나노 입자생성 및 제어기술연구" 과제의 보고서로 제출합니다.

2004. 2. 24

유 치 기 관 명 : 서울대학교
연 구 단 장 : 최 만 수
연 구 원 : I. Altman
〃 : P. Pikhitsa
〃 : 송 자 경
〃 : 정 재 인
〃 : 권 순 박
〃 : 서 정 수
〃 : 양 상 선
〃 : 김 영 정
〃 : 이 상 훈 외 28인
위탁연구기관명 :
위탁연구책임자 :

보고서 초록

<table>
<tr><td>과제관리번호</td><td></td><td>해당단계
연구기간</td><td>2000.10.1~2003.9.30</td><td>단계 구분</td><td>2 / 3</td></tr>
<tr><td rowspan="2"><u>연구사업명</u></td><td>중 사 업 명</td><td colspan="4">특정연구개발사업</td></tr>
<tr><td>세부사업명</td><td colspan="4">창의적연구진흥사업</td></tr>
<tr><td rowspan="2">연구과제명</td><td>중 과 제 명</td><td colspan="4"></td></tr>
<tr><td>세부(단위)과제명</td><td colspan="4">물질제조를 위한 나노입자 생성 및 제어기술 연구</td></tr>
<tr><td>연구책임자</td><td>최 만 수</td><td>해당단계
참여연구원수</td><td>총 : 38 명
내부: 1 명
외부: 37 명</td><td>해당단계
연구비</td><td>정부: 1,900,000 천원
기업: - 천원
계 : 1,900,000 천원</td></tr>
<tr><td>연구기관명 및
소속부서명</td><td colspan="2">서울대학교
정밀기계설계공동연구소</td><td colspan="2">참여기업명</td><td></td></tr>
<tr><td>국제공동연구</td><td colspan="5">상대국명 : 상대국연구기관명 :</td></tr>
<tr><td>위 탁 연 구</td><td colspan="5">연구기관명 : 연구책임자 :</td></tr>
<tr><td colspan="4">요약(연구결과를 중심으로 개조식 500자이내)</td><td>보고서
면수</td><td>244</td></tr>
<tr><td colspan="6">본 연구단에서는 나노 입자의 크기, 형상, 결정상 및 성분을 제어하기 위한 새로운 이론적, 실험적인 기술들을 개발, 확립하고, 나노 입자의 위치제어를 위한 새로운 나노 입자 패턴 방법을 고안하였다. 새롭게 개발한 레이저를 이용한 에어로졸 제어기술은, 기상 중에서 생성되는 나노 입자들에 CO_2 레이저를 조사하여 단성분 혹은 복합체 나노 입자의 크기와 모양, 결정상, 조성까지도 제어할 수 있었으며, 나노튜브의 전계방출 특성에 필적할 만한 새로운 탄소 나노 입자를 제조할 수 있었다. 또한 본 연구단은 코팅된 나노 복합재료의 합성을 위한 새로운 기상 코팅 기술을 고안하였으며, 새로운 나노 입자 패터닝 방법을 개발하였다. 이론적으로 다분산 비구형 나노 입자의 성장을 예측할 수 있는 효율적인 모델링 기술들과 실험적으로 비구형 나노 입자의 성장 측정하는 광산란 기법들을 개발하였다. 금속 연소를 통해 특이한 발광특성을 나타내는 산화마그네슘 입자를 제조하였고, 또한 응집되지 않은 나노입자의 합성을 위해 정전분무 기술, 입자의 균일한 증착을 위해 내부제트를 이용한 화학 증착기술을 개발하였다.</td></tr>
<tr><td rowspan="2">색 인 어
(각 5개 이상)</td><td>한 글</td><td colspan="4">나노입자, 에어로졸, 탄소나노입자, 입자성장모델링, 금속연소, 패터닝</td></tr>
<tr><td>영 어</td><td colspan="4">Nanoparticle, Aerosol, Carbon nanoparticle, Particle growth modeling, Matal combustion, patterning</td></tr>
</table>

요 약 문

Ⅰ. 제 목

물질제조를 위한 나노입자 생성 및 제어기술 연구

Ⅱ. 연구배경 (연구개발의 목적 및 필요성)

화염, 응축, 열플라즈마 등과 같은 열적 수단을 이용하는 에어로졸 제조공정은 나노입자나 나노입자로 구성된 박막이나 벌크 물질을 제조하는데 매우 유용하므로 많은 관심을 끌고 있다. 나노미터 크기를 갖는 입자의 발생, 성장 및 부착 뿐만 아니라 열과 유동을 제어하는 것은 이와같은 에어로졸 기술에 있어서 핵심요소라 할 수 있다. 그러므로 에어로졸과 열 유동을 제어하는 기술의 확립은 나노입자로 구성된 물질제조에 있어서 매우 중요한 부분이다.

Ⅲ. 연구개발의 내용 및 범위

본 나노입자 제어 기술 연구단은 (1) 단성분 및 복합 나노입자의 크기, 형상, 결정상 및 조성제어를 위한 새로운 제어방법 확립, (2) 새로운 나노입자 패터닝 방법 개발, (3) 나노입자 성장연구를 위한 새로운 이론적, 실험적 방법 개발, (4) 현재까지 밝혀지지 않은 나노입자의 생성과 성장에 관한 새로운 현상들을 규명하는데 목표를 두고 있다.

Ⅳ. 연구내용 및 연구결과

화염내 레이저 조사를 이용하는 새로운 에어로졸 제어기술은 나노입자의 크기, 형상 및 결정상을 제어할 수 있을 뿐만 아니라, 복합 나노입자의 조성을 제어할 수 있었다 (1개의 특허 등록 및 3개 특허 출원중). 아세틸렌 화염에서 레이저를 조사했을 때, 임계전이에 의해 높은 결정성을 갖는 속이 빈 쉘형상의 탄소 나노입자가 연속적으로 생성되는 놀라운 현상을 발견하였다. 이 방법에 의해 생성된 속이 빈 탄소 나노입자는 탄소 나노튜브에 필적할만한 전계방출 특성을 나타냈다 (1개의 특허 등록 및 3개의 특허 출원중).

● 본 연구단은 코팅된 복합 나노입자 합성을 위한 새로운 기상 코팅법을 개발하였다. 코어물질과 연료를 공급하는 외부노즐과 내부노즐로 구성된 슬라이딩 버너를 이용하여 다양한 나노입자 산화물을 균일한 나노미터 두께로 코팅할 수 있는 단일공정을 가능하게 하였다 (1개 특허 출원중).

● 본 연구단은 새로운 나노입자 패터닝 방법을 개발하였다. 기존의 리소그래피와 전기장 및 입자하전을 이용한 단분산입자 유도방법을 결합하여 노이즈가 없는 선 및 점 형태의입자 패턴을 성공적으로 만들어 낼 수 있었다 (2개 특허 출원중).

● 본 연구단은 다분산 비구형입자의 성장을 예측할 수 있는 효율적이며 새로운 모델링 방법인 구간해석법과 더욱 간단한 바이모달모델을 개발하였다.

● 본 연구단은 비구형 나노입자 성장을 측정하는 새로운 방법인 평면 광산란을 이용하여 프렉탈 응집체를 측정할 수 있는 선측정 방법을 개발하였고 탄성적, 동적 광산란방법을 병합하여 응집체의 농도, 크기변수, 부피분율을 측정하는 방법을 개발하였다.

● 본 연구단은 상변화로 인해 나노입자가 작은 크기로 쪼개지는 놀라운 현상을 발견했다. 화염내와 진공상태의 전자빔조사 현미경에서 20nm 크기의 산화철 입자는 3 에서 5

나노미터 크기로 40nm 크기의 산화주석 입자는 10 나노미터 크기로 변화하였다.

● 본 연구단은 최초로 금속연소로 만들어진 망간 및 크롬이 도핑된 산화마그네슘 결정에서 선 스펙트럼 피크을 발견했다.

● 비응집된 나노입자의 합성이나 입자의 균일한 증착을 위해 각각 정전분무, 내부제트를 이용한 화학 증착방법을 제안하였다 (두 개의 특허 등록, 1개의 특허 출원중).

V. 활용계획

나노입자의 크기, 형상, 결정상, 조성과 및 나노입자를 이용한 패턴증착은 나노구조물이나 나노장치들의 특성과 성질을 결정한다. 성질이 제어된 단성분 및 복합 나노입자의 기상합성법과, 나노패터닝 및 나노코팅을 포함하는 본 연구단의 새로운 발견은 나노입자 연구와 그 적용 분야에 있어서 비약적 발전이라고 볼 수 있다. 나노입자는 나노구조물이나 장치들을 만드는데 있어 기본 골격이므로 본 연구단의 이러한 성과들이 나노입자 연구와 그 응용에 광범위한 영향을 줄 것이라고 믿는다. 나노입자 성장에 대한 새로운 측정방법 및 이론방법의 개발은 이미 에어로졸 과학 분야에 중요한 기여를 했다고 생각한다.

SUMMARY

○ **Title**

Nano Particle Generation and Control for Materials Processing

○ **Background**

Aerosol processes using thermal means such as flames, condensation, thermal plasma, etc. draw special attention to manufacture nano particles and nanophase film or bulk materials. Not only generation, growth, and depositio mechanisms of nanometer sized particles but also the heat and fluid flow are the essential for determining the final characteristics of nanoparticles, so the establishment of control techniques of aerosol and heat flow plays an important part in the manufacture of nanophase materials.

○ **Objectives and scope**

The National CRI Center for Nano Particle Control aims at (1) establishing new control methods to control the size, morphology, and crystalline phase of single component and composite nanoparticles (2) developing new methods to make patterns of nanoparticles (3) developing new theoretical and experimental methods to investigate the growth of nanoparticles (4) elucidating novel phenomena related to particle generation and growth that have not been explored.

○ **Results**

● Our new control strategy utilizing laser irradiation in a flame is not only confirmed to successfully control the size, morphology, and crystalline phase of nanoparticles, but also to control the phase segregation in composite nanoparticles **(1 Patent registered and 3 Patents pending).** Surprisingly, the laser irradiation in an acetylene flame was found to continuously generate hollow shell-shaped carbon nanoparticles of high crystallinity with mass quantity through critical transition. These hollow carbon nanoparticles exhibited field emission comparable to carbon nanotubes**(1 Patent registered and 3 Patents pending).**

● We developed a new gas phase coating method for the synthesis of coated nano composite particles. Sliding burner consisting of outer coating nozzle and inner nozzles supplying a core material and fuels enables one step process to make uniform and nano coating of oxides of various materials on different kinds of nanoparticles **(1 Patent pending).**

● We developed new methods of patterning of nanoparticles. We combined conventional lithography and monodisperse nanoparticle transport utilizing electrical field and nanoparticle charging.

(2 Patents pending).

● We developed novel modeling methods to predict the growth of polydisperse non-spherical nanoparticles. A new efficient sectional method and much simpler bi-modal models for non-spherical particles were developed .

● We developed new methods for measuring the growth of non-spherical nanoparticles. These include an *in-situ*line measurement of fractal aggregate growth by utilizing planar light scattering and

a method for measuring concentration, size parameters, volume fraction of aggregates by combining elastic and dynamic light scattering methods.

- We discovered a surprising phenomenon of the fragmentation of nanoparticles due to phase transformation. 20 nm Fe_2O_3 and 40 nm SnO_2nanoparticles were transformed into 3-5 nm Fe_2O_3 and 10 nm SnO_2 nanoparticles both in a flame and in an electron beam irradiating microscope under vacuum.
- For the first time, we observed extremely sharp line spectra from Mn or Cr doped MgO nanocrystals made from metal combustion.
- Electrospray or jet assisted chemical vapor deposition methods were proposed for the synthesis of non-agglomerated nanoparticles or uniform deposition of particles, respectively **(2 Patents registered and 1 Patent pending).**

○ **Significance**

Size, morphology, crystalline phase, composition of nanoparticles and their patterned deposition determine the properties and quality of nanostructured materials and nanodevices. Our novel inventions covering gas phase synthesis of single component and composite nanoparticles with controlled properties, nanoparticle patterning, and nanocoating should be breakthroughs in the field of nanoparticle research and applications. We believe these achievements give broad impacts on nanotechnology field since nanoparticles are fundamental building blocks for nanostructured materials and nanodevices. Developments of new measurement and theoretical methods for the growth of nanoparticles have been already considered to be significant contributions in the field of aerosol science.

Table of Contents

Chapter 1. Introduction

● **Importance of nanotechnology and nanoparticle research**

Nanotechnology is recognized as an emerging key technology for the 21st century. The Bush administration's 2003 budget seeks more than $700 million for the National Nanotechnology Initiative. Other countries such as Japan, Western European countries, Korea have also begun to recognize the importance of nanotechnology and fund at significant levels. This is because of scientific convergence of physics, chemistry, biology, materials and engineering at nanoscale, and of the importance of the control of matter at nanoscale on almost all technologies. **Nanoparticle manufacturing/control is an essential component of nanotechnology because 1) nanoparticles themselves are building blocks for nanotechnology, 2) the specific properties are realized at nanoparticle, or nanolayer level, and 3) assembling and patterning of nanoparticles are prerequisite to make nanostructured materials and nanodevices.**

Needless to say, many people recognize the importance of nanoparticle research. The small size of nanoparticles that is responsible for unusual optical, electrical, magnetic, chemical and mechanical properties of nanoparticles with sizes usually less than 100 nm makes them useful for new applications or remarkable improvements on existing applications.

● **Critical issue on nanoparticle research**

There are basically two different methods to synthesize nanoparticles; liquid based wet chemistry method and gas-phase aerosol method. Each method has pros and cons. In the present project, **we focus on gas-phase aerosol method due to the following advantages.** Gas phase processes are generally purer than liquid-based processes since even the most ultra-pure water contains traces of impurity. Aerosol methods are usually continuous processes that are needed for practical production while wet chemistry is a batch process that can result in different quality from batch to batch. However, there exists a critical issue for aerosol methods to be overcome before being developed as a practical nanotechnology.

Controllability is now a key issue for realizing practical nanotechnology, i.e., controlling the size, morphology, crystalline phase, composition of single component or composite nanoparticles and their patterned deposition are demanding tasks. **Breakthroughs on these important problems will open the door for immediate applications of nanoparticles** such as in cosmetics, catalysts, electron emission display, data storage, fuel cell, etc.

The control of heat and fluid flow are also essentials for the mastery of controllability of nanoparticles since heat transfer, fluid flow and mass transfer govern not only the generation and growth of nanoparticles, but also the transport and deposition of them.

● **How to solve this issue ; Breakthroughs are needed**

We believe that our control strategies covering both the generation and growth of nanoparticles (single component and composite) and the patterning of synthesized nanoparticles should be breakthroughs on this field giving broad impacts on nanotechnology field since these control technologies are fundamentals to the establishment of nanostructured materials and nanodevices.

We pursue the mastery of controllability for nanoparticle generation, growth, transport and depositon to provide a clear solution to the above problems.

More specifically, National CRI Center for Nano Particle Control aims at (1) establishing new control methods to control the size, morphology, and crystalline phase of single component and composite nanoparticles (2) developing new methods for patterning of nanoparticles (3) developing new theoretical and experimental methods to investigate the growth of nanoparticles (4) elucidating novel phenomena related to particle generation and growth that have not been explored.

Chapter 2. State-of-the-art

● **International activities**

Pratsinis' group in the ETH of Switzerland has carried out experimental and theoretical studies on synthesis of metal and ceramic nanoparticles using aerosol techniques in flame. Recently, they have focused on the flame spray pyrolysis (FSP) which can employ a wide array of liquid precursors for functional nanoparticle synthesis (Madler et al., 2002; Mueller et al., 2003). Okuyama's Group in Hiroshima University has tried to setup the spray pyrolysis method, one of the aerosol methods for synthesizing nanoparticles using liquid-to-particle conversion route, by applying the salt-assisted and ultrasonic sprayed utilities (Lenggoro et al., 2001; Okuyama and Lenggoro, 2003). Kauppinen's group in VTT of Finland has investigated the crystal morphology and phase of titania nanoparticles during the aerosol synthesis (Ahonen et al., 2002). Fissan's group in Gerhard-Mercator-University Duisburg in Germany has described the deposition process and the trajectory of charged, metallic nanoparticles on the substrate surface (Krinke et al., 2002). To understand the gas-to-particle conversion and nanoparticle properties, Zachariah's group in University of Minnesota has developed the molecular based modeling tools (Efendiev and Zachariah's, 2003). Friedlander's group in UCLA has presented the self-preserving size distribution theory for fractal-like particles under Brownian coagulation (Dekkers and Friedlander, 2002). Biswas' group in Washington University has studied on the formation and growth dynamics of aerosols in high temperature environments (combustion aerosols), especially concerning the health effects of nanoparticles (Miller et al., 2001).

Recent researches on nanoparticles conducted by each group as described above have their own significant contributions to the construction of nanotechnology. **Our cutting-edge novel methods that we have developed have been very well recognized worldwidely.**

● **Domestic activities**

In Korea, Hee-Dong Jang's group in KIGAM synthesized the titania and silica nanoparticles in a diffusion flame reactor by adjusting the precursor concentration and gas flow rates as control variables (Jang and Kim, 2001). Multi-component phosphor nanoparticles have been synthesized using the ultrasonic spray pyrolysis by Seung-Bin Park's group in KAIST (Kang et al., 2003). Another group in KAIST led by Sang-Soo Kim has worked on the electrospray of nanoparticles including the direct measurement technique by freezing (Ku and Kim, 2002).In a furnace reactor, the nanoparticle morphology affected by corona ion was investigated by Kang-Ho Ahn's group in Hanyang University (Ahn et al., 2001) and the characteristics of nanoparticles generated in a furnace reactor were described by Jung-Ho Hwang's group in Younsei University (Ji et al., 2002). Nanoparticle growth by coagulation in silane plasma reactor was analyzed (Kim and Kim, 2002) and the change in particle charge distribution during the rapid growth of particles was investigated by Kyo-Seon Kim's group in Kangwon University. The various modes of composite titania/silica nanoparticles were prepared through

vapor-phase hydrolysis and their characteristics were evaluated by Sun-Geon Kim's group in Chungang University (Lee et al., 2002). The change in particle size of fractal agglomerates during Brownian coagulation was calculated and the change in particle size distribution undergoing condensational growth was revealed (Park et al., 2002) by Kyoo-Won Lee's group in K-JIST.

During the last two phases, we have developed novel control strategies in nanoparticle synthesis and its patterning including Coalescence Enhanced Synthesis using laser irradiation in flame, *in-situ* gas-phase coating method utilizing the modified sliding burner, nanoparticle patterning, a novel model for non-spherical nanoparticle growth, and new experimental methods to measure the growth of non-spherical nanoparticles. These novel and creative works have never been attempted in the filed of nanotechnology and have been already considered to be significant achievements in the field. Furthermore, during the 3rd phase , more concrete establishment and its practical applications of our novel strategies will be accomplished and finally our works give significant contributions toward the realization of nanotechnology.

Chapter 3. Methods, Results and Discussion

3.1. Development of new control strategy for nanoparticle generation and growth

3.1.1. Study of synthesis and growth control of silica/titania composite nanoparticles using "Coalescence Enhanced Synthesis".

● Introduction

Control of particle formation and property of composite nanoparticle has not been attempted much even though there is a growing demand for the multi-component materials. A multi-component system shows complex features in generation, evolution of particles and its formation mechanism and structural properties are poorly reported. We applied the present coalescence enhanced synthesis method to SiO_2/TiO_2 composite nanoparticles in flame. It is shown that size and morphology of SiO_2/TiO_2 particles can be successfully controlled by the present method. Also we show that crystallization of SiO_2/TiO_2 nanoparticles can be controlled by the present method.

Our method (Coalescence Enhanced Synthesis) was confirmed to successfully control size, morphology, crystalline phase of SiO_2/TiO_2 nanocomposite particles for the first time. There has been no report so far on the in situ controllability of the structural properties of nano-sized SiO_2/TiO_2 particles in flame. This finding may imply that continuous acquisition of multi component nanoparticles with changing structural property could be possible. Previously, we proposed a new control method using CO_2 laser irradiation ("Coalescence Enhanced Synthesis", see Fig. 3.1.1.1) for nanoparticle synthesis and its mechanism was thoroughly investigated. First, we applied our method for the synthesis of non-crystalline SiO_2 particles at high concentration. Three different mechanisms such as generation, coalescence and evaporation effect were found depending on the irradiation heights in a flame and it was shown that particle size of silica particles could be successfully controlled with CO_2 laser irradiation. Second, this control method was applied to control the growth of crystalline TiO_2 particles. In this case, original fractal aggregates were completely transformed into spheres with a considerable reduction of volume, which was attributed to the coalescence effect that can reduce collision cross-sections of particles.

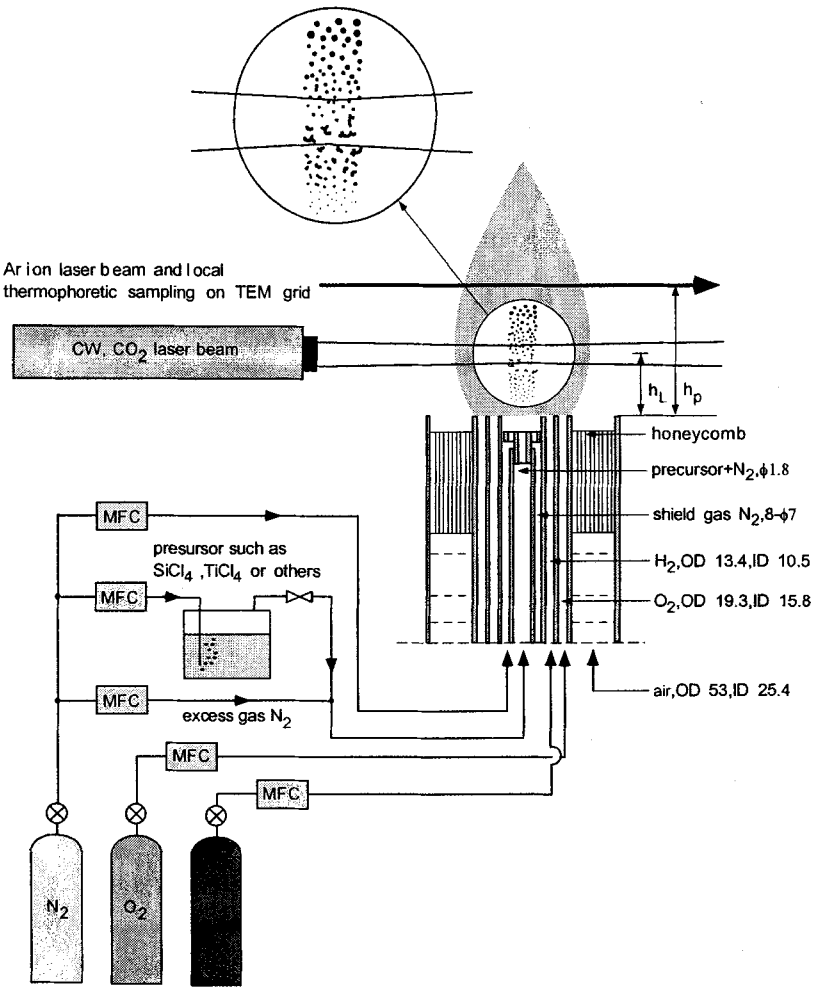

Fig. 3.1.1.1. Coalescence Enhanced Synthesis of Nanoparticles.

● Methods

SiO_2/TiO_2 particles were generated in an oxy-hydrogen diffusion flame by hydrolysis and oxidation of $SiCl_4$ and $TiCl_4$. These $SiCl_4$, $TiCl_4$ liquids were used as the precursors for SiO_2, TiO_2 respectively. Carrier gases (oxygen) passed through each bubbler were mixed before they were injected through the center nozzle of the burner. A bubbler containing $TiCl_4$ liquid was maintained at 60 °C while $SiCl_4$ bubbler was maintained at 24 °C because of its relatively low vapor pressure compared with $SiCl_4$. Four experimental conditions were chosen to study the effect of CO_2 laser beam irradiation on size, morphology and crystallization of SiO_2/TiO_2 composite nanoparticles. The flow rates of precursors, fuel, oxidizer, and other gases are given in Table 2. In each experimental condition, total flow rates of gases injected through the center nozzle were maintained constant via addition of dilution gas to keep the same residence time in CO_2 laser heated region. A laminar diffusion flame burner composed of six concentric stainless-steel tubes was used and a high power CW CO_2 laser (10.6 μm in wavelength) was employed to heat rapidly flame-generated particles. The experimental apparatus and the flame temperature profile of the burner have been described in detail in our previous report. Local thermophoretic sampling of SiO_2/TiO_2 particles on TEM grid was made for observation of its morphology, size and crystallization. SiO_2/TiO_2 particles moving along the flame were also thermophoretically deposited onto a water-cooled quartz tube (6 mm in the outer diameter) for further examination of composition, phase and crystallization. The particles are repeatedly collected after short deposition time of 2 minutes to prevent undesirable thermal heating during powder collection. In this report, the height of CO_2 laser irradiation and particle collection is denoted as h_L and h_P respectively.

Table 3.1.1.1. Experimental Conditions

Experimental Conditions	Case 1	Case 2	Case 3	Case 4
Measured mol % of Ti	15	21	29	40
Carrier gas O_2 for $TiCl_4$ (cc/min)	100	200	200	200
Carrier gas O_2 for $SiCl_4$ (cc/min)	100	100	80	50
Dilution gas O_2 (cc/min)	109	0	50	71
Q_{total} (cc/min)	360			
H_2 (l/min)	2.5			
O_2 (l/min)	5.0			
Shield gas N_2 (cc/min)	700			
Dry air (l/min)	70			

The particles were imaged using a transmission electron microscope (JEM 200CX, JEM 3000F). In order to determine the composition of the collected powders X-ray spectrometry (EDS) was

conducted. The compacted pellets (5 mm in diameter) made from collected powders were studied with a scanning electron microscope equipped with EDS (JSM 5600).The compositions were measured several times for different selected areas (~300μm ×250μm) and then averaged. A X-ray diffractometer (MAC/Science, MXP18XHF-22) was used to determine crystalline phase of collected SiO_2/TiO_2 powders. The sizes of TiO_2 crystallites were estimated from the Scherrer equation after fitting each peak to a Gaussian profile and correcting the profile for the instrumental broadening. Structural properties of the SiO_2/TiO_2 powders were examined with FT-IR spectroscopy using a Bomen DA 8 spectrometer. The samples were diluted with KBr and the spectra were collected with a spectral resolution of 1.93 cm^{-1}. The Raman spectra were obtained using a France Jobin-Yvon T64000 with excitation wavelength 514.5 nm, with a spectral resolution of 1.8 cm^{-1}.

● Results and discussion

The evolution of SiO_2/TiO_2 particles in flame has been investigated for Case 2. The TEM image shows that particles are formed even in very low height from the burner exit (at 3 mm) due to oxidation of $SiCl_4$, $TiCl_4$ vapors. Generated particles grow along the height in flame from highly aggregated particles (at 3-7 mm) to more sintered non-spherical particles (at 10-15 mm) and finally to spherical particles at 18 mm asa result of coalescence. The changes in molar ratios of Ti to Si during generation of SiO_2/TiO_2 particles have been studied using EDS analysis of collected powders. Measured Ti mol % at 8 mm was 42 % and Ti mol % decreases along the heights from ca. 23-25% (at 10-18 mm) to 21 % at 23 mm. This change in compostion is due to the difference in reaction rates of two precursors. Activation energy for chemical reaction of $TiCl_4$ is much lower than that of $SiCl_4$ (Ehrman, et al., 1998). Thus, TiO_2 particles are more likely to form than SiO_2 particles. That is why Ti mol % is higher at lower heights and decreases as subsequent particle generation occurs. It is very interesting whether the present "Coalescence Enhanced Synthesis" can be applied to a multi-component system where particle generation occurs in relatively long regions.

Fig. 3.1.1.2 shows the change of size and morphology of SiO_2/TiO_2 particles captured at 15 mm from the burner surface with and without CO_2 laser beam irradiation for Case 2. Without CO_2 laser beam irradiation, large spherical particles and aggregates with large primary particle size (ca. 30-40 nm) are observed. As CO_2 laser power increases, the original large particles with non-uniform morphology are changed into more-sintered particles and finally into spherical particles under a 2214W CO_2 laser beam irradiation as shown in Fig. 3.1.1.2(b).

The substance volume of non-spherical particles is characterized using the following statistical relationship between the number of primary particles in an aggregate, N_p, the projected area equivalent diameter, d_a and the mean primary particle diameter, d_{pm}. (Koylu, et al., 1995)

$$N_p = 1.15\left(\frac{d_a}{d_{pm}}\right)^{2.18} \qquad (3.1.1.1)$$

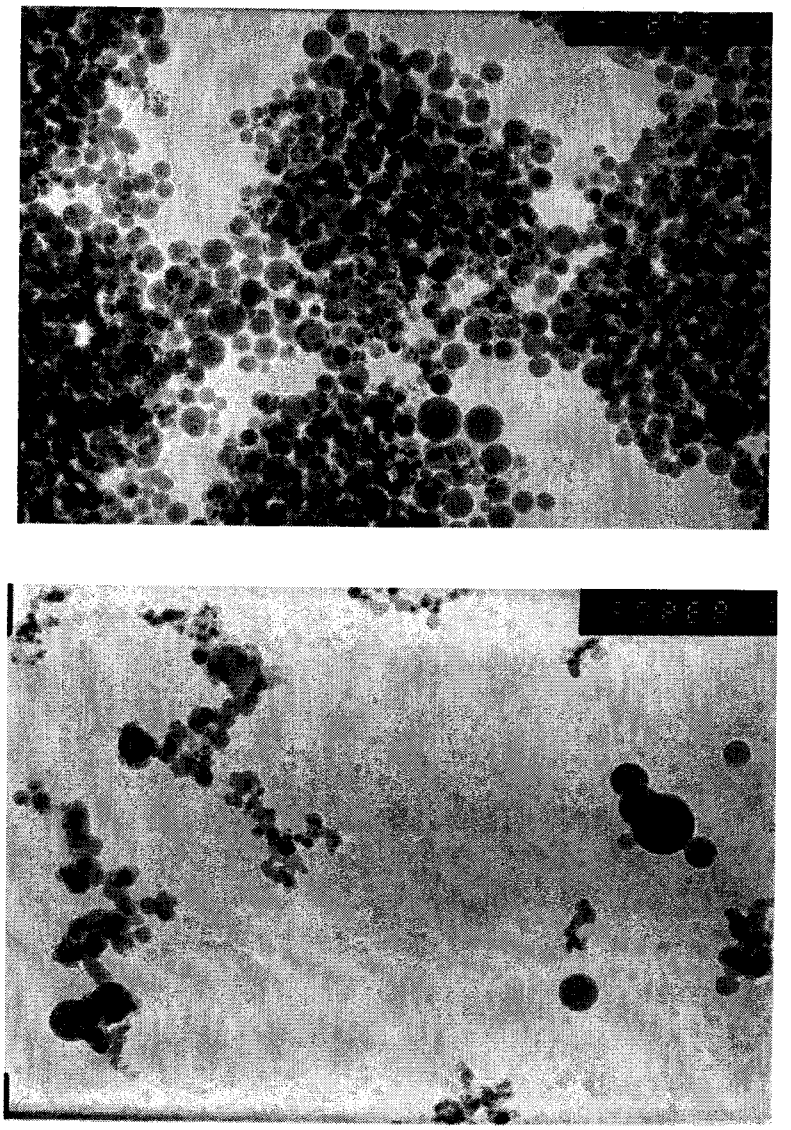

Fig. 3.1.1.2. TEM photographs of SiO_2/TiO_2 particles captured at 15 mm with and without CO_2 laser beam irradiation for Case 2; h_P=15mm, h_L=10mm.

From TEM image analysis using above characterization, it is found that the average volume of particles has decreased by ca. 10 times. The volume mean diameter of particles decreased from 100.8 nm (P = 0W) to 46.2 nm (P = 2214W). This change in particle volume confirms that the present method is to synthesize much smaller, spherical SiO_2/TiO_2 particles resulted from reduction of collision cross-sections of particles by enhancing coalescence of early stage particles in flame. Fig. 3.1.1.3. shows that size distributions of particles both with and without CO_2 laser irradiation are well approximated by log-normal size distributions. It is clear that size reduction and narrower size distribution can be obtained even with composite nanoparticles using the present "Coalescence Enhanced Synthesis".

The effect of CO_2 laser irradiation on crystallization of SiO_2/TiO_2 particles has also been investigated. Four experimental conditions with different mol % of Ti are chosen to verify the effect of CO_2 laser irradiation on crystallization. Fig. 3.1.1.4. shows X-ray diffraction patterns of powders collected at 55 mm from burner surface with (P = 2200W) and without CO_2 laser irradiation. It is very interesting that CO_2 laser irradiation can change crystallinity of nano-sized SiO_2/TiO_2 particles in flame. The crystallite sizes of anatase TiO_2 estimated using Scherrer equation are shown in Table. 3.1.1.2

Table 3.1.1.2 Crystallitesize estimated from Scherrer equation

	Case 1	Case 2	Case 3	Case 4
P = 0W	amorphous	amorphous	7.2 nm	12.4 nm
P = 2200W	amorphous	8.8 nm	12.0 nm	19.11 nm

Without CO_2 laser irradiation, crystallization of SiO_2/TiO_2 particles depends on the molar ratios of Ti to Si. As the content of Ti increases, peaks for anatase phase of TiO_2 appears and their intensity increases with increasing content of Ti. With CO_2 laser irradiation, the intensity of peaks for anatase phase of TiO_2 increases and the estimated crystallite sizes also increase except for Case 1 which has the lowest Ti content of 15 mol %. The possible reasons for crystallization with CO_2 laser irradiation will be discussed later.

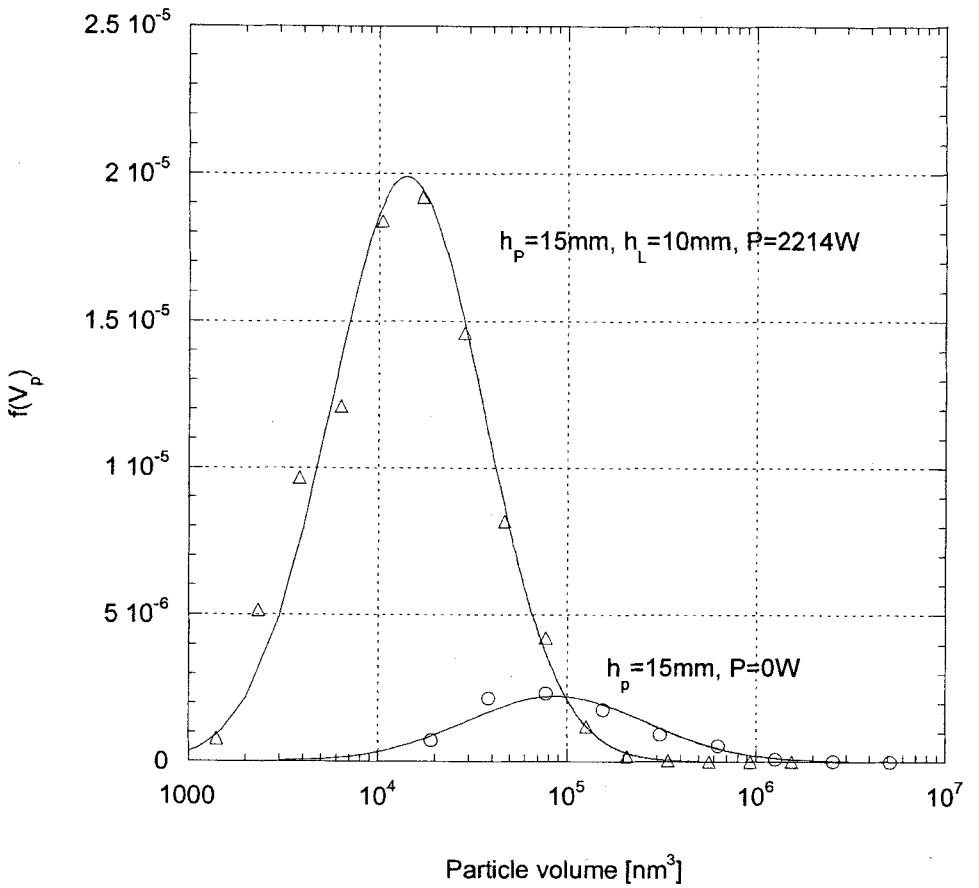

Fig. 3.1.1.3. Volume distribution of SiO_2/TiO_2 particles with and without CO_2 laser irradiation Case 2, h_P=15mm, h_L=10mm.

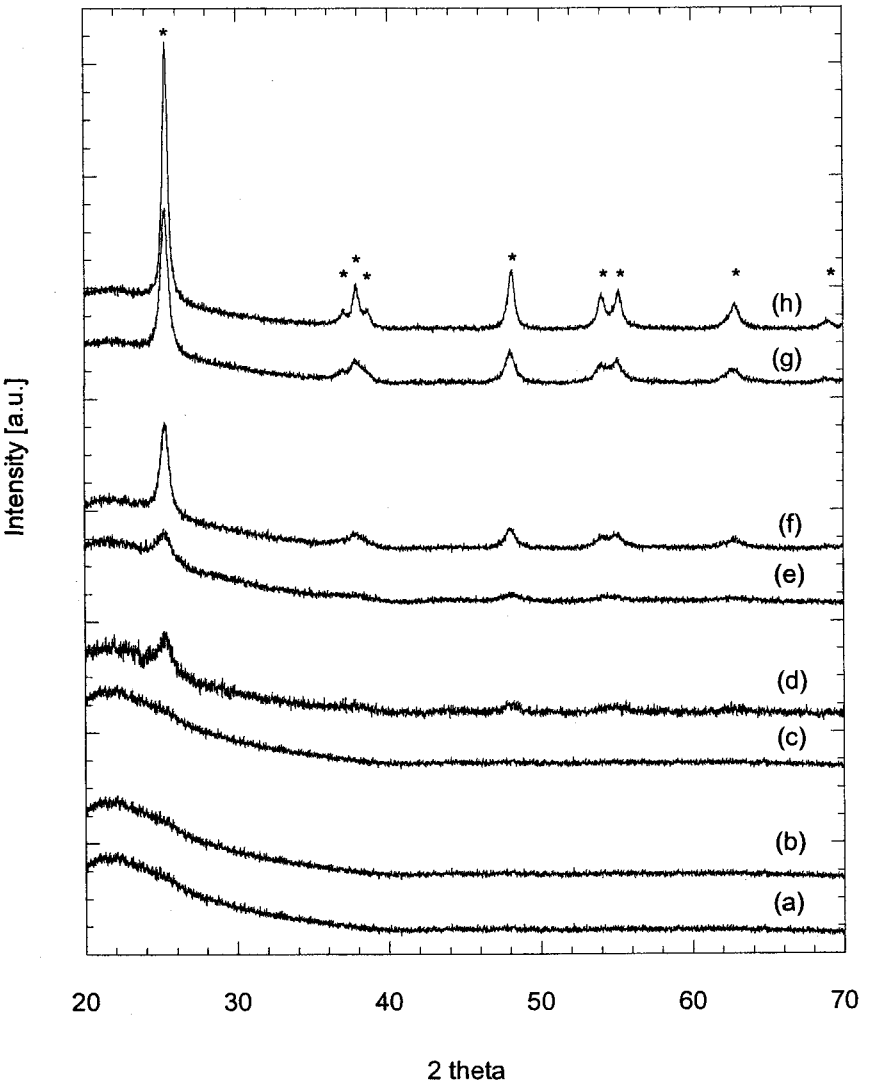

Fig. 3.1.1.4. X-ray diffraction patterns of collected powders of different Ti mol% with and without CO_2 laser beam irradiation; h_P=55 mm, h_L=28 mm.

(a) Case 1, 0W, (b) Case 1, 2200W (c) Case 2, 0W, (d) Case 2, 2200W

(e) Case 3, 0W, (f) Case 3, 2200W (g) Case 4, 0W, (h) Case 4, 2200W.

note: * in the figure denotes peaks of anatase phase

The effect of irradiating laser power on the crystallization of SiO_2/TiO_2 particles is shown in Fig. 3.1.1.5. The peak for (101) reflection of anatase TiO_2 appears when a 820W CO_2 laser beam is applied and its intensity increases with the laser power. Crystallite sizes estimated from Sherrer equation also increased with the increase of irradiating laser power from 6.9 nm for 820W, 7.9 nm for 1520W and 8.8 nm for 2200W.

Fig. 3.1.1.6 shows TEM photographs of SiO_2/TiO_2 particles collected at 55 mm with and without CO_2 laser irradiation for Case 2. Without CO_2 laser irradiation, amorphous SiO_2/TiO_2 particles are observed in TEM image. When 2200W CO_2 laser beam is applied at 28 mm, crystallite domains of TiO_2 with the size of 8-10 nm were observed.

Fig. 3.1.1.7. and Fig. 3.1.1.8. also confirm that crystallization occurs when CO_2 laser irradiation is applied. FT-IR spectra of collected SiO_2/TiO_2 powders are shown in Fig. 3.1.1.7. Without CO_2 laser irradiation (Fig. 3.1.1.7(a).), four bands are observed and their positions and the assignments of these bands are as follows: (i) 800 cm^{-1} for symmetric ν(Si-O-Si) stretching vibration; (ii) 950 cm^{-1} for ν (Si-O-Ti) vibration; (iii) 1090 cm^{-1} for asymmetric ν(Si-O-Si) stretching vibration; (iv) 1190 cm^{-1} for asymmetric ν(Si-O-Si) stretching vibration. (Dutoit, et al., 1995). Another band at 612 cm^{-1} attributed to the Ti-O-Ti bonding (Mohamed, et al., 2002) appears for powders collected at 55 mm when 2200W CO_2 laser beam is irradiated at 28 mm. (Fig. 3.1.1.7(b)). Raman spectra (Fig. 3.1.1.8) also confirm that crystallization of the SiO_2/TiO_2 particles in flame can be controlled with CO_2 laser irradiation. Bands at 952 and 1100 cm^{-1}both are assigned to ν(Si-O-Ti) vibrations. The crystallization with CO_2 laser irradiation is confirmed by the bands at 515 and 638 cm^{-1} which are attributed to crystalline anatase phase of TiO_2. (Dutoit et al., 1995).

Several possible reasons for crystallization by CO_2 laser irradiation are examined as follows. There are two possible types of interaction between TiO_2 and SiO_2: physically mixed (the formation of segregated TiO_2 micro-domains) and chemically bonded (the formation of Ti-O-Si linkages). According to previous studies, segregated TiO_2 domains are formed as the content of Ti atoms increases because silica could accommodate Ti atoms in the network in a certain limit. As shown in Fig. 3.1.1.4., the peaks for crystalline TiO_2 of anatase phase are observed in X-ray diffraction pattern with increasing mol % of Ti.

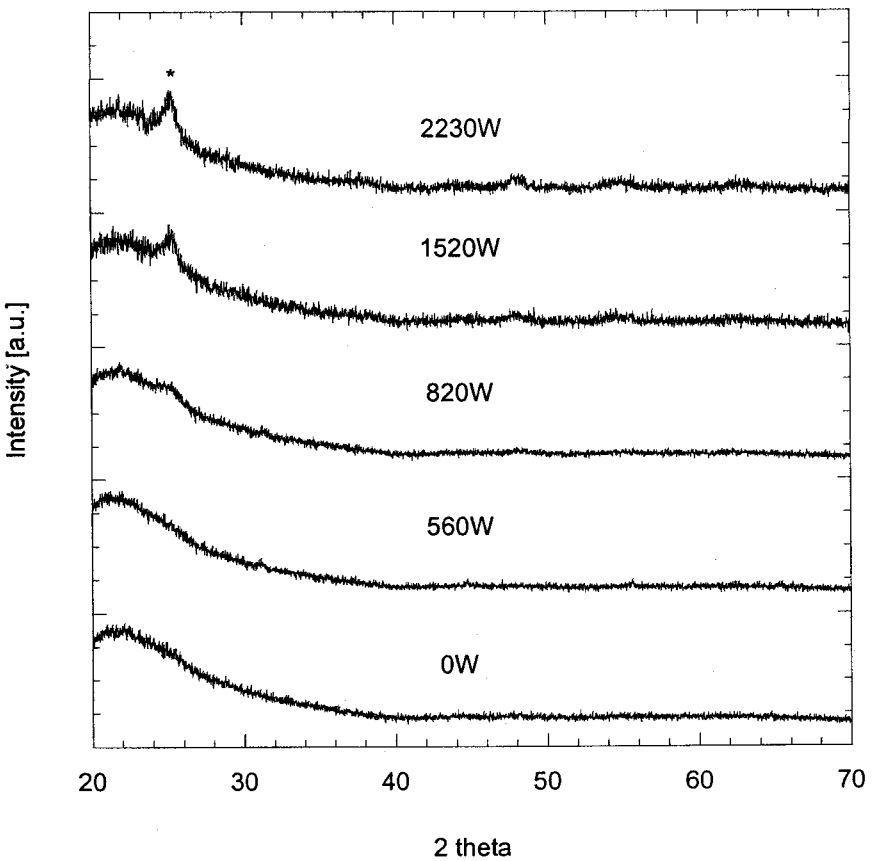

Fig. 3.1.1.5. X-ray diffraction patterns of collected powders at different powers of irradiating CO_2 laser beam for Case 2 (22 mol% of Ti); h_P=55mm, h_L=28mm.
note: * in the figure denotes the strongest peak of anatase phase
(2 theta = 25.3° for the (101) reflection)

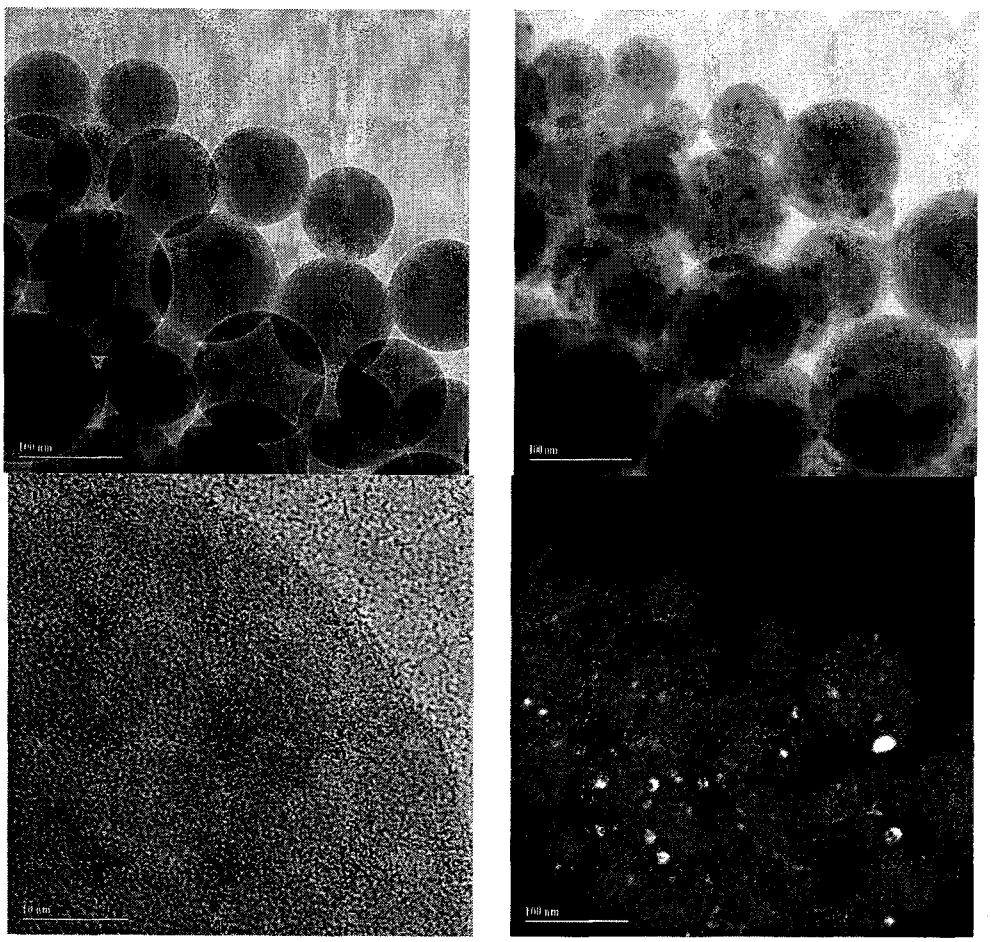

Fig. 3.1.1.6. TEM photographs of SiO_2/TiO_2 particles with and without CO_2 laser beam irradiation for Case 2 (22 mol% of Ti); h_P=55mm, h_L=28mm.
(a) 0W, (b) 2200W, (c) HR-image of crystallite, (d) Dark field image.

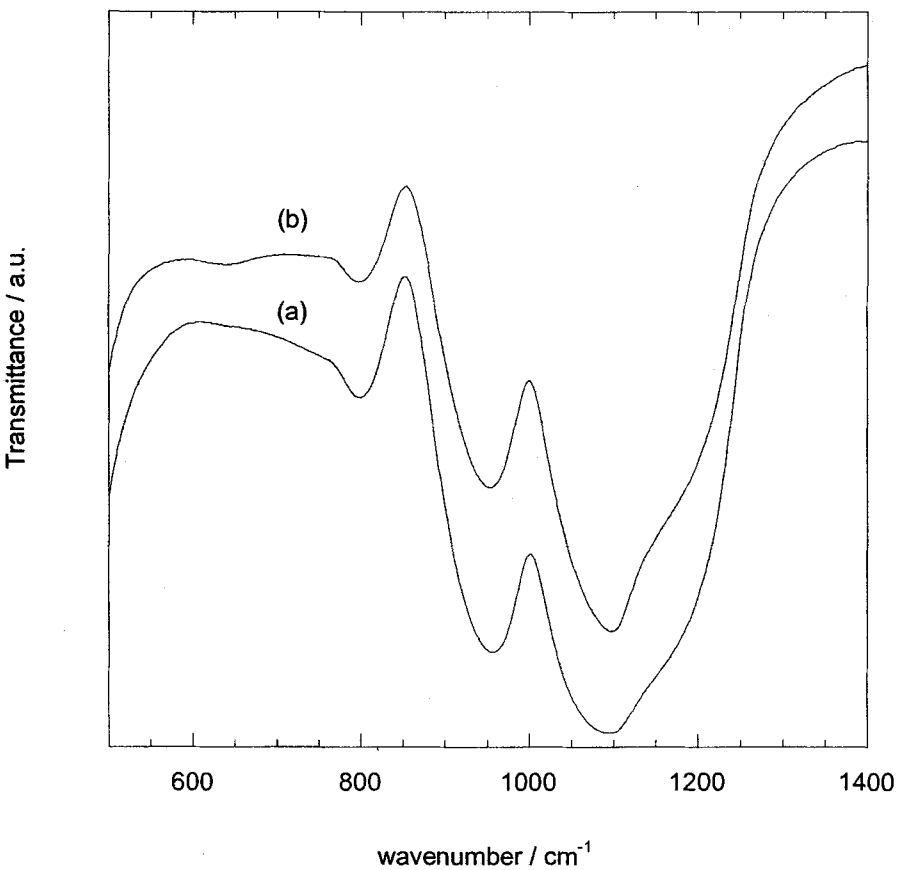

Fig. 3.1.1.7. FT-IR spectra of collected SiO_2/TiO_2 powders with and without CO_2 laser beam irradiation for Case 2 (22 mol% of Ti); h_P=55mm, h_L=28mm.
(a) 0W, (b) 2200W.

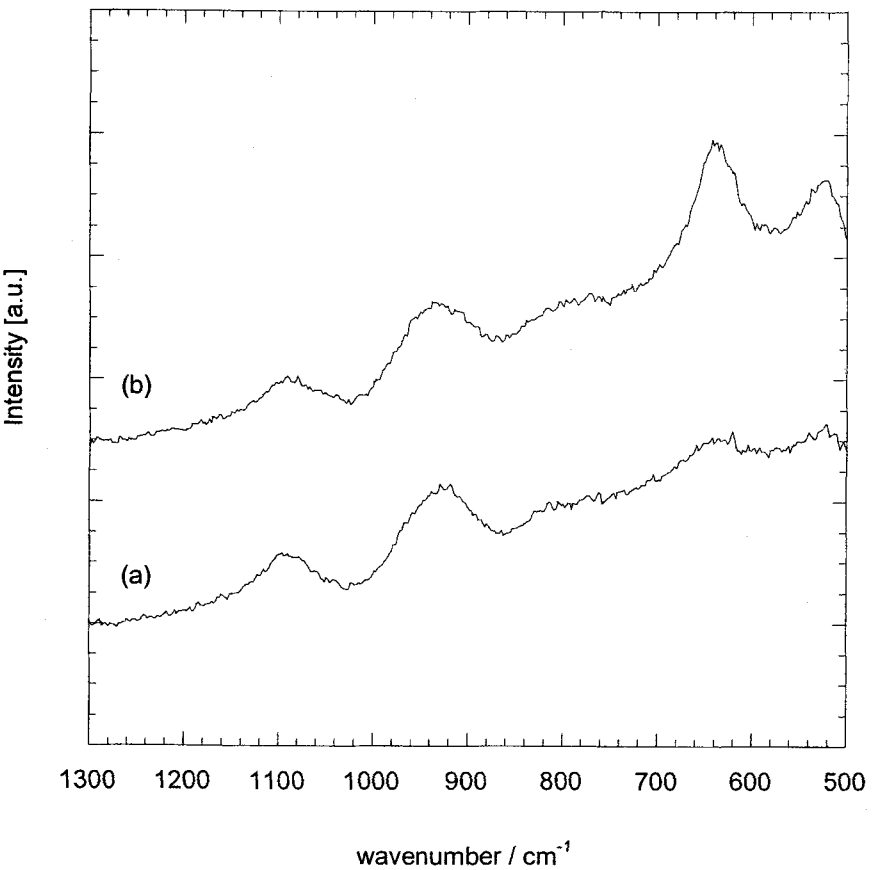

Fig. 3.1.1.8. Raman spectra of collected SiO_2/TiO_2 powders with and without CO_2 laser beam irradiation for Case 2 (22 mol% of Ti) ; h_P=55mm, h_L=28mm.
(a) 0W, (b) 2200W.

In order to verify if there is a change in molar ratio of SiO_2/TiO_2 particles, molar content of Ti in SiO_2/TiO_2 particles with and without CO_2 laser irradiation were measured with energy dispersive X-ray spectrometry (EDS). The result shows that there is a little change in composition within observational error (ca. 1 %) between collected powders with and without CO_2 laser irradiation. No evidence of possible recondensation of evaporated silica is found in TEM photographs sampled at heights, which are 5 mm higher than the position of CO_2 laser irradiation at various irradiation heights. This means that crystallization with CO_2 laser irradiation could not be explained by evaporation of silica from the SiO_2/TiO_2 particle surface, which would lead to change in composition or structural arrangement.

The possibility of breakage of Si-O-Ti bonding was also investigated with the evaluation of FT-IR results. According to Dutoit et al. and Klein et al., the ratio of the band intensity due to v (Si-O-Ti) at ca. 950 $cm^{-1}$to that due to v(Si-O-Si) at ca. 1190 cm^{-1} is a useful measure for the Ti dispersion in $SiO_2/TiO_2$and Si-O-Ti connectivity (Ti dispersion) is defined as follows

$$D_{(Si-O-Ti)} = \frac{I_{(Si-O-Ti)}}{I_{(Si-O-Si)}} \times \frac{x_{Si}}{x_{Ti}} \qquad (3.1.1.2)$$

$I_{(Si\text{-}O\text{-}Ti)}$ and $I_{(Si\text{-}O\text{-}Si)}$ denote the corresponding Gaussian-type integrals at 950 and 1190 cm-1, respectively, and xi equals the molar fraction of each species. Following the accepted band assignments, the spectral region of 750-1350 cm^{-1} has been deconvoluted into Gaussian curves using the IR spectra obtained for Case 1 to Case 4 with and without CO_2 laser irradiation. The results show that the ratio of the band does not change with CO_2 laser irradiation. This means that there is little possibility of breakage of Si-O-Ti bonding. The ratios of the bands and estimated values of $D_{(Si\text{-}O\text{-}Ti)}$ with various mol % of Ti are given in Table. 3.1.1.3.

Table 3.1.1.3. Estimated $I_{(Si\text{-}O\text{-}Ti)}/I_{(Si\text{-}O\text{-}Si)}$ and $D_{(Si\text{-}O\text{-}Ti)}$

	Case 1	Case 2	Case 3	Case 4
$I_{(Si\text{-}O\text{-}Ti)}/I_{(Si\text{-}O\text{-}Si)}$	1.06	1.24	1.15	0.96
$D_{(Si\text{-}O\text{-}Ti)}$	5.98	4.97	2.69	1.44

The ratio of the bands increased as Ti content increases from 15 to 21 mol %. This means that more Si-O-Ti bondings are forming and most of Ti atoms for Case 1 are well dispersed in silica structure. As Ti content increases more, the ratios of the bands decrease, which implies that silica structure is not able to accommodate all Ti atoms and additional Ti tends to form a segregated TiO_2 domain rather than to form Si-O-Ti bonding. The observational error for this estimation is ca. 3 %. The measured connectivity $D_{(Si\text{-}O\text{-}Ti)}$ for flame-generated SiO_2/TiO_2 is 5.98 for Case 2 (15 mol % of Ti).

The value from the results of previous studies for similar molar content of Ti was 2.9 (16 mol %, Dutoit et al.) and 6.5 (17 mol %, Klein, et al., 1996). This shows that Ti atoms in flame-generated SiO_2/TiO_2 particles are well dispersed in spite of the different reaction rates of precursors because high flame temperature enhances liquid or solid state diffusion.

Fig. 3.1.1.9. shows the effect of thermal annealing on powders collected at 55 mm without CO_2 laser irradiation. The powder for Case 2 without CO_2 laser irradiation is amorphous as deposited and shows crystalline peaks for anatase phase of TiO_2 after annealing at 900 °C for 30 min with the heating rate of 10 °C/min. The powder which has 15 mol % of Ti (Case 1) remained amorphous even after annealing. It is interesting that there is also no crystallization effect with CO_2 laser irradiation for Case 1 (Fig. 3.1.1.4(a), (b).). This means that flame generated SiO_2/TiO_2 particles become thermally more metastable as the Ti mol % increases and that, there exists uncoordinated TiO_2 nano-domains in SiO_2/TiO_2 particles because of the stress and strain. This existence of uncoordinated domain implies that the arrangement of species in flame could be controlled using CO_2 laser irradiation and its optical, catalystic properties could be changed with the irradiating CO_2 laser power. To our knowledge there has been no report so far on the in situ controllability of the structural properties of nano-sized SiO_2/TiO_2 particles in flame. Further studies are ongoing to investigate the effect of CO_2 laser irradiation on the crystallization of early stage SiO_2/TiO_2 particles where particle generation is still occurring and the mixing of SiO_2 and TiO_2 is not completed.

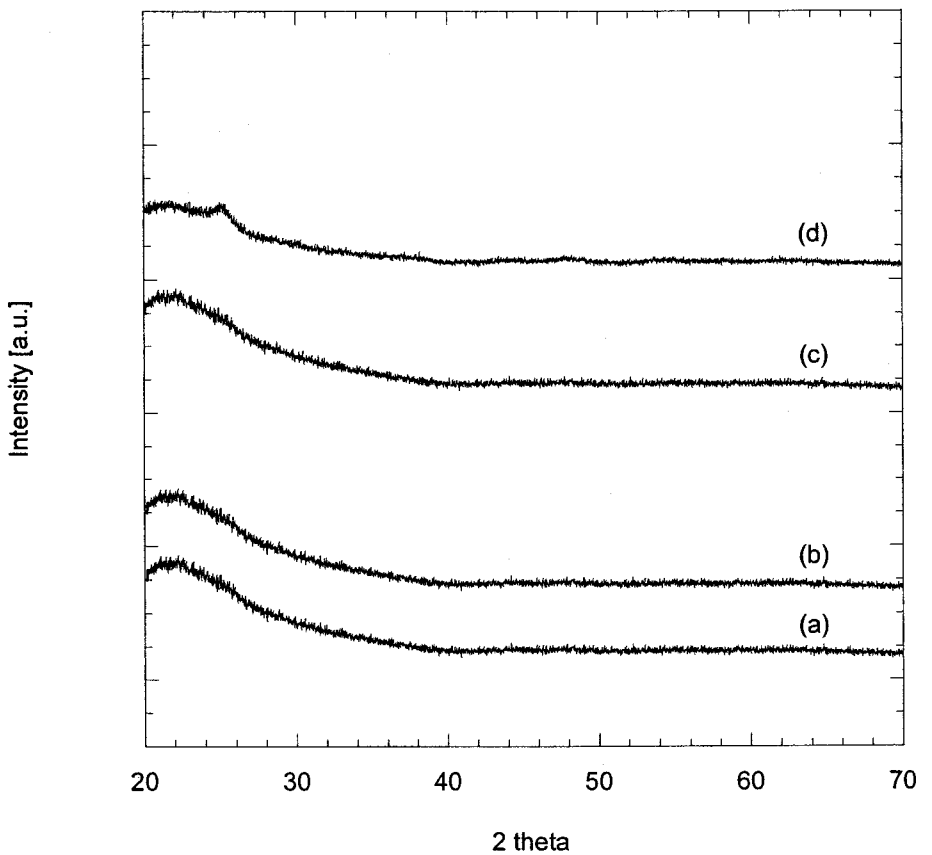

Fig. 3.1.1.9. X-ray diffraction patterns of collected SiO_2/TiO_2 powders with thermal annealing h_P=55mm, h_L=28mm, without CO_2 laser irradiation.
(a) Case 1, as deposited, (b) Case 1, annealed at 900°C,
(c) Case 2, as deposited, (d) Case 2, annealed at 900°C.

3.1.2. Study of synthesis and growth control of shell shaped carbon nanoparticle

● Introduction

Since the discovery of fullerenes and carbon nanotubes all new nanocarbon materials draw much attention expecting their superiority in electrical, optical, mechanical properties, etc. Recently we reported the synthesis of new kind of nanocarbon, namely, shell-shaped hollow carbon nanoparticles. X-ray diffraction (XRD) analysis shows high crystallinity of our particles. As one can see in transmission electron microscope (TEM) pictures these particles consist of alternating bent and flat graphene shells leading to possible sp^2/sp^3bonding hybridization on their junction. The great part of the junctions in our particles may be a reason for a lot of unusual properties. Motivated by this, we study electron spin resonance (ESR) spectra of our particles and measure magnetization with a superconducting quantum interference device (SQUID). We measure electrical field emission from our particles as well. It is worth noting that samples for the field emission experiments were made by means of direct *in-situ* deposition of flame generated particulate onto substrate unlike the multi-step sample preparation conventional for carbon nanotubes. Taking into account the higher manufacturability of fabrication of our particles and a possible easiness of their uniform deposition we may suggest them as a perspective material for electron field emitters.

● Methods

The experimental setup for particle generation consists of a co-flow burner and a CO_2 laser as shown in Fig. 3.1.2.1.. The co-flow burner we used consists of several coaxial annular nozzles in order to inject different gases into the system separately. Chemically pure grade acetylene is supplied through the center nozzle having a diameter of 2.0 mm at the flow rate of 0.1 lpm. Pure hydrogen and oxygen/nitrogen mixture having 25% oxygen mole-concentration is supplied at the flow rates of 1.0 and 2.0 lpm, respectively, through the next nozzles (I.D. = 10.5 mm, O.D. = 13.4 mm and I.D. = 15.8 mm, O.D. = 19.3 mm) to form an annular shaped co-flow diffusion flame. Nitrogen shield is also injected between the center and hydrogen nozzles to control C_2H_2 pyrolysis. Air is supplied through the outermost nozzle to stabilize the flame. The flame was irradiated with a CO_2 laser (Bystronic, BTL 2800) beam (wavelength 10.6 m). The laser power could be controlled up to the laser limit of 2800 W. The radiant emittance of the flame at specific wavelengths was measured with a spectrometer (Acton Research Co, Spectra Pro 300i) in order to determine the flame temperature. The geometry was chosen to measure the emittance from exactly the same region that is irradiated. The burner slide in the vertical direction provides a possibility to measure flame luminosity from different heights. The spectrometer was calibrated using a tungsten lamp (Sciencetech Inc., QTH 100W). The light scattering, laser-induced incandescence (LII), laser-induced PAH fluorescence (PLIF) techniques were also utilized in order to characterize flame at different conditions. The particles generated in flame were thermophoretically sampled either on copper grids using a localized sampling device or on a quartz tube.

The morhology of shell-shaped carbon nanoparticles we synthesized was studied with TEM and HRTEM. From the images we determined average number of graphene shells and the intersheet spacing in our particles. The particle crystallinity was checked with X-ray diffraction analysis. The lattice parameters were found. ESR spectra from collected particles were measured with a Bruker ESP 300E spectrometer operating at X-band at the temperatures ranged from 2 K to 300 K. These spectra are useful in order to describe the temperature dependent spin behavior in our particles. Magnetic properties of our particles were studied with a SQUID magnetometer (Quantum Design, MPMS 7) over a temperature range of 2 to 300 K at magnetic fields up to a device limit of 7 T. These measurements together with ESR spectra allow one to elucidate the origin of different contributions in total particle magnetization.

Being a good gas adsorbent our particles are covered with oxygen during SQUID measurements at low temperatures. We utilized a device peculiarity of SQUID system consisting of the presence of a little amount of oxygen in the system in order to vary oxygen coverage just during measurements. Then the extra magnetization caused by additional oxygen coverage can be obtained with higher precision than the one at known experiments on study of oxygen magnetism. The high precision could be reached since we covered with oxygen the same sample at all the measurements. Then the extra magnetization is only the difference between the magnetization measured at different coverage. The precision we achieved allowed us to plot the extra magnetization as the universal function of applied

magnetic field and temperature. For the first time we were able to claim that the extra magnetization caused by carbon coverage with oxygen does not obey the Curie-Weiss law at low temperatures.

Electron emission from carbon nanoparticles deposited on metal coated-p+-Si wafer was investigated. Field emission tests were performed in a vacuum chamber at the pressure of 1 10^{-7} Torr. A positive voltage was applied to the anode using Keithley-248 and current was detected at the anode as a function of the applied field. The anodewas phosphor coated ITO glass. The experimental data were fitted into the Fowler-Nordheim plot. Carbon nanoparticles were treated under hydrogen plasma of 100W in power. The effect of hydrogen plasma on emission properties of carbon nanoparticles was estimated. The emission stability of carbon nanoparticles was tested. The field emission from our particles was compared with that from carbon nanotubes showing good performance.

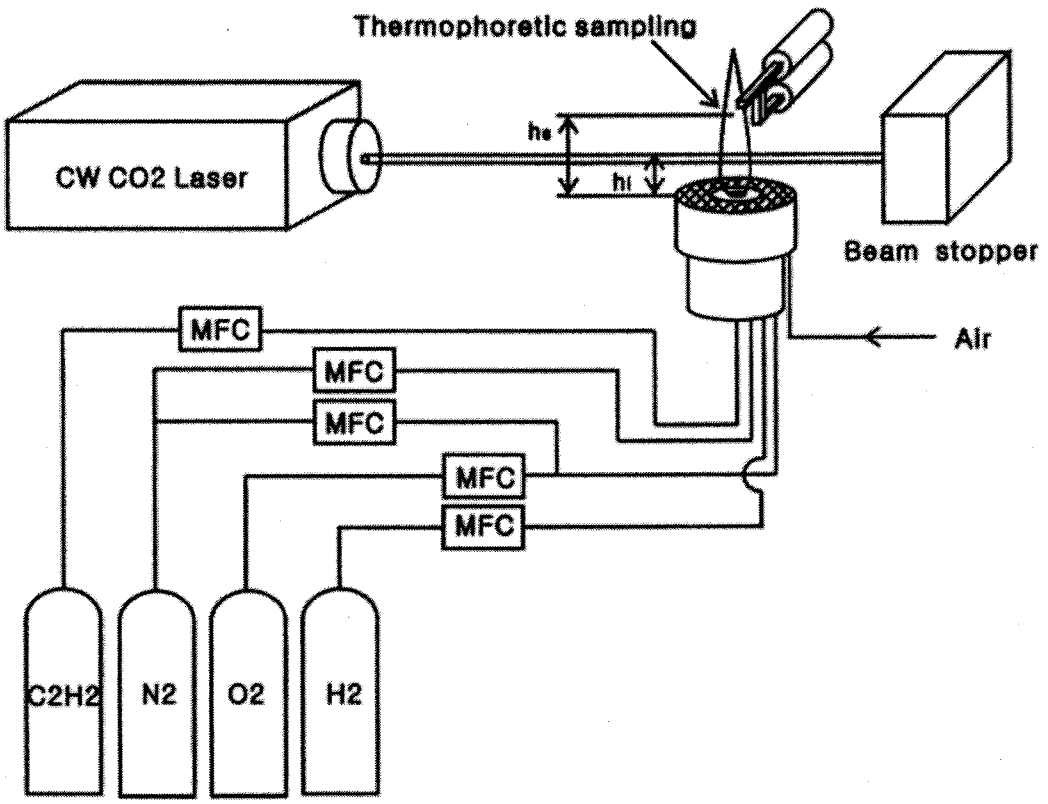

Fig. 3.1.2.1. Schematic of the experimental setup to produce shell-shaped carbon nanoparticles

● Results and discussion

Using TEM images of collected particles we established that the flame irradiation by a CW CO_2 beam leads at certain conditions to the transition of conventional soot generation to the formation of shell-shaped hollow carbon nanoparticles. The typical TEM images of soot and shell-shaped particles are given in Fig. 3.1.2.2 and Fig. 3.1.2.3, respectively. Without laser irradiation soot starts to generate at a height about 10 mm from the burner edge. The HRTEM image of shell-shaped carbon nanoparticles we synthesized is given in Fig. 3.1.2.3.. As one can see particles look like hollow multilayer onions. We found the average number of graphene sheets to be about 15. The characteristic distance between graphene sheets is about 3.45 Å . As one can also see there are two different regions in our particles, namely, flat and bent regions. The junctions between these regions (see arrow in Fig. 3.1.2.3.) are a considerable part of our particles. The TEM images (see Fig. 3.1.2.3.) clearly show the uniformity and identity of the particles and the absence of any deviations in structure in a raw product of acetylene conversion.

The typical X-ray diffraction pattern of shell-shaped carbon nanoparticles is given in Fig. 3.1.2.4.. The particle lattice parameters calculated from the X-ray diffraction pattern assuming the hexagonal structure are a = 2.44 Å and c= 6.90 Å that corresponds to the intersheet distance observed in the TEM image. The quite narrow (002) X-ray peak at about 25 ° has a non-perfect shape. It suggests the possible presence of two kinds of carbon regions having a different structure. After deconvolution of this peak, we obtained that (002) peak consists of a narrow peak centered at 25.74 ° and a broad peak centered at 24.53 °. Obviously, the narrow peak corresponds to graphene sheets (the estimated interlayer distance is 3.46 Å). Although the broad peak is usually ascribed to the presence of disordered (amorphous) carbon phase, we consider that the broadness would be due to deformed carbon regions at junctions between graphene layers. The absence of amorphous phase is discussed below where results of ESR measurements are interpreted. The relatively large broad peak (its area is 2 times bigger than the narrow peak area) indicates a significant fraction of these bent sheets in our particles. Then the mean interlayer distance at the bent region can be estimated from the position of the broad peak as 3.63 Å . The difference between the interlayer distances in the flat and bent regions may be distinguished directly in the HRTEM image as well.

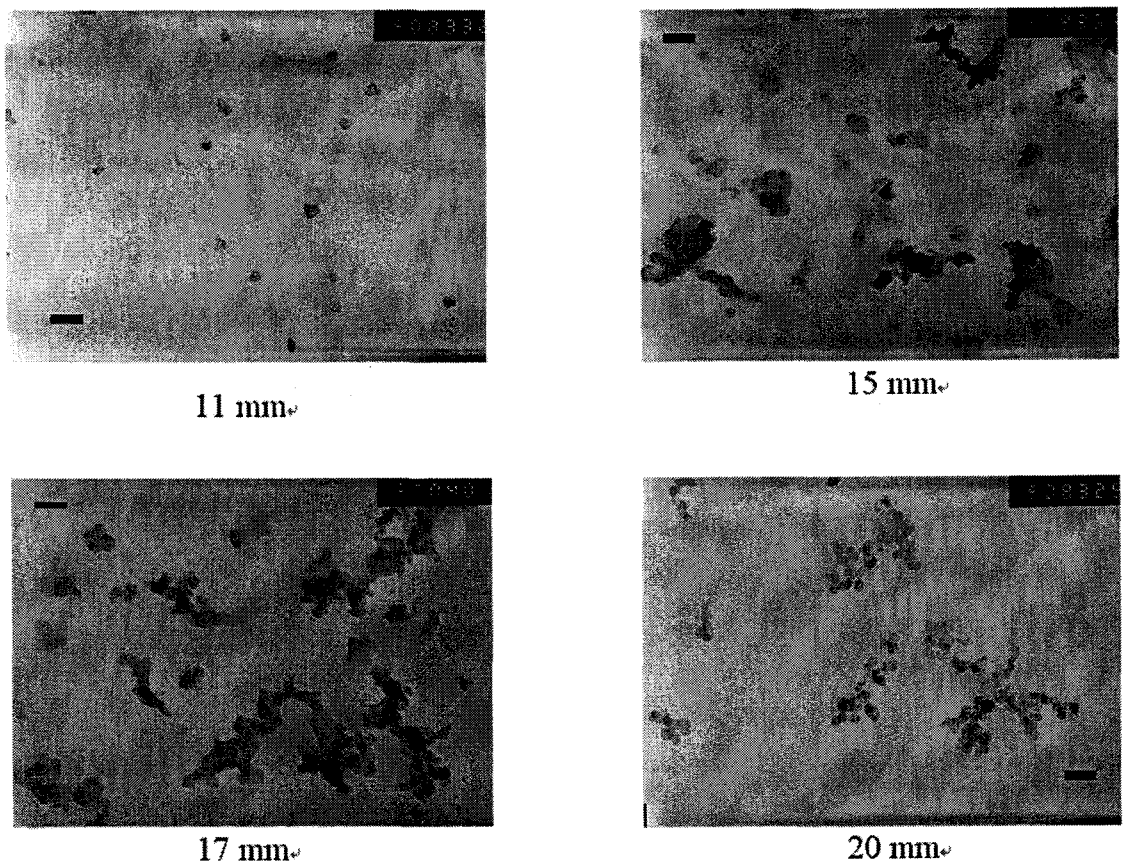

Fig. 3.1.2.2. TEM images of soot collected at different heights. Scale bars represent 100 nm

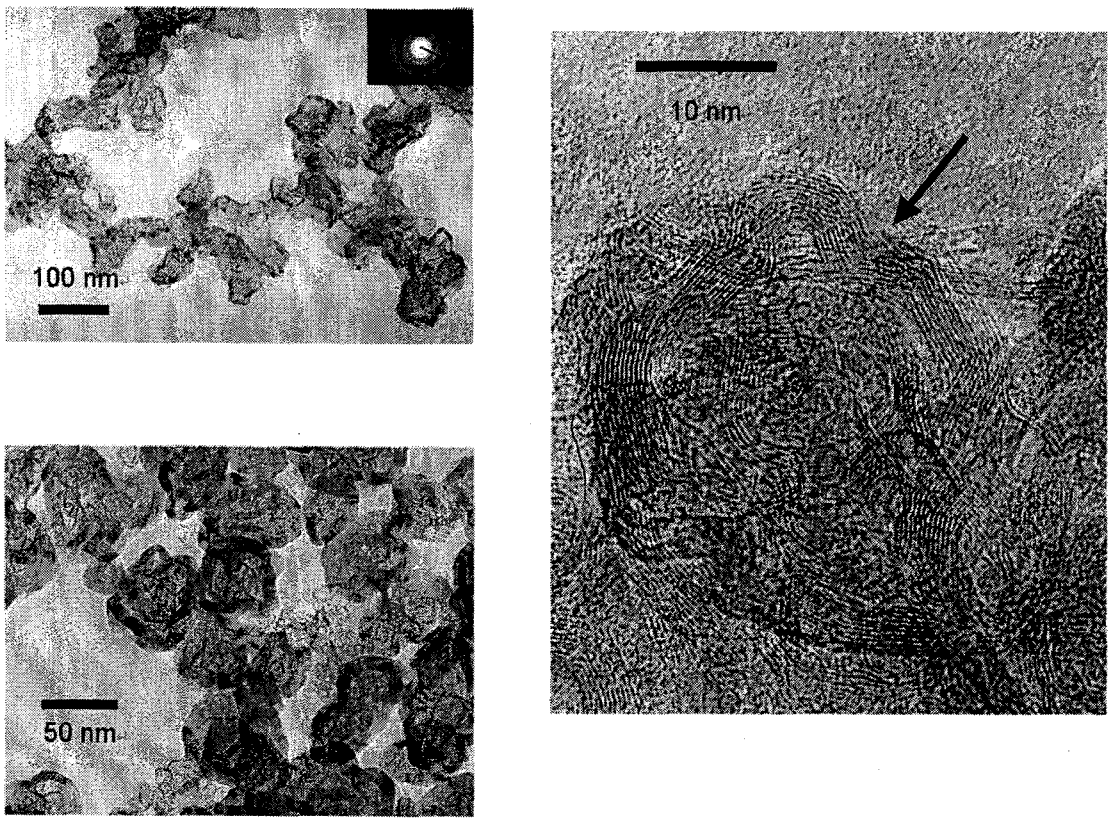

Fig. 3.1.2.3. TEM/HRTEM images of shell-shaped carbon nanoparticles.

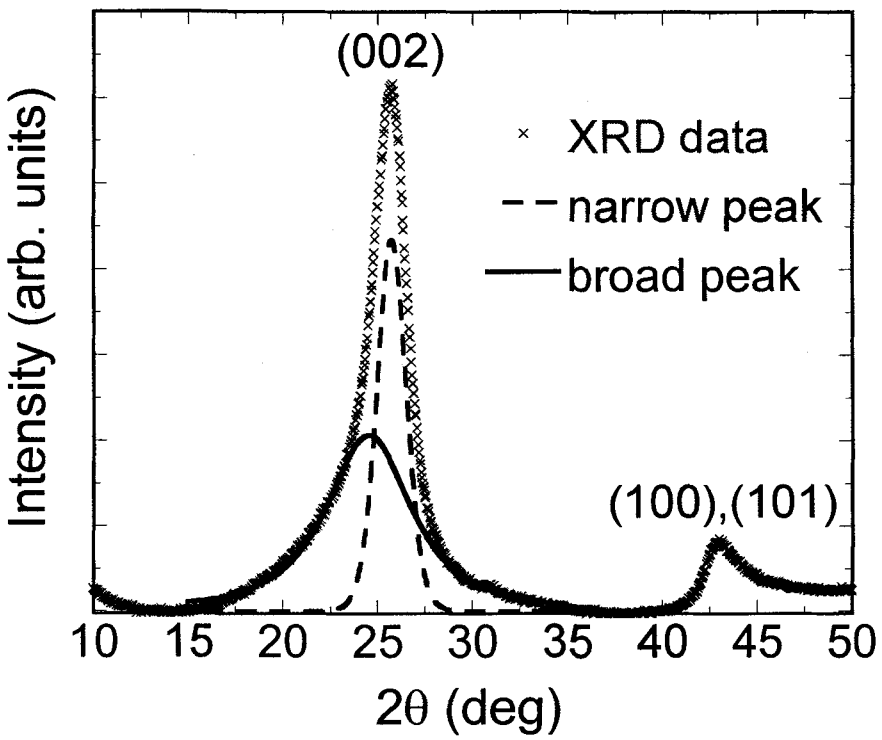

Fig. 3.1.2.4. X-Ray diffraction pattern from shell-shaped carbon nanoparticles

In order to investigate particulate evolution in our flame we irradiated flame at different heights applying different laser powers. It was found that flame shape changes dramatically when laser power exceeding of 1400 W is applied at the height about 9 mm from the burner edge. The typical flame photographs at different regimes of flame irradiation are shown in Fig. 3.1.2.5. clearly demonstrating the change of flame conditions when irradiated at 9 mm. It should be noted that shell-shaped carbon particle generation starts simultaneously with the change of the flame shape. The production rate of shell-shaped particle generation is about 5 g/hour.

The quantitative information about the variation of flame conditions was derived from the measured flame luminosity. When the flame is irradiated at positions, where soot exists and no change in particulate properties is observed at any applied laser powers the flame luminosity only increases continuously with the laser power. However, when the laser irradiates the flow at a position, where no particulate is found, namely, at the height of 9 mm from the burner edge, and the laser power exceeds a certain value (about 1400 W in our experiment), the flame luminosity changes abruptly. Fig. 3.1.2.6. shows the flame luminosity at wavelength λ= 600 nm vs. the applied laser power measured at different flame heights. Note once again that shell-shaped particle generation starts together with the abrupt jump of the flame luminosity.

In order to determine particle temperature when flame is irradiated we studied the ratio of the flame luminosity with and without laser irradiation upon the wavelength. This ratio is given in the Wien limit of the Planck function by

$$\ln\left(\frac{I_\lambda}{I_{\lambda 0}}\right) = \ln\left(\frac{f_V}{f_{V0}}\right) + \frac{hc}{k_B \lambda}\left(\frac{1}{T_{p0}} - \frac{1}{T_p}\right) \qquad (3.1.2.1)$$

where fV is the particle volume fraction and the subscript "0" denotes the value when there is no laser irradiation. It is obvious that the slope of $ln(I/I_0)$ upon the inverse wavelength gives the change of reciprocal particle temperature and allows one to derive the actual particle temperature. The result of such a procedure made for measurements at different irradiated heights is given in Fig. 3.1.2.7.. The abrupt jump of particle temperature is seen at the laser power about 1400 W when flame is irradiated at 9 mm while temperature increases continuously at other irradiation heights.

Let us carefully analyze the variation of the flame temperature and the properties of generated particles under the laser irradiation. Note that unlike the known papers on the laser-driven pyrolysis when acetylene was photosensitized there is no gaseous species in the flow that are able to absorb the laser irradiation in our case. It is worth noting that these shell-shaped hollow carbon nanoparticles are formed within the laser beam during the time not exceeding 1 ms that is much shorter than a typical time of 100 ms corresponding to occurrence of internal rearrangement processes in carbon. The fact that only the irradiation case at the height of 9mm (where soot does not exist) generates carbon onions clearly indicates that the generation is not related to the transformation of the existing soot that had

been studied by others. Then we can conclude that we observed a previously unknown pathway of acetylene conversion into crystalline nanocarbon. The distinctive feature of this pathway is a direct graphitization occurring on the surface of a growing particle from nuclei instead of conventional "mechanical" addition of acetylene and polycyclic aromatic hydrocarbons (PAHs) leading to generation of amorphous soot. It is the laser irradiation that switches the regimes of particle generation. Indeed, a mechanical agglomeration of gaseous species resulting soot formation does not require overcoming a high activation barrier. In turn, the direct graphitization such as $C_2H_2 \rightarrow 2C+H_2$, for instance, being an exothermic reaction is a highly activated one. Being absorbed the external radiation brings the additional energy which allows the particle to be heated up in a critical way, i.e., a temperature jump. The jump is caused by a non-monotonous dependence of overall heat release on the surface of the particle growing from gas via an activated chemical reaction upon the particle temperature. Such a non-monotonous dependence had been established when the surface growth of oxide nanoparticles during metal combustion was considered. Obviously, at lower temperatures the addition of gaseous species alone is possible while suppressing the activated surface chemical reaction. The application of laser irradiation changes the situation. At a certain laser irradiance exceeding the critical value the activation barrier can be overcome and surface graphitization reaction occurs generating crystalline particles. Exothermic reaction heats up the particle further and enables the temperature jump to occur. At the same time the carbon evaporation leading to the carbon clusters generation with a high rate brings new nuclei into the system. The latter provides the self-sustained process of the acetylene conversion. At the higher irradiated positions where the particulate has already become amorphous soot via the conventional (PAH agglomeration) mechanism, the activation energy becomes so large that the absorption of the laser irradiation even at the highest power used in the study could not heat particles up to the graphitization temperature. Then it becomes understandable why the switching from amorphous soot formation to the generation of shell-shaped hollow carbon nanoparticles occurring in the critical way is possible in our experiment only at the certain irradiation height.

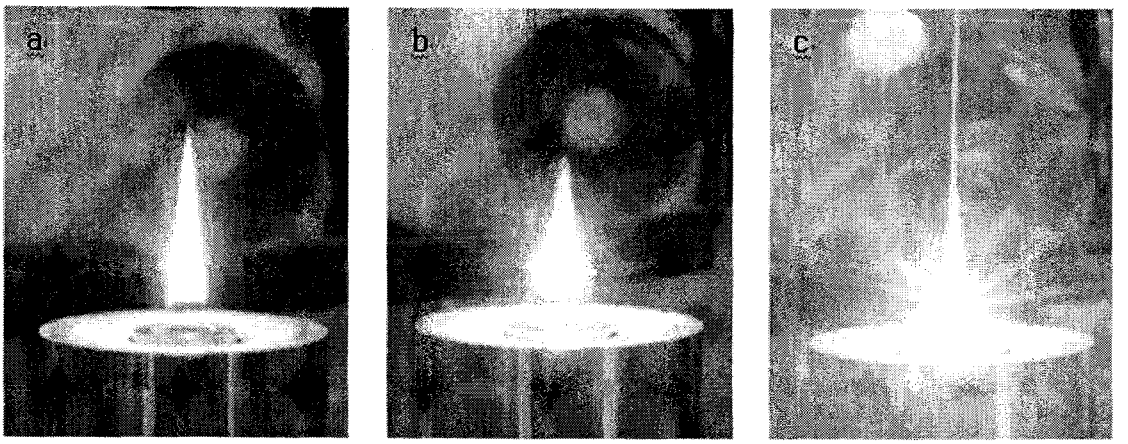

Fig. 3.1.2.5. Photographs of the flame at different irradiation conditions:

a. Without irradiation;

b. Height 15 mm, power 1500 W.

c. Height 9 mm, power 1500 W.

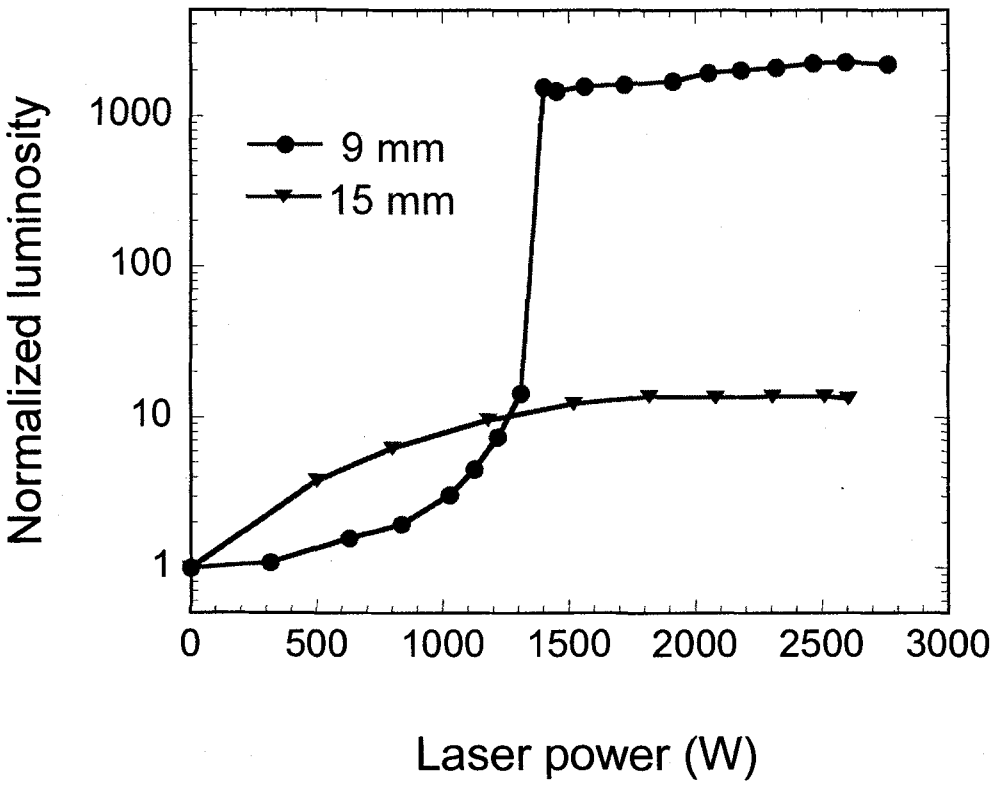

Fig. 3.1.2.6. Flame luminosity at wavelength λ=600nm vs. the applied laser power at different flame heights. Values are normalized on the case of no laser irradiation.

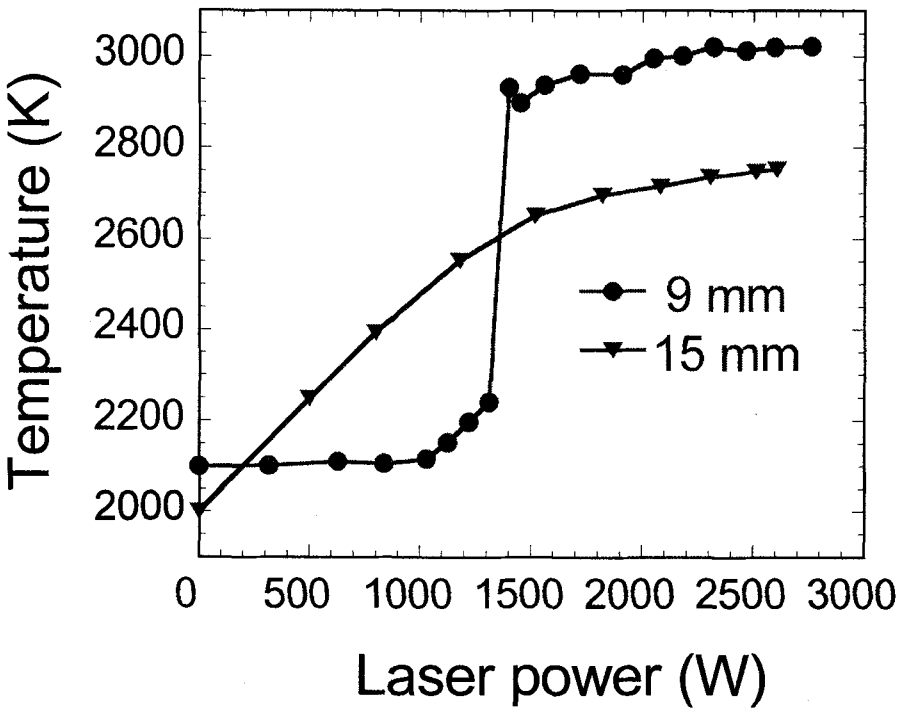

Fig. 3.1.2.7. Dependence of particle temperature upon the laser power at different irradiated heights.

Electron emission from our carbon nanoparticles deposited on metal coated-p^+-Si wafer was investigated. Field emission tests were performed in a vacuum chamber at the pressure of 1 10^{-7} Torr. A positive voltage was applied to the anode using Keithley-248 and current was detected at the anode as a function of the applied field. Anode was phosphor coated ITO glass. As shown in Fig. 3.1.2.8., the emission current of the order of microampere can be detected at the electric field of 2.5 ~ 3.8 V/m depending on deposition time (number of turns). Onset electric field intensity of 2.5 V/m is similar to the value reported for the carbon nanotubes. The experimental data were well fitted into Fowler-Nordheim plot as shown in the inset of Fig. 3.1.2.8., which implies that electron transport mechanism is governed by the Fowler-Nordheim model. Shell-shaped carbon nanoparticles were treated under hydrogen plasma of 100W in power. The effect of hydrogen plasma on emission properties of carbon nanoparticles was estimated. A significant degradation of the field emission characteristics of CNTs was reported recently especially under O_2 ambient. The emission stability should be fully addressed for commercialization of carbon nanoparticles as electron emitters in a field emission display and various vacuum microelectronic devices. The emission stability of carbon nanoparticles was tested and shown in Fig. 3.1.2.9.. In the vacuum of 1 x 10^{-7} Torr, the electron emission from carbon nanoparticles was very stable and little degradation in emission current was found in the 1 x 10^{-6} Torr of O_2 ambient, but a small degradation in emission current was detected at 5 x 10^{-6} Torr O_2 exposure.

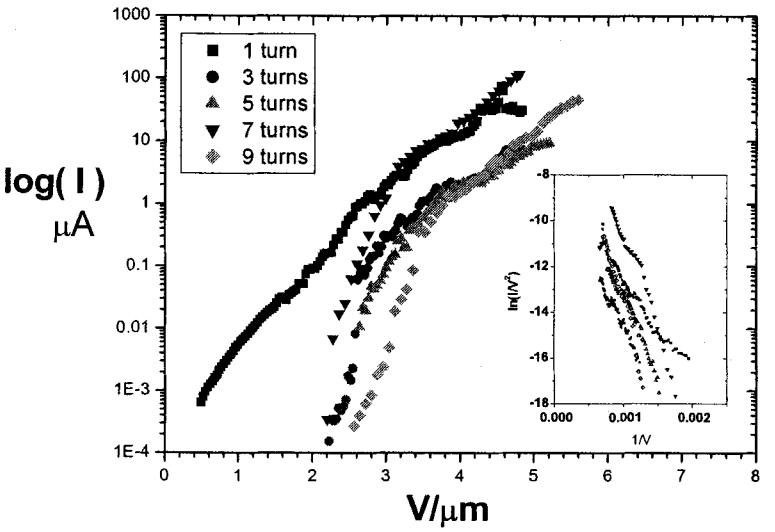

Fig. 3.1.2.8. Field emission current vs. applied field.
Inset illustrates Fowler-Nordheim dependence

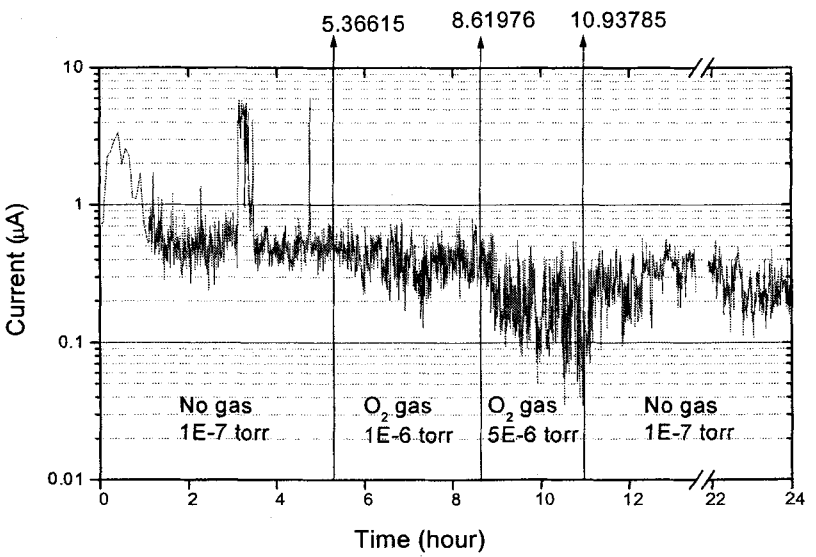

Fig. 3.1.2.9. Emission stablility of shell-shaped carbon nanoparticles

3.1.3. Jet assisted aerosol CVD to control particle transport and deposition

● Introduction

It was proposed a novel aerosol CVD method utilizing high temperature internal jets in the conventional silica tube reactor, and demonstrated the validity of the jet-assisted method for SiO_2 deposition by not only achieving substantial increases of efficiency (and rate) of particle deposition, but also by reducing axially non-uniform deposition zone significantly. In the present work, we extended our earlier work (Choi et al. 2002) to multi-component deposition. The same principle of the increase of thermophoresis and the reduction of particle travel distance by using a high temperature inner jet will be applied to the enhancement of multi-component particle deposition of SiO_2/GeO_2 as shown in Fig. 3.1.3.1. Particularly, it is very important to obtain the uniformity of composition (SiO_2/GeO_2), since controlling concentration of each component of the perform is essential to change the optical property. The proposed jet-assisted CVD method for multi-component deposition is expected to yield the enhancement of uniformity of composition as well as deposition efficiency and the tapered entry length.

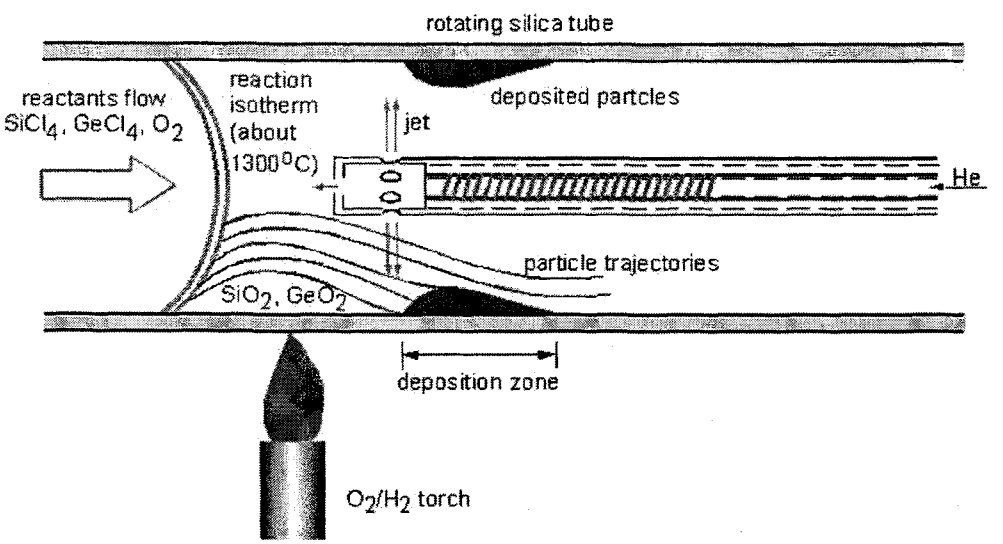

Fig. 3.1.3.1 Schematic diagram of jet assisted CVD method.

● Methods

The experimental setup for the multi-component deposition process used in the present work is nearly the same as that in our earlier work (Choi et al. 2002). An oxy-hydrogen torch heats a rotating silica tube of I.D. 28 mm and O.D. 32 mm and traverses at the constant speed of 10 cm/min over the pass length of 50 cm following the one dimensional transport system. The rotating speed of the silica tube is 60 rpm. High temperature jet gas is injected through a heated inner tube, which is inserted inside the silica tube. Various chemical gases such as $SiCl_4$, $GeCl_4$ and $POCl_3$ are entrained into a

silica tube by passing carrier gas, O_2, through each liquid dopant source contained in the bubbler whose temperature is maintained at 26 °C. The flow rates of carrier gas (O_2), jet gas (helium or N_2) and fuels (H_2 and O_2) are controlled and measured by mass flow controllers (respectively, TYLAN, FC-260, FC-280SA, FC-280S, FC-2920). Two infrared thermometers and a B-type thermocouple (Omega, Pt with 6 percent Rh Pt with 30 percent Rh) were used for measurement of the surface temperature of the rotating silica tube and jet exit temperature of helium gas, respectively. Emissivities of 0.98 for the high-temperature thermometer and 0.9 for the low-temperature thermometer were used (Cho and Choi 1995). Each mass flow rate of $SiCl_4$, $GeCl_4$ and $POCl_3$ is obtained by measuring the mass change of each bubbler for a given time interval during deposition process using the electronic balance (OHAUS, GT-8000). Noting that the overall deposition efficiency can be obtained by comparing the actually deposited particle mass with the maximum possible deposition mass, the following relations could be suggested in multi-component deposition process:

$$E = \frac{\Delta tube}{\Delta SiCl_4 \times \frac{M_{SiO2}}{M_{SiCl4}} + GeCl_4 \times \frac{M_{GeO2}}{M_{GeCl4}} + \frac{1}{2} \times \Delta POCl_3 \times \frac{M_{P2O5}}{M_{POCl3}}} \qquad (3.1.3.1)$$

where Δ and M denote the weight change and molecular weight, respectively. The constant of 1/2 in denominator results from the peculiarity of $POCl_3$ oxidation (one mole of P_2O_5 is generated from two moles of $POCl_3$). After deposition process, the perform is cut offinto pieces along the axial direction so that the axial variations of the deposition thickness were examined under an optical microscope (Mitutoyo, FS60) to determine the uniformity of particle deposition. Of interest for the multi-component deposition process is the uniform composition of each component. EPMA, that is, an electron probe micro analyzer (JEOL, JXA-8900R) is used to analyze the variation of composition along the axial direction.

Major parameters of the present study for the verification of jet gas are the flow rates of helium jets varying from 0.5 to 2.0 l/min and jet temperatures of 970 and 1050 °C while each mass flow rate of $SiCl_4$and $GeCl_4$ is fixed as 1.43 and 0.27 g/min, respectively. A little amount of $POCl_3$ (0.05 g/min) is used in order to reduce the process temperature. As mentioned earlier, it is required to analyze the composition of the deposited layer (or concentration of each component) in the multi-component deposition.

● Results and discussion

Fig. 3.1.3.2 shows the variation of GeO_2 mass fraction along the axial direction for conventional and jet-assisted method with various temperatures when the helium jet flow rate is 1.5 l/min. The composition for the case of the jet injection becomes uniform along the axial direction, while the conventional method yields the non-uniform composition variations. It is observed that GeO_2 mass fraction in jet-assisted is smaller than the one in the conventional case due to an inverse reaction of

$GeCl_4$ induced by high temperature jet gas. Accordingly, GeO_2 mass fraction decreases as the jet temperature increases from 970 to 1050 °C. For the verification of reverse reaction of $GeCl_4$, mole fraction of GeO_2 in the deposited layer for the conventional case was measured with various maximum surface temperatures of silica tube, whichare somewhat higher than the temperature of the hot zone inside the tube. Fig. 3.1.3.3 ensures the effect of reverse reaction of $GeCl_4$, that is, GeO_2 mole fraction decreases as the maximum surface temperature. Generally, the maximum incorporation of $GeCl_4$ occurs at temperatures near 1850 K with smaller concentrations in the deposits at both lower and higher temperatures (Nash et al., 1984). Fig. 3.1.3.3 is in a good agreement with the previous analysis which suggested that the inefficient incorporation of $GeCl_4$ was due to a limited reaction rate for $T <$ 1850 K and due to an unfavorable equilibrium in the oxidation of $GeCl_4$ for $T >$ 1850 K.

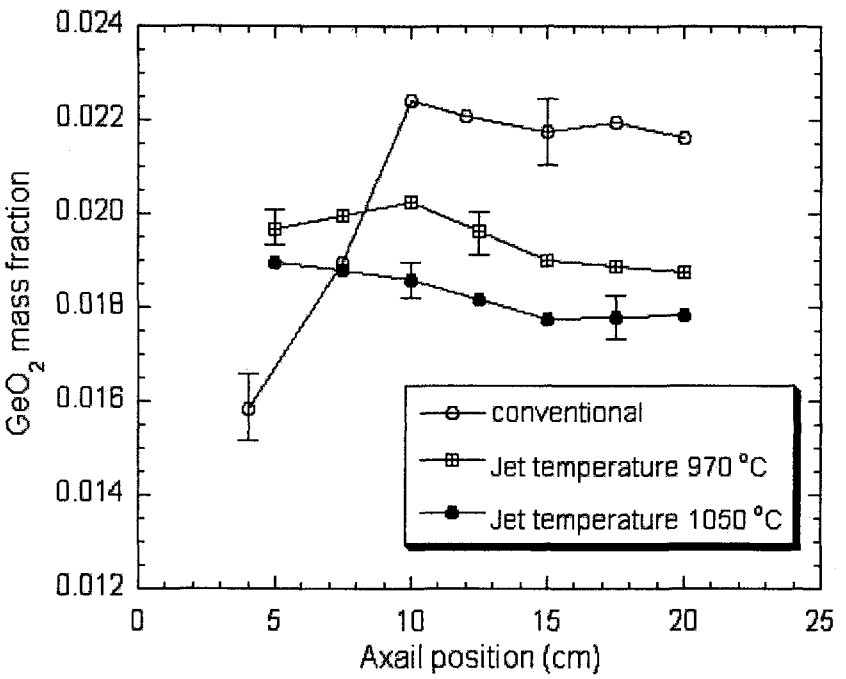

Fig. 3.1.3.2 Axial variation of GeO_2 mass fraction for the conventional and the present jet-assisted method for different jet temperatures at 1.5 l/min flow rate of helium jet.

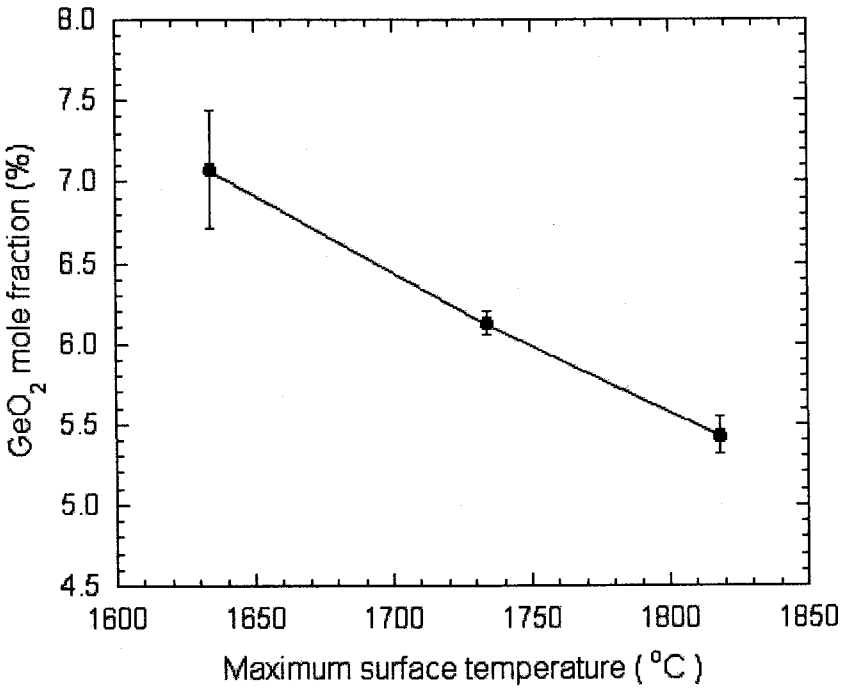

Fig. 3.1.3.3. GeO_2 mole fraction for various maximum surface temperatures; mass flow rates of $SiCl_4$ and $GeCl_4$are 1.0 and 0.25 g/min, respectively.

After the deposition process, the perform was cut along the axial direction, then the deposition thickness was measured by using the optical microscope (Mitutoyo, FS60) and scanning electron microscope (JEOL, JSM-T200). Fig 3.1.3.4 shows the SEM image of deposited layer for the conventional case (the axial position is 20 cm), when the deposition process was performed for 3 passes. It reveals that the deposition layer is sintered and its thickness for each pass is about 10 m. From the above measurement, the axial profiles of particle deposition were obtained for different jet temperatures (Fig. 3.1.3.5(a)) and for different jet flow rates (Fig. 3.1.3.5(b)). For the proper representation of the variation of deposition thickness, the deposition mass instead of the deposition thickness is used. The deposition mass can be obtained from the density of the measuring point and the deposition thickness, which is directly related to the deposition volume. The density for the measuring position was acquired from the composition by EPMA and the density of each component; the values of density for SiO_2 and GeO_2 are 2.20 and 3.64 g/cm^3, respectively (Bailar *et al.* 1973). As shown in Fig. 3.1.3.5, the jet-assisted method yields more deposition mass than the conventional case.

Furthermore, Fig. 3.1.3.5(a) reveals that the deposition mass increases with the jet temperature due to a higher thermophoretic force. Fig. 3.1.3.5(b) shows that the deposition mass increases with the increasing jet flow rate up to 1.5 l/min. Whereas, further increase of jet flow rate above 1.5 l/min results in the slight decrease of the deposition mass due to the increase of total inlet flow including reactant gases. Cho and Choi (1995) have shown that particles are more easily swept downstream for higher inlet flow rates, and as a result, the formation of particles may be limited near the tube wall. Of

interest in Fig. 3.1.3.5 is the axially non-uniform particle deposition zone from the torch starting position, i.e., the tapered entry length. The present jet-assisted method yields the considerable reduction of the tapered entry length; it is reduced from about 20 cm in the conventional MCVD process to 11~12 cm. Choi et al. (2002) have already shown that jet-assisted aerosol CVD method can yield the considerable reduction of the tapered entry length for SiO_2 particle deposition, since the radially injected jet gas pushes particles toward the tube wall, hence, shortens the particle trajectory before deposition. Fig. 3.1.3.5 ensures that the same principle could be also applied to the multi-component deposition process.

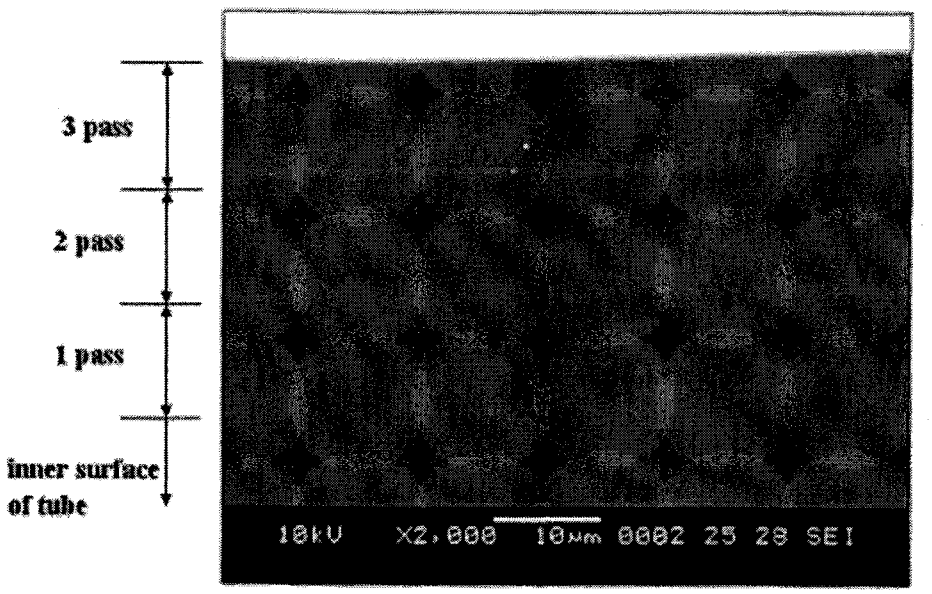

Fig. 3.1.3.4. SEM image of the deposited tube.

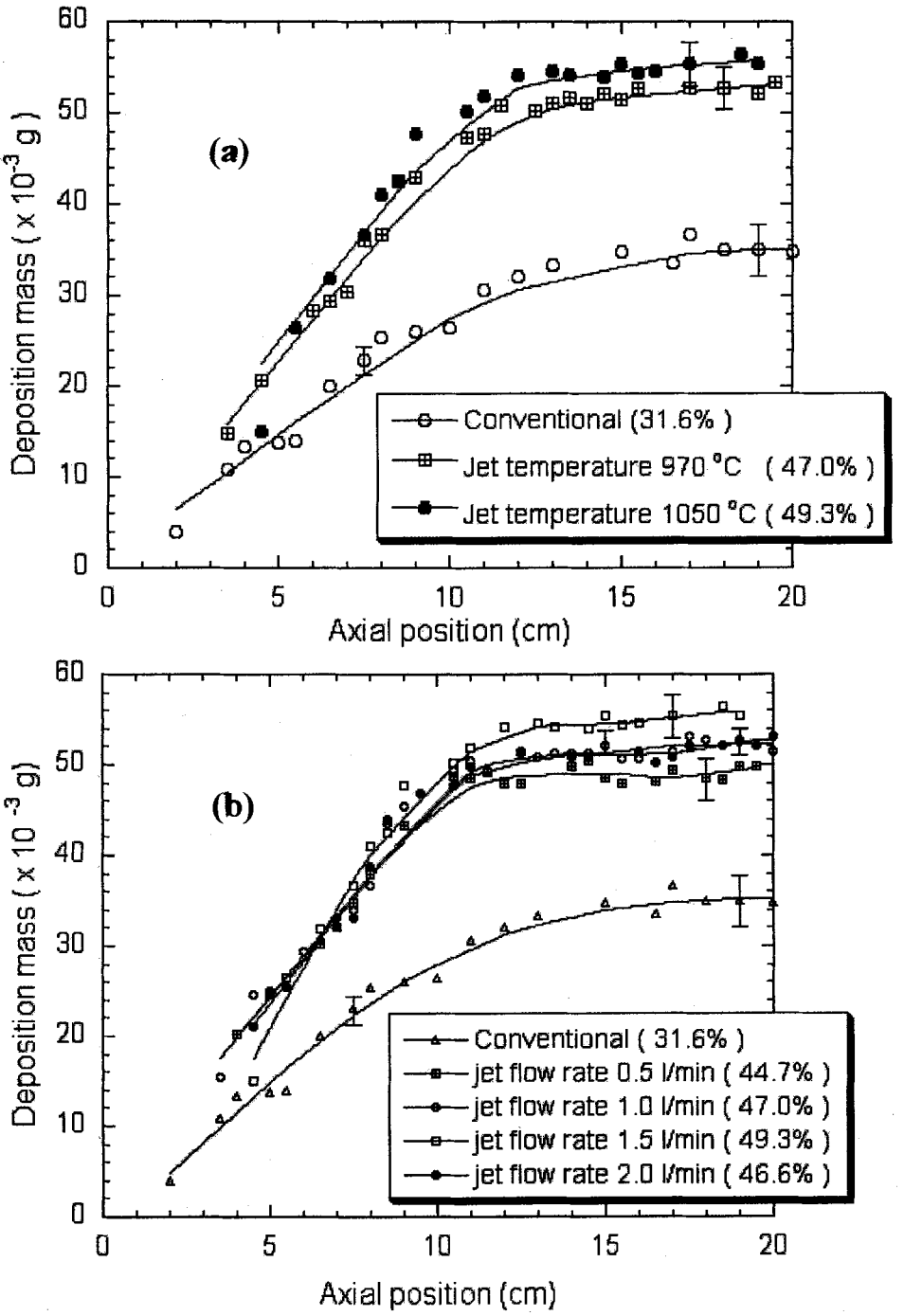

Fig. 3.1.3.5. Axial variations of deposition mass for the conventional and the present jet-assisted method; (a) for different jet temperatures at 1.5 l/min of jet flow rate and (b) for different jet flow rates at jet temperature of 1050 °C.

Although the above results in Fig. 3.1.3.5 successfully demonstrated the validity of jet-assisted method, these discussions are confined to the overall performance of particle depositionin the MCVD process. Contrary to the single-component deposition process, it is required to analyze the deposited layer of each component in the multi-component deposition. As shown in Fig. 3.1.3.6, the deposition mass profile for each component along the axial direction can be easily obtained from the overall deposition mass from Fig. 3.1.3.5 and the measured composition from Fig. 3.1.3.2. As one can expect, it is observed that a significant improvement for the uniformity of the deposited film of each component.

Since the oxidation of $GeCl_4$ to GeO_2 proceeds incompletely resulting in the large portion of $GeCl_4$ in effluent gases, the overall efficiency of particle deposition, which is defined earlier, is considered to be smaller in a multi-component than in a single component, particularly SiO_2 deposition system. Noting that the overall efficiency is the ratio between the deposited mass and maximum possible particle mass, the incomplete conversion into particles yields relatively low efficiency. In order to support the above discussion firmly, the efficiencies were examined for various $GeCl_4$ mass flow rates from 0.2 to 1.0 g/min, while SiCl4mass flow rate is fixed to 2 g/min. Since the efficiency of particle deposition varies with the inlet flow rate (Cho and Choi 1995), itis needed to fix the total amount of the gas mixture entrained into the silica tube for the exact comparison. Hence, total inlet flow is kept at a constant value of 1.92 l/min with various excess O_2. It is observed that the overall deposition efficiency decreases with increasing the $GeCl_4$ mass flow rate in Fig. 3.1.3.7.

Fig. 3.1.3.8 clearly shows that the overall deposition efficiencies increase considerably at injecting high temperature helium jet radially. In the present study, the deposition efficiency for the conventional case is 32 %. As jet temperature increases, efficiencies increase significantly. For the jet temperature of 970 $^{\circ}C$, the deposition efficiencies are found to be enhanced to 40 %, 45 %, 47 % and 46 % for jet flow rates of 0.5, 1.0, 1.5 and 2.0 l/min, respectively. For jet temperature of 1050 $^{\circ}C$, the similar trend can be observed, in which efficiencies become 45 %, 47 %, 49 % and 47 % for each jet flow rate. The results are summarized in Table 3.1.3.1. Therefore, the present jet-assisted aerosol CVD achieved approximately 53 % increase of efficiency (and rate) from the conventional method.

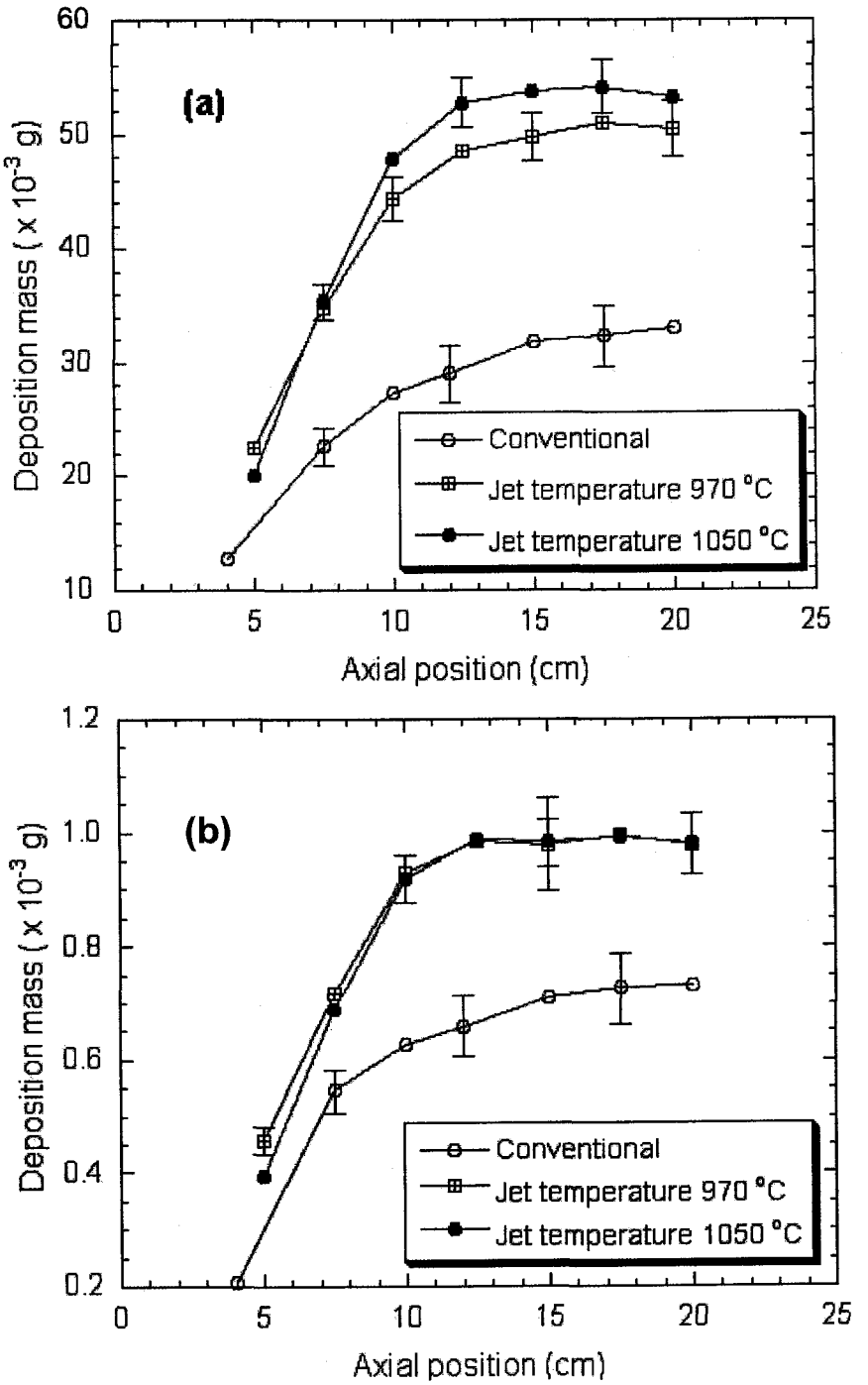

Fig. 3.1.3.6. Axial variations of deposition mass of each component for different jet temperatures at 1.5 l/min flow rate of helium jet; (a) SiO_2 and (b) GeO_2.

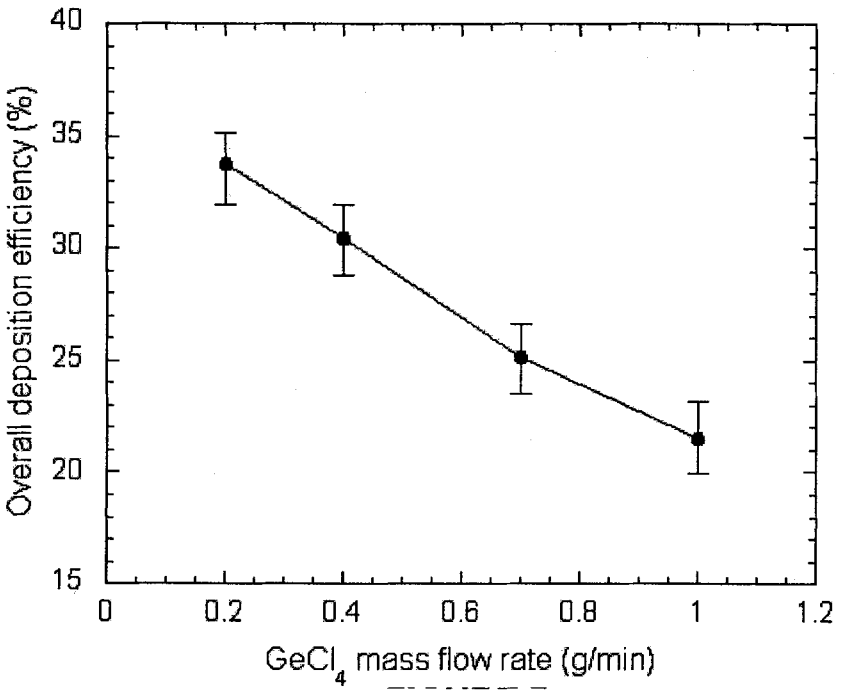

Fig. 3.1.3.7. Overall deposition efficiency for various $GeCl_4$ mass flow rates; $SiCl_4$ mass flow rate is 2 g/min, and total inlet flow rate is 1.92 l/min.

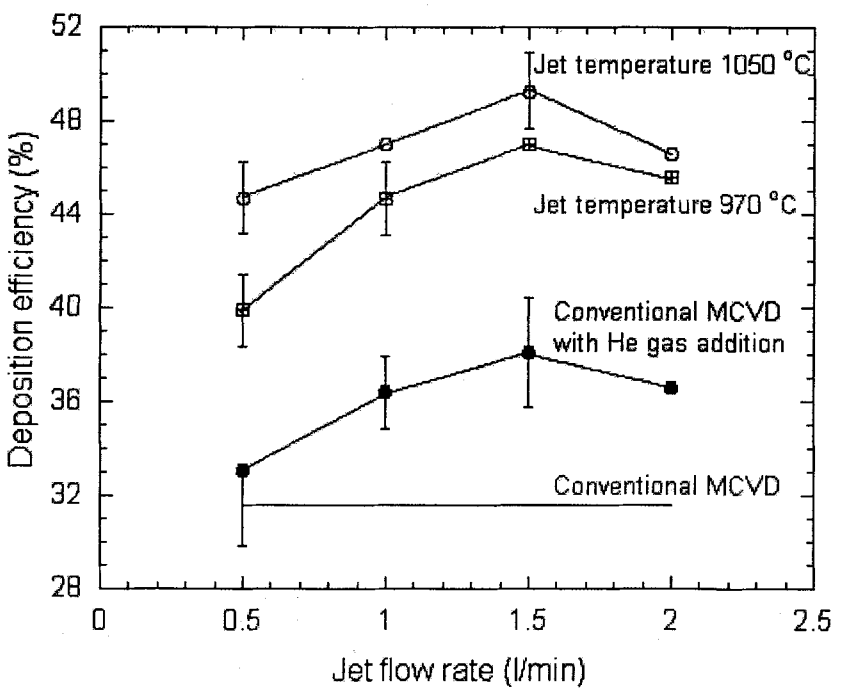

Fig. 3.1.3.8. Comparison of deposition efficiencies between the conventional and the present jet-assisted cases for different jet flow rates temperatures.

Table 3.1.3.1. Particle deposition efficiencies for different jet flow rates and jet temperatures.

		Jet flow rate (l/min)			
		0.5	**1.0**	**1.5**	**2.0**
Jet temperature [°C]	**970**	40% (±1.5%)	45% (±1.6%)	47% (±1.6%)	46% (±1.6%)
	1050	45% (±1.5%)	47% (±1.6%)	49% (±1.6%)	47% (±1.6%)
Conventional MCVD		36% (±1.8%)			

Note that there is the optimum jet flow rate for the enhancement of overall efficiency as examined in Fig. 3.3.3.5. We also performed the case in which helium is simply added to the stream of carrier gas ($SiCl_4$, $GeCl_4$, $POCl_3$ and O_2) using the conventional method without the inner tube. Since the deposition efficiency could be improved by simply adding helium in the conventional MCVD (Akamatsu et al. 1977; O'Connor et al. 1977), it is required to examine whether the observed increase of efficiency is due to the addition of helium or not. As shown in Fig. 3.1.3.8, deposition efficiencies for jet-assisted cases substantially exceed the cases with simply adding helium gas in the conventional method. This conclusively confirms that the present jet-assisted method is more effective.

For the practical use of the present jet-assisted MCVD method, it is required that the validity of another jet gas which is much cheaper than helium should be examined. Here, nitrogen is used as jet gas in substitute for helium. Fig. 3.1.3.9 shows the overall deposition efficiency for different jet gases; the jet temperature is fixed to 980 °C. It is observed that nitrogen jet gas injection yields the increase of efficiencies as much as the case of helium jet gas. It should be noted that the maximum efficiency occurs at flow rate of 0.37 l/min for nitrogen, while helium jet gas yields the maximum efficiency at 1.5 l/min. It has been reported that helium with high thermal diffusivity makes sure the improvement of deposition (Akamatsu *et al.*, 1977; O'Connor *et al.*, 1977). Although nitrogen has diffusivity lower than that of helium, smaller amount of nitrogen yields the enhancement of efficiency as much as helium.

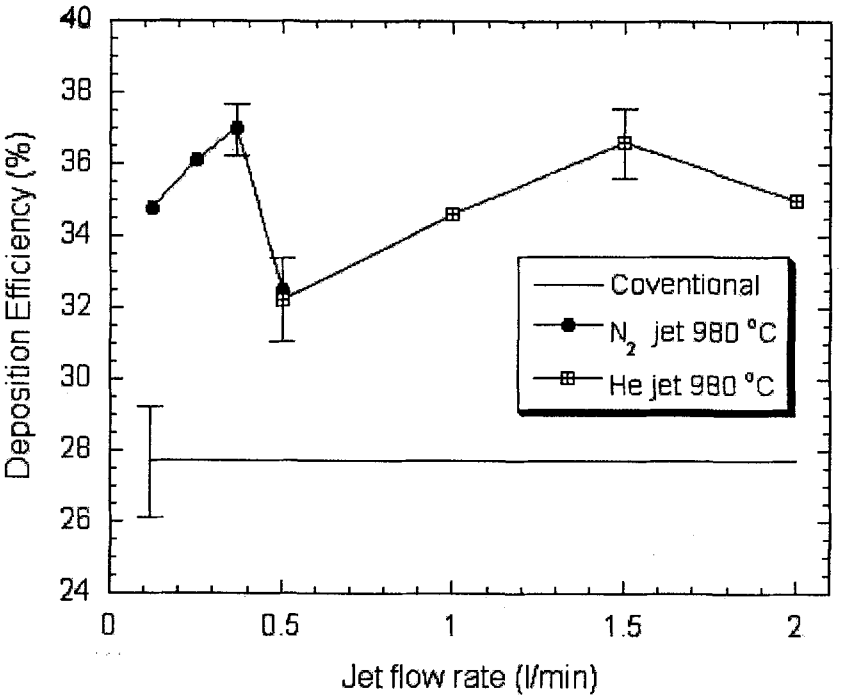

Fig. 3.1.3.9. Overall efficiencies for different jet gases.

This result can be explained by considering the difference of molecular weight between two gases. Noting that the present method utilizes the high temperature jet gas pushing the particles into the inner surface of tube wall, the jet gas with high density is expected to have an advantage over the gas with relatively low density, which is attributed to more inertial force supplied to particles. Therefore, the smaller amount of nitrogen than helium yields the similar effect on particle deposition.

3.1.4. Electrospray assisted CVD for synthesis of unagglomerated nanoparticles

● Introduction

Nanoparticle preparation has been of considerable interest for the manufacture of nanophase materials that have unique and improved propertiessuch as lower melting temperature, enhanced catalytic activity and higher self-diffusion coefficient, compared to conventional coarse-grained materials.Chemical vapor deposition (CVD) is one of the most typical gas-phase aerosol processes for producing high-purity nanoparticles. However, the generated nanoparticles in CVD processes are in the form of aggregates due to their coagulations in the high temperature. Recently, many attempts have been tried to combine the ionization of gases or the unipolar charging of particles into CVD methods to generate non-agglomerated nanoparticles because unipolarly charged particles undergo mutual electrostatic repulsions, and hence, have reduced particle collisions and growths.

Xiong et al.(1992) theoretically showed that electrical charges during gas-phase particle generation process can reduce the average particle size and narrow the broadness of the size distribution. Adachi et al.(1995, 1999) applied the ionization CVD methods using a radioactive source and corona discharger to the development of a particle-free film formation process. Choy et al.(2000, 2002) developed a cost-effective deposition technique which is referred to as electrostatic spray assisted vapor deposition (ESAVD) to fabricate various nanocrystalline films. ESAVD involves spraying atomized precursor droplets across an electric field, where the charged droplets undergo decomposition and/or chemical reactions in the vapor phase in the vicinity of the heated substrate. Using this method, they produced stable, solid films with good adhesion to the substrate.

In addition, for the application to the quantum electron device, the research on the patterning of the charged nanoparticles has been made recently (Krinke et al., 2001). In this case, bipolar charger such as ^{241}Am and ^{85}Kr was used for the charging of the particles. However, its charging ratio is too small (for example, about 10% at a diameter of 30 nm) to prepare patterning samples at a high deposition rate. Furthermore, a differential mobility analyzer (DMA) is needed for producing unipolarly charged monodisperse nanoparticles. Therefore, in the application of future quantum electrical devices, one-step process to produce unipolarly charged nanoparticles without any additional attachments (i.e., charger and DMA) is required. Ahn et al.(2001) recently reported an electrospray assisted CVD (ES-CVD) method to synthesize non-agglomerated and unipolarly charged nanoparticles in the reactor. They injected tetraethyl orthosilicate (TEOS) liquid precursor directly into the high temperature reactor by an electorospray method and produced less agglomerated SiO_2 particles compared to a conventional vapor-feeding (evaporation) CVD method. The generated particles were charged by a fraction of about 80%. In this work, the production of much smaller, non-agglomerated, narrowly size-distributed and unipolarly chargedspherical nanoparticles by the electrospray assisted CVD method has been experimentally studied through a precise control of electrospray. For determining the versatility of this ES-CVD method, titania and zirconia nanoparticles as well as silica were produced and their sizes and morphologies were investigated.

● Methods

The experimental setup used in this study is shown in Fig. 3.1.4.1. The system consists of an electrospray source, a tube-type CVD furnace and an electrostatic sampler. The electrospray capillary was made of stainless steel with an inner diameter of 300 m. A stainless steel tube of 1/4, 10 mm apart from the capillary, was used as a counter electrode. Liquids were supplied into the capillary nozzle by a high resolution syringe pump (Model PHD 2000, Harvard Apparatus) and a high voltage of 2-4 kV was applied to the capillary nozzle through a high DC voltage source (HER-10R3, Matsusada Co. Ltd.). In all our experimental cases, electrosprays were generated at the positive polarity. The counter electrode tube was connected to an electrometer (model 6512, Keithley Instruments Inc.) for measuring the electric current carried by electrospray and the stability of the spray was monitored by this current. For the accurate monitor of a stable spray, spray conditions were precisely observed by means of a CCD camera and TV monitor. Tetraethyl orthosilcate (TEOS, $Si(OC_2H_5)_4$), titanium tetraisopropoxide (TTIP, $Ti(OC_3H_7)_4$) and zirconium tetra butoxide (ZTB, $Zr(OC_4H_9)_4$ 50 vol. % solution in 1-butanol) were used as liquid precursors for the synthesis of SiO_2, TiO_2 and ZrO_2 particles, respectively. These liquids were directly electrosprayed for generation of charged precursors. N_2 gas of 1 l/min was used as a carrier gas. Sprayed droplets and consequently their vapors werecontinuously introduced into a CVD furnace reactor, which hadtwo heating zones, each of 120 mm length and 13 mm inner diameter. Metal oxide nanoparticles were generated by the thermal decomposition of the precursor vapors in the high temperature region of the reactor maintained between 700 and 850 °C. For determining the particle charging effect on the size and morphology of particles generated in the reactor, the precursors were also fed into the CVD reactor via a conventional evaporator which containsa syringe pump for delivering liquids at a known rate.Same concentrations of the precursors were used in both electrospray and conventional evaporation method for comparison.

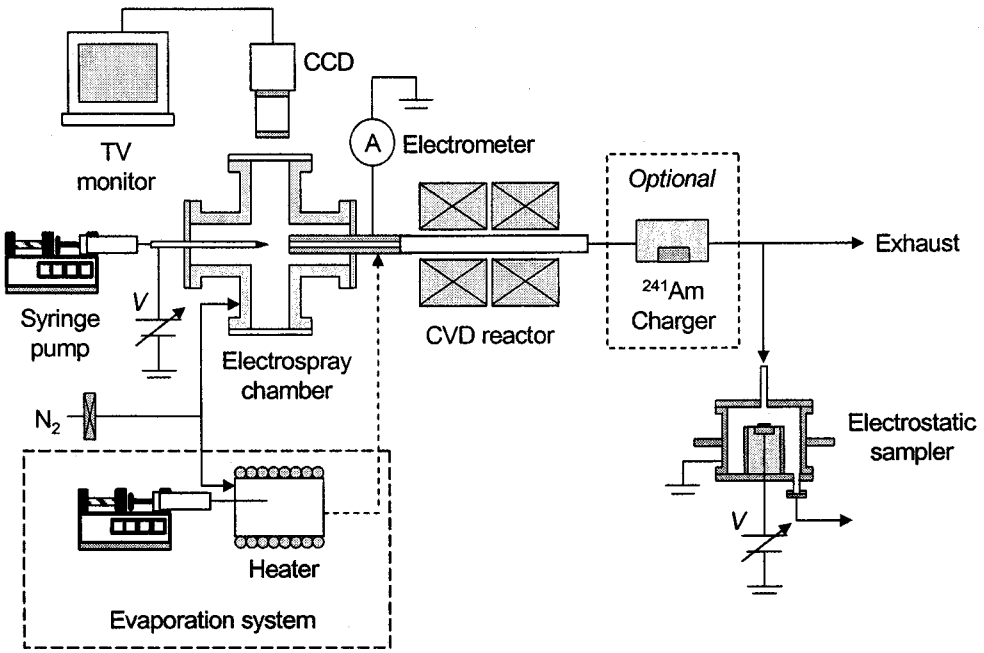

Fig. 3.1.4.1. Schematic of experimental apparatus for electrospray assisted CVD.

● Results and discussion

Let us compare the morphology of nanoparticles produced by electrospray assisted CVD (ES-CVD) and conventional CVD method. Fig. 3.1.4.2 shows the SEM images of silica nanoparticles generated by these methods. In each case, precursor vapor concentration was 1.5 $\times 10^{-6}$ mol/L. The pictures indicate a definite difference in the morphology of the produced particles in two methods. In the conventional method, considerably agglomerated silica particles were produced as expected. In the ES-CVD method, however, isolated and non-agglomerated nanoparticles were obtained even though primary particle sizes were almost the same in both cases. The morphology of uncharged (i.e. unsampled) particles was examined in the rear of the electrostatic sampler. A small amount of agglomerated particles was also detected. However, their fraction was still small compared to the conventional case shown in Fig. 3.1.4.2(b).

Fig. 3.1.4.3(a) shows the general physics of the gas-to-particle conversion process in conventional CVD. The CVD method involves complicate phenomena such as chemical reaction, condensation, evaporation, coagulation and sintering. In particular, both coagulation and sintering affect the final size and morphology of particles (Nakaso et al., 2001). Therefore the produced particles are usually randomly agglomerated and their size distributions are widely dispersed (σ_g= 1.4 ~ 1.6). However, in the ES-CVD process (see Fig. 3.1.4.3(b)), coagulation and growth of particles were suppressed, and as a result, the generated particles showed small size, spherical shape and narrower size distribution (σ_g~1.2). This is considered due to the effect of ions generated by electrospray. The details about ion generation in electrospray and ion effect on the particles are discussed below.

Monodisperse and highly charged precursor droplets are generated by electrospray. These charged

droplets are evaporated while being introduced into a CVD reactor with N_2 carrier gas. During the evaporation of the charged droplets, it is considered that the ions are produced by the following two processes.

One is usually referred to as the charged residue model (CRM) and was first proposed by Dole *et al.*(1968). As the solvent evaporates and a droplet shrinks, the charge density in the droplet surface increases. If the electric field of the droplet surface is equal to the surface tension, the droplet becomes unstable (Rayleigh, 1882) and the droplet explodes into smaller

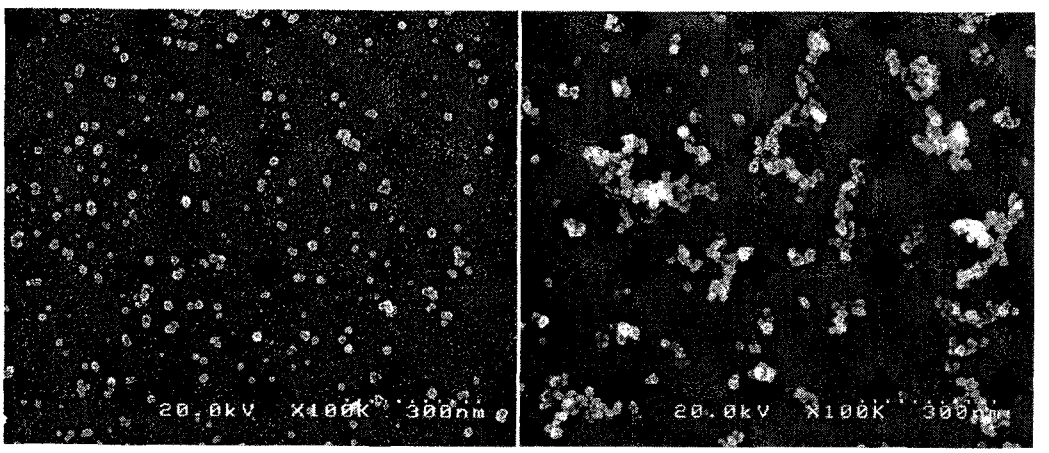

(a) **(b)**

Fig. 3.1.4.2. Comparison of size and morphology between silica nanoparticles generated by ES-CVD and (b) conventional CVD. The generation temperature is 850 °C.

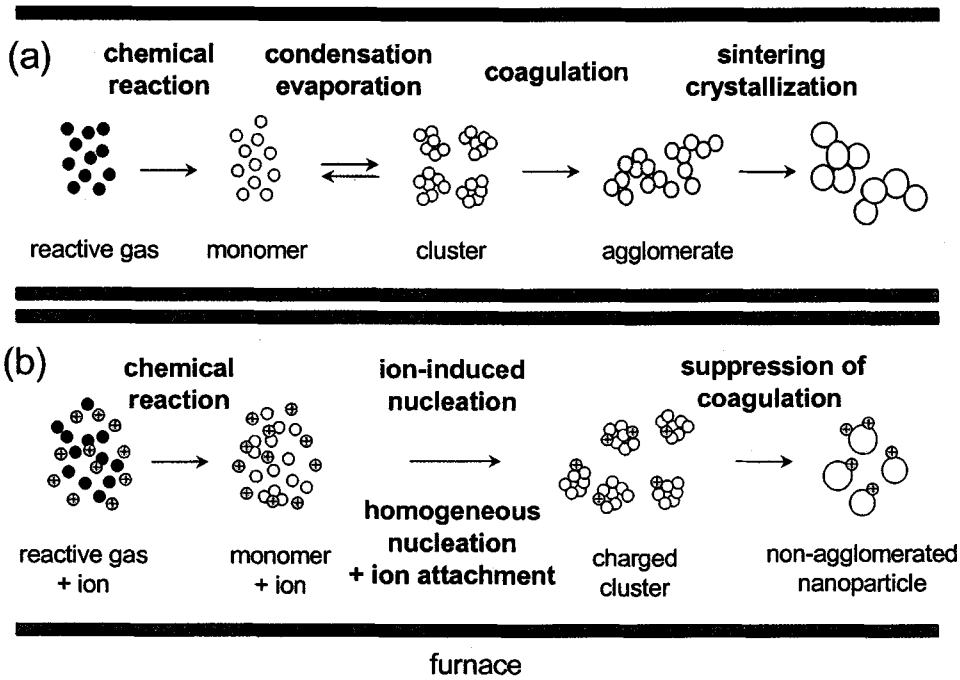

Fig. 3.1.4.3. Processes of particle formation in
(a) conventional CVD and (b) ES-CVD.

ones via the so-called Coulomb fissions and droplet evaporations are repeated and continued until the small droplets are converted into gas phase ions. This process is usually used to explain the generation of large mass of ions and clusters. Another process is the ion evaporation model (IEM), originally proposed by Iribarne and Thomson (1976). This modelalso initially involves solvent evaporation and droplet Coulomb fission. However, for the case of small droplets of about 10 nm, these droplets remain below the Rayleigh limit through the dissociation of ions from the droplet surface (i.e. ion evaporation) before these droplets reach the Coulomb fission stage. Small single ions are usually generated by this process. Fig. 3.1.4.3(b) shows the particle formation process supposed in the ES-CVD. The ions generated by either of two processes described above are mixed with the precursor vapors and introduced into a reactor. These ions probably act as seeds for ion-induced nucleation or/and they are attached to the particles already synthesized by homogeneous nucleation. Therefore, the most of the synthesized particles are charged. In particular, ions generated in electrospray are all unipolar, and thus, all charged particles have single polarity. Repulsive forces work among the unipolarly charged particles and the coagulations of the produced particles are suppressed by the forces.

The effect of precursor concentration on the nanoparticles produced by the ES-CVD was investigated. Fig. 3.1.4.4 shows the SEM images of silica nanoparticles generated with different precursor vapor concentration (i.e. feed rate of liquid precursor). The change in the geometric mean diameter measured from SEM image analysis with the precursor vapor concentration is shown in Fig

3.1.4.5. These figures clearly indicate that the particle size increases with increasing the precursor concentration. Therefore, the diameter of the produced particle can be easily controlled between about 10 nm and 40 nm by changing the feed rateof precursor. Non-agglomerated spherical nanoparticles were obtained at the low precursor concentration. However, at the higher precursor concentration, more or less agglomerated nanoparticles were also discovered. This is probably due to not enough ions for suppressing the coagulations of the particles generated at a higher concentration condition. In order to control the morphology of the particles generated at a higher precursor concentration, more charges should be introduced into the reactor by means of another additional ion source.

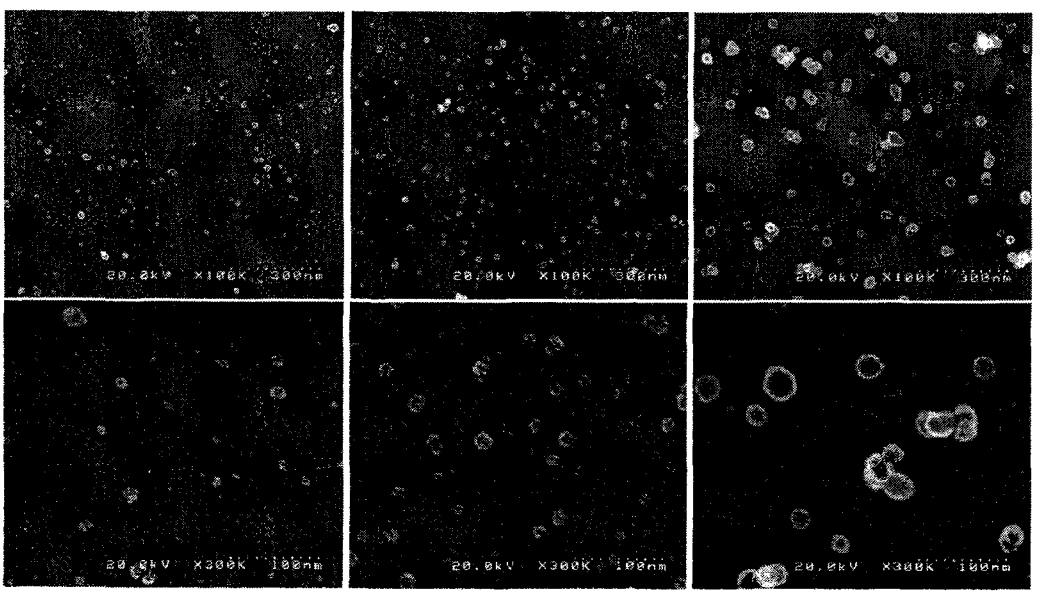

1.5 x 10^{-7}mol/L **1.5 x 10^{-6}mol/L** **3.7 x 10^{-6}mol/L**

Fig. 3.1.4.4. SEM images of the silica nanoparticles generated under various precursor concentrations. The generation temperature is 850 °C.

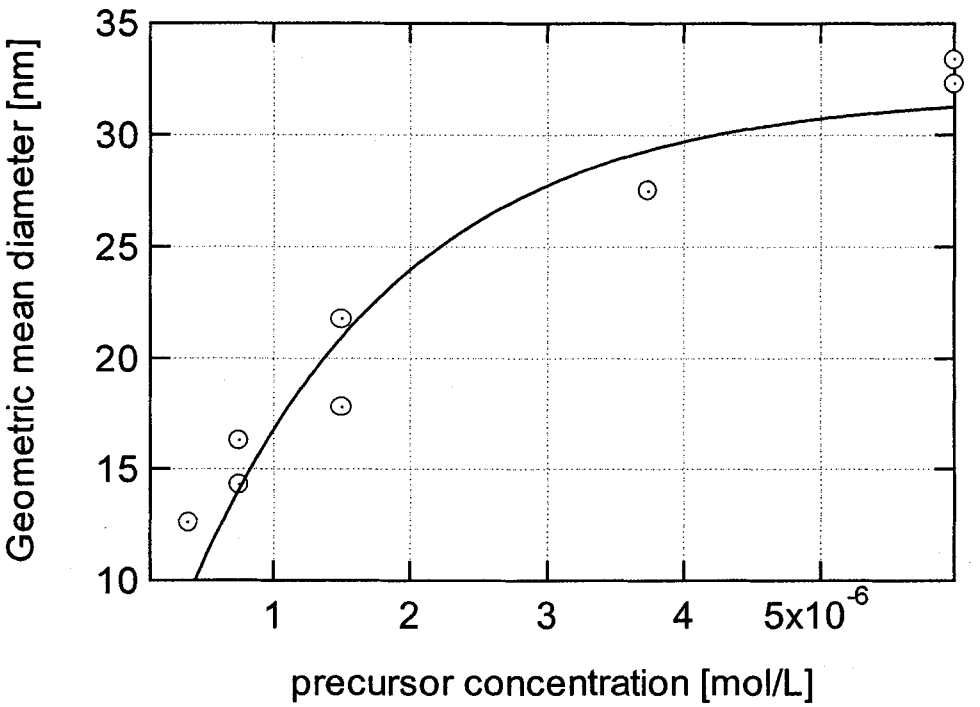

Fig. 3.1.4.5. Change in the geometric mean diameter of silica nanoparticles with precursor concentration.

In addition to silica nanoparticles, titania and zirconia nanoparticles were also synthesized using the ES-CVD. Fig. 3.1.3.6 and Fig. 3.1.3.7 show the SEM images of titania and zirconia nanoparticles, respectively. In each figure, (a) and (b) parts represent the nanoparticles generated by the ES-CVD and conventional CVD method, respectively. As is seen from the figures, non-agglomerated titania and zirconia nanoparticles were able to be obtained through the ES-CVD method. Therefore, this ES-CVD is certainly a useful method for the synthesis of non-agglomerated and unipolarly charged nanoparticles for a variety of materials. Furthermore, this ES-CVD presents possibilities to be applied to patterning process using unipolarly charged nanoparticlesand to the synthesis of multi-component nanoparticles by mixing several precursors or introducing multi electorspray sources.

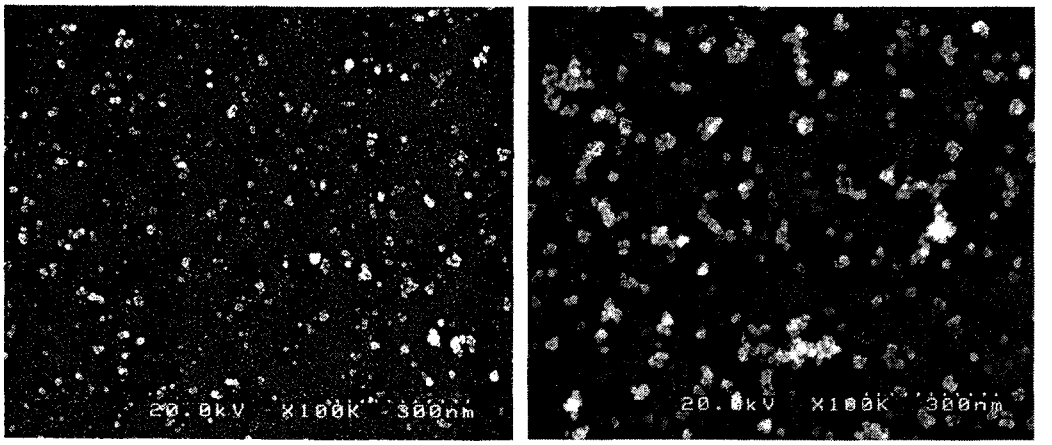

(a) **(b)**

Fig. 3.1.4.6. Comparison of size and morphology between titania nanoparticles generated by (a) ES-CVD and (b) conventional CVD.
The generation temperature is 700 °C.

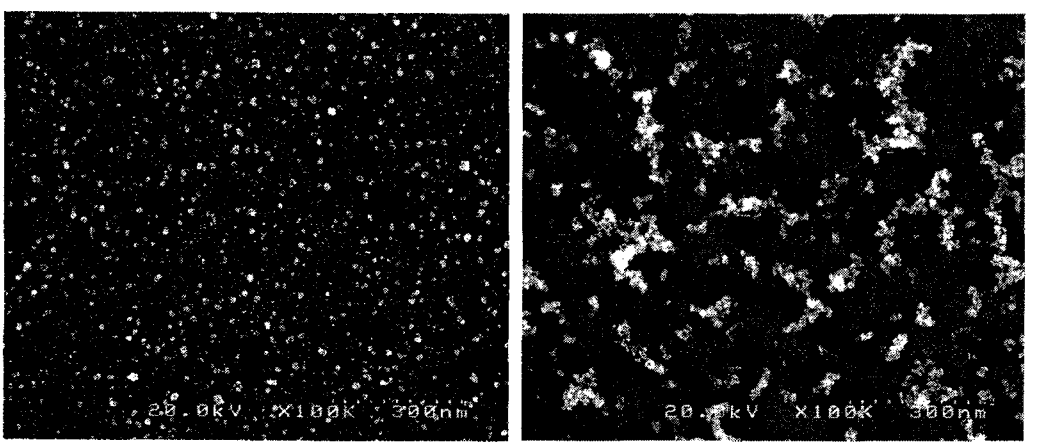

(a) **(b)**

Fig. 3.1.4.7. Comparison of size and morphology between zirconia nanoparticles generated by (a) ES-CVD and (b) conventional CVD.
The generation temperature is 700 °C.

3.1.5. Nano-oxide generation by metal combustion

● Introduction

Over several decades, the study of crystalline lattice defects has derived a considerable impetus from the need to understand the control exerted by defects on most technologically important properties of solids. Among different types of structures investigated, MgO is in the forefront of research. Having the simplest (rock-salt) lattice structure and the large energy gap MgO is a suitable ground to test theoretical models describing properties of defects and to compare their prediction with experimental results. One of key-role defects being studied in MgO crystals is Mn^{2+} (Low, 1957; Watanabe, 1960; Powell, 1960; Walsh, 1961; Feher, 1964; Solomon, 1966; Koidl, 1976; Rubio, 1979; Du, 1985; Kuang, 1988; Yu, 1989; Gordon, 1989), which substitutes magnesium in octahedral sites. The interest for MgO:Mn^{2+} structure is caused by both the easiness of preparation of this valence state of the manganese ion in MgO host and the clear way of its theoretical description. However, despite the long history ofstudies, there has been no direct observation of an excited state of Mn^{2+}ion in MgO whose energy is a subject of theoretical debates (Du, 1985; Kuang, 1988). Note that the excited states of Mn^{2+} in octahedral sites in some different matrices (Langer, 1965; Langer, 1966; Greene, 1968; Bantien, 1988; Yamashita, 1997) as well as the states of Mn^{4+} in MgO (Prener, 1953; Henderson, 1968; Dunphy, 1990) are known to produce sharp zero-phonon lines (ZPLs).

In the present research we report for the first time the observation of ZPLs originating from electron transitions of Mn^{2+} ion in MgO matrix. These lines were observed in macroscopic photoluminescence (PL) from nanocrystals synthesized by combustion. To our best knoweledge this is the first observation of extremely sharp emission lines from nanocrystals. Note that it was believed that the nanosize would broaden the lines. The simultaneous appearance of a pair of zero-phonon lines in PL from transition metal defects as in our system has not yet been reported as well. The values of energies of observed lines allow one to choose the crystal-field strength in MgO which magnitude is one of the main parameters being used in the theoretical modeling. Taking into account the recent finding on carbon nanotubes growth on MgO nanocubes and the prediction of a new type of nanoscale optoelectronic circuitry based on MgO nanocrystals, our finding becomes very important for applications.

● Methods

The nanocrystals of MgO were synthesized by burning out Mg particles in air as described elsewhere (Shoshin, 2002). We used Mg particles (Alfa Aesar) with size about 2÷4 mm and nominal purity of 99.98%. Actually, the purity of Mg in use (that was checked with the inductively coupled plasma (ICP) analysis) was higher and the main impurity was Mn with a content of 12.8 ppmw. The MgO nanocrystals obtained after Mg particle burning were also checked with ICP to show Mn content of 2.3 ppmw. The close value (about 3 ppmw) was derived from electron spin resonance (ESR) spectra (see below). No other impurity was found in MgO. The synthesized MgO particles look

perfect cubes (see Figure 3.1.5.1a) with the average size about 30 nm. In the same Figure the electron diffraction pattern of the particles is presented. The electron diffraction ring pattern simulation performed for MgO fits the experimental results demonstrating a good crystallinity of particles. X-ray diffraction analysis also confirms it. By deposition the product of Mg combustion onto a substrate the MgO films were also produced. Figure 3.1.5.2 shows transmission electron microscope (TEM) pictures of such a film.

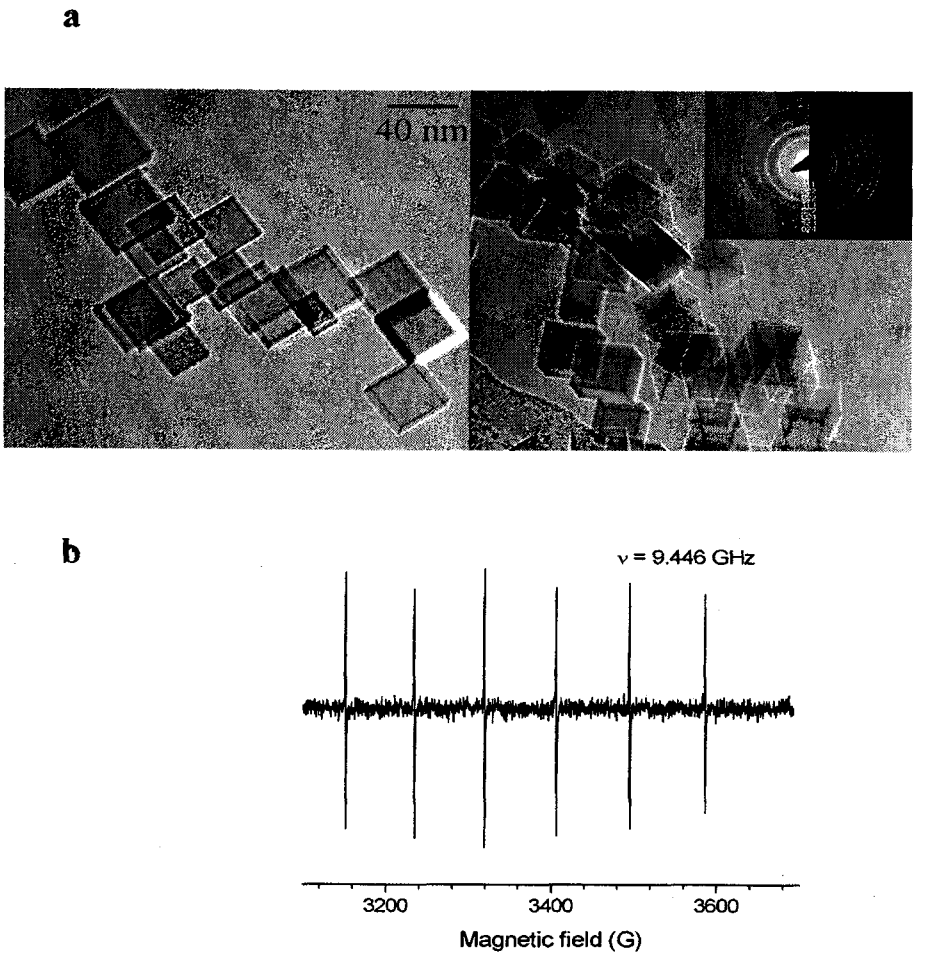

Figure 3.1.5.1. Structural characteristics of MgO nanocrystals.(a) TEM images. Inset shows the electron diffraction pattern together with the ring pattern simulation. (b) Derivative ESR spectrum of MgO nanocrystals. Sextet parameters (see text) correspond to Mn^{2+} ion in MgO host.

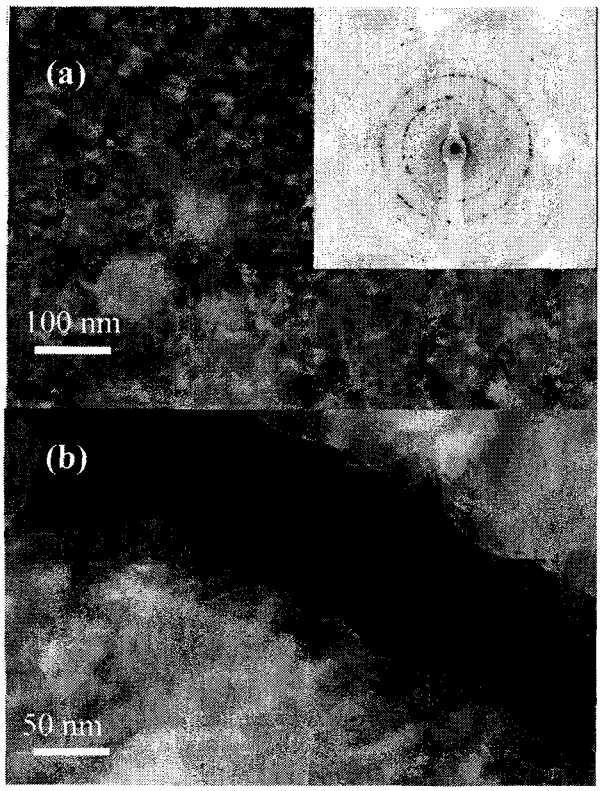

Figure 3.1.5.2. TEM images of nanocrystalline MgO film. The electron diffraction pattern in (a) confirms the high crystallinity of the film; (b) taken at a film edge region demonstrates the film integrity.

By deposition the product of Mg combustion onto a substrate the MgO films were also produced. Figure 3.1.5.2 shows transmission electron microscope (TEM) pictures of such a film. In order to check the valence state of Mn ion in MgO particles we carried out ESR measurements at X-band. We found the sextet (see Figure 3.1.5.1b) with parameters g=2.0016 and A=8110-4 cm^{-1} corresponding to $MgO:Mn^{2+}$ system (Low, 1957) at both measurement temperatures (77 K and 300 K). The peak-to-peak width of components at microwave power below the ESR saturation was about 0.5 G. The narrowness of the ESR peaks together with the sextet parameters give evidence that all Mn^{2+} ions occupy cubic sites in our MgO particles. In order to measure PL MgO nanopowder was pressed into pellets. The cryostat allowed to cool samples down to about 10 K. PL was excited by continuous-wave (CW) He-Cd (*exc*=325 nm) and Ar-ion (*exc*=514.5 nm) for CW PL measurements, and by pulsed Nd:YAG laser (*exc*=266 nm) for time-resolved photoluminescence (TRPL) measurements. The 150 W Xenon lamp with a scanning monochromator was used in order to obtain photoluminescence excitation (PLE) spectra. In all the cases the excitation density did not exceed of 1 W/cm^2. At the PL yield measurements the incident laser intensity was changed with metallic neutral density filters. The spectra were detected with a 0.85 m double monochromator (SPEX 1403) equipped with a R943-02

GaAs PMT (for CW PL and PLE measurements) and with a 0.5 m spectrometer (Acton Research) equipped with an intensified photodiode array (1024 pixels) detector (TRPL measurements).

● Results and discussion

The typical CW PL spectra measured at 10 K are shown in Figure 3.1.5.3a. Two sharp ZPLs are clearly seen. At 10 K the first line peaking at 659.23 nm has a full width at half maximum (FWHM) of 0.7 \AA\ and the second one peaking at 735.45 nm has a FWHM of 1.9 . Note that unlike quantum dots (QDs) which exhibit sharp lines only in microscopic PL (Notomi, 1996) (in the case when emission from an individual QD is distinguished) our particles emit sharp lines in macroscopic PL (when emission from all particles come to the detector). As one can see the second ZPL (the 735 nm ZPL) is accompanied with conventional phonon replicas (Imbusch, 1981; Henderson, 1989), while the first ZPL (the 659 nm ZPL) does not produce these replicas. The temperature evolution of ZPLs is shown in Figure 3.1.5.3b,c. The intensity of the found ZPLs strongly depends on the measurement temperature showing a temperature quenching. The line intensities vs. temperature are given in Figure 3.1.5.4a. The function $1/[1+Kexp(-EA/T)]$ demonstrates a good fit to the experimental points. The activation energy EA is of 360 K for the 659 nm ZPL and of 460 K for the 735 nm ZPL. The PL yield that is a dependence of ZPL intensity, I, upon the incident laser power, P, is shown in Figure 3.1.5.4b. It exhibits $I \sim Pn$ law with $n1$ (one- photon excitation). This dependence was observed for both the CW excitation and the pulsed one.

The typical spectra measured at 10 K with the 5 sec gate at different delay times after the Nd:YAG laser excitation are shown in Figure 3.1.5.5. The ZPLs broadness is caused by the low spectral resolution of the spectrometer enabling to measure TRPL at a wide region. All the spectra demonstrate similar features that corresponds to the similar decay of the ZPLs and the continuous background. The decays of background luminescence at different wavelengths replotted from the TRPL spectra are shown in Figure 3.1.5.6. Figure 3.1.5.7 demonstrates the luminescence decay of the ZPLs.

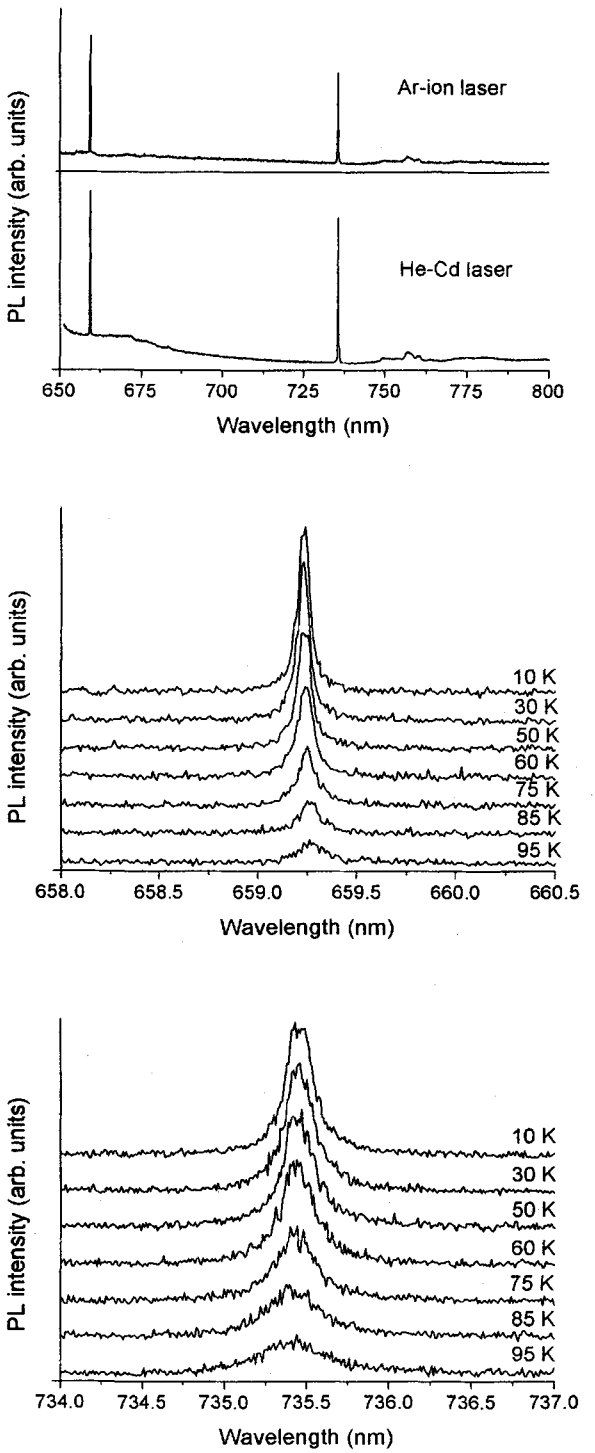

Figure 3.1.5.3. CW PL spectra. (a) PL spectra excited by different lasers at 10 K. Two sharp ZPLs are clearly distinguished. (b), (c) Temperature evolution of the 659 nm ZPL and the 735 nm ZPL, respectively. The spectra are offset. Measurements were done under the Ar-ion laser excitation.

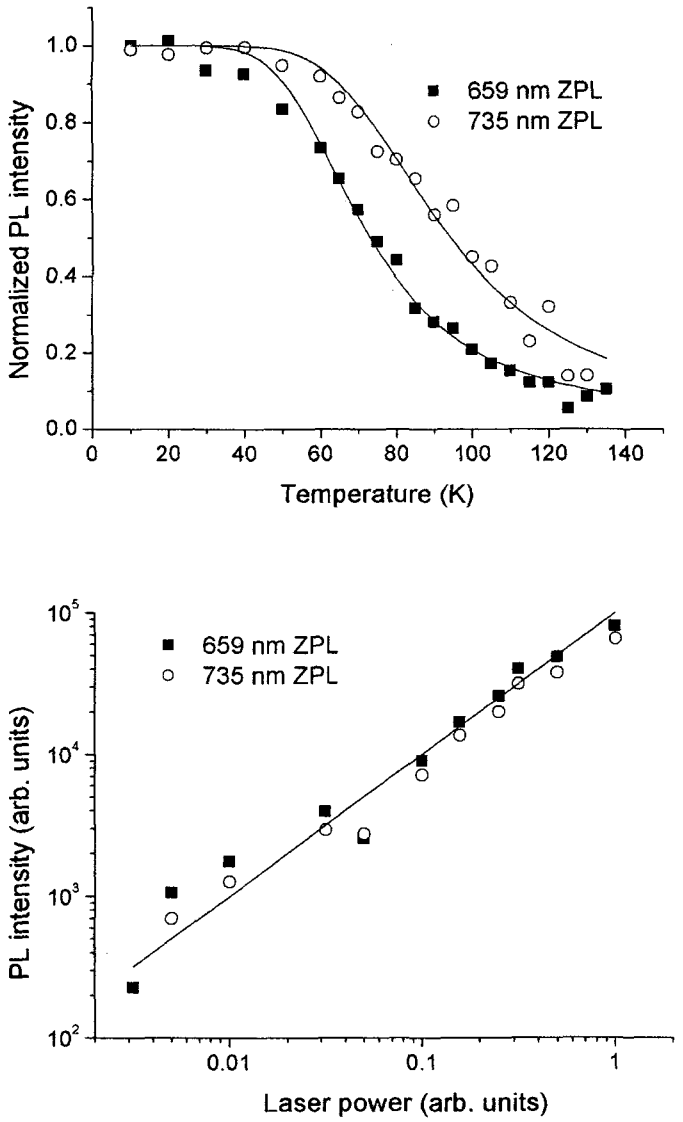

Figure 3.1.5.4. Results of ZPLs studies. (a) PL intensity of ZPLs normalised to the value at 10 K vs the temperature. Solid lines show fitting with the function *1/[1+Kexp (-EA/T)]* (see text) (b) PL yield. The solid line corresponding to the *I~P1* dependence (one-phonon excitation) is a guide for eye.

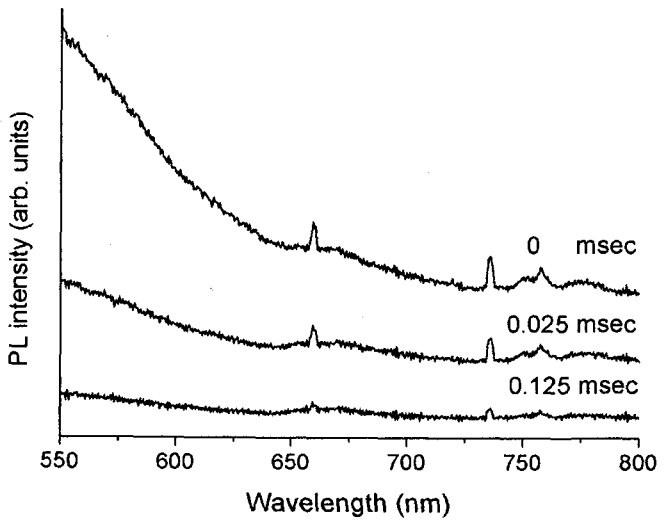

Figure 3.1.5.5. PL spectra at 10 K corresponding to different delay times after the Nd:YAG laser excitation. The spectra are offset. The ZPLs broadness is caused by the low spectral resolution of the spectrometer enabling to measureTRPL at a wide region.

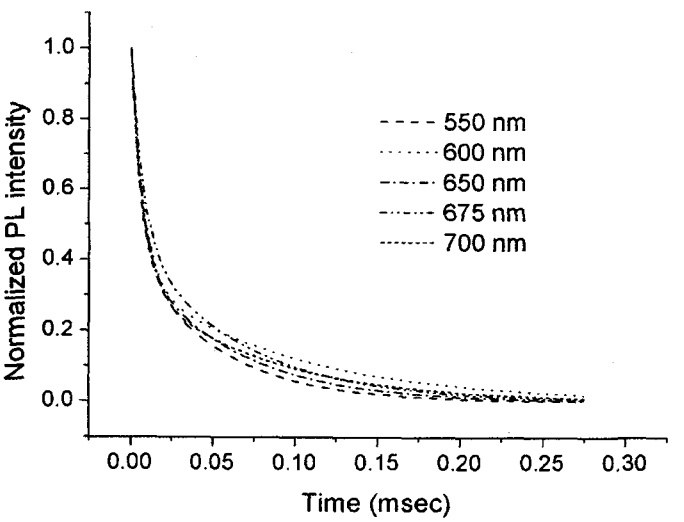

Figure 3.1.5.6. Decay of background luminescence at different wavelengths after the Nd:YAG laser excitation at 10 K. Intensities are normalized to initial values.

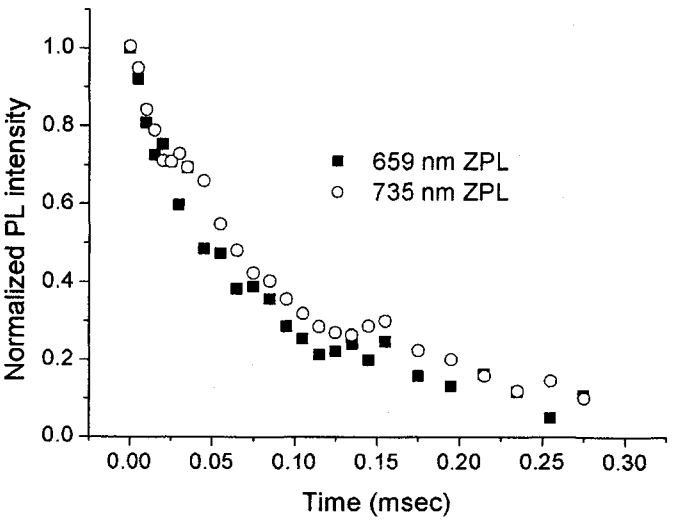

Figure 3.1.5.7. Decay of ZPLs luminescence after the Nd:YAG laser excitation at 10 K. Intensities are normalized to initial values.

As one can see both the background and ZPLs show the characteristic luminescence decay time of 0.1 msec, though the background also experiences an initial fast decay.

In order to obtain the bare PLE spectra of the ZPLs we took the PLE spectra for emission exactly at the ZPLs wavelengths and at the wavelengths shifted from the ZPLs on 1-2 nm. The PLE spectrum at the wavelength close (but not coinciding) to a ZPL can be considered as the PLE spectrum of the background at the ZPL wavelength. Then the difference between the PLE spectra at the ZPLs wavelength and at those close to the ZPLs gives the bare PLE spectra of the ZPLs. These bare PLE spectra of the ZPLs obtained at 10 K are shown in Figure 3.1.5.8. Note that the relatively high noise in the PLE spectra is caused by the weakness of PL under the scanned Xenon lamp excitation. Nevertheless, the similarity of the bare PLE spectra of both ZPLs can be concluded. The PLE spectra show that ZPLs can be excited in a wide energy range. The latter corresponds to the ZPLs observation under excitation with different lasers covering a broad range (laser wavelengths of 266 nm, 325 nm and 514.5 nm). At room temperature no bare PLE spectra were found.

Let us analyze the experimental results. The ZPLs come from a forbidden electric dipole transition. This is typical for transition metal ions (Imbusch, 1981; Henderson, 1989). Based on the result of ESR measurements the transition metal ion in our case is Mn^{2+} in MgO matrix. For such Mn^{2+} ion in an octahedral environment other than MgO only one ZPL in luminescence is usually observed. Such ZPL corresponds to the transition from the lowest excited $^4T_1(^4G)$ state onto the ground $^6A_1(^6S)$ state. Other excited states decay by the nonradiative relaxation dropping onto the lowest excited state and PL from all excited states except the lowest one is suppressed (Imbusch, 1981). The appearance of two ZPLs in our system indicates that there is an excited state, which does

not decay by the nonradiative transition. It may be possible if this state is weakly coupled with phonons. Then a lack of phonon replicas for the 659 nm ZPL becomes clear. At the same time the $^4T_1(^4G)$ - $^6A_1(^6S)$ transition is characterized by a large value of the Huang-Rhys parameter (Imbusch, 1981; Henderson, 1989) giving the pronounced phonon replicas of the 735 nm ZPL. In order to confirm that both ZPLs observed in the PL really belong to Mn we additionally measured PL from nanocrystals with different Mn content. Such nanocrystals were produced by burning out Mg particles at the presense of Mn-containing salt ($MnCl_2$). For all impurity levels checked (up to a few hundreds ppmw) intensities of both ZPLs increased with the Mn content increase. The ratio of intensities remained constant, which allows one to claim that the same center of impurity is responsible for the found ZPLs. Also we produced MgO:Cr^{3+} nanocrystals that exhibited sharp lines at 698.07 nm (R-line) and at 703.79 nm (N-line) (see Figure 3.1.5.9). This wavelength exactly coincide with that reported for bulk MgO:Cr^{3+} system (Imbusch, 1964; Larkin, 1973). The absence of Cr^{3+}-originating lines in MgO nanocrystals different from those in the bulk matrix confirms the absence of the specific nanocrystal sites occupied by substituted ions, which existence might be brought in question in order to explain the origin of ZPLs in the MgO:Mn^{2+} system. The latter shows that the finite size of our MgO nanocrystals does not affect the energy levels of a substituted ion.

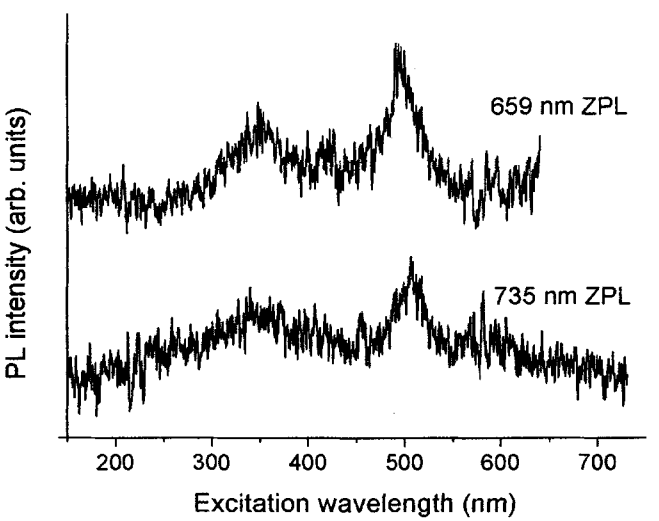

Figure 3.1.5.8. Bare PLE spectra of ZPLs taken at 10 K. The spectra are offset.

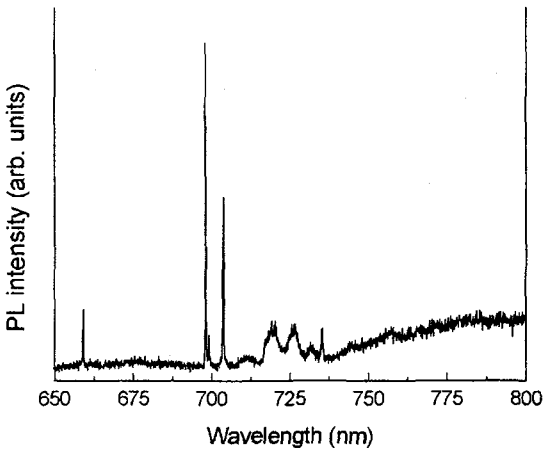

Figure 3.1.5.9. PL spectrum from nanocrystalline MgO doped with Mn and Cr excited by Ar-ion laser at 10 K.

We have to emphasize that despite many years of MgO:Mn^{2+}study ZPLs have not been reported previously even for bulk neither in emission nor in absorption. Then the exact values of energy levels of Mn^{2+}ion in octahedral sites of MgO have not been known for such (probably the simplest) transition ion crystalline matrix system.

Let us assign the 659 nm ZPL for a transition by using the Tanabe-Sugano diagram for the 3d5 system (Tanabe, 1954; Knig, 1977). As we noted before the 735 ZPL undoubtedly comes from the $^4T_1(^4G)$ - $^6A_1(^6S)$ transition. The energy of this transition corresponds to *Dq/B* 1.5 where *Dq* is the crystal-field strength and *B* is the Racah parameter. Note that such a large value of *Dq/B*corresponds to latest calculations (Yu, 1989)}. At so high a value of *Dq/B* the next state $^4T_2(^4G)$ coming from splitting of the ^4G term in the crystal field lies at about 5000 cm-1 higher than the $^4T1(^4G)$ state. Since the energy difference between $^4T^2(^4G)$ and $^4T_1(^4G)$ states is more than three times larger compared to the distance between two observed ZPLs then the 659 nm ZPL can not come from the 4T1(4G) - 6A1(6S) transition. At the same time the large energy separation between two ZPLs observed (about 1500 cm^{-1}) does not allow one to assign the 659 nm ZPL for the $\$^4T_1(^4G)$ - $^6A_1(^6S)$ transition of Mn^{2+}ion in a site other than the octahedral one as far as the 735 nm ZPL is assigned to the $^4T_1(^4G)$ - $^6A_1(^6S)$ transition of Mn^{2+} ion in the octahedral site. However, at Dq/B ~ 1.5 a state coming from splitting of the 2I term appears within the needed energy region and matches observation. We claim that just the transition from this state onto the ground $^6A_1(^6S)$ state gives the 659 nm ZPL. Then, because states from different electron terms are responsible for two observed ZPLs two essentially different Huang-Rhys parameters may correspond to the transitions. It leads to the absence of phonon replicas for the 659 nm ZPL (which is likely weakly coupled withphonons) and the existence of them for the 735 nm ZPL. Note that the idea similar to ours which uses $\^2I$ term in order to match the experimental data to the Tanabe-Sugano diagram was previously applied to ZnS:Mn^{2+} system (Langer, 1965). The authors (Langer, 1965) also discussed how so strongly forbidden free-ion transition between the ground state

^6S and the ^2I level becomes allowed in the presence of the crystalline field. Note once again that although the above idea utilizing ^2I term in order to explain the origin of the 659 nm ZPL looks unconventional, it is the only way to explain so unforeseen a fact as an appearance of the second ZPL originating from the same transition ion in the matrix (which to our best knowledge has not been observed previously).

As one can see in Fig. 3.1.5.7 both ZPLs exhibit a similar luminescence time decay. It seems to be difficult to explain how the lines arising from different spin manifolds can have the same lifetimes. Even transitions originating from the same level of ions occupying different sites should have different lifetimes. Then we have to conclude thatthe luminescence decay shown in Fig. 3.1.5.6 has nothing to do with the pure radiative lifetimes of emitting states (which can be sufficiently short in nanocrystals (Yan, 1998; Smith, 2000) and the luminescence decay time likely corresponds to the time decay ofstates exciting ZPLs. If the ZPLs are excited from the same states (see below), then the similarity of the time decay for both ZPLs becomes clear. The decay of background luminescence similar to the ZPLs decay (see Figs. 3.1.5.5-7) gives an evidence that the long time background luminescence is excited by the same mechanism as the ZPLs are (from the same states). Note that the fast decaying part of the backgroung luminescence (lying beyond the present research) may be attributed to the luminescence of F-centers (Rosenblatt, 1989).

The next question that should be discussed is why ZPLs found in the present paper have not been observed previously despite numerous studies of the MgO PL. The answer to this question is important in order to understand our finding. Note that ZPLs originating from Mn^{2+}transitions in cubic crystalline field were seen before only in PL of narrow-band materials. The thermal quenching and the PL yield observed in the present paper for ZPLs are similar to those for the PL, when the emitting states are excited from some close electron states. For such a wide-gap substance as is MgO these states should lie deep inside the forbidden band and therefore can not exist in ordinary MgO crystals. Then the energy transfer between the environment and excited states of Mn^{2+} ion does not occur making the Mn^{2+}ion excitation impossible. It explains why in usual MgO crystals ZPLs were not observed. Note that if nanoparticles are generated by vapor condensation during combustion a high concentration of structural defects in particle substance takes place (Altman, 2001; Pikhitsa, 2001). It appears due to the fast rate of particle formation and exhibits itself via anomalously high light absorption found in our recent studies of wide-gap nanooxides (Shoshin, 2002; Altman, 2001; Pikhitsa, 2001). Just the presence of these defects, which is a distinctive feature of particles synthesized by combustion, leads to the existence of states deep inside the forbidden band and to the possibility to excite a Mn^{2+} ion in MgO matrix and therefore to the appearance of the Mn2+-originating ZPLs in PL. This idea of the ZPLs excitation corresponds to the observed similarity of the PLE spectra (see Fig. 3.1.5.8), which give the information about the density of states exciting the ZPLs. It should be added that the easiness of the excitation of the Cr^{3+}-originating ZPLs even in bulk is related to a specific charge state of the Cr^{3+} ion which itself is a defect in the MgO matrix.

The present paper demonstrates that combustion nanooxides give wayto excite perfect ZPLs from

them unlike nanocrystals synthesised in another way (Bulyarskii, 2000). We believe that the combustion nanocrystals can be utilized in optical nanodevices due to extraordinary discreteness of the system energy levels with the performance better than that of QDs. It can be a breakthrough in optical nanoelectronics taking into account the recently reported carbon nanotubes-MgO circuitry that can provide a local access to optical elements of nanoscale.

3.1.6. Patterning of nanoparticles

● Introduction

Nanoparticles have been of great interests in the manufacture of nanomaterials or nano-structured materials since they have unique physical properties (electrical, optical, magnetic, and mechanical) compared to the bulk materials. For example, nanoparticles can display lower melting temperature, higher self-diffusion coefficient and enhanced catalytic activity. Their properties are greatly dependent on their size, morphology and crystal phase, which motivates many researchers to attempt to control these parameters of nanoparticles. The application of the nanoparticles in electronic device structures such as quantum devices, field emission display, and single electron transistors requires the precise control of their size and the accurate assembly of their position onto the desired patterns in two or three dimensions. New approaches for the nanoparticle patterning, thus, have been recently explored.

Mesquida and Stemmer used atomic force microscope (AFM) to draw local charge patterns on a substrate by applying voltage pulses between the tip and the substrate and then deposited colloidal nanoparticles on the charge patterned substrate. Similarly, Krinke et al. described a method to pattern aerosol nanoparticles with narrow lines using a contact charging between a sharp metal tip and an insulating substrate. Though these approaches can fabricate nanoscale patterns with the resolution of 100 nm, the fabrication of such charge patterns using the methods is too time- consuming. Jacobs and Whitesides have developed a parallel charge pattern process based on soft lithography to overcome the time lag. The process uses a conductive flexible polydimethylsiloxane (PDMS) stamp to pattern an electret thin film by injecting and trapping charges over areas of ~1 cm2. With this PDMS stamp, the directed deposition of nanoparticles from a powder, gas phase aerosol and liquid phase suspension onto charge patterns was demonstrated and the accomplished resolution reached about 800 nm. Recently, Krinke et al. reported the deposition of monodisperse and spherical nanoparticles (the most desirable particles in many potential applications on nanotechnology) from gas phase on oxidized silicon surfaces by the transfer of charge patterns using a PDMS stamp printing. However, the nanoparticle patterns were arbitrarily formed irrespective of the stamp patterns, and thus, the pattern sizes were largely deviated from those of the stamp. The reason was mainly due to the less-smooth stamps with cracks produced during the metallization of the stamps.

In this article, we report a parallel process for accurate nanoparticle patterns onto the substrate by means of combining nanoparticle mobility control and the contact charge transfer through gold coated PDMS stamp. PDMS stamps were coated by metal with a sputter method instead of a thermal evaporation to reduce buckles on the stamps. Nanoparticle line patterns with the resolution of 500 nm were successfully made on the substrate and the particle patterns were nearly consistent with those of the stamp. To our knowledge, 500 nm line

patterns probably represent the highest resolution so far achieved through parallel methods for nanoparticle patterning.

● Methods

Figure 3.1.6.1 shows the experimental apparatus to generate, classify and deposit aerosol nanoparticles. The system mainly consists of a tube furnace, a ^{210}Po radioactive neutralizer, a differential mobility analyzer (DMA, modified from a Vienna DMA) and a sampler for collecting aerosol particles. Silver aerosol nanoparticles are generated by an evaporation-condensation method. Ag wool-typed material is evaporated in a tube furnace at the temperature of 1000°C and condensed into particles in a cooling system (~ 10°C). The particles continue to grow by their coagulations, which lead to polydisperse aerosols with diameters in the range of 5-50 nm. The particles carried with a clean nitrogen gas at a constant flow rate of 1 l/min are bipolarly charged by passing in a ^{210}Po radioactive neutralizer and then introduced into a DMA. DMA is an instrument used to sort nanometer particles, with high accuracy, according to their electrical mobilities (or sizes) while keeping them suspended in gas phase. Singly charged monodisperse (equal-sized) nanoparticles can be classified by applying the appropriate electric field in the DMA and these charged particles are then fed into a sampler in which a charge patterned substrate is placed in the center. These singly charged particles are deposited onto the charge patterned dots or lines having the opposite polarity to the particles. No external electric field is applied to the sampler. In all experiments, Ag nanoparticles with a diameter of 20 nm were selected through DMA for pattern deposition.

Charge patterned substrates are prepared by contact charging with PDMS stamps. The PDMS stamps are fabricated by cast molding. The PDMS elastomer used in this study is Sylgard 184 obtained from Dow Corning. The elastomer is mixed at a 10:1 ratio with its curing agent to obtain PDMS viscous solution and then placed in a desiccator for about 1 hr to remove bubbles generated during mixing. Figure 3.1.6.2 shows the procedure for fabricating a conductive PDMS stamp. Masters are patterned by means of an electron beam lithography with a pattern generator working at 30 keV energy. PDMS viscous solution is poured on top of the master having a relief structure on its surface and then cured at 100°C for 1 hr, and then, released from the master. The area of the stamps is 1 cm^2. The patterned surface of the PDMS stamps has to be electrically conductive to allow contact charging. Metal coating was made on the surface of the PDMS stamps by a sputter method instead of a thermal evaporation which has been known to cause cracks or buckles on the surface of PDMS during cooling procedure. The 4" wafers supporting the PDMS stamps were mounted 15 cm away and 25 degree tilted from the metal source in a sputter system. The stamps were rotated at 10 rpm to get a uniform layer. A 10 nm thin layer of Cr was coated as an adhesion promoter on the stamp and then a 90 nm thick layer of gold followed. The sides of

the PDMS stamps were simultaneously coated by the sputter system. Cracks or buckles which probably hinder a perfect contact charge transfer from the stamp onto the substrate were overcome by this sputter coating approach.

Figure 3.1.6.3 shows charge-pattern transfer and nanoparticle deposition processes. Polymethylmethacrylate (PMMA, 0.1 μm film on a silicon wafer) was used as a charge storage medium. <100> p-doped silicon wafer was cleaned with 1% solution of hydrofluoric acid to remove the native oxide. PMMA was coated on the wafer by a spin coater and then the PMMA-coated wafer was baked at 90°C for 1 hr under vacuum. PDMS stamp was moved down and touched to the PMMA-coated substrate. A pulse voltage of -14V (100 Hz) generated by a pulse generator was applied between the stamp and the back side of the substrate for about 10 seconds to generate charge patterns onto the substrate.

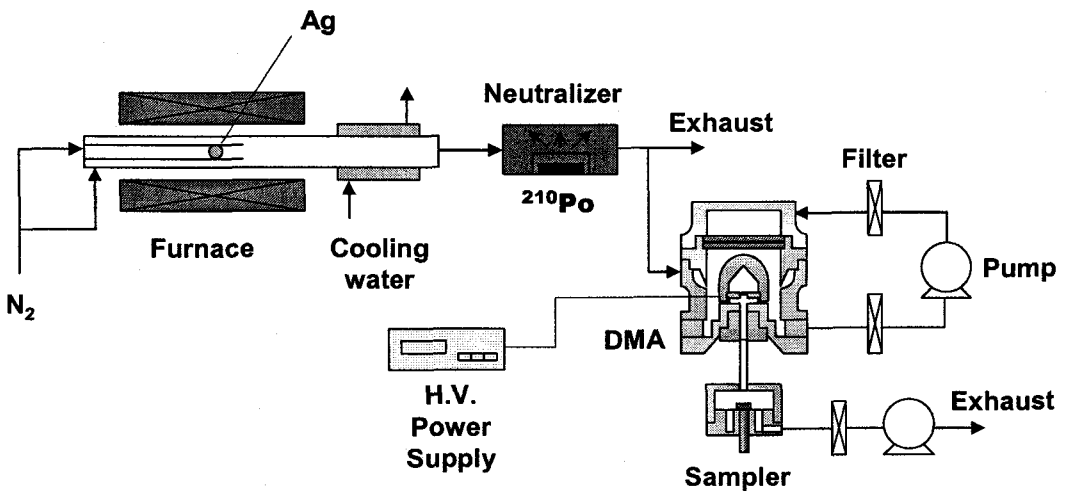

Figure 3.1.6.1. Experimental setup for the synthesis, classification and deposition of monodisperse nanoparticles.

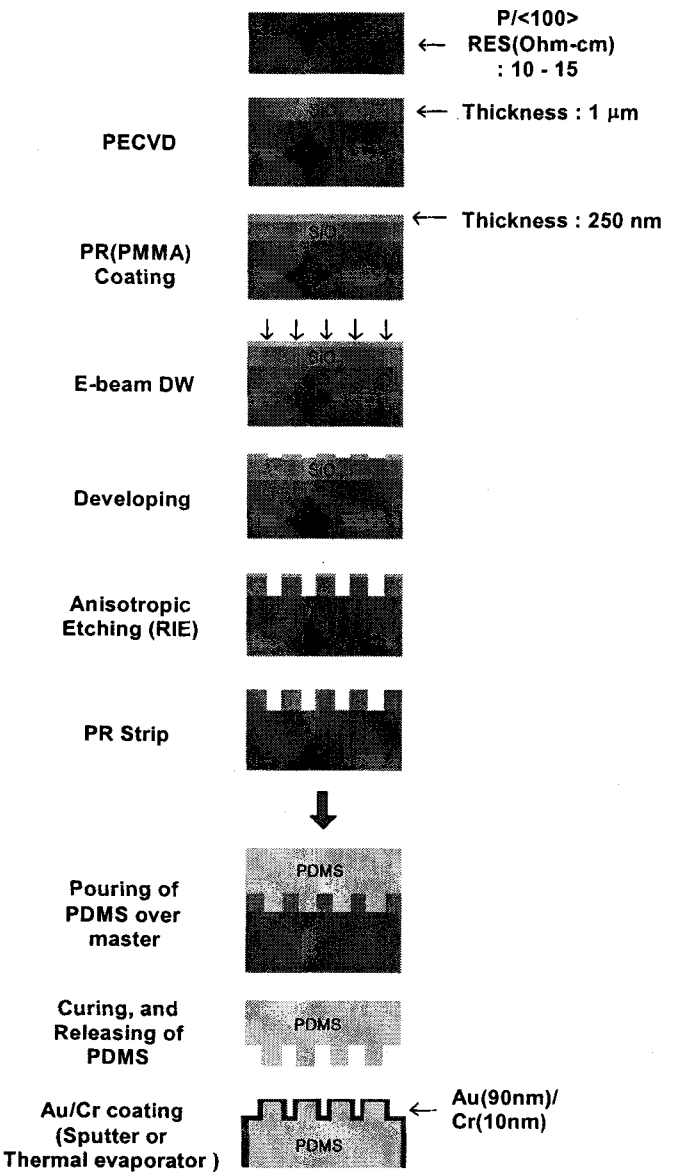

Figure 3.1.6.2. Schematic illustration of the procedure for fabricating a conductive PDMS stamp.

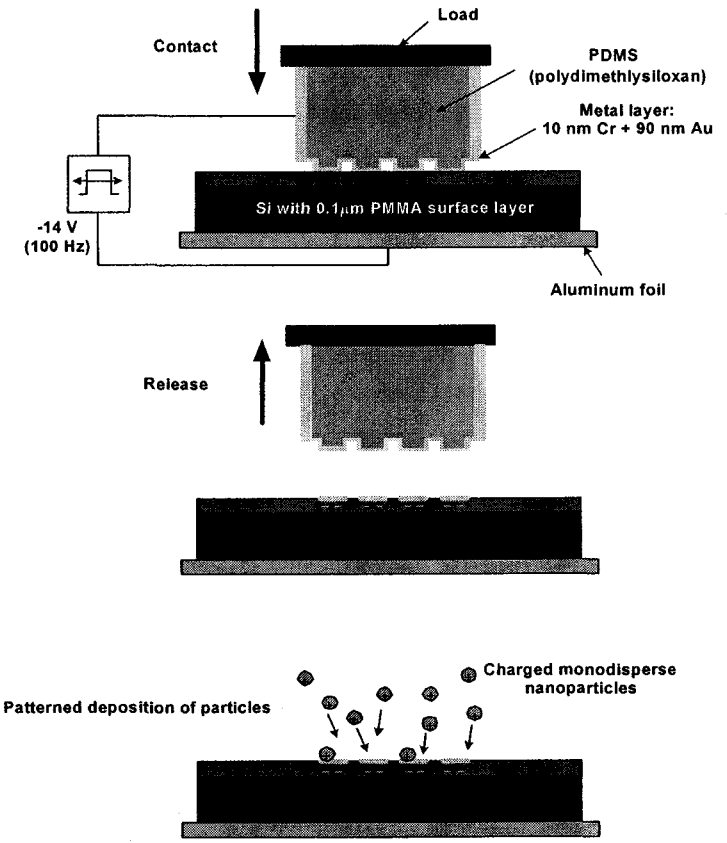

Figure 3.1.6.3. Process of parallel charge patterning and nanoparticle deposition.

● Results and discussion

Figure 3.1.6.4 shows the size and morphology of silver nanoparticles deposited in the present experimens. Nearly spherical silver nanoparticles with the controlled sizes could be generated by the DMA classification depending on applied DMA voltages. These size-controlled monodisperse nanoparticles are deposited onto the charge patterned substrate. The generation of size-controlled spherical nanoparticles is considerably significant in the nanoparticle pattern deposition because the patterned metal particles with different sizes maybe exhibit the different characteristics, for example, different catalytic properties that may be used for the growth of nanotubes or nanowires.

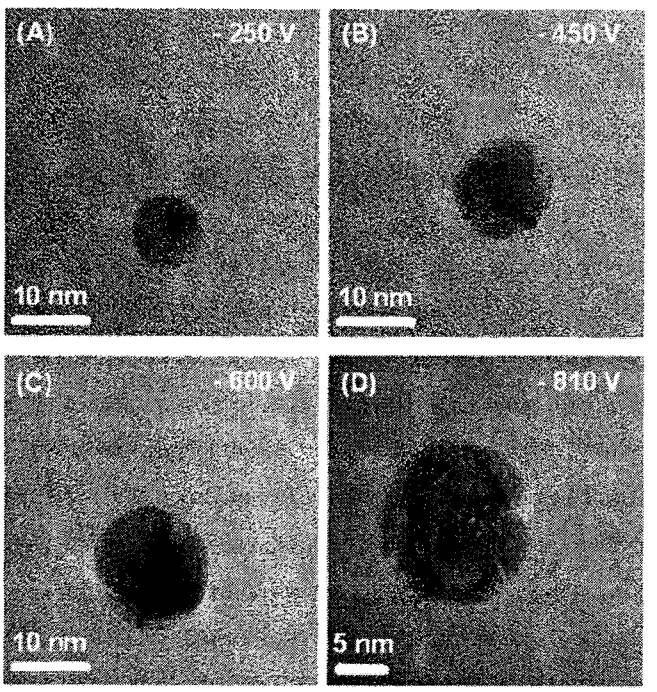

Figure 3.1.6.4. Transmission electron microscope (TEM) images of silver nanoparticles classified at different DMA voltages:
(a) -250 V (b) -450 V (c) -600 V (d) -810 V.

We improved the pattern deposition using the metal-coated PDMS stamps by a sputter as an alternative method of a thermal evaporation. Figure 3.1.6.5(a) and (b) shows SEM images of electrical conductive PDMS stamps coated with metals (Au: 90 nm/ Cr: 10nm) by a thermal evaporator and a sputter, respectively. In case of the stamp coated by a thermal evaporator, the metal layer on the stamp was not smooth but had cracks or buckles, as expected. Thermal expansion and contraction of the PDMS stamp during the heating and cooling processes may cause buckles on metal layer. When a sputter method was used without any thermal process, the layer on the top of the stamp showed no cracks (see Fig. 3.1.6.5(b)).

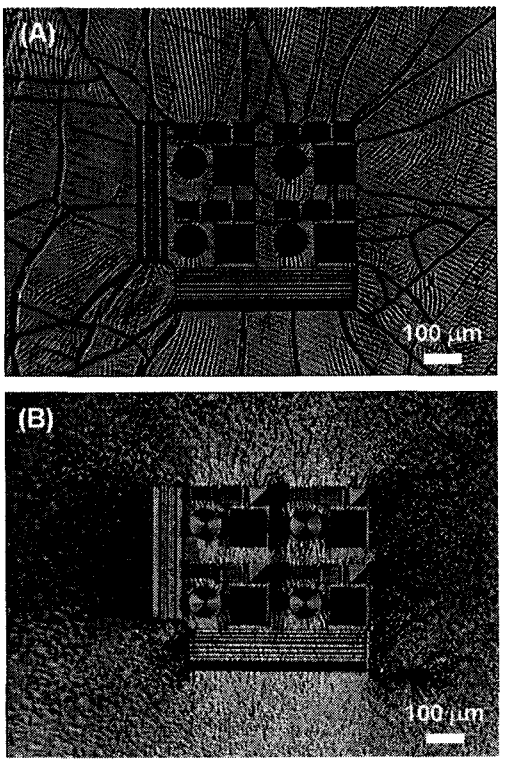

Figure 3.1.6.5. Microscope images of electrical conductive PDMS stamps. The PDMS stamps are coated with metal (Au: 90 nm/ Cr: 10 nm) by (a) a thermal evaporator and (b) a sputter method.

Figure 3.1.6.6 shows (a) the shape of a PDMS stamp with arrays of 1x1 μm^2 sized dot and (b) the resulting 20nm nanoparticle pattern deposition using the same stamp. The scanning electorn microscope (SEM) image of the deposited nanoparticle pattern is in a good accordance with that of the PDMS stamp. Charge pattern, therefore, was successfully transferred to the substrate according to the accurate pattern size of the stamp. Nanoparticle line patterns with a width of about 500 nm were also successfully accomplished as shown in Fig. 3.1.6.7. A line-structured stamp (line width: 500 nm, pitch: 1.5 μm and the height: 1 μ m) was used to fabricate the line patterns (see Fig. 3.1.6.7(a)). To our best knowledge, nanoparticle pattern with 500 nm wide lines would represent the highest resolution compared to those of the most recent studies using the parallel pattern process. Pattern deposition with 100 nm wide lines was also attempted using this method and the result was shown in Fig. 3.1.6.8. Charge pattern was partially transferred to the substrate, and thus, some parts of the line deposition were missed. Also, the widths of particle-deposited lines (~150-300 nm) were wider than those of the stamp. As discussed later this poor pattern deposition with 100nm resolution is due to imperfect manufacture of metal coated PDMS stamp. This result,

therefore, would suggest that the particle pattern deposition can be possible even with near 100 nm resolution using this method, if well defined precise stamp can be fabricated.

Figure 3.1.6.9 shows atomic force microscopy (AFM) images of PDMS stamps: (a) 2D and (b) 3D images of the stamp with arrays of a 1x1 μm^2 sized dot and (c) 2D and (d) 3D images of the stamp with arrays of a 500 nm wide line (e) 2D and (f) 3D images of the stamp with arrays of a 100 nm wide line, respectively. As shown in Fig. 3.1.6.9(a)-(d), the patterns of both 1x1 μm^2 sized dots and 500 nm wide lines stamps show good uniformity and smooth structure. However, for the 100 nm line-patterned stamp, line patterns were roughly structured and the heights of lines were also nonuniform (See Fig. 3.1.6.9(e) and (f)). In the study of Jacobs et al., two parallel charge lines with about 220 nm width were obtained by using a stamp carrying even 1 m wide lines due to slightly higher height at the edge compared to the center of lines. Similar result was shown in the study of Krinke et al., where discontinuous two lines were formed at both edges of the lines of the stamp with a width of 1 m. These are all due to the cracks in the metal layer of the stamps as mentioned before. In our study, considerably uniform and smooth surface pattern structures have been successfully fabricated even in the stamp with 500 nm lines by the sputtering metal coating method without any thermal process, and thus, nanoparticle lines were deposited on the desired patterns. The successful pattern deposition according to the pattern size of stamp is mainly attributed to a well-patterned flat surface of the stamp and a perfect charge transfer resulting from a good contact between the stamp and the substrate. For the 100 nm resolution, we could not fabricate a well-patterned mold, and thus, the resulting stamp was also poorly made in patterns. Further studies, therefore, are required to fabricate uniformly structured stamps as well as to metalize the stamp without any deformation of the pattern of the stamp for achieving 100 nm resolution.

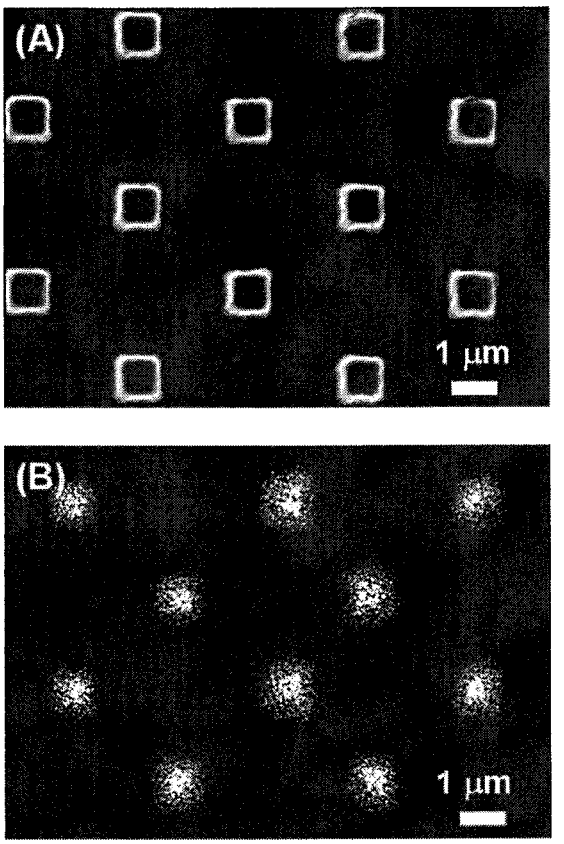

Figure 3.1.6.6. Scanning electron micrographs of (a) a PDMS stamp with arrays of a 1x1 m2 dot and (b) the resulting nanoparticle pattern deposition.

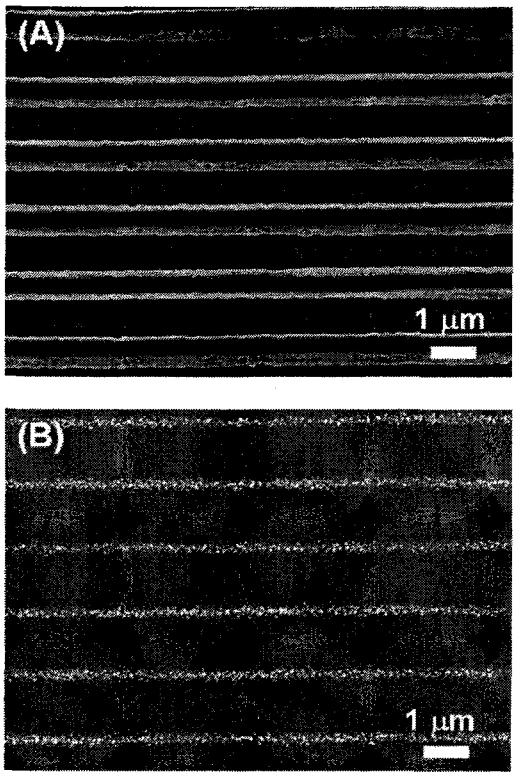

Figure 3.1.6.7. Scanning electron micrographs of (a) a PDMS stamp with 500 nm width lines and (b) the resulting nanoparticle pattern deposition.

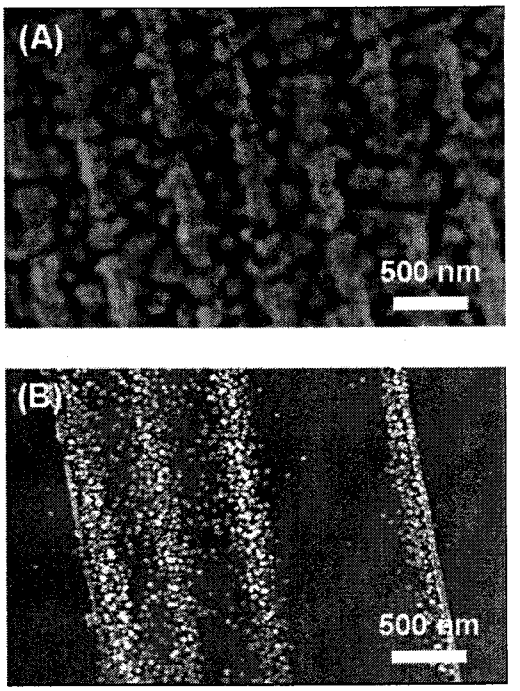

Figure 3.1.6.8. Scanning electron micrographs of (a) a PDMS stamp with 100 nm width lines and (b) the resulting nanoparticle pattern deposition.

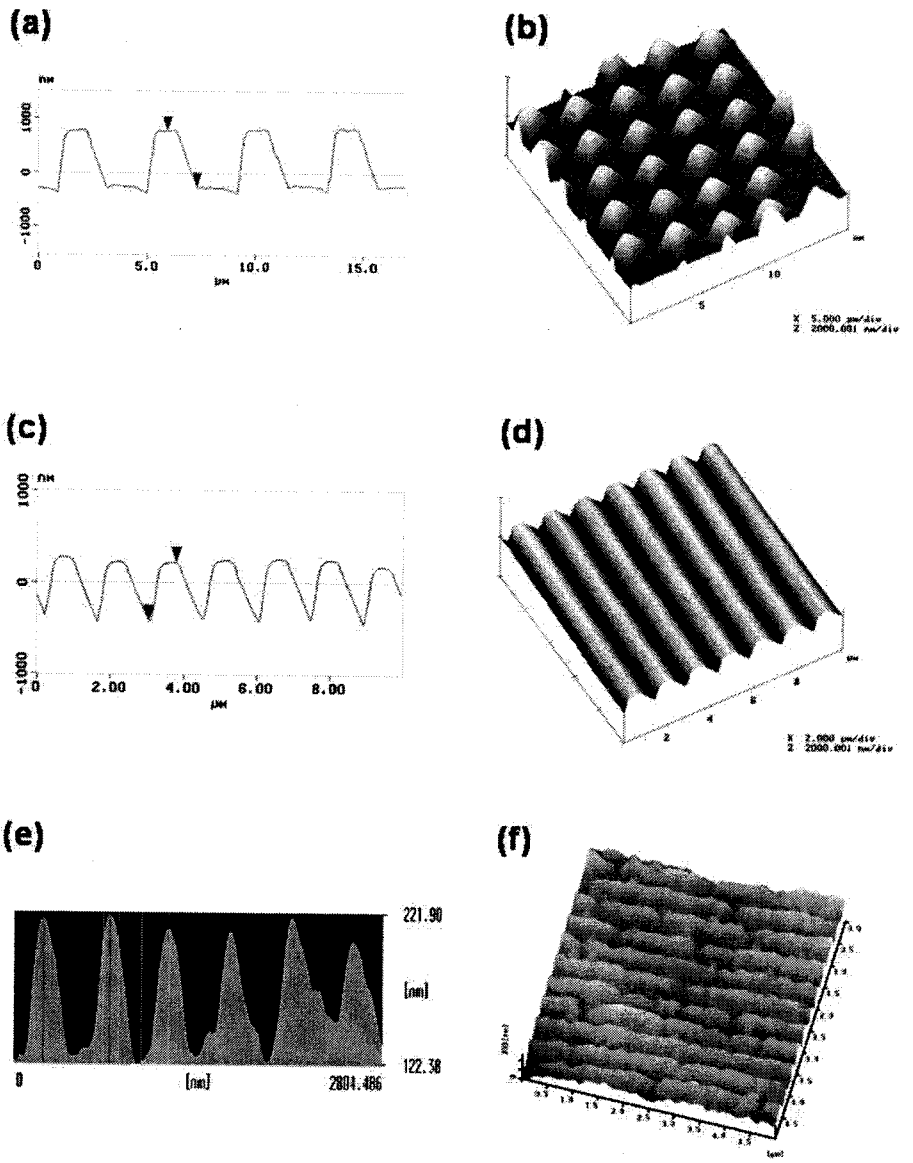

Figure 3.1.6.9. 2D and 3D AFM images of PDMS stamps. (a), (b) 1x1 μm^2 sized dots; (c), (d) 500 nm wide lines; and (e), (f) 100 nm wide lines.

3.2. Development of new theoretical and experimental method for non-spherical nanoparticle growth

3.2.1. Modelling of spatially 2D aerosol dynamics

3.2.1.1. Tubular furnace reactor

● Introduction

Furnace and flame reactors have been widely used to produce a variety of particles with different sizes and morphologies. Most of these aerosol reactors are spatially non-uniform, therefore, multi-dimensional systems (Gurav et al, 1993; Cho and Choi, 2000). Spatial transport mechanisms such as convection, diffusion, thermophoresis, and deposition should be considered in these multi-dimensional aerosol systems. Particles generated from gas phase reactions begin to grow as they collide with one another. If every pair of the colliding particles is fused instantaneously, particles can be assumed as unagglomerate shapes. Some solid particles that have finite characteristic times for coalescence usually become non-spherical aggregates (Lee and Choi, 2000, 2002; Lee et al., 2001c). These particles may coalesce to become more compact structures as they passthrough high temperature zone. It is, therefore, important to understand the dynamics of non-spherical particles in spatially multi-dimensional geometries.This would require accurate modeling of the growth and transport of non-spherical polydisperse particles undergoing collision, coalescence, and nucleation in multi-dimensional reactors.

Several non-spherical particle dynamicsmodels have been proposed during past ten years. To characterize the size and morphology of aggregate particles, more than two properties of a particle need to be introduced independently. Volume and surface area of an aggregate particle have been often employed as two independent variables (Koch and Friedlander, 1990 Xiong and Pratsinis, 1993 Tsantilis and Pratsinis, 2000 Jeong and Choi, 2001). Xiong and Pratsinis (1993) developed an elaborate two-dimensional sectional model, in which the term two-dimension implies the internal coordinates, i.e., the particle volume and surface area. In the model, they divided the particle volume and surface area domains into a finite number of sections, respectively, and calculated the transfers of sectional particle volume concentrationbetween the divided sections as a result of coagulation and coalescence. Though this model could produce very accurate simulation results if a sufficient number of sections is used (Wu and Biswas, 1998), it requires extensive computation. Hence, it is very difficult to apply this model to solve the spatially multi-dimensional problem of polydisperse, non-spherical particle growth. The quite simple monodisperse model proposed by Kruis et al. (1993) could be utilized for the simulations of spatially multi-dimensional problem. But this model inherently cannot predict polydispersity; therefore, it could not simulate properly the problem having both nucleation and growth simultaneously. Tsantilis and Pratsinis (2000) proposed a one-dimensional sectional method assuming that the particle surface area in the given section would decrease

monotonically due to coalescence effect, but they did not consider the effect of coagulation on the change of surface area of aggregates. Recently, authors have developed a very efficient non-spherical sectional model (Jeong and Choi, 2001). In this model, the particle volume domain alone is divided into a number of sections and within each divided section, sectional equations for volume and surface area conservations of particles are solved. This sectional method not only maintains as high accuracy as that ofthe detailed two-dimensional sectional model (Xiong and Pratsisnis, 1993), but also reduces the numerical computational load significantly. More specifically, it requires only about 1/1000 of calculation time compared to the elaborate two-dimensional sectional model (Jeong and Choi, 2001).

Because of the excessive computational demands, previous numerical simulations on non-spherical particle dynamics have been limited to spatially one-dimensional problems (Xiong et al., 1993; Seto et al., 1997; Tsantilis and Pratsinis, 2000; Lee et al., 2001a, 2001b; Nakaso et al., 2001) or assumed simplified monodisperse distribution of aggregates (Schild et al., 1999; Johannessen et al., 2000). Previous studies on non-spherical particle dynamics are reviewed below.

Akhtar et al. (1991) investigated titania aggregate growth by comparing the particle size distributions predicted by the spherical sectional model with the experiment data. The spatially one-dimensional and spherical particle dynamics simulation underestimated the average sizes of particles. However, a good agreement was obtained when a coagulation enhancement factor was employed. Tsantilis and Pratsinis (2000) simulated titania particle growth in a tube furnace reactor with their version of the aggregate sectional model. Assuming a plug-flow one-dimensional geometry, they compared the predicted particle sizes with the experimental data of Akhtar et al. (1991). The results of the aggregate aerosol dynamics model agreed better with experiment data than those of the spherical aerosol dynamics model did. However, they did not take into account the multi-dimensional effects of spatial transport processes inside the tube reactor. Johannessen et al. (2000) presented a mathematical model for the growth of aggregate alumina particles, including the kinetics of coagulation and coalescence, which was combined with calculations of the detailed fields of temperature, velocity and gas species distributions in a two-dimensional co-flow diffusion flame. However, they assumed monodisperse aggregate and primary particle distributions and instantaneous particle nucleation. Schild et al. (1999) also used a monodisperse model for aggregate particle growth interfaced to the commercial computational code FLUENT. It was demonstrated that there were considerable spatial dispersions of gas mixture and aggregate particles as well. The monodisperse model does not require heavy computationalloads and thus its application to the multi-dimensional problems is straightforward. However, it should be noted that the monodisperse model cannot take into account the effectof polydispersity of particle size distribution obviously; therefore, it performs poorly especially when new particles form simultaneously together with collision and coalescence processes, which often leads to a bi-modal particle distribution (Landgrebe and Pratsinis, 1990 Jeong and Choi, 2001).

In summary, it is hard to find studies on the growth of polydisperse non-spherical particles in a multi-dimensional reactor. Motivated by this, the present study carries out a numerical analysis of

non-spherical polydisperse particle growth undergoing collision, coalescence, nucleation, convection, diffusion, deposition and thermophoresis in a two-dimensional tubular reactor.

● Methods

Heat and mass transfer analysis in a two-dimensional tubular furnace reactor

Figure 3.2.1.1.1 is a schematic diagram of the two-dimensional axi-symmetric tubular furnace reactorthat was used in the experimental study of Akhtar et al. (1991). Titanium tetrachloride ($TiCl_4$) is introduced into the reactor with argon carrier gas and oxygen. Titania (TiO_2) particles are generated due to oxidation of $TiCl_4$ and move to the downstream undergoing coagulation, coalescence, convection, diffusion, and thermophoresis. Some particles deposit on the reactor walls. To investigate the evolution of aggregate particles, spatial transport phenomena should be incorporated in the particle dynamics calculation. In the numerical analysis, it is assumed that particle formation and motion do not disturb the flow and temperature distributions, since the volume fraction of the TiO_2 particles dealt in the present study isnegligible compared to that of the gas mixture (see Figure 3.2.1.1.5b). Continuity, momentum, energy and species equations of the gas mixture are first solved. Distributions of velocity, temperature and species concentration fieldsare then used to simulate the aggregate particle growth. Buoyancy effect is not taken into account because the average axial flow velocity is sufficiently high. In most part of the reactor except inlet and outlet, the ratio of the Grashof number over the square of the Reynolds number which indicates the ratio of the buoyancy force to the inertial force is much smaller than unity (Gr/Re^2= 0.001 ~ 0.1). Therefore, it is reasonable to neglect buoyancy effect (Incropera and DeWitt, 1990). A finite volume method (FVM) based on the SIMPLE algorithm (Patankar, 1980) is implemented to solve the laminar, axi-symmetric steady-state flow and heat transfer. The continuity equation (Eq. (3.2.1.1.1)) and the generalized conservation equations for velocity, temperature, and gas species (Eq. (3.2.1.1.2)) in a cylindrical two-dimensional coordinate are described:

$$\frac{\partial(\rho U)}{\partial x}+\frac{\partial(\rho V)}{\partial r}=0, \tag{3.2.1.1.1}$$

$$\rho U\frac{\partial \phi}{\partial x}+\rho V\frac{\partial \phi}{\partial r}=\frac{\partial}{\partial x}\left(\rho\Gamma\frac{\partial \phi}{\partial x}\right)+\frac{1}{r}\frac{\partial}{\partial r}\left(r\rho\Gamma\frac{\partial \phi}{\partial r}\right)+Source,\quad \phi=U,V,T,C_i \tag{3.2.1.1.2}$$

The terms on the left hand side (LHS)in Eq.(3.2.1.1.2) describe the influence of convection, and the first and second terms on the right hand side (RHS) describe diffusions or conduction. The last term represents the source term due to the oxidation of $TiCl_4$ (the rate constant and activation energy for the reaction were obtained from Akhtar et al., 1990). 15*500 grid system was chosen for the analysis of momentum, heat and mass transfers (Park et al., 1999) and less than 10^{-5} residues were set for convergence. More details about the numerical techniques can be found elsewhere (Park et al.,

1999).

Non-spherical particle dynamics in a two-dimensional tubular reactor

Following the recentlydeveloped sectional model for the analysis of growth of polydisperse non-spherical particles (Jeong and Choi, 2001), each of two sets of sectional equations describes the evolution of particle volume and surface area concentrations, respectively.

$$\rho U\frac{\partial}{\partial x}\left(\frac{Q_{l,v}}{\rho}\right)+\rho V\frac{\partial}{\partial r}\left(\frac{Q_{l,v}}{\rho}\right)=\frac{1}{r}\frac{\partial}{\partial r}\left(r\rho\overline{D_{l,v}}\frac{\partial}{\partial r}\left(\frac{Q_{l,v}}{\rho}\right)-rV_T Q_{l,v}\right)+\delta_{l-1}Iv_0$$
$$+\left(\frac{1}{2}\sum_{i=1}^{l-1}\sum_{j=1}^{l-1}\bar{\beta}_{i,j,l}^{1,v}Q_{i,v}Q_{j,v}-Q_{l,v}\sum_{i=1}^{l-1}\bar{\beta}_{i,l}^{2,v}Q_{i,v}-\frac{1}{2}\bar{\beta}_{l,l}^{3,v}Q_{l,v}^2-Q_{l,v}\sum_{i=l+1}^{m}\bar{\beta}_{i,l}^{4,v}Q_{i,v}\right) \quad (3.2.1.1.3)$$

$$\rho U\frac{\partial}{\partial x}\left(\frac{Q_{l,s}}{\rho}\right)+\rho V\frac{\partial}{\partial r}\left(\frac{Q_{l,s}}{\rho}\right)=\frac{1}{r}\frac{\partial}{\partial r}\left(r\rho\overline{D_{l,s}}\frac{\partial}{\partial r}\left(\frac{Q_{l,s}}{\rho}\right)-rV_T Q_{l,s}\right)+\delta_{l-1}Ia_0$$
$$+\left(\frac{1}{2}\sum_{i=1}^{l-1}\sum_{j=1}^{l-1}\bar{\beta}_{i,j,l}^{1,s}Q_{i,s}Q_{j,s}-Q_{l,s}\sum_{i=1}^{l-1}\bar{\beta}_{i,l}^{2,s}Q_{i,s}-\frac{1}{2}\bar{\beta}_{l,l}^{3,s}Q_{l,s}^2-Q_{l,s}\sum_{i=l+1}^{m}\bar{\beta}_{i,l}^{4,s}Q_{i,s}-Q_{l,s}\bar{\mathrm{H}}_l\right), \quad (3.2.1.1.4)$$

where particle volume and surface area concentrations of the l-th section are defined by

$$Q_{l,v}=\int_{v_{l-1}}^{v_l}[n(v)v]dv\,,\quad Q_{l,s}=\int_{v_{l-1}}^{v_l}[n(v)a]dv \quad (3.2.1.1.5)$$

and $Q_{l,s}\bar{\mathrm{H}}_l$ represents the effect of surface area reduction due to coalescence.

The integrated properties of volume and surface concentrations of the l-th section, $Q_{l,v}$, and $Q_{l,s}$, are described per unit mass of the mixture gas to consider non-isothermal systems (Patankar, 1980; Wu and Flagan, 1988). These two coupled sectional equations are solved simultaneously by taking account of the spatial transport mechanisms (refer to Jeong and Choi (2001) for the definition of each coefficient in Eqs. (3.2.1.1.3) and (3.2.1.1.4)). Brownian particle diffusion is included in the first term on the RHS of each equation. Here, $\overline{D_{l,v}}$ and $\overline{D_{l,s}}$ are the sectional-average diffusion coefficients of volume and surface area, respectively, as defined by:

$$\overline{D_{l,v}}=\frac{1}{(v_l-v_{l-1})}\int_{v_{l-1}}^{v_l}D_p dv \quad (3.2.1.1.6a)$$

$$\overline{D_{l,s}}=\frac{1}{(a_l-a_{l-1})}\int_{v_{l-1}}^{v_l}D_p da \quad (3.2.1.1.6b)$$

where D_p the particle diffusion coefficient (Xiong and Pratsinis, 1993). From the relation of $a = a_0\left(\frac{v}{v_0}\right)^{D_s/3}$, $\overline{D_{l,s}}$ in Eq. (3.2.1.1.6b) can be rewritten as:

$$\overline{D_{l,s}} = \frac{D_{s,l}}{3(v_l^{D_{s,l}/3} - v_{l-1}^{D_{s,l}/3})} \int_{v_{l-1}}^{v_l} D_p v^{(D_{s,l}/3-1)} dv \qquad (3.2.1.1.6b^*)$$

where $D_{s,l}$ represents the surface fractal dimension of l-th section ranging from 2 to 3. The second terms on RHS of Eqs. (3.2.1.1.3) and (3.2.1.1.4) describe the influence of the thermophoretic particle motion. The symbol V_t refers to the radial thermophoretic velocity as defined by (Lee et al., 2001a):

$$V_t = -\frac{K\mu}{\rho T}\frac{\partial T}{\partial r} \qquad (3.2.1.1.7)$$

where K is the thermophoretic coefficient, which is assumed to be equal to 0.55(Kim and Pratsinis, 1988; Lee et al., 2001a, b). The third terms on the RHS account for the generation of monomer particles by gas phase reaction. They are included solely in the equations for the first volume section (l=1). The rest terms on the RHS correspond to the effects of the particle coagulation and coalescence. The Brownian collision frequency function, β, involved in the coagulation coefficients has a form of the Fuchs' interpolation (Seinfeld, 1986), which covers from the free molecular to the continuum regime. The collision diameter, dc, is used to replace the characteristic diameter in the collision frequency function following the works of Kruis et al.(1993)and Tsantilis and Pratsinis (2000). A couple of different models for the characteristic coalescence time oftitania particles have been proposed in the literature (Kobata et al., 1991 Xiong et al., 1993):

Kobata et al. $\tau_f = 7.4\times10^{16} T d_p^4 \exp(\frac{3.1\times10^4}{T})$ (3.2.1.1.8a)

Xiong et al. $\tau_f = 8.3\times10^{24} T d_p^4 \exp(\frac{3700}{T})$. (3.2.1.1.8b)

The deposition process of TiO_2 particles on the reactor wall is also incorporated by imposing the boundary conditions at the wall: $Q_{l,v}, Q_{l,s} = 0$, at r=R while the reactor wall is assumed to be impermeable for gas species, and thus all the radial derivatives of the gas species mass fraction at the wall are zero in Eq. (3.2.1.1.2).

The procedure to obtain the surface fractal dimension, $D_{s,l}$, for each section is as follows. First, sectional volume and surface area conservation equations (Eqs. (3.2.1.1.3) and (3.2.1.1.4)) are solved simultaneously with the values of $D_{s,l}$'s obtained one axial grid earlier. Then, from the resulting $Q_{l,s}$ and $Q_{l,v}$, $D_{s,l}$'s at the present position can be determined using the relation given in Eq. (3.2.1.1.9) below (Jeong and Choi, 2001):

$$\frac{Q_{l,s}}{Q_{l,v}} = \frac{3a_0}{D_{s,l} v_0^{\frac{D_{s,l}}{3}}} \frac{\left(v_l^{\frac{D_{s,l}}{3}} - v_{l-1}^{\frac{D_{s,l}}{3}}\right)}{(v_l - v_{l-1})} \tag{3.2.1.1.9}$$

Eqs. (3.2.1.1.3) and (3.2.1.1.4) are solved again with new coagulation and coalescence coefficients determined from these surface fractal dimensions to obtain solutions for new $Q_{l,s}$ and $Q_{l,v}$. Several iterations of the above procedure are needed to acquire converged solutions.

Simplified one-dimensional analysis

Simplified one-dimensional analysis has also been carried out for the comparison with the two-dimensional solutions. The simplified one-dimensional non-spherical sectional equations for particle volume (Eq. (3.2.1.1.10)) and surface area (Eq. (3.2.1.1.11)) can be expressed using the mixing-cup average axial flow velocity $\overline{U}$ as follows:

$$\rho\overline{U}\frac{d}{dx}\left(\frac{Q_{l,v}}{\rho}\right) = \delta_{l-1} I v_0 + \left(\frac{1}{2}\sum_{i=1}^{l-1}\sum_{j=1}^{l-1}\overline{\beta}_{i,j,l}^{1,v} Q_{i,v} Q_{j,v} - Q_{l,v}\sum_{i=1}^{l-1}\overline{\beta}_{i,l}^{2,v} Q_{i,v} - \frac{1}{2}\overline{\beta}_{l,l}^{3,v} Q_{l,v}^2 - Q_{l,v}\sum_{i=l+1}^{m}\overline{\beta}_{i,l}^{4,v} Q_{i,v}\right) \tag{3.2.1.1.10}$$

$$\rho\overline{U}\frac{d}{dx}\left(\frac{Q_{l,s}}{\rho}\right) = \delta_{l-1} I a_0 + \left(\frac{1}{2}\sum_{i=1}^{l-1}\sum_{j=1}^{l-1}\overline{\beta}_{i,j,l}^{1,s} Q_{i,s} Q_{j,s} - Q_{l,s}\sum_{i=1}^{l-1}\overline{\beta}_{i,l}^{2,s} Q_{i,s} - \frac{1}{2}\overline{\beta}_{l,l}^{3,s} Q_{l,s}^2 - Q_{l,s}\sum_{i=l+1}^{m}\overline{\beta}_{i,l}^{4,s} Q_{i,s} - Q_{l,s}\overline{\mathrm{H}}_l\right). \tag{3.2.1.1.11}$$

In solving these equations, diffusion, thermophoresis and deposition are excluded in contrast to Eqs. (3.2.1.1.3) and (3.2.1.1.4). This simplified version has been compared with the present detailed two-dimensional analysis.

● Results and discussion

Comparison with experimental data

First, we have carried out numerical simulation of particle growth in a furnace reactor with the experimental conditions used by Akhtar et al. (1991) and compared the predicted results with their measured data: reactor length L=0.6m, reactor radius R=0.0159m, inlet flow rate Q_{in}=1.7 or 3.5lpm, inlet $TiCl_4$ concentration C_{in}=1.56e-5 or 9.34e-6 mol/L and furnace set temperature, T_{max}=1373K. Figure 3.2.1.1.2 shows the comparison between predicted temperature profiles and the previous measured data inside the tubular furnace reactor. The thick solid line, square and diamond symbols represent the previously-measured wall temperature and centerline gas temperatures for the flow rates of 1.7 lpm and 3.5 lpm, respectively (Akhtar et al., 1991). The measured wall temperature is used as wall boundary condition for the simulation. The radiation compensation has been taken into account for comparison with the previous thermocouple measurements. The predicted temperature profiles are in reasonable agreement with the measured data.

The simplified version of the spatially one-dimensional calculations described in Eqs. (3.2.1.1.10) and (3.2.1.1.11) has been first performed and compared with experimental data and the previous simulations done by Tsantilis and Pratsinis (2000). Spatially two-dimensional calculations will be discussed later. The spherical sectional model by Gelbard et al.(1980), the monodisperse aggregate model by Kruis et al. (1993) and the aggregate discretization model by Tsantilis and Pratsinis (2000) were chosen for the comparisonwith the present approach in simulation aspect. The characteristic coalescence times proposed by Kobata et al. and Xiong et al. (Eqs. (3.2.1.1.8a) and (3.2.1.1.8b)) were used for each aggregate particle dynamics analysis.

As shown in Figure 3a and 3b for different precursor concentrations, C_{in}=1.56e-5 mol/L and C_{in}=9.34.e-6 mol/L, the spherical model underpredicts the particle size distributions as expected. This is because the spherical particles have smaller collision diameters than the non-spherical and fractal-like aggregates. The monodisperse model gives relatively good results despite its simplicity. The predicted monodisperse sizes are close to the average sizes of experimental data since particle generation has been complete at the measured location (exit of the tube) and a uni-modal distribution is built up. As mentioned earlier, however, the monodisperse model may lead to significant errors when the particle sizes have a bi-modal distribution due to the generation of particles (Landgrebe and Pratsinis, 1990 Jeong and Choi, 2001). The size distribution of aggregate surface area equivalent diameters predicted by Tsantilis and Pratsinis (2000) shows reasonable agreement with the measurementsdone by Differential Mobility Particle Size (Akhtar et al.,1991). However, their model predicts a much broader distribution as shown in Figure 3b, when the characteristic coalescence time of Kobata et al. (Eq. 3.2.1.1.8a) is applied. One of the possible explanations would be that their model neglects the effect of coagulation on coalescence. The present result of the size distribution of collision diameters shows better agreement with the experimental data. The discrepancy in the left part of the size distributions would be partially attributed to particle deposition on the reactor wall and sampling loss in experiment. In addition, the radial variation of flow, temperature and particle

properties was not considered in the simplified one-dimensional calculations.

A spatially two-dimensional calculation has also been carried out for the same conditions. Figure 4 shows three normalized particle size distributions obtained at different radial (r/R=0, r/R=0.65, and r/R=0.96). The characteristic coalescence time for TiO_2 particle modeled by Kobata et al., (1991) was used in the calculation. Considerable variations of aggregate particle size distributions are clearly seen with respect to radial positions at the same axial position. The measured size distribution is placed between the predictions of r/R=0.96 and r/R=0, which implies that the measured particle size distributions may depend strongly on the location of the measuring probe in such a spatially inhomogeneous system. Even though the simplified version of spatially one-dimensional model would give reasonable prediction for aggregate size distributions, the detailed information at different radial positions cannot be obtained without relying on spatially two-dimensional approach.

Spatial distributions

The spatial evolutions of the size distribution of aggregate particles have been investigated with the conditions of reactor length L=0.7m, reactor radius R=0.015m, inlet flow rate Q_{in}=3lpm, inlet $TiCl_4$ concentration C_{in}=1.e-5 mol/L and maximum wall temperature, T_{max}=1400K.

Figure 3.2.1.1.5 is a set of contour plots for the spatial distributions of temperature and aggregate particle sizes. The plots display only half of the tubular reactor because the reactor is assumed to be axi-symmetric. Figure 3.2.1.1.5a is a contour plot for the local temperature distribution. Temperature distribution is spatially inhomogeneous throughout the reactor. More specifically, the gas temperatures near the wall region are higher than near the center region in the axial distances up to x~0.5m, but this is reversed in the downstream region (~0.5m<x<0.7m). As a result, particles are transported by thermophoresis from the wall to the center in the former region and from the center to the wall in the latter one. The spatial distributions of the particle properties such as volume concentration, number concentration, geometric mean diameters, etc. are shown in Figure 3.2.1.1.5b to Figure 3.2.1.1.5g.

The spatial distribution of the particle volume concentration is shown in Figure 5b. Higher particle volume concentration is observed adjacent to the wall region. In the region close to the wall where gas mixture is heated high enough for chemical reaction of $TiCl_4$, a large amount of monomer particles are generated immediately and flow downstream. Since the oxidation of TiCl4 begins to occur near the hot wall, $TiCl_4$ precursor in the core part diffuses toward the wall compensating the consumption of the precursor near the wall. In the exit region, the particle volume concentration near the center region decreases due to thermophoretic particle transport from the core region to the wall.

The distributions of total aggregate particle number concentration N_t and geometric mean collision diameter dgc are plotted in Figures 3.2.1.1.5c and 3.2.1.1.5d, respectively. The generation and coagulation of particles determine the evolution of N_t. The value of N_t increases up to x=0.3m, while the geometric mean collision diameter d_{gc} remains as small as the monomer size up to x=0.3m. This indicates that the formation of monomer particle is dominant in this region. N_t has a local minimum near the wall in the region 0.04<x<0.08m, wherethe particle coagulation would play a role in

decreasing number concentration and increasing the size as shown in Figures 3.2.1.1.5c and 3.2.1.1.5d. For x >0.4m, the monomer particle generation begins to stop from the wall region while coagulation continues. In this region, the total particle number decreases due to coagulation and the geometric mean size of the aggregate particles rapidly increases. An interesting feature is observed near the exit: N_t increases again near the wall accompanied with the reduction of d_{gc}. The particle volume concentration also increases. This would be attributed mainly to thermophoresis that causes small aggregate particles in the core region to move toward the colder wall region. Particle size distributions of this region will be further examined later.

Figure 3.2.1.1.5e shows the contour plot for the geometric standard deviation of the aggregate particle size distribution, σ_g. In the fore part of the reactor up to x=0.4m, σ_g is almost unity indicating again monodisperse particle size distribution due to the dominant monomer generation, which is also consistent with the results of geometric mean collision diameter shown in Figure 3.2.1.1.5d. As particles grow by coagulation, large size aggregate particle coexists with the small monomer particles which are still being produced. In this situation, the particle size span becomes wider and σ_g increases. The value of σ_g becomes the maximum in the region near x=0.4m where there is an abrupt increase in the size of aggregate particle due to the rapid decrease of monomer number. Aggregate particles near the wall are larger than those near the core as demonstrated in Figure 3.2.1.1.5d, thus, σ_g near the wall is also higher. After the chemical reaction ceases, coagulation process dominates and reduces the particle size span. Therefore, σ_g continues to decrease and reach an asymptotic value as the particle moves out of the tube.

The non-spherical particle dynamics model is capable of predicting the evolution of the number and size of primary particles composing the aggregate particles, whereas the spherical particle dynamics model obviously cannot distinguish the aggregate from the primary particle. Figures 3.2.1.1.5f and 3.2.1.1.5g are the contour plots of the geometric mean primary particle diameter d_{gp}, and the number of primary particles per aggregate particle n_{gp}, respectively. From the entrance to the middle of the reactor, the geometric mean diameter of the primary particle d_{gp} remains as monomer size and the number of primary particles n_{gp} is almost unity due to the dominant monomer generation, as mentioned earlier. A local increase in n_{gp}, however, is observed at about $0.03<x<0.18$ m where coagulation depletes plenty of small particles. The enhanced coagulation in this region should be attributed to the ineffective coalescence because of low temperatures, which results in aggregates having larger collision diameters. The sudden change of local distributions of d_{gp}, n_{gp}, and d_{gc} occurs in the middle of the reactor where chemical reaction ceases. As can be seen from the radial distribution, the size and number of the primary particles in the wall region are generally larger, since high temperatures promote not only particle generation and coalescence, but also coagulation. Thus, aggregates composed of larger primary particles in size and number may be present close to the wall while those of smaller primary particles would be placed in the center region.

The geometric standard deviation of the primary particle size distribution σ_{gp} is shown in Figure 3.2.1.1.5h. While the evolution pattern of σ_{gp} is similar to that of aggregate particles, σ_g, σ_{gp} has smaller values. It is well known that the primary particle size distribution is usually narrower than the aggregateparticle size distribution (Tsantilis and Pratsinis, 2000).

Figures 3.2.1.1.6a and 3.2.1.1.6b demonstrate the spatial non-uniformity of particle size distributions in another way. The aggregate size distributions near the centerline (Figure 3.2.1.1.6a) and near the wall (Figure 3.2.1.1.6b) are shown for three axial positions (x=0.3, 0.5 and 0.7 m). Under the given temperature and residence time, titania particles are not fully sintered to become spheres but become chain-like aggregates. For the particles flowing along the centerline (r/R=0, Figure 3.2.1.1.6a), the sizes of aggregate particles continue to increase. In this case, the increase of x simply means the increase of residence time for particles to grow into bigger aggregates. Bi-modal distributions appear at x=0.3 m and 0.5 m. A different aspect is, however, observed for the size evolution of the particles moving close to the wall (r/R=0.96, Figure 3.2.1.1.6b). Contrary to the monotonic increase of particle sizes along the centerline in Figure 6a, the sizes of aggregates particles near the wall first increase and then decrease. A large number of small particles appear placed in the right part of the size distribution at x=0.7 m. This would be attributed mainly to thermophoresis and possibly to particle diffusive transport that causes small aggregate particles in the center region to move toward the wall region. We also carried out additional calculation ignoring thermophoresis terms and the resulting aggregate particle size distributions near the wall arepresented in Figure 3.2.1.1.6c. Compared with the size distributions in Figure 3.2.1.1.6b, the aggregate particles at x=0.7 m has a narrower distribution with less amount of smaller particles. This clearly demonstrates that thermophoresis plays an important role in the two-dimensional furnace reactor. The significantly different evolution features of the particle size distributions at different radial positions imply that the increase of residence time will not always guarantee the increase of the mean particle size if the spatial transport of particles plays a significant role in the non-uniform system. It can be also inferred that the simplification of multi-dimensional problem to one-dimensional problem (e.g. a transformation of $\vec{u}\cdot\nabla\phi \rightarrow \frac{\partial\phi}{\partial t}$ or $\overline{U}\frac{\partial\phi}{\partial x}$) may introduce significant errors for that situation.

Higher wall temperatures cause faster monomer generation and more frequent collisions resulting in bigger aggregate sizes. At the same time, coalescence producing more compact aggregates will be also enhanced with a small number of large primary particles, and thus the aggregates would havesmaller collision cross sections. In addition, high process temperature renders a shorter particle residence time due to gas expansion, which may delay particle growth by coagulation. In Figures 3.2.1.1.7a and 3.2.1.1.7b, the mean sizes of the aggregate particles are much larger for T_{max}=1000K than for T_{max}=1800K at both the radial positions (r/R=0.0 and 0.96). At T_{max} =1800K, primary particles composing aggregates to become large-sized primary particles, and thus aggregates have more compact structures. Note that the size difference between primary and aggregate particles is not large

compared to the case of T_{max}=1000K. On the other hand, at T_{max}=1000K, aggregate particles cannot easily coalesce therefore, the aggregate particles consist of much more and smaller primary particlesas evidenced from the large difference between the primary and aggregate particle sizes shown in Figures. 3.2.1.1.7a and 3.2.1.1.7b. Correspondingly, aggregates obtained at T_{max} =1000K have larger collision diameters, which would result in larger sizes.

Comparison of one- and Two-dimensional analyses

Finally, it is worth examining whether the simplified version of the spatially one-dimensional analysis could model the multi-dimensional system approximately. Figures 3.2.1.1.8a and 3.2.1.1.8b show the comparison of the geometric mean primary particle diameter d_{gp} and the geometric standard deviations of aggregate particle distributions σ_g obtained from one-dimensional and two-dimensional analyses for different inlet flow rates. At lower flow rates, the one-dimensional approach seems to produce the results with reasonable agreements with the mixing-cup averages of the two-dimensional approach. However, at higher flow rates, the discrepancy becomes substantial. Low inlet flow rates cause thermal effects to penetrate more effectively in the radial direction. As a result, more uniform temperature and concentration can be obtained and the one-dimensional analysis may produce reasonable agreement with the two-dimensional one. The geometric mean primary particle diameter decreases with increasing inlet flow rate because a high flow rate shortens the particle residence time, and the difference in d_{gp} between the two analyses increases (Figure 3.2.1.1.8a). The evolution of the mixing-cup averages of σ_g for different flow rates are also shown in Figure 3.2.1.1.8b. A peak σ_g is seen for both flow rates. The maximum σ_g occurs at the region where the monomer generation and particle coagulation modes contain approximately equal number of particles and the chemical reaction is almost complete (Landgrebe and Pratsinis, 1990). While the one-dimensional solutions show sharp peaks of σ_g at certain axial position, the mixing-cup averaged results of the two-dimensional approach show broader peak. This is because the values of σ_g have significant variation in the radial direction even at the same axial position.

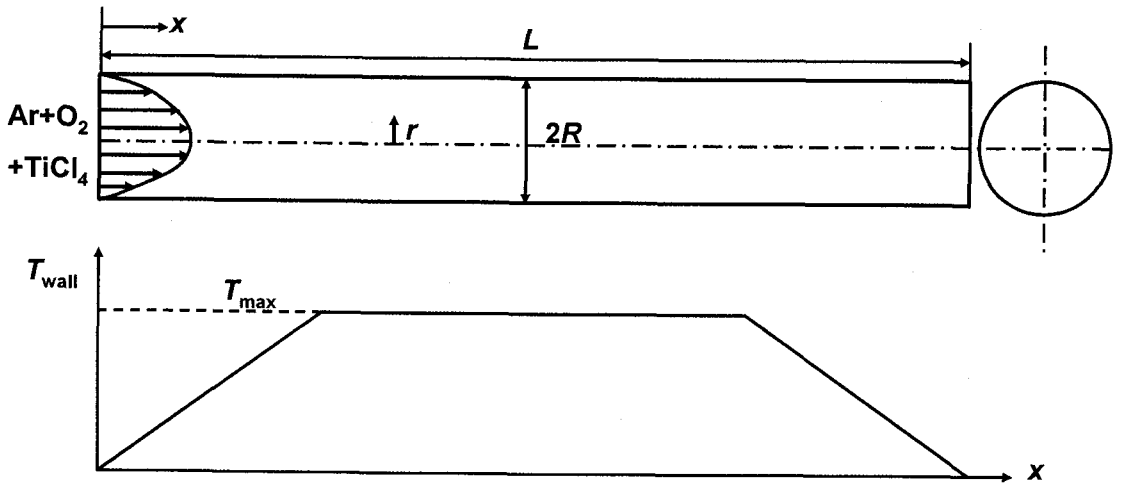

Figure 3.2.1.1.1. Schematic diagram of calculation domain for a tubular furnace reactor.

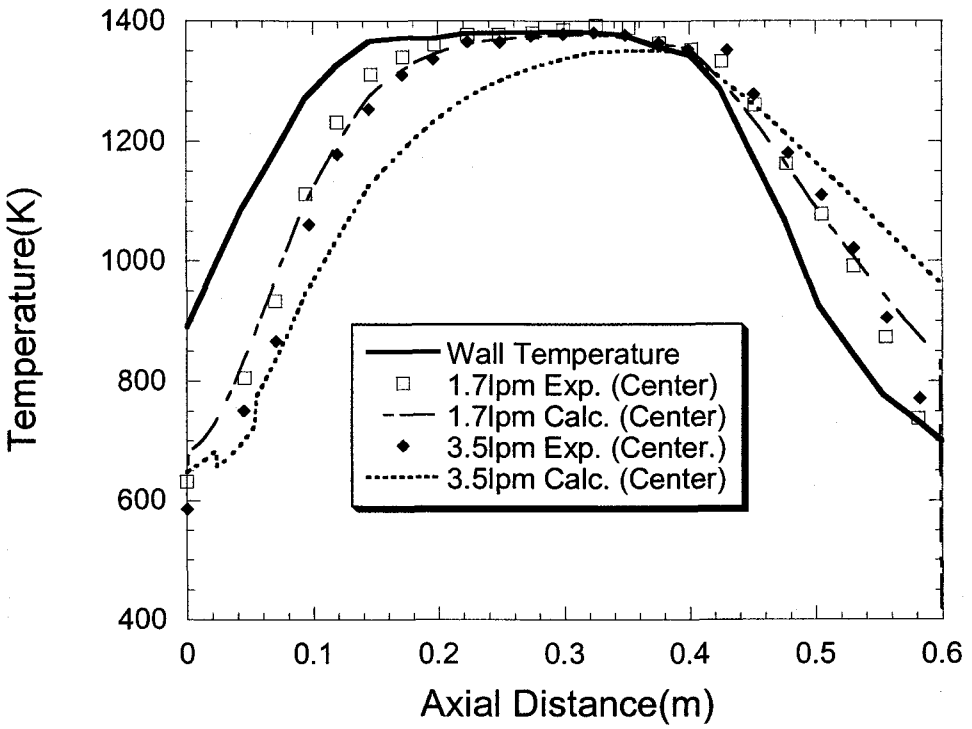

Figure 3.2.1.1.2. Comparison between calculated temperatures and the previous data (Akhtar et al., 1991) in the reactor. (L=0.6m, R=0.0159m, Q_{in}=1.7 or 3.5lpm, C_{in}=1.56e-5 or 9.34e-6 mol/L, T_{max}=1373K)

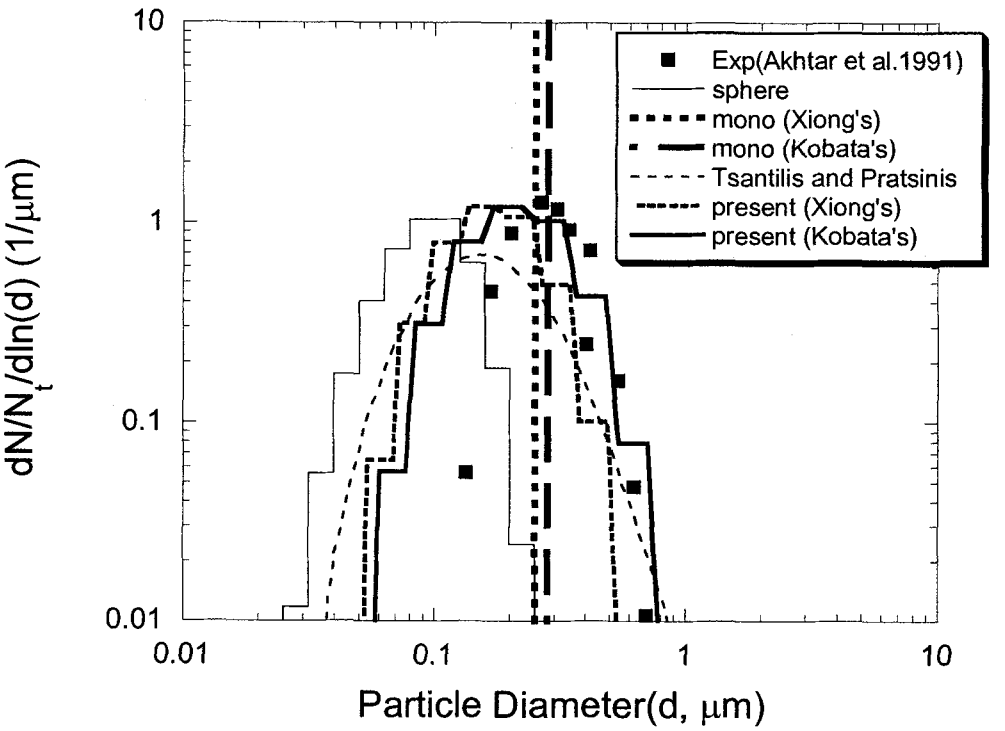

Figure 3.2.1.1.3a. Normalized aggregate particle size distributions obtained from one-dimensional models and the previous experimental data C_{in}=1.56E-5mol/L.

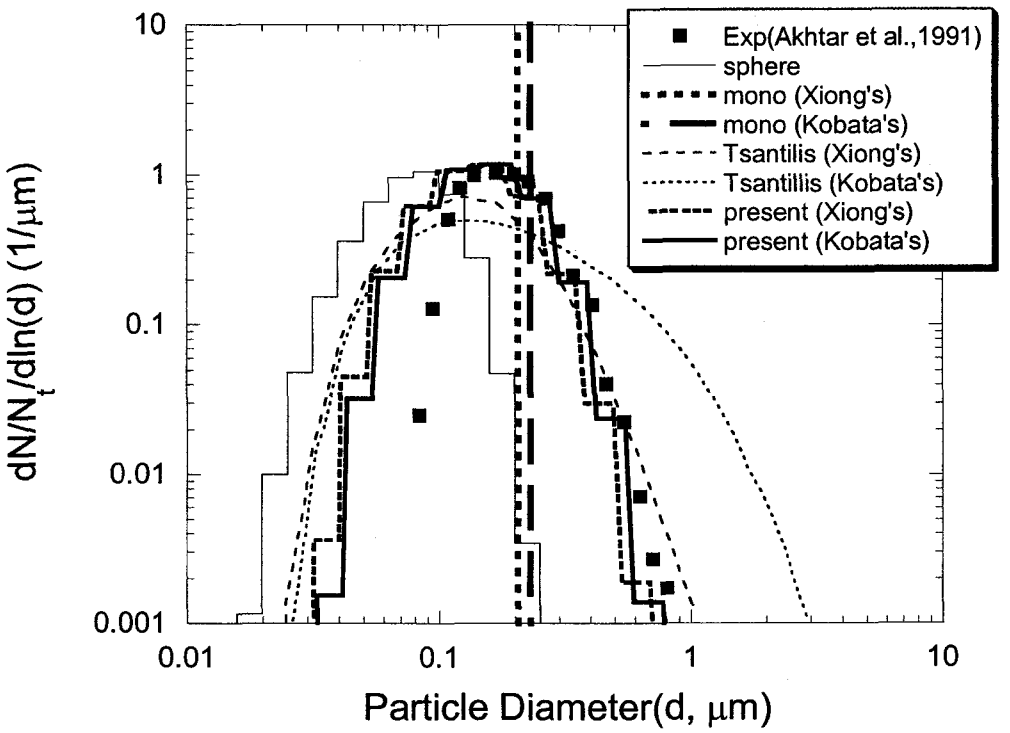

Figure 3.2.1.1.3b. Normalized aggregate particle size distributions obtained from one-dimensional models and the previous experimental data C_{in}=9.34E-6mol/L.

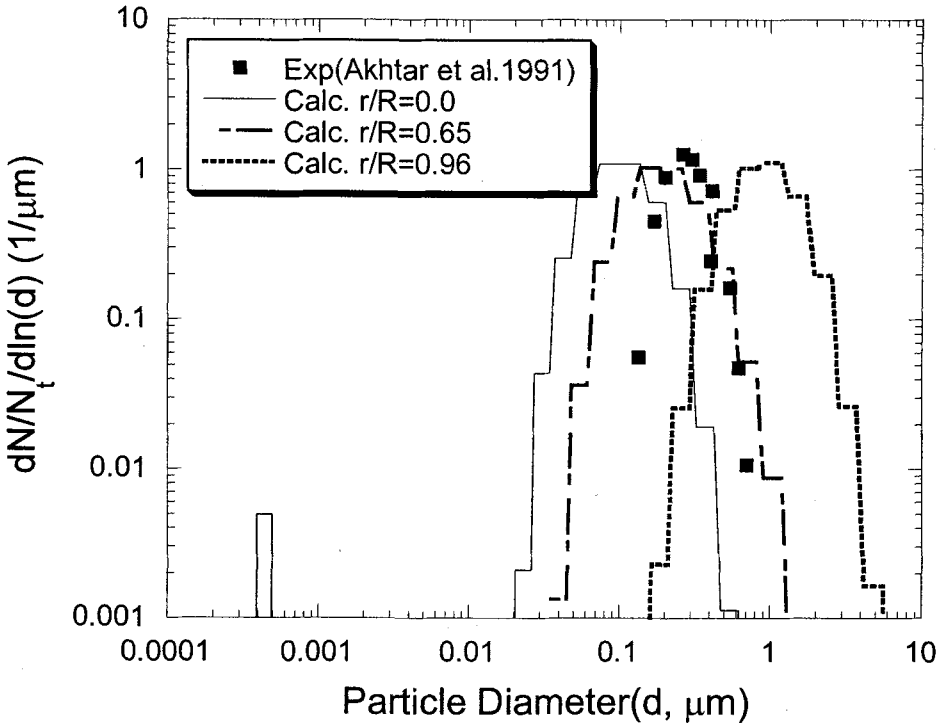

Figure 3.2.1.1.4. Comparison of the normalized aggregate particle size distributions of spatially two-dimensional analysis with the previous data; C_{in}=1.56E-5mol/L.

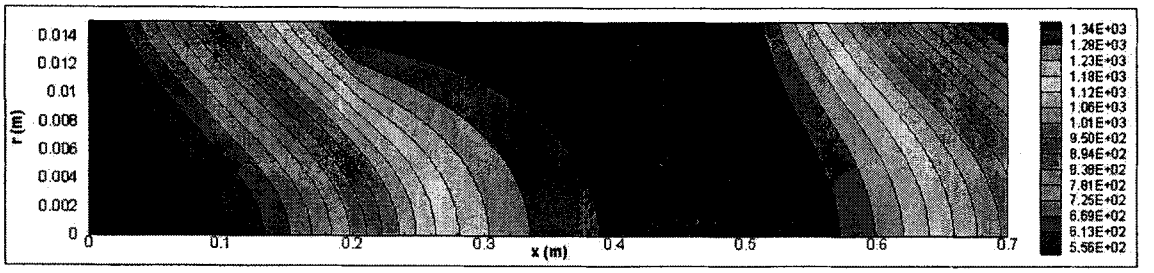

(a)

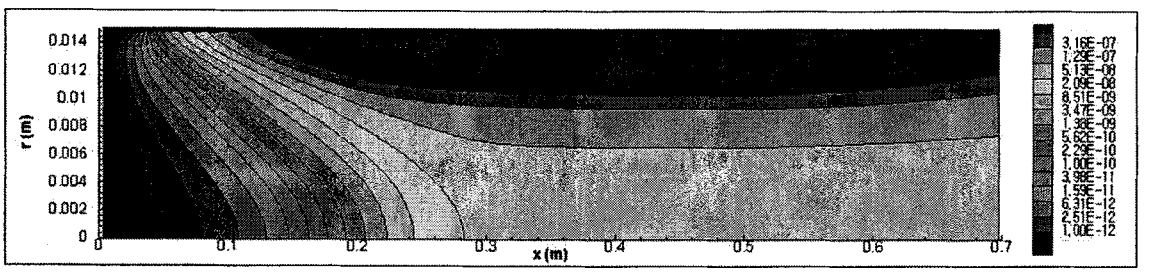

(b)

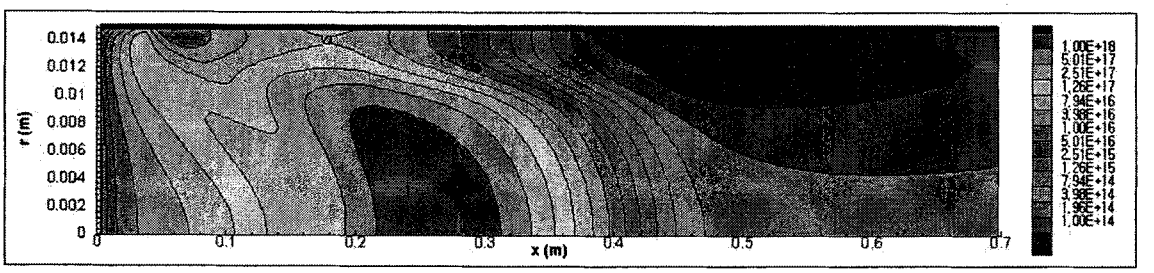

(c)

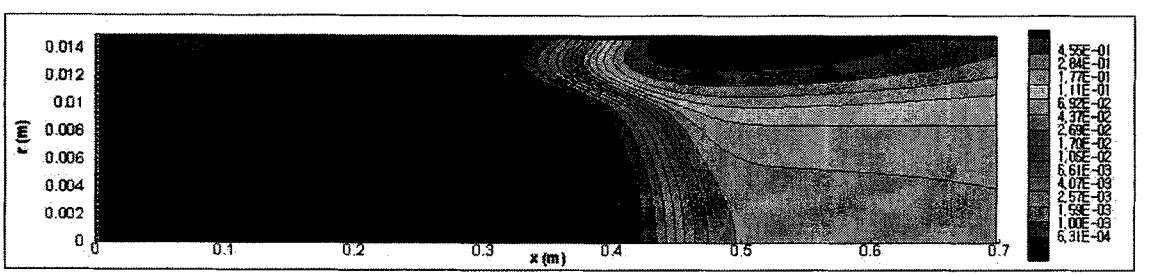

(d)

Figure 3.2.1.1.5. Contour plots for the spatial distribution of (a) gas temperature, (b) particle volume concentration, (c) aggregate number concentration and (d)geometric mean diameter of aggregate for standard condition.
(L=0.7m, R=0.015m, T_{max}=1400K, Q_{in}=3lpm, C_{in}=1.e-5 mol/L)

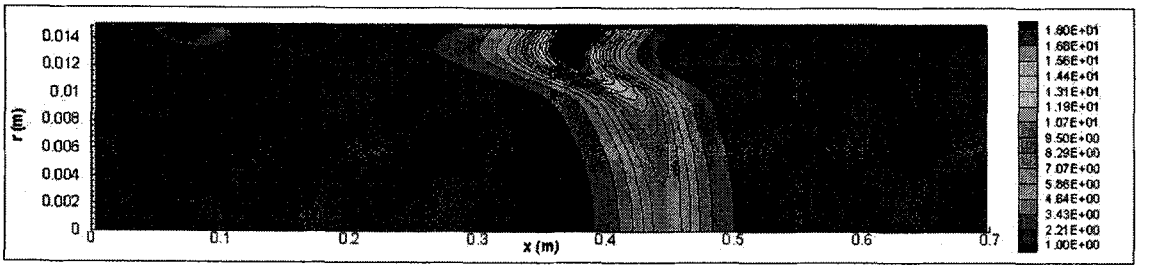

(e)

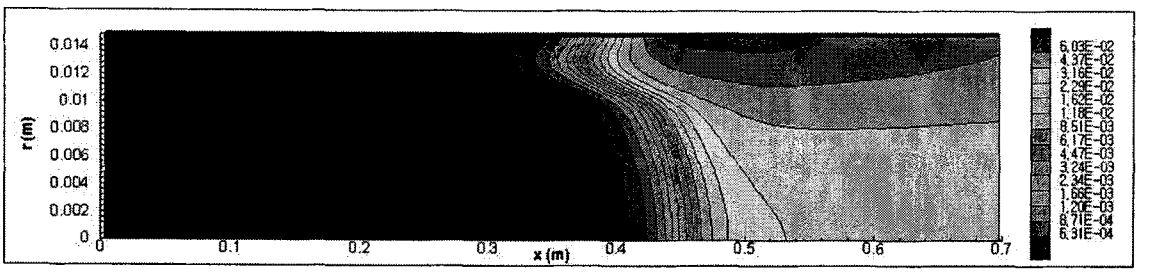

(f)

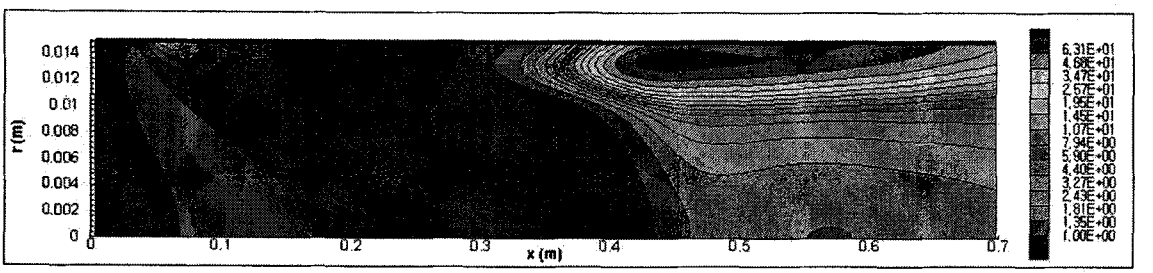

(g)

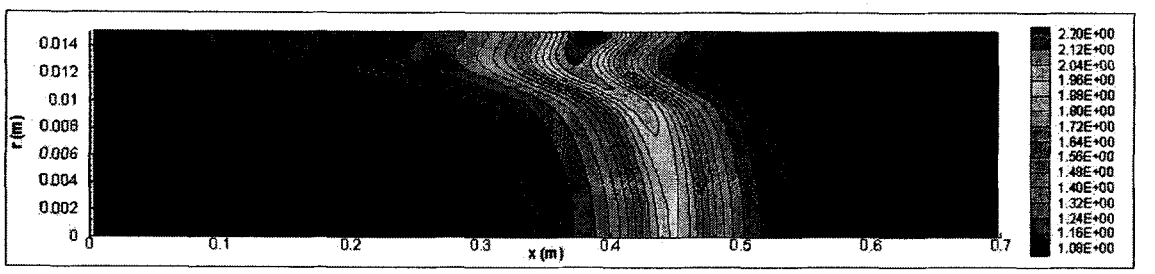

(h)

Figure 3.2.1.1.5. Contour plots for the spatial distribution of (e) geometric standard deviation of aggregate particle size distribution, (f) geometric mean diameter of primary particle (g) primary particle number per aggregate (h) geometric standard deviation of primary particle size distribution for standard condition. (L=0.7m, R=0.015m, T_{max}=1400K, Q_{in}=3lpm, C_{in}=1.e-5 mol/L)

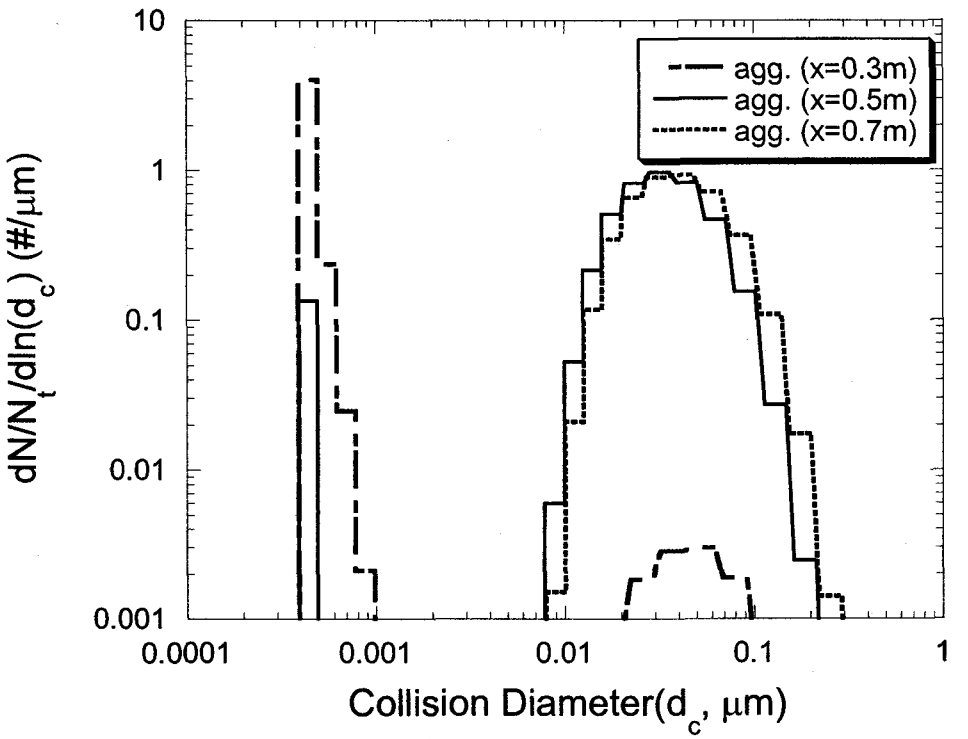

Figure 3.2.1.1.6(a). Normalized aggregate particle size distributions at the centerline for different axial locations. (T_{max}=1400K, Q_{in}=3lpm, r/R=0.96)

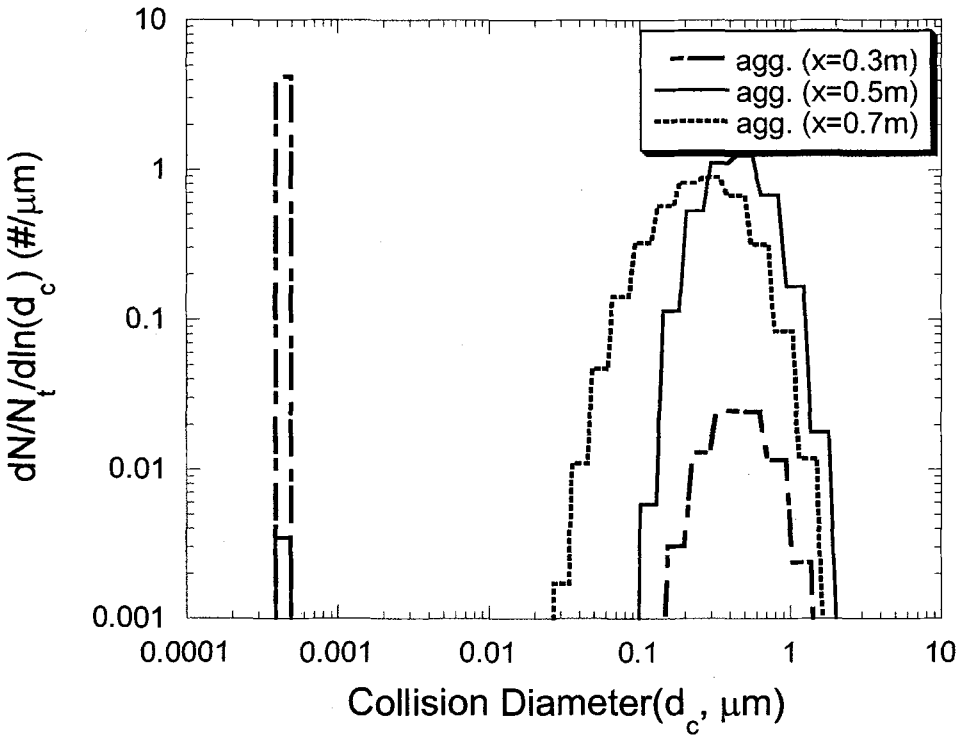

Figure 3.2.1.1.6(b). Normalized aggregate particle size distributions near the wall for different axial locations. (T_{max}=1400K, Q_{in}=3lpm, r/R=0.96)

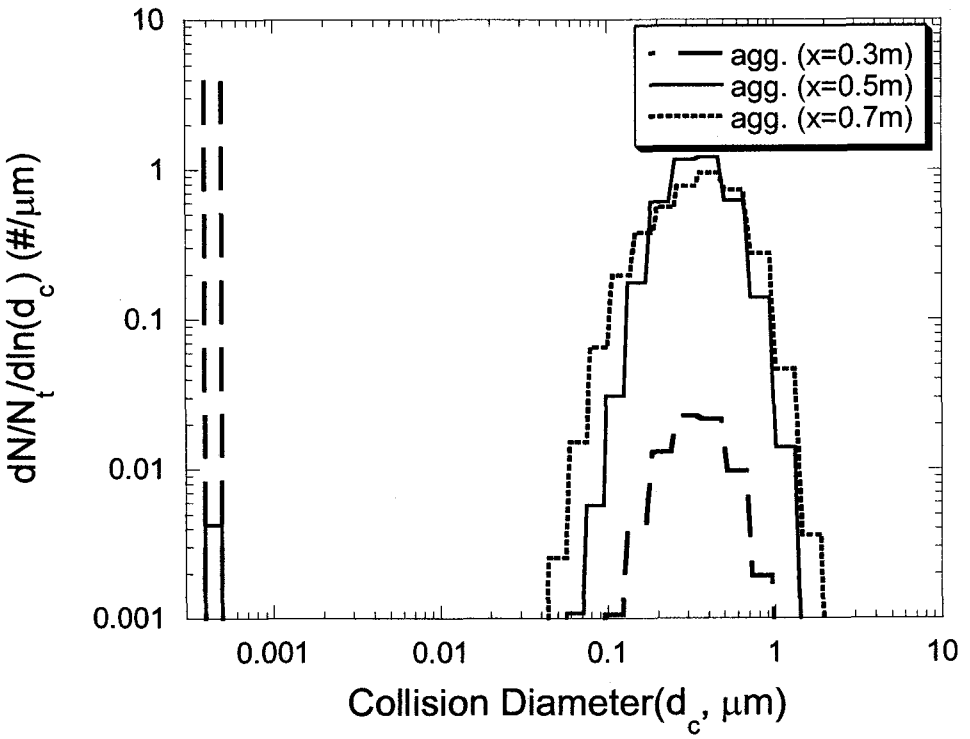

Figure 3.2.1.1.6(c). Normalized aggregate particle size distributions near the wall for different axial locations when particle thermophoresis is neglected.
(T_{max}=1400K, Q_{in}=3lpm, r/R=0.96)

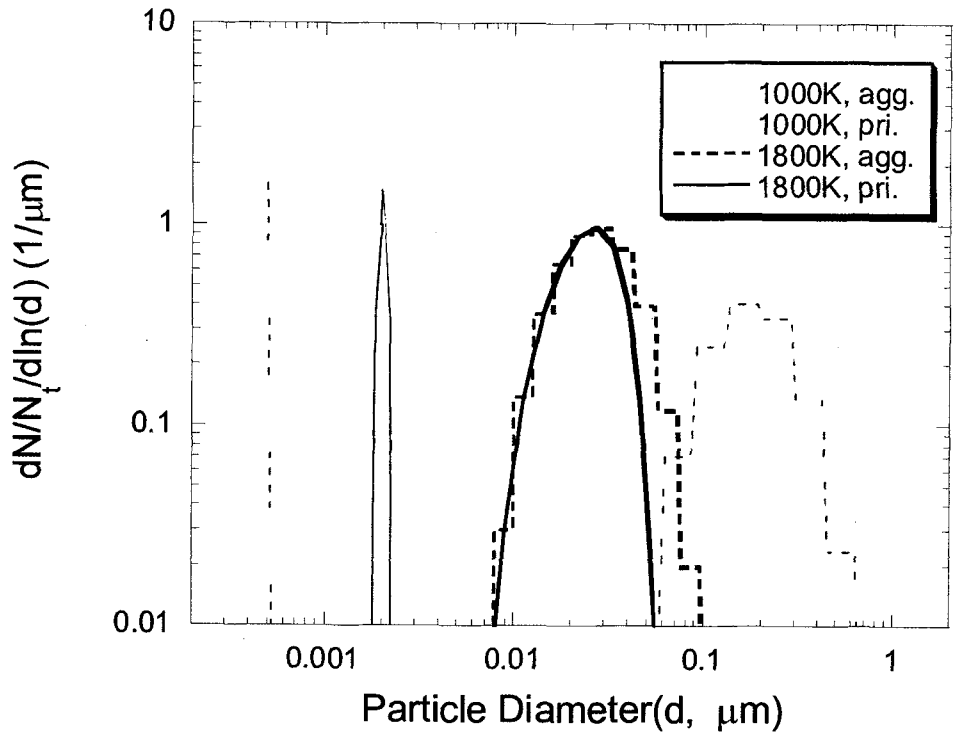

Figure 3.2.1.1.7(a). Normalized aggregate and primary particle size distributions at the centerline for different wall temperatures. (Q_{in}=3lpm, x=0.7m, r/R=0.96)

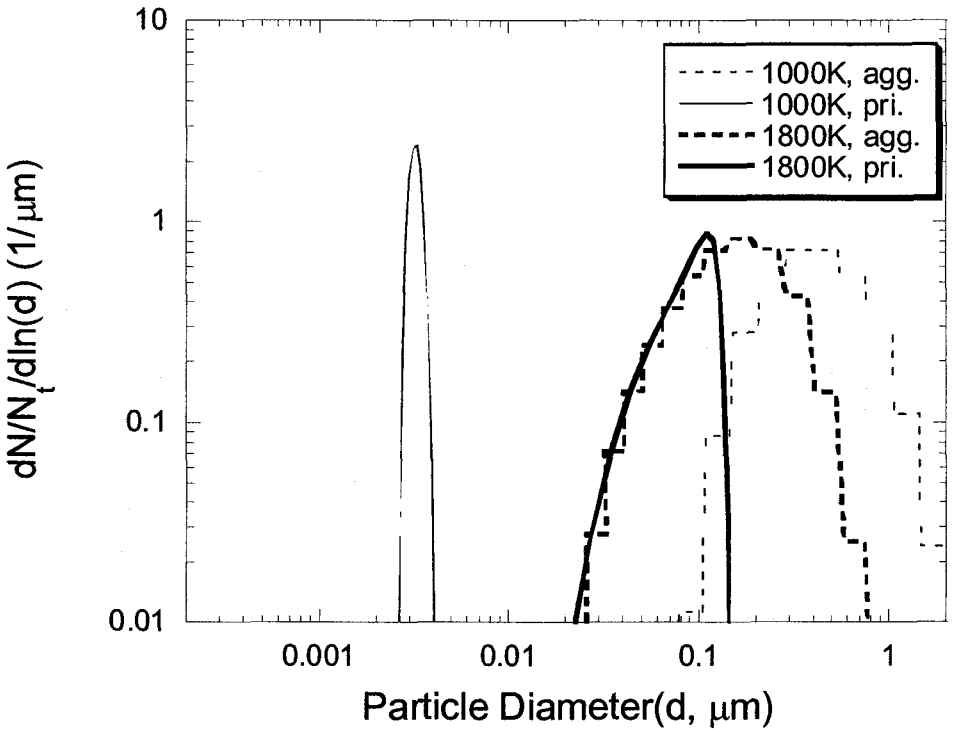

Figure 3.2.1.1.7(b). Normalized aggregate and primary particle size distributions near the wall for different wall temperatures. (Q_{in}=3lpm, x=0.7m, r/R=0.96)

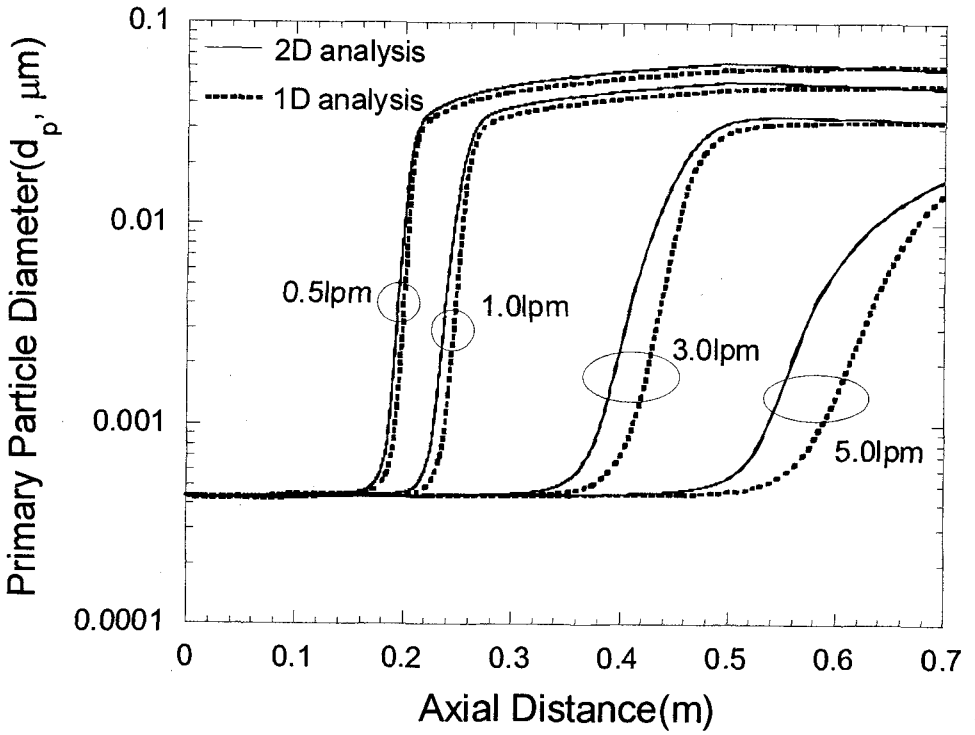

Figure 3.2.1.1.8(a). Comparison of one- and two-dimensional analyses on the evolution of geometric mean primary particle diameter along the axial distance for various inlet flow rates. (T_{max}=1400K)

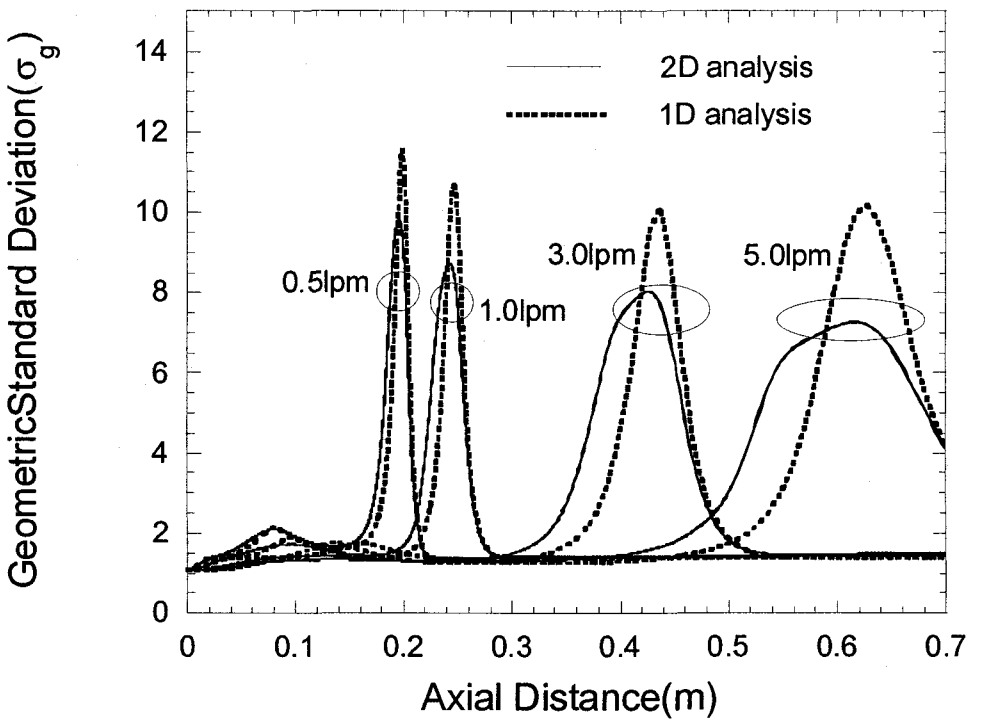

Figure 3.2.1.1.8(b). Comparison of one- and two-dimensional analyses on the evolution of geometric standard deviation of aggregate particle size distribution along the axial distance at various inlet flow rates. (T_{max}=1400K)

3.2.1.2. Coflow diffusion flame

● Introduction

Flame aerosol processes have been widely used for the synthesis of various nanoparticles with different mechanical, electrical and optical properties (Pratsinis, 1998; Wooldridge, 1998). Size and morphology of particles are strongly affected by flame temperature, transport processes inside the flame and particle generation characteristics connected with chemical reactions (Lee and Choi, 2002; Lee et al., 2001). Nanoparticles generated during flame synthesis often have irregular non-spherical shapes. In addition, most flame reactors utilize non-uniform and spatially multi-dimensional geometry. Thus, it is desirable to simulate the growth of non-spherical particles in multi-dimensional flame systems.

Co-flow diffusion flame reactors are frequently utilized for the manufacture of high purity nanoparticles (Lee and Choi, 2000). However, it is hard to find simulation studies on the axi-symmetric two-dimensional co-flow diffusion flames with the generation of particles. Especially, little has been known about the effects of the addition of precursor vapors, such as $SiCl_4$ and $TiCl_4$, on combustion phenomena and also on the growth of generating particles. Co-flow diffusion flames provide spatially two-dimensional flow and temperature fields involved with multi-step H_2/O_2chemistry and precursor chemical reactions. In addition, polydisperse non-spherical particle growth modeling requires considerable computation efforts, thus, has been so far limited only for simple one-dimensional problems.

Studies on the measurement of temperature and species concentration in co-flow diffusion flames accompanied with particle generation are also few in number. Though extensive studies about the formation and growth of particles in a spatially one-dimensional counter-flow flame have been done experimentally (Chung and Katz, 1985; Zachariah et al., 1989; Chung et al., 1991; Hung et al., 1992), only a small number of numerical studies on the generation and growth especially for aggregate particles have been carried out. Lee et al. (2001) investigated the evolution of non-spherical particles in a counter-flow diffusion flame considering the effects of coagulation, coalescence and transport processes in a one-dimensional flow field. They carried out the combustion analysis with detailed multi-step chemical reactions of hydrogen/oxygen gases including simultaneous oxidation and hydrolysis of $SiCl_4$. Allendorf et al. (1989) measured temperatures in silica generating co-flow diffusion flame using spontaneous Raman scattering from oxygen. Recently, Hwang et al. (2001) measured the distributions of temperature and OH radical concentrations in a silica-generating co-flow diffusion flame by using coherent anti-Stokes Raman spectroscopy (CARS) and planar laser-induced fluorescence (PLIF).

As described, the fundamentals of particle generating co-flow diffusion flame are not yet fully understood because chemical reaction and particle growth take place extremely fast in typical process conditions, and short residence times accompanied with high process temperatures make it difficult to simulate particle generation and growth (Pratsinis, 1998). Moreover, particles generated in flame have

spatially inhomogeneous distributions and also have non-spherical fractal-like structures changing by coalescence and coagulation. Consequently, the combustion analysis and non-spherical particle dynamics simulation for the spatially non-uniform co-flow diffusion flame have not been carried out yet. Johannessen et al. (2000, 2001) combinedcomputational fluid dynamics with a mathematical model for the particle dynamics to simulate the synthesis of fine titania and alumina particles in co-flow diffusion flames. They employed a monodisperse model of Kruis et al.(1993), and thus the effect of polydispersity was not taken into account. Yu et al. (1998) developed a two-dimensional, axi-symmetric, discrete-sectional model applied to a laminar hydrogen/air diffusion flame. They accounted for the spatial transport processes that could influence the particle dynamics and investigated their effects on the evolution of particle size distribution in flame. However, they assumed spherical particles. Very recently, Jeong and Choi (2003) performed a numerical simulation for the polydisperse non-spherical particle dynamics in an axi-symmetric tubular furnace reactor accounting for spatial transportation phenomena.

Motivated by this, we have carried out a simulation of generation and growth of polydisperse non-spherical nanoparticles in a spatially two-dimensional flame for the first time. Combustion analysis of two-dimensional, multi-component chemically reacting fluid flows has been first done by considering detailed chemical kinetics (51 reactions, 20 species); oxygen-hydrogen combustion and $SiCl_4$ chemical reactions, variable transport and thermodynamic properties. General dynamic equation (GDE) describing non-spherical particle formation and growth is then solved. An efficient sectional model which is based on the solution of two sets of 1-D sectional equation (Jeong and Choi, 2001) has been adopted to solve the non-spherical dynamics equation for this two-dimensional geometry. This two-dimensional approach provided the information on the particle size distribution in both axial and radial directions. Simple monodisperse model was also used as a comparison and an alternative approach for the complex multi-dimensional problems because of its computational efficiency. Temperatures and particle sizes obtained from the two-dimensional combustion and aerosol dynamics calculations were compared with experimental data.

● Methods

Combustion analysis of a particle generating co-flow diffusion flame

Figure 3.2.1.2.1 shows a schematic diagram of the axi-symmetric co-flow flame considered in this study. The burner consists of several coaxial annular nozzles and its configuration and inlet conditions are the same as those used in the experimental research of Hwang et al. (2001) except N_2 shield nozzle. Hwang et al. (2001) used eight holes located around the center nozzlewhich have been simplified in the present study as a coaxial annular nozzle having an equivalent flow rate. Pure nitrogen or mixture of nitrogen and silicon tetrachloride ($SiCl_4$) areintroduced through the innermost nozzle whose radius is 1.0 mm. Nitrogen shield gas is supplied through the annular nozzle next to the innermost nozzle. Hydrogen and oxygen are provided through the next nozzles (Ri=5.25 mm, Ro=6.7 mm and R_i=7.9 mm, R_o=9.65 mm), and air is provided through the outermost nozzle (R_i=12.7 mm,

R_o=26.55 mm) for the stability of the flame.

Fluid flow, temperature, and concentration fields of each species in this complex silica generating co-flow flame can be obtained by simultaneously solving the mass, momentum, species, and energy conservation equations. The governing equations are given as a vector form forthe cylindrical coordinate as follows (Kim, 2002; Shuen et al., 1993; Venkateswaran et al., 1995).

$$\frac{\partial \mathbf{Q}}{\partial t}+\frac{\partial \mathbf{E}}{\partial z}+\frac{\partial \mathbf{F}}{\partial r}+\mathbf{H}=L(\mathbf{Q}_v)+\mathbf{H}_v+\mathbf{W} \tag{3.2.1.2.1}$$

$$, \quad \mathbf{Q}=\left[\rho \;\; \rho u \;\; \rho v \;\; e \;\; \rho_1 \;\; \cdots \;\; \rho_{ns-1}\right]^t \tag{3.2.1.2.2}$$

where Q is the vector of variables. **E** and **F** are the convective fluxes, and linear differential operator, L, means the viscous flux operator. **H**, $\mathbf{H}_v$, and **W** are axi-symmetric inviscid, viscous and chemically reacting source terms, respectively. The superscript *t* means the transpose of matrixand the subscript *ns* stands for the total number of chemical species.

From the equation of state,

$$p=\sum_{k=1}^{ns}\frac{\rho_k}{M_k}\mathbf{R}T \quad , \tag{3.2.1.2.3}$$

The set of equations in Eqs. (3.2.1.2.1) and (3.2.1.2.3) can be complete using the global species conservation equation:

$$Y_{ns}=1-\sum_{k=1}^{ns-1}Y_k \tag{3.2.1.2.4}$$

In this study, two sets of reaction model were used (Ho et al., 1992; Kim, 2002):9 species model for the case of no silica generation and 20 species model for the case of silica formation. In the presence of oxygen and water vapor, there exist two pathways for the formation of silica particles for the reaction of SiCl4. The overall reaction of oxidation and hydrolysis of SiCl4 can be expressed (Powers, 1978; Kochubei, 1997):

$$SiCl_4+O_2 \Rightarrow SiO_2+2Cl_2 \tag{3.2.1.2.5-a}$$

$$SiCl_4+2H_2O \Rightarrow SiO_2+4HCl \tag{3.2.1.2.5-b}$$

and the gas phase reaction of $SiCl_4$ was modeled based on the semi-global approximation using rate-determining steps adapted by Lee et al. (2001). Nitrogen gas was assumed to be inert. Since the compressible effects such as the change of gas density due to chemical reaction can be significant, the equations were solved by means of the preconditioning method. The preconditioning method has an advantage in relaxing the stiffness aroused from the large eigen-value discrepancy (Choi and Merkle, 1993). The preconditioning matrix used in this study can be found in the previous literature (Shuen et al., 1993; Venkateswaran et al., 1995). Detailed numerical schemes used also can be found in Kim (2002) Choi (1997). For the spatial discretization, the finite volume method (FVM) was used and the general flux difference splitting (FDS) scheme was adopted to retain upwind characteristics for convective fluxes. The governing equations are highly nonlinear and their solution requires a good initial guess. For the given flow conditions, a solution for the case without $SiCl_4$ addition was first obtained and then the simulations for the flame with $SiCl_4$ addition were performed using the previous calculation results obtained without SiCl4 addition as an initial guess. Flame ignition was induced by temporarily increasing the temperature (to 2000 K) at a few grid points after some fixed iterations.

The computational domain is bounded by the inlet and exit boundary in the axial direction,by the axis of symmetry and a lateral zone in the radial direction (see Figure 3.2.1.2.1). Parabolic velocity profile was assumed for N_2+$SiCl_4$ gas at the center nozzle and annular profiles were used for the other gas inlet boundaries. In order to stabilize the flame, a large amount of air was provided through the outermost nozzle in the previous experimental conditions by Hwang et al. (2001). Their outermost nozzle was equipped with 1 mm-spaced honeycomb, thus the velocity profile of air at the outmost nozzle exit was assumed to be flat. The exit boundary in the z direction was located sufficiently far from the nozzle exit such that the propagation of boundary-induced disturbances into the region of interest was minimized (Katta and Roquemore, 1995). At the symmetric axis at r=0 mm, radial velocity component was set to be zero and the other variables were assumed to have zero gradients. The gradients of all dependent variables were assumed to be zero at the exit and the lateral boundaries. At the wall boundary, zero velocity and zero concentration gradient of species were given. Different domain sizes were tested to ensure that the numerical results were independent of the calculation domain size. 184 x 162 non-uniform orthogonal meshes were located in the axial and radial direction of the flame, respectively. The computation domain was z=0~200 mm in axial direction and r=0~106.2 mm in radial direction. Grid points were clustered more near the nozzle exit and the axis of symmetry.

Non-spherical particle dynamicsanalysis

After the distributions of velocity, temperature and species in a co-flow diffusion flame were obtained,non-spherical particle dynamics has been solved for the present one-way coupling problem. The evolution of the particle size distribution can be described by the integro-differential general dynamic equations including the influence of convection, diffusion, thermophoresis, coagulation, sintering (or coalescence) and generation:

$$\nabla\cdot(\mathbf{u}n)=\nabla\cdot[D\nabla n]+\nabla\cdot[nK\nu\nabla\ln T]+\left[\frac{\partial n}{\partial t}\right]_{coagulation}+\left[\frac{\partial n}{\partial t}\right]_{sintering}+S \qquad (3.2.1.2.6)$$

where the last source term S represents the particle formation rate. In this study it was assumed that there were no free energy barriers for particle nucleation, and the thermodynamic critical particle could be set equal to a single SiO_2 monomer molecule(Xiong et al., 1993; Pratsinis, 1998). Therefore, the rate of the monomer particle formation was identical to the chemical reaction of $SiCl_4$. The reaction rate constant for oxidation suggested by Powers (1978) and that for hydrolysis by Kochubei (1997) wereused in the calculations.

Non-sphericity of particles can be characterized by the surface fractal dimension, D_s, ranging from 2 to 3 (Xiong et al., 1993) defined below:

$$a=a_0\left(\frac{v}{v_0}\right)^{\frac{D_s}{3}} \qquad (3.2.1.2.7)$$

Non-spherical particle dynamics equation (Eq. (3.2.1.2.6)) can be approximated by two sets of sectional equations that take into account the evolutions of l-th sectional volume concentration ($Q_{l,v}$) and surface area concentration ($Q_{l,s}$) (Jeong and Choi, 2001):

$$\nabla\cdot(\mathbf{u}Q_{l,v})=\nabla\cdot[\overline{D}_v\nabla Q_{l,v}]+\nabla\cdot[Q_{l,v}K\nu\nabla\ln T]+\frac{1}{2}\sum_{i=1}^{l-1}\sum_{j=1}^{l-1}\overline{\beta}_{i,j,l}^{1,v}Q_{i,v}Q_{j,v}$$
$$-Q_{l,v}\sum_{i=1}^{l-1}\overline{\beta}_{i,l}^{2,v}Q_{i,v}-\frac{1}{2}\overline{\beta}_{l,l}^{3,v}Q_{l,v}^2-Q_{l,v}\sum_{i=l+1}^{m}\overline{\beta}_{i,l}^{4,v}Q_{i,v}+\delta(l-1)Iv_0 \qquad (3.2.1.2.8\text{-a})$$

$$\nabla\cdot(\mathbf{u}Q_{l,s})=\nabla\cdot[\overline{D}_s\nabla Q_{l,s}]+\nabla\cdot[Q_{l,s}K\nu\nabla\ln T]+\frac{1}{2}\sum_{i=1}^{l-1}\sum_{j=1}^{l-1}\overline{\beta}_{i,j,l}^{1,s}Q_{i,s}Q_{j,s}$$
$$-Q_{l,s}\sum_{i=1}^{l-1}\overline{\beta}_{i,l}^{2,s}Q_{i,s}-\frac{1}{2}\overline{\beta}_{l,l}^{3,s}Q_{l,s}^2-Q_{l,s}\sum_{i=l+1}^{m}\overline{\beta}_{i,l}^{4,s}Q_{i,s}+\delta(l-1)Ia_0-Q_{l,s}\overline{H}_l \qquad (3.2.1.2.8\text{-b})$$

where $\overline{\beta}$'s are the inter- and intra-sectional coagulation coefficients and $\overline{H}$'s are the sintering coefficients.Their definitions can be found from Jeong and Choi (2001). These coupled two sets of one-dimensional sectional equations are solved for each volume section considering the spatial transport mechanisms. It was also assumed that the axial particle diffusion would be negligible compared to axial convection

The rate of sinteringof nanoparticles is an important parameter to predict the final size of primary particles. The sintering rate is typically estimated based on the bulk material properties such as solid-state diffusivity for crystalline materials and viscosity for amorphousmaterials. However, for silica, which is known to be coalesced by a viscous flow mechanism, the predictions using the properties of bulk materials have been in poor agreement with experimental data (Ehrman, 1998). In the present study, the hybrid model (Lee et al., 2001) combining atomistic diffusion model which took into account the effect of internal pressure (Ehrman, 1999) and viscous flow sintering model (Xiong et al, 1993) was used for the modeling of coalescence of nanoparticles.The effect of section spacing was checked using different sets of section spacing.

● Results and Discussion

Flame temperature distributions

Figure 3.2.1.2.2 shows the radial temperature distributions of the flame with or without SiCl4 addition at three different heights from the burner nozzle (5 mm, 20 mm and 33 mm). Previous measurement data of Hwang et al. (2001) are compared with the prediction results carrier gas N_2= 153.2 m*l*/min, $SiCl_4$=70.3 ml/min, H_2+N_2=1 *l*/min+1 *l*/min, O_2+N_2= 2 *l*/min+2 *l*/min, dry air= 80 *l*/min. Good agreement on temperature profiles between the simulation results and measurements was obtained for both cases at different positions. The results clearly demonstrate that the co-flow diffusion flames have spatially non-uniform temperature distributions of. At z=5 mm, the radial temperature distribution has its maximum located at r=7.5 mm, not at the centerline. At this height, the predicted temperature profile is almost identical with the measured temperatures for both cases with and without $SiCl_4$ addition. This indicates that the effect of $SiCl_4$ additions on flame temperature is negligible at this lower height because $SiCl_4$ vapor injected at the centerline cannot have sufficient residence time to diffuse outward in the radial direction. At z=20 mm, where particles are intensively generated, the addition of $SiCl_4$ to the flame plays an important role (Hwang et al., 2001). Though the differences are small in the outer region of r > 5.0 mm, the effect of $SiCl_4$ addition is obvious near the center region (0 mm < r < 5.0 mm). At r=1.4 mm (temperature inversion point), the distribution of the temperature without SiCl4 addition and that with SiCl4 addition are intersected each other. In the region 0 mm < r <1.4 mm where SiO_2 particle generation rate is low, the addition of $SiCl_4$ causes temperature to decrease (about 350K near the axis) due to the increase in momentum and also in the specific heat of the $SiCl_4$-N_2 mixture gas which is about 70% larger than that of unmixed N_2 in the preheated region. These results are supported by the observation of Allendorf et al. (1989) who reported that the flame temperature would decrease in the preheated zone when SiCl4 was supplied in to a methane-oxygen flame. On the contrary, in the region 1.4 mm < r < 5.0 mm, the opposite tendency is observed, which is attributed to the exothermic heat releases through oxidation and hydrolysis reactions of $SiCl_4$ (Lee et al., 2001). At z=33 mm, the temperature has its maximum near the axis region, which is typical for co-flow diffusion flames. At this height, significant formation of silica particles takes place at the centerline. The temperature distribution obtained by increasing $SiCl_4$

reaction is higher than that neglecting $SiCl_4$ addition. An increase by about 95 K is observed in the centerline, which is attributed to $SiCl_4$ chemical reactions though the flow rate of SiCl4 added (70.3 m*l*/min) is much lower compared to that of H_2 (1000 m*l*/min). Hwang et al. (2001) reported the temperature increase in the region where silica particles were formed would be due to heat release during exothermic chemical reactions of $SiCl_4$ oxidation and hydrolysis. It should be noted that the flame temperature decrease in the preheated zone and the increase in reacting particle formation zone have not been theoretically reported before.

The discrepancy between the predicted and measured temperature profiles near the nozzle center region may be attributed to the difference of the burner configuration from Hwang et al. s experimental setup (Hwang et al.,2001). In their experiment, N_2 shield gas was injected through eight circular holes around the center nozzle but the eight circular holes were simplified in this study as acoaxial annular nozzle having an equivalent flow rate.

Growth of non-spherical particles

Figure 3.2.1.2.3 shows the total particle generation rate at the centerline (r=0 mm), which is a sum of hydrolysis and oxidation of $SiCl_4$ vapor in the flame. Reaction starts at z~10 mm and completes at z~19 mm. The chemical reactions strongly depend on the localized flame temperature and the concentration of water vapor. Especially, when water vapor is supplied sufficiently and temperature is relatively low, hydrolysis becomes a dominant reaction. At high temperature, however, oxidation dominates over hydrolysis (Lee et al., 2001). For these flame conditions, both reactions are comparable each other and thus should not be neglected.

Simulation result for the evolution of primary particle size was also compared with the experimental measurement done by the local thermophoretic sampling and TEM image analysis (Kim, 2002). As shown in Figure 3.2.1.2.4, though there is some discrepancy, the results obtained by the numerical simulation reasonably follow the growth of primary particle along the centerline. It is also shown that hybrid sintering model gives more agreeable result than the atomistic diffusion model of Ehrman (1999) which underpredicted the sintering rate for large particles as was suggested by Lee et al. (2001) from the study of the silica particle growth in a counter-flow diffusion flame.

The distributions of particle sizes are presented in Figure 5 for different conditions: carrier gas N_2=200 m*l*/min, SiCl4=25 m*l*/min, H_2= 2.5 l/min, O_2=5 *l*/min, dry air=70 *l*/min. Particle size distributions for radial positions (r=0, 2.55, and 4.15 mm) at two different heights from the burner surface and are shown in Figure 3.2.1.2.5-(a) (z=10 mm) and Figure 3.2.1.2.5-(b) (z=20 mm). The silica particles generated in flame have much different size distributions depending on theradial positions even at the same axial position. At z=10 mm, particle formation from gas phase chemical reaction of $SiCl_4$ dominatesnear the centerline, thus a large amount of monomer-sized particles exist. Especially at r=2.55 mm, particles have a bimodal distribution; the particles generated earlier grow into larger aggregate by coagulation and coexist with very small particles generated at this location. On the contrary, only particles of small sizesare found at r=0 mm and larger particles of unimodal

distribution are present at r=4.15 mm. When the particles move toward z=20 mm (Figure 3.2.1.2.5-(b)), particle generation is ceased in the centerline region and the particle distribution shifts to larger sizes. Particles at r=0 mm have a unimodal distribution and have been grown to much larger ones compared to those shown at z=10 mm.The particle number concentration, however, decreases with the increase of axial distance z owing to coagulation process. Note that the number concentration of smaller particles at r=4.15 mm is higher in Figure 3.2.1.2.5-(b) than in Figure 3.2.1.2.5-(a). These small particles have been entrained from the outer region where a large amount of smaller particles are present.

Figures 6 shows the distributions of the surface fractal dimensions, D_s for different radial locations at z=10 mm (Figure 3.2.1.2.6-(a)) and z=20 mm (Figure 3.2.1.2.6-(b)). If D_s=2, particles are fully sintered sphere, and if D_s is close to 3, no sintering takes place and particles are irregular aggregates. Therefore, the value of D_s ranging from 2 to 3 represents the extent of sintering or the extent of non-sphericity. Particles at z=20 mm (Figure 3.2.1.2.6-(b)) have smaller values of surface fractal dimension than those at z=10 mm (Figure 3.2.1.2.6-(a)). This suggests that fractal-like aggregate particles change into more spherical ones owing to fast coalescence process while passing through the flame region of high temperature.

Comparison between the sectional model and the monodisperse model

In general, a sectional model consumes far more computing time than the simpler one assuming a monodisperse distribution especially to obtain the solutions of spatially multi-dimensional problems. Then, if particles have a relatively narrow size distribution or small polydispersity, the monodisperse aerosol dynamics model could be an alternative choice (Kruis et al., 1993; Schild et al., 1999). Figure 3.2.1.2.7 shows the evolution of the total number concentrations predicted by the polydisperse (sectional approach) and monodisperse models at different radial positions along the axial coordinate. In Figure 3.2.1.2.8, the primary particle diameters obtained by the two models are also compared. The polydisperse simulation predicted lower particle number concentration and larger primary particle diameter than the momodisperse one did. This result can be easily explained because monodisperse particles have smaller collision rates than polydisperse particles. If the particles have a bimodal size distribution due to the simultaneous particle generation and coagulation, the discrepancy would become significant. However, when chemical reaction is completed, the particles have a unimodal size distribution and then the discrepancy would decrease. For r=0, the particle size distribution at z=10 mm (Figure 3.2.1.2.5-(a)) is very narrow because of intensive particle formation and it can be considered a monodisperse distribution. In this case, the two models showed a good agreement. However, in the downstream region, the difference of two predictions became relatively large which was attributed to broader size distributions. The same trend can be found for the particles at r=5.75 mm.

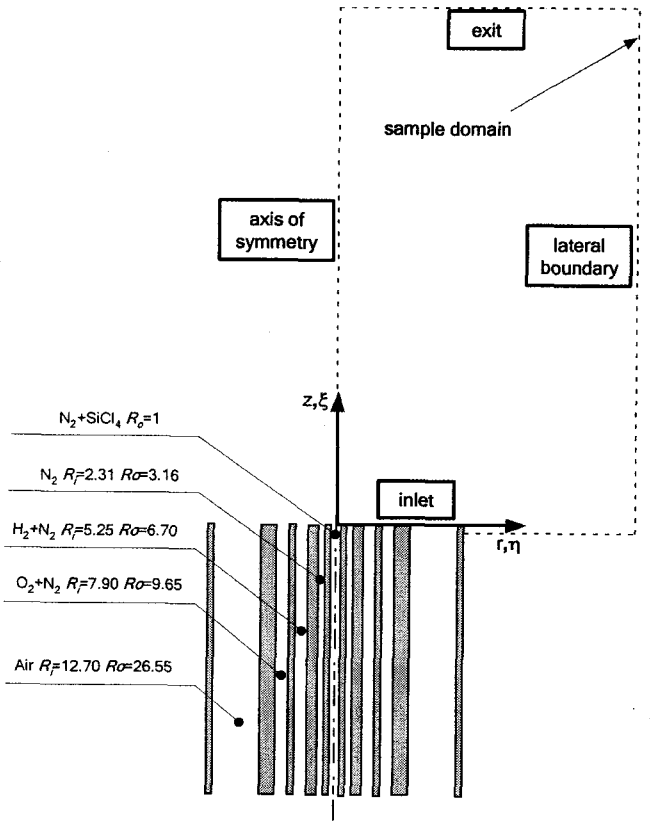

Figure 3.2.1.2.1. Schematic diagram of a silica generating co-flow diffusion flame

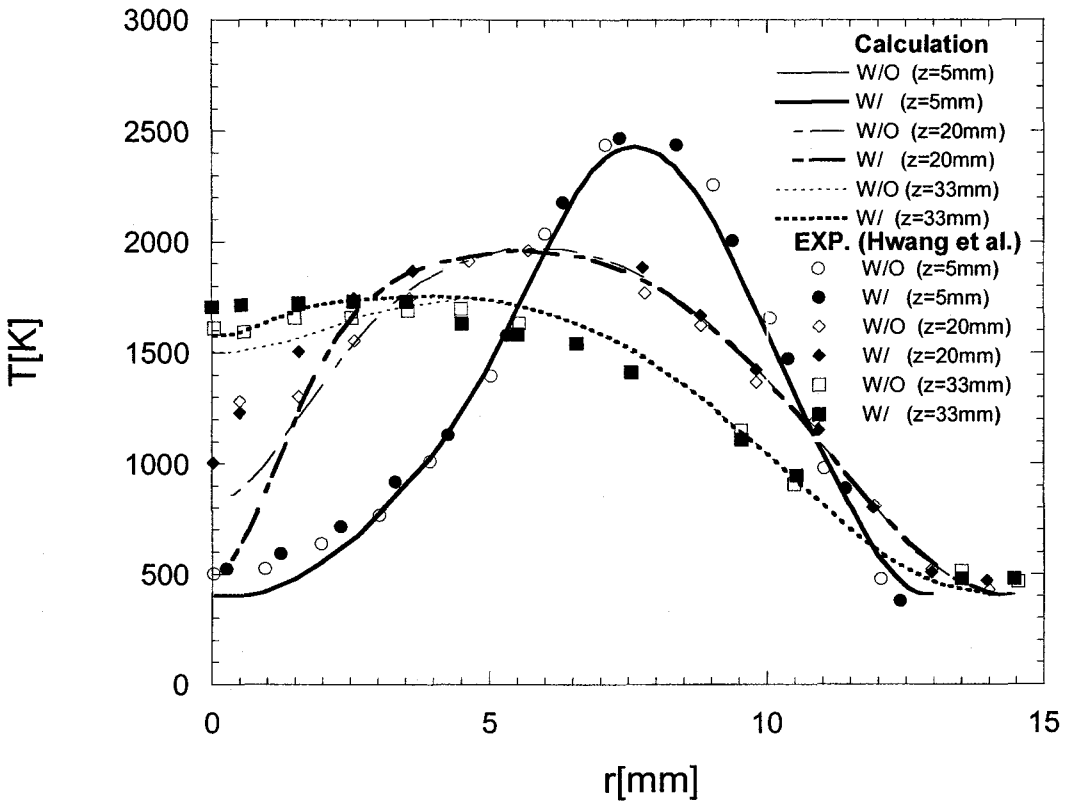

Figure 3.2.1.2.2. Predicted and measured flame temperature profiles with or without $SiCl_4$ addition.

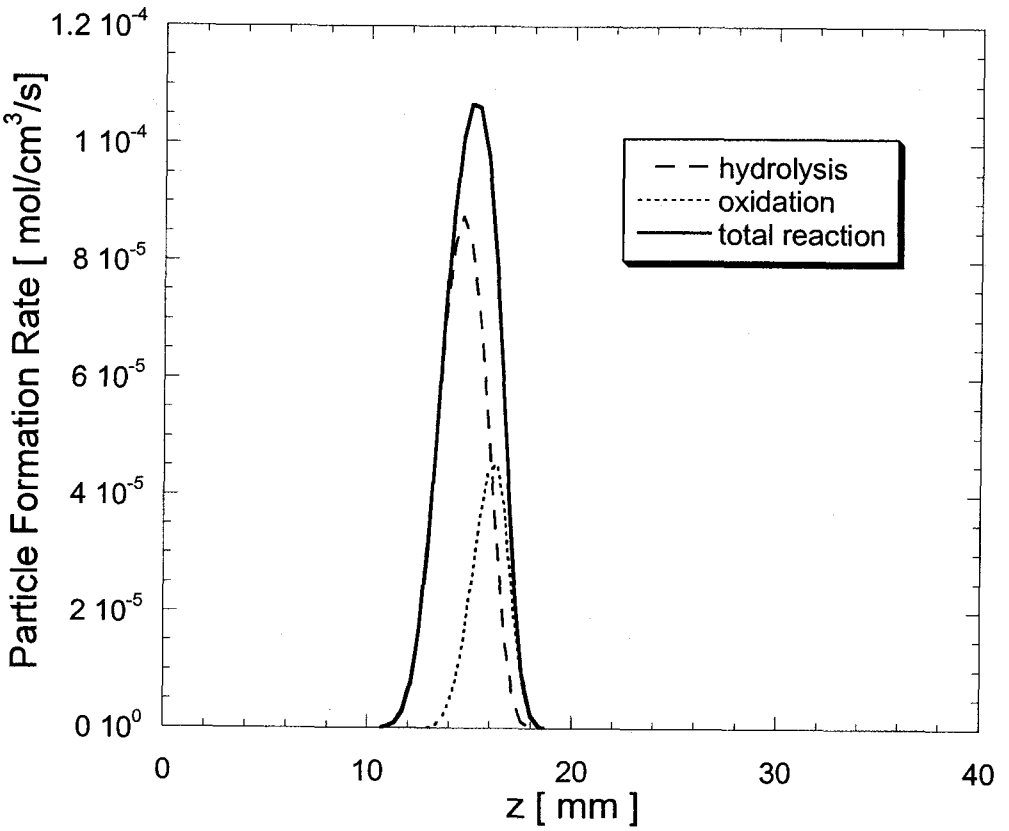

Figure 3.2.1.2.3. Particle formation rate by hyrolysis and oxidation of $SiCl_4$.

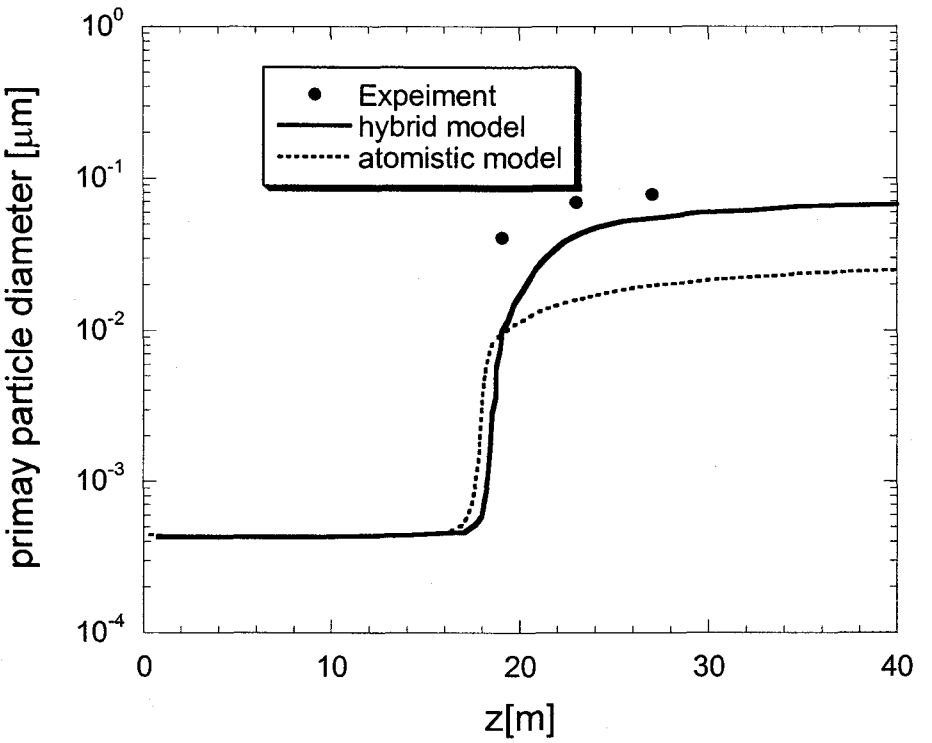

Figure 3.2.1.2.4. Comparison of the evolution of primary particle size along the centerline between the simulation and experimental data.

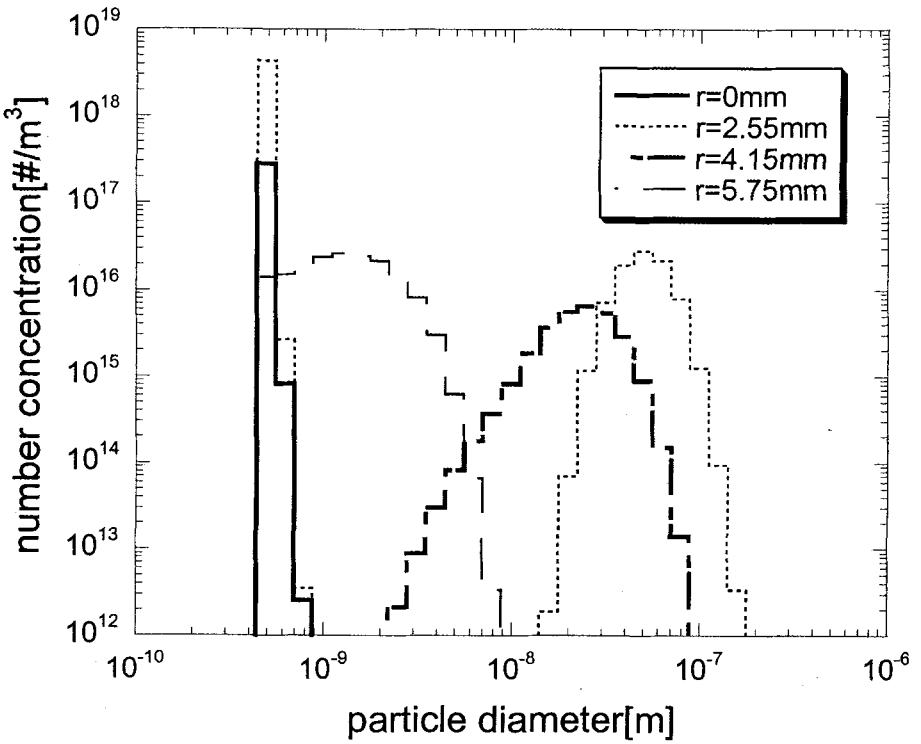

Figure 3.2.1.2.5-(a). Particle size distributions for different radial positions at z=10 mm

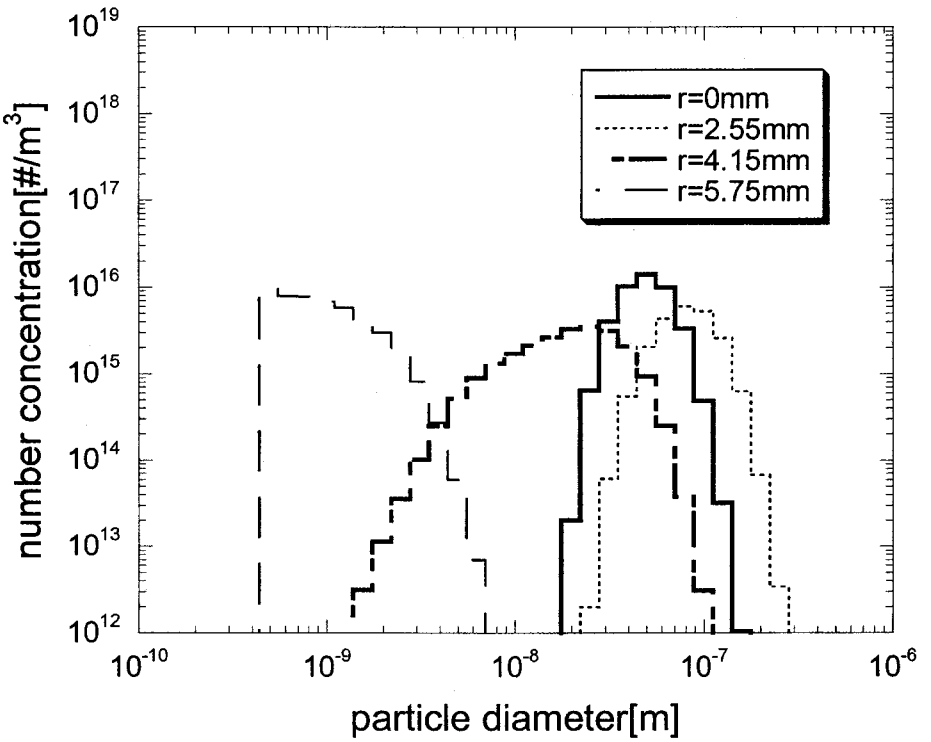

Figure 3.2.1.2.5-(b). Particle size distributions for different radial positions at z=20 mm.

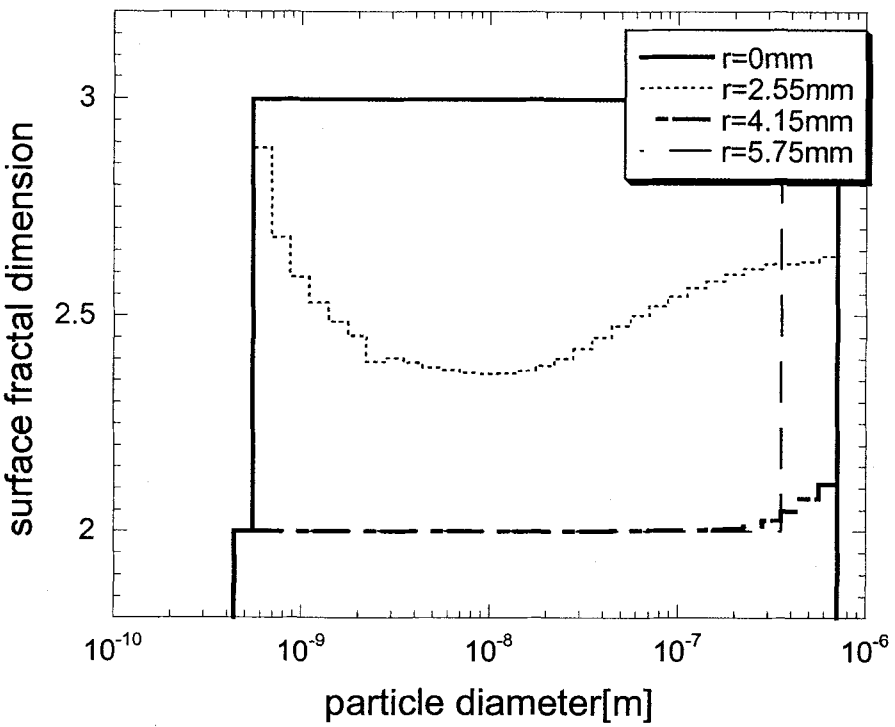

Figure 3.2.1.2.6-(a). Surface fractal dimension distributions for different radial positions at z=10 mm.

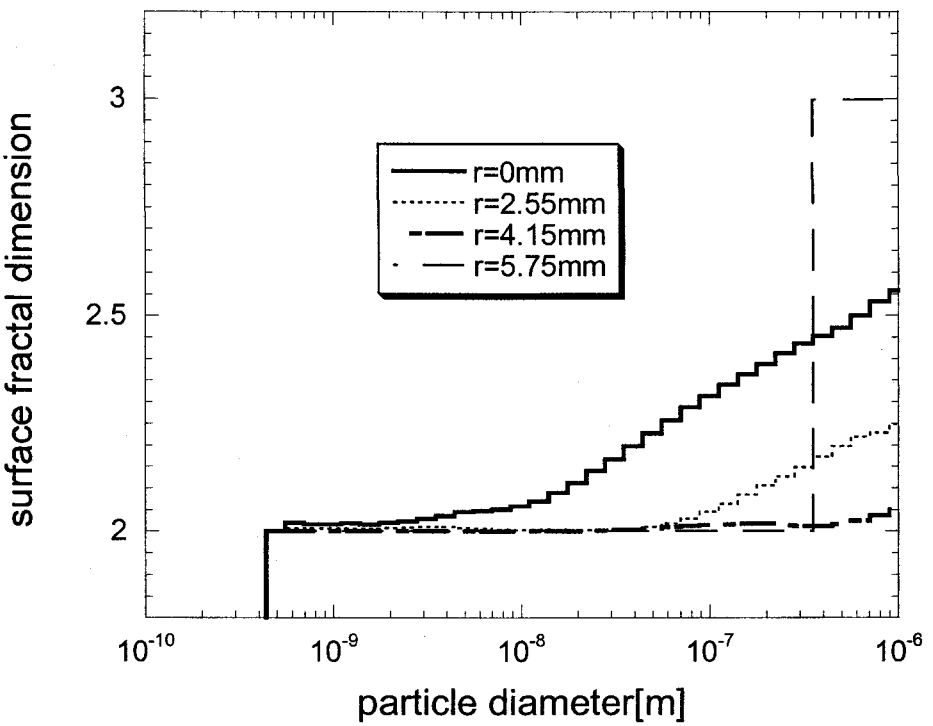

Figure 3.2.1.2.6-(b). Surface fractal dimension distributions for different radial positions at z=20 mm.

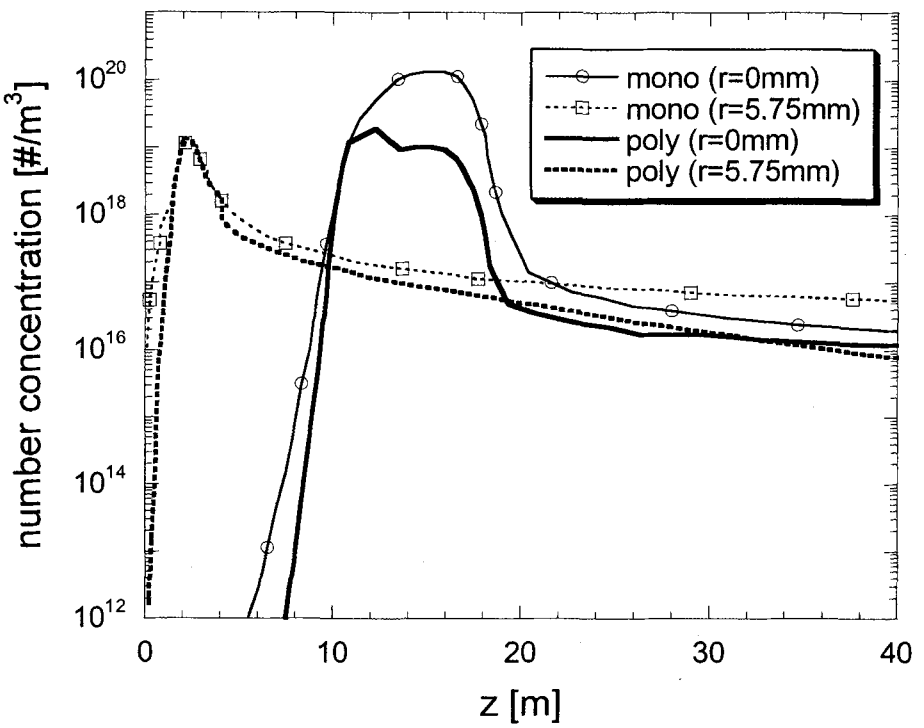

Figure 3.2.1.2.7. Comparison of the evolution of total number concentrations between the present sectional model and the monodisperse model.

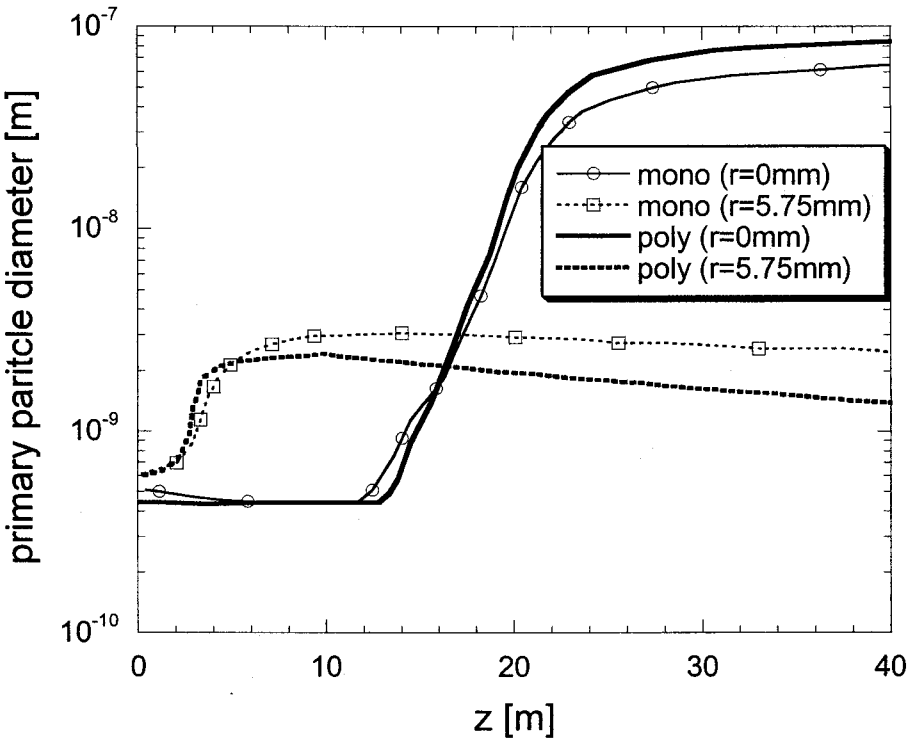

Figure 3.2.1.2.8. Comparison of the evolution of primary particle size between the present sectional model and the monodisperse model.

3.2.2. Simple bimodal method to simulate the growth of non-spherical nanoparticles

● Introduction

Particle formation by gas phase reactions is one of the important industrial processes for large-scale manufacture of high purity particles. In this process, non-spherical aggregate particles often form especially when particles are generated at high concentrations (Pratsinis, 1998). Proper control of size and morphology of the non-spherical particles not only requires the development of new control strategy (Lee and Choi, 2000, 2002; Lee et al., 2001a), but also the development of efficient numerical methods to simulate the growth of non-spherical particles.

To investigate the growth of non-spherical particles, Koch and Friedlander (1990) took into account the change of particle surface areas due to coalescence. In their work a characteristic coalescence time for aggregate particles was introduced. Xiong and Pratsinis (1993) developed a two-dimensional sectional model in which the particle volume and surface area wereused as internal coordinates. This detailed model can predict the morphological evolution of aggregate particles undergoing nucleation, coagulation and coalescence accurately by increasing the number of divided volume and surface area sections. However, the model requires heavy computational load, and therefore has been limited to solve simplified aerosol systems such as spatially one-dimensional systems (Seto et al, 1997; Lee et al, 2001b). Kruis et al.(1993) proposed a simple monodisperse model for the non-spherical particle evolution, which agreed well with the two-dimensional sectional model when new particle generation was absent. Because of its computational efficiency, this monodisperse model has been effectively used to simulate the growth of non-spherical particles in spatially multi-dimensional systems (Schild et al., 1999; Johannessen et al., 2000, 2001). However, when nucleation and other particle growth mechanisms coexist, this model can not properly describe the particle dynamics due to inherent monodisperse assumption. Jeong and Choi (2001) proposed a new non-spherical sectional model which solves coupled two sets of one-dimensional aerosol dynamics sectional equations describing the change of volume and surface area concentrations of non-spherical polydisperse particles. Compared to the detailed two-dimensional sectional model (Xiong and Pratsinis, 1993), the model yielded accurate polydisperse size distributions of non-spherical particles with very good agreement while reducing the computation time by 1000 times or more. Although this efficient sectional model can be utilized to predict the evolution of polydisperse non-spherical particles in multi-dimensional reactors (Jeong and Choi, 2003), it still needs considerable computation load. Thus, it is desirable to develop a much simpler method that can secure both accuracy and computation efficiency for modeling the non-spherical particle growth undergoing nucleation, coagulation and coalescence.

Motivated by this, we propose a simple bimodal model for non-spherical particle dynamics, which represents the particle size distribution using two discrete monodisperse modes. The proposed bimodal model is evaluated against the previous non-spherical monodisperse model and the more rigorous sectionalmodel by comparing their accuracy and computational efficiency. The present bimodal model

not only agrees very well with the detailed polydisperse sectional model, but also reduces computation time greatly even when nucleation and growth of particles coexist.

● Methods

Modeling for non-spherical particle growth

Monodisperse Model (Kruis et al., 1993)

Assuming monodisperse distributions of aggregate and primary particles, one can describe the monodisperse particle system under isothermal conditions by solving three differential equations shown below (Kruis et al., 1993):

$$\frac{dN_t}{dt} = -\frac{1}{2}\beta N_t^2 + I, \tag{3.2.2.1}$$

$$\frac{dV_t}{dt} = Iv_0, \tag{3.2.2.2}$$

$$\frac{dA_t}{dt} = -\frac{1}{\tau}(A_t - N_t a_s) + Ia_0 \tag{3.2.2.3}$$

where N_t is the particle total number concentration, V_t the total particle volume concentration and At the total particle surface area concentration. The symbol I represents the nucleation rate of particles with volume v_0. The symbol τ in Eq. (3.2.2.3) represents the characteristic coalescence time and asis the surface area of a spherical particle of volume va (=Vt/Nt). The Brownian collision coefficient β, which has a form of Fuchs' interpolation formula (Seinfeld, 1986) covering from the free molecular regime to the continuum regime, is a function of the collision diameter, dc, which can take into account the effects of non-sphericity of aggregate particles (Kruis et al., 1993).

Though the monodisperse model has been widely used as a very attractive simulation tool to describe the evolution of integrated properties of the particle size distribution when particles have a relatively narrow unimodal distribution, it does somewhat underpredict the particle collision frequency (Landgrebe and Pratsinis, 1990). Moreover, if particle nucleation is not instantaneous, a large accumulation mode composed of particles generated earlier coexists with a smaller nucleation mode. The monodisperse model cannot adequately model this bimodal particle size distribution due to its inherent monodisperse limitations.

The present non-spherical bimodal model

We propose a simple non-spherical bi-modal model by introducing the particle size distribution

with two discrete modes: one for particle generation and the other for coagulated larger aggregates. Figure 3.2.2.1 is a schematic representation of the proposed bimodal model. The present bimodal model employs two discrete modes: one for the nucleation mode, Mode 1 and the other for the accumulation mode, Mode 2. Although the width of the twomodes depicted in the figure is exaggerated for clarity, each mode of the bimodal model is considered to have a monodisperse size distribution in view of particle volume. The average volume of Mode 2, v_2, is r times larger than v_0 and rincreases following the growth of aggregate particles by coagulation and coalescence. The representative volume of Mode 1 is fixed as the volume of nucleated particle v_0. Therefore, volume and surface area concentrations for Mode 1 can be straightforwardly determined once the evolution of number concentration, N_1, for Mode 1 is solved. However, for Mode 2 representing non-spherical aggregates that grow due to both coagulation and coalescence, the evolution of volume concentration, V_2, and surface area concentration, A_2, should be solved simultaneously with solving the evolution of the number concentration, N_2.

There are three possible coagulation processes to be considered: (a) intra-mode coagulation in Mode 1, (b) intra-mode coagulation in Mode 2 and (c) inter-mode coagulation between Mode 1 and Mode 2. Consider first the intra-mode coagulation in Mode 1. One could simply assume that every particle created by binary intra-mode coagulation in Mode 1 directly enters Mode 2 as was previously done for spherical particle dynamics model(Megaridis and Dobbins, 1990). More specifically, this means when two particles of volume $_{v0}$ in Mode 1 collide with each other, the resulting particle of volume $2v_0$ should belong to Mode 2 while N1 and V1 are reduced by two units and by $2v_0$, respectively and N_2 and V_2 are increased by one unit and by $2v_0$, respectively. However, if Mode 2 has a much larger size v2 than v_0 (r>>1) as is usual, this process will result in considerable error. For example, if v_2 is 10^4 times larger than v_0 (r=104), a single binary coagulation in Mode 1 will lead to an increment of one unit for N2 but very small increment of V_2 which is 1/5000 unit of v_2. This will result in the decrease of the average volume of Mode 2 (v_2) by the intra-mode coagulation of Mode 1, which is physically unreasonable. An alternative way used in the present study is to apportion the resulting particles of size $2v_0$ between two modes, Mode 1 and Mode 2, while preserving the particle number and volume as described below.

When two nucleated particles with size v_0 in Mode 1 collide with each other, a single new particle with volume $2v_0$ is formed, whose size does not coincide with the mean size of Mode 1 nor with Mode 2 except when r =2. In the present study, instead of dumping the particle directly into Mode 2, the particle of volume $2v_0$ has been apportioned between the two modes according to the particle volume ratio as shown in Figure 1: (r-2)/(r-1) unit for Mode 1 and 1/(r-1) for Mode 2. Then, for Mode 1, a decrease of two units by the collision and an increment of (r-2)/(r-1) unit by the allotment lead to a net decrease of $N1$ by r/(r-1) unit and therefore a net decrease of V_1 by r $v0$/(r-1) as a result of a single intra-mode coagulation in Mode 1. For Mode 2, the single intra-mode coagulation in Mode 1 results in an increment of N_2 by 1/(r-1) unit, along with an increment of V_2 by rv_0/(r-1). This way of apportioning the particles of size $2v_0$ not only preserves both the particle number and volume, but also

eliminates the problem of the previous spherical model (Megaridis and Dobbins, 1990) that is a possible decrease of mean size of Mode 2 after particle collision in Mode 1.

Inter-mode coagulation between Mode 1 and Mode 2 and the intra-mode coagulation in Mode 2 can be straightforwardly formulated. When a particle in Mode 1 and a particle in Mode 2 collide each other, a new particle of volume $(r+1)v_0$ is generated and the particle can be assumed to be laid in Mode 2. Then, a single inter-mode coagulation between Mode 1 and Mode 2 reduces N_1 by one unit with a decrease of V_1 by v_0 and an increase of V_2 by v_0 but brings no change in N_2. Finally, single intra-mode coagulation in Mode 2 reduces N_2 by one unit but does not change V_2, because the newly generated particle of volume $2rv_0$ should be remained in Mode 2. The rate of particle formation, I, only changes N_1. Consequently, the governing equation for the change of N_1 can be written by:

$$\frac{dN_1}{dt} = -\frac{1}{2}\beta_{11}N_1^2\left(\frac{r}{r-1}\right) - \beta_{12}N_1N_2 + I \tag{3.2.2.4}$$

where β_{11} is the collision frequency function of the intra-mode coagulation in Mode 1 and β_{12} is the collision frequency function of the inter-mode coagulation between Mode 1 and Mode 2. Since the representative size of Mode 1 is fixed as v_0, β_{11} could remain constant during the calculation if temperature and gas properties are not changed. Similarly, the governing equations for the evolution of N_2 and V_2 can be described as follows:

$$\frac{dN_2}{dt} = \frac{1}{2}\beta_{11}N_1^2\left(\frac{1}{r-1}\right) - \frac{1}{2}\beta_{22}N_2N_2, \tag{3.2.2.5}$$

$$\frac{dV_2}{dt} = \frac{1}{2}\beta_{11}N_1^2\left(\frac{r}{r-1}\right)v_0 + \beta_{12}N_1N_2v_0, \tag{3.2.2.6}$$

where β_{22} is the collision frequency function for the intra-mode coagulation in Mode 2. It is noted that the factor for the intra-mode coagulation process in Mode 1 is $1/(r\text{-}1)$ for N_2 in Eq. (5) whereas the factor for V_2 in Eq (3.2.2.6) is $r/(r\text{-}1)$.

It can be assumed that total surface area concentration of aggregate particles (A_t) is reduced by coalescence alone; it does not change by coagulation. Since nucleated particles in Mode 1 are assumed spheres, the change of the surface area by coalescence should be described only for Mode 2, A_2. The governing equation for the evolution of A_2 is written by:

$$\frac{dA_2}{dt} = \frac{1}{2}\beta_{11}N_1^2\left(\frac{r}{r-1}\right)a_0 + \beta_{12}N_1N_2a_0 - \frac{1}{\tau}(A_2 - N_2a_{2s}), \tag{3.2.2.7}$$

where a_0 represents the surface area of spherical particle of volume v_0 ($a_0 = (36\pi)^{1/3} v_0^{2/3}$) and a_{2s} is the smallest possible surface area of the particle with volume v_2 ($=V_2/N_2$).

The volume concentration of Mode 1, V_1, and the surface area concentration, A_1, are easily evaluated from N_1:

$$V_1 = N_1 v_0 \tag{3.2.2.8},$$

$$A_1 = N_1 a_0 \tag{3.2.2.9}$$

The total integrated quantities of N_t, V_t, and A_t are the sums of the values of the two modes:

$$N_t = N_1 + N_2 \tag{3.2.2.10}$$

$$V_t = V_1 + V_2 \tag{3.2.2.11}$$

$$A_t = A_1 + A_2 \tag{3.2.2.12}$$

Eq. (3.2.2.8) can be rewritten in the form of an ordinary differential equation using Eq.(3.2.2.4) by:

$$\frac{dV_1}{dt} = v_0 \frac{dN_1}{dt} = -\frac{1}{2}\beta_{11} N_1^2 \left(\frac{r}{r-1}\right) v_0 - \beta_{12} N_1 N_2 v_0 + I v_0 \tag{3.2.2.13}$$

For the limiting case in which all the Brownian collision frequency functions β_{11}, β_{12}, and β_{22} are assumed to be a constant value of β_c, the addition of Eq. (3.2.2.4) and (3.2.2.5) reduces to the monodisperse case:

$$\frac{dN_t}{dt} = \frac{d}{dt}(N_1 + N_2) = -\frac{1}{2}\beta_c \left(N_1^2 + 2N_1 N_2 + N_2^2\right) + I$$
$$= -\frac{1}{2}\beta_c N_t^2 + I \tag{3.2.2.14}$$

which is identical to Eq. (3.2.2.1). Furthermore, the addition of Eq.(3.2.2.6) and Eq. (3.2.2.13) also leads to Eq. (3.2.2.2):

$$\frac{dV_t}{dt} = \frac{d}{dt}(V_1 + V_2) = Iv_0 \tag{3.2.2.15}$$

Four equations including Eqs. (3.2.2.4), (3.2.2.5), (3.2.2.6) and (3.2.2.7), are to be solved for the solution of the present non-spherical bimodal dynamics while the monodisperse model needs three differential equations (Eqs. (3.2.2.1), (3.2.2.2) and (3.2.2.3)). The collision diameter, dc, is adopted to consider the non-sphericity of aggregate particles as defined by Kruis et al., (1993):

$$d_c = d_p(n_p)^{1/D_f} \tag{3.2.2.16}$$

where d_p and n_p represent the diameter and the number of primary particles, respectively. Kruis et al.(1993) and Tsantilis and Pratsinis (2000) used the collision diameter to consider non-spherical particle growth and used the mass fractal dimension D_f as a commonly encountered value of 1.8.

The diameter of average volume, dav, and the geometric mean collision diameter, dgcare the parameters selected to compare the monodisperse model, the sectional model and the present bimodal model. The diameter of average volume (mass) is defined as below (Hinds, 1999):

$$d_{av} = \left(\frac{6V_t}{\pi N_t}\right)^{1/3} = \left(\frac{6}{\pi}v_a\right)^{1/3} \tag{3.2.2.17}$$

Whereas only dav can be obtained from the monodiperse model, the geometric mean (volume equivalent) diameter, d_{gv} ($=\left(6v_g/\pi\right)^{1/3}$) can be obtained from the present bimodal model because the model has two discrete modes of different size. From the definition, v_g of the bimodal model can be derived as follows:

$$\ln v_g = \frac{N_1 \ln v_1 + N_2 \ln v_2}{N_t} \tag{3.2.2.18-a}$$

$$v_g = v_1^{\frac{N_1}{N_t}} \times v_2^{\frac{N_2}{N_t}} \tag{3.2.2.18-b}$$

The geometric standard deviation, σ_g for the bimodal model indicating the degree of polydispersity, can be also derived as follows:

$$\ln^2 \sigma_g = \frac{N_1 \ln^2(v_1 / v_g) + N_2 \ln^2(v_2 / v_g)}{9N_t} \qquad (3.2.2.19)$$

It should be noted that when the nucleation mode (Mode 1) disappears and only the accumulation mode (Mode 2) survives after the end of particle generation, the particle size distribution of the bimodal model reduces to a monodisperse distribution. Then, the prediction of the bimodal model become identical to that of a monodisperse model (σ_g=1). Note also that the geometric standard deviation of the bimodal model does not reflect the accurate polydispersity of the actual accumulation mode which approach a self-preserving distribution (Landgrebe and Pratsinis, 1990).

● Results and Discussions

The simulation results of the non-spherical titania particle growth are presented for the conditions of initial $TiCl_4$ mole fraction, $\phi = 0.1$ and temperature, T=1400K assuming monomers as the smallest particles (Ulrich, 1971; Xiong and Pratsinis, 1991). Results obtained from three different methods are shown for comparison: the sectional model by Jeong and Choi (2001), the monodisperse model by Kruis et al. (1993) and the present bimodal model. Here, the total particle number concentration, Nt, and the monomer production rate are shown in Figure 3.2.2.2, and the diameter of average volume, d_{av}, and the geometric mean collision diameter, d_{gc}, are presented in Figure 3.2.2.3. The first-order reaction scheme of $TiCl_4$ oxidation (Pratsinis et al., 1990) was used in this study.

The agreement between the present bimodal model and more detailed sectional model is shown to be good for all three parameters while the monodisperse model overpredicts the number concentration and underpredict the diameter of average volume significantly. After the early stage, (t>10-4 s), particles grow due to coagulation with the chemical reaction being still active, which makes the shape of the particle size distribution bimodal (see Figure 3.2.2.5). During the development of bimodal size distributions, the prediction results of the monodisperse model obviously deviate from those of the sectional model. The bimodal model, on the other hand, yields the results that agree very well with those of the sectional model even for dgc. When the chemical reaction comes to an end, the particle size distributions lose their bimodality and the monodisperse model and the bimodal model predict almost the same results.

The size of primary particles and the number of primary particles per aggregate predicted by the different approaches are compared in Figure 3.2.2.4. The geometric mean values of np and dp are plotted for the bimodal and sectional model calculations. The present bimodal model produced almost identical results with those obtained from the sectional model. The primary particle diameter of Mode 2, d_{p2}, and the number of primary particles per aggregate of Mode 2, n_{p2}, are also presented ($d_{p2}=6V_2/A_2$ $n_{p2}=A_2^3/(36\pi V_2^2 N_2)$). The results for Mode 2 may be important for comparison with the experimental data, since the particles in Mode 1 are too small to be detected by the conventional

measurement devices. It is noted that d_{p2} continues to increase and becomes the same value of d_p beyond t=0.3 s approximately when particle formation or chemical reaction ceases. Note also that n_{p2} initially increases due to particle coagulation and later decreases due to particle coalescence.

Figure 3.2.2.5 shows the evolutions of the aggregate number concentration as a function of volume equivalent diameter. The continuous lines are predicted by the sectional model and the bars are the results of the bimodal model. It should be noted that each mode of the bimodal model is assumed to be a monodisperse distribution. The characteristic size of Mode 1 for the bimodal model is fixed ($v_1=v_0$) while only the number concentration, N_1, varies with time. It is shown that the bars predicted by the bimodal model follow well the detailed size distributions obtained by the sectional method for the number concentrations of aggregate volume equivalent diameter. At later times (t=1.0 and 10.0 s), the nucleation mode disappears and the accumulation mode alone survives. When this happens, Mode 1 does not make any contributions, so the computational process becomes identical to that of the monodisperse model.

The geometric standard deviations of the aggregate volume distribution, σ_g, the collision diameter distribution, σ_{g,d_c}, and the primary particle distribution, σ_{g,d_p}, are presented in Figure 3.2.2.6. The results of the two models agree well until t=0.3 s. At this time, the bimodal model accurately predicts the sudden peak of σ_g. Maximum values occur near the end of the chemical reaction, when the two modes composed of fine and coarse particles contain approximately an equal number of particles (Landgrebe and Pratsinis 1990). It is noted that when the chemical reaction comes to an end (t>~0.3 s), the σ_{g,d_p} predicted by the sectional model drops to unity, which indicates the monodisperse distribution of primary particles. The constant values of σ_g and σ_{g,d_c} at these times suggestthat the aggregate particle size distribution reaches a self-preserving form. The fact that σ_{g,d_p} always has smaller values than σ_g and σ_{g,d_c}, tells that the primary particles have narrower size distributions than the aggregate particle distributions as observed in many experimental and simulation studies (Seto et al, 1997; Tsantilis and Pratsinis, 2000). The predictions of the bimodal model coincide wellwith those of the sectional model, especially for the positions and heights of peaks. It should be also noted that, however, once the bimodal distribution collapses into a unimodal distribution after the end of particle formation process, σ_g and σ_{g,d_c} of the bimodal model should become unity while those of the sectional model approach asymptotic values.

Finally, Figure 3.2.2.7 shows the comparison of V_t and A_t among the three models. All the models precisely preserve V_t. The mondisperse model, however, overpredicts At while the bimodal model shows excellent agreement with the sectional model. In Figure 3.2.2.7, the prediction results assuming that particles always retain spherical shape (spherical sectional model, Gelbard et al., 1980) are also presented. Note that At predicted by the non-spherical sectional model is about an order of magnitude

larger compared to that predicted by the spherical sectional model. This implies that the use of the spherical particle dynamics models may lead to significant errors in the simulations where incomplete aggregate coalescence takes place and particle surface area is an important factor for particle growth mechanisms. In addition, the performance of the proposed bimodal model was examined for different temperatures and initial $TiCl_4$ mole fractions. Although the results are not presented in this paper, the proposed bimodal model showed good agreement with the detailed sectional method.

It should be stressed again that in addition to showing good agreement with the detailed sectional method, the typical computation times of the bimodal model(4.177 s) is almost at the same level of that of the monodisperse model (e.g. 2.410s). The sectional model, however, requires several hours (e.g. 222min 47s, rx=2.0, 86 sections used) for the same problem. This suggests that the present bimodal model would be utilized as a simple and efficient simulation tool for non-spherical particle dynamics undergoing coagulation, coalescence and nucleation in highly complex systems. The calculations were performed using a Digital Alpha Workstation (DEC 21164, 533MHz).

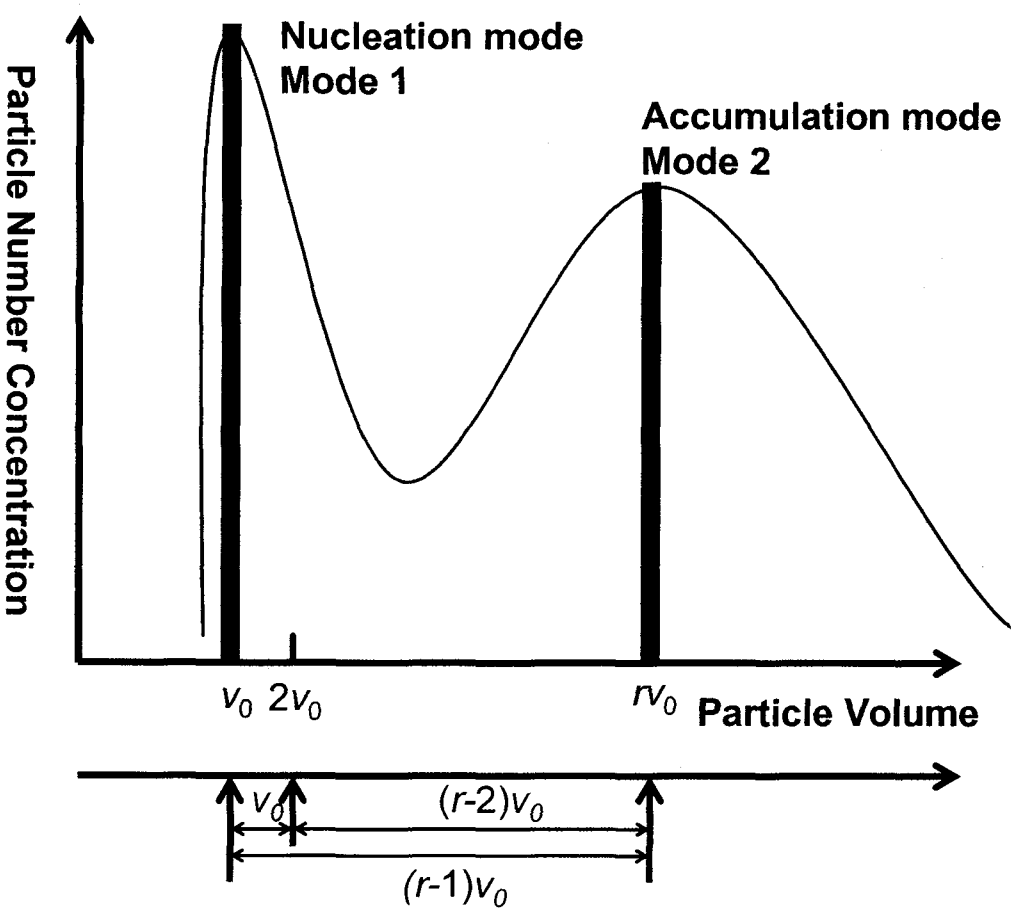

Figure 3.2.2.1. Schematic of the present bimodal model.

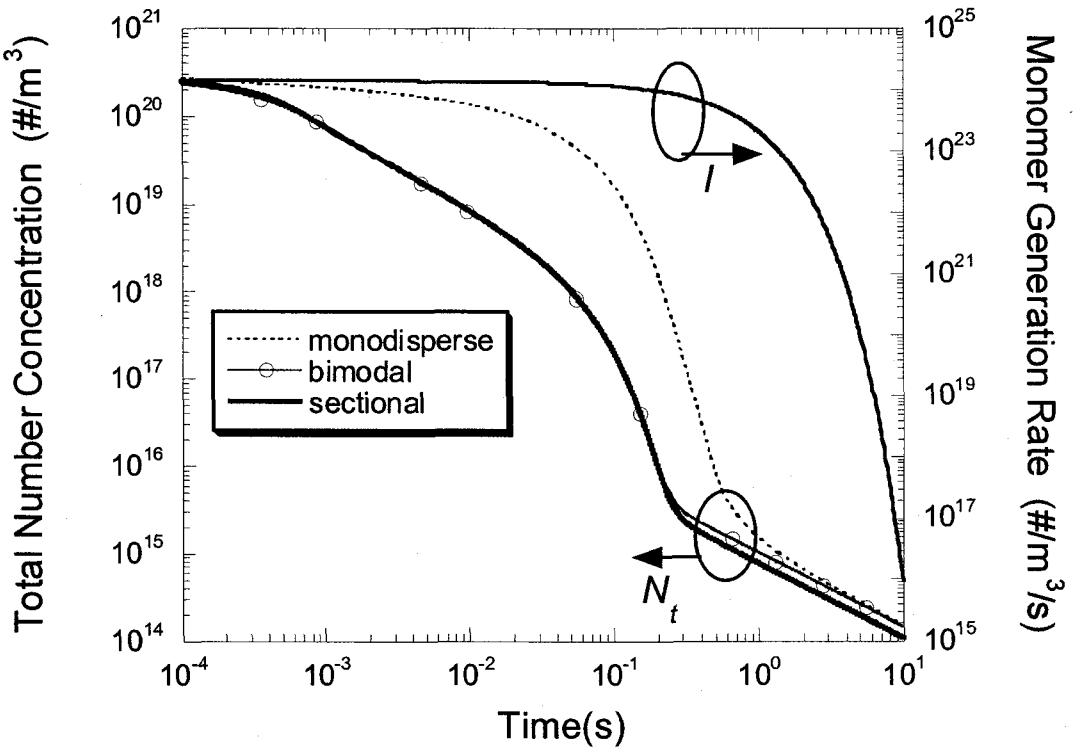

Figure 3.2.2.2. Comparison of evolution of titania particle: total number concentrations predicted by the monodisperse model, the present bimodal model and the sectional model are presented along with the monomer generation rate.

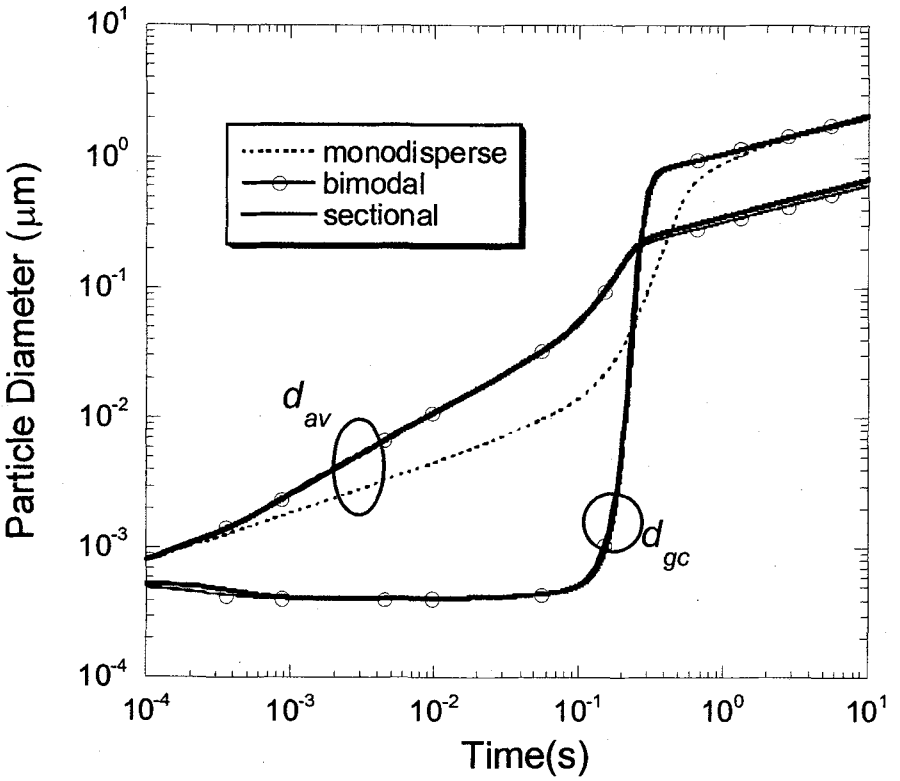

Figure 3.2.2.3. Comparison of evolution of titania particle: diameter of average volume and geometric mean collision diameter predicted by the monodisperse model, the present bimodal model and the sectional model.

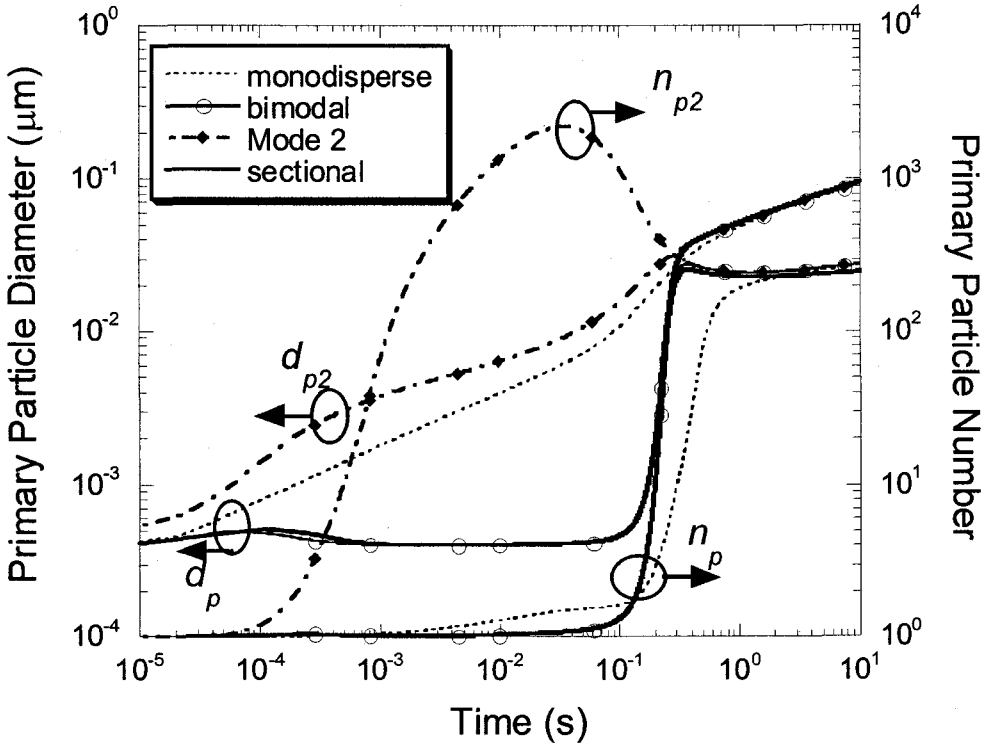

Figure 3.2.2.4. Comparison of evolution of average primary particle diameter and average number of primary particle per aggregate predicted by the monodisperse model, the present bimodal model and the sectional model. Primary particle diameter and number of Mode 2 obtained from the bimodal model are also shown.

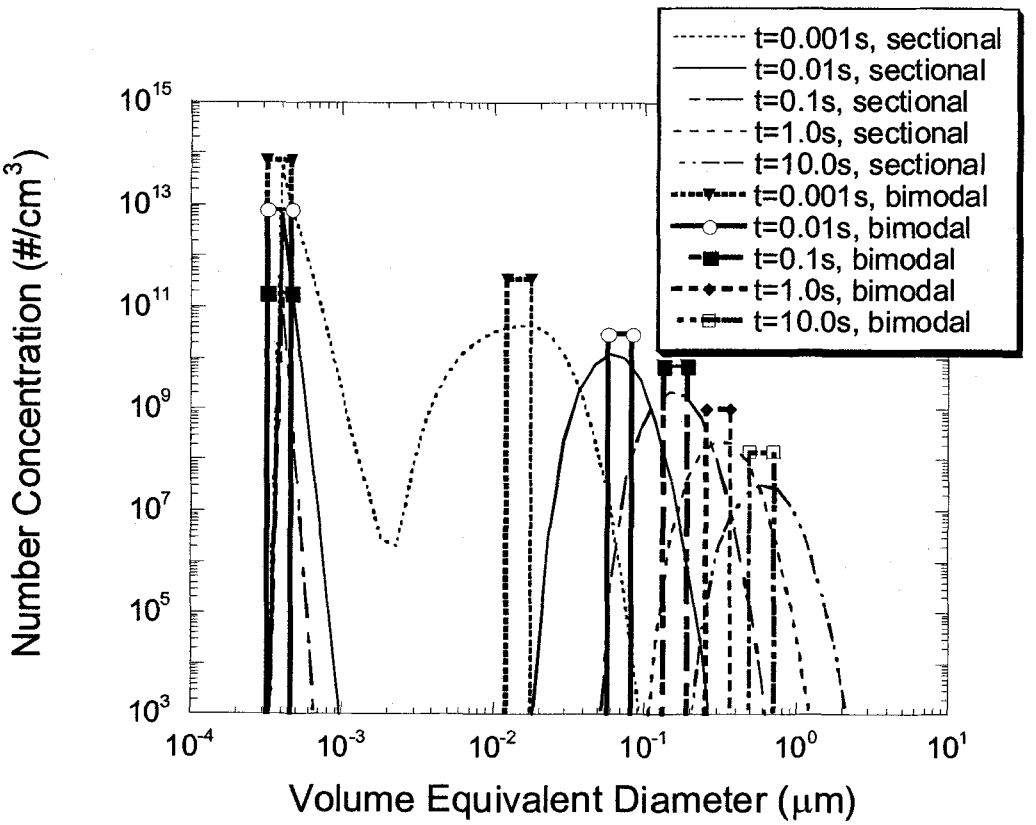

Figure 3.2.2.5. Aggregate number concentration as a function of volume equivalent diameter predicted by the present bimodal model and the sectional model.

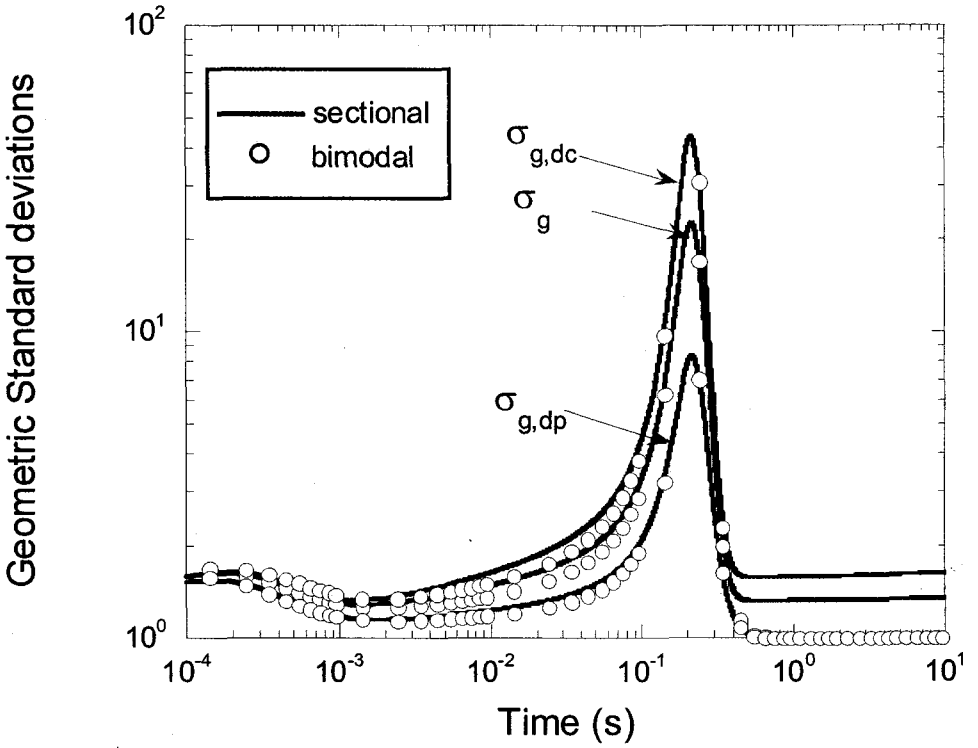

Figure 3.2.2.6. Evolution of geometric standard deviations of volume distribution, collision diameter distribution and primary particle diameter distribution predicted by the present bimodal model and the sectional model; for monodisperse model, σ_g, $\sigma_{g,dc}$ and $\sigma_{g,dp}=1$.

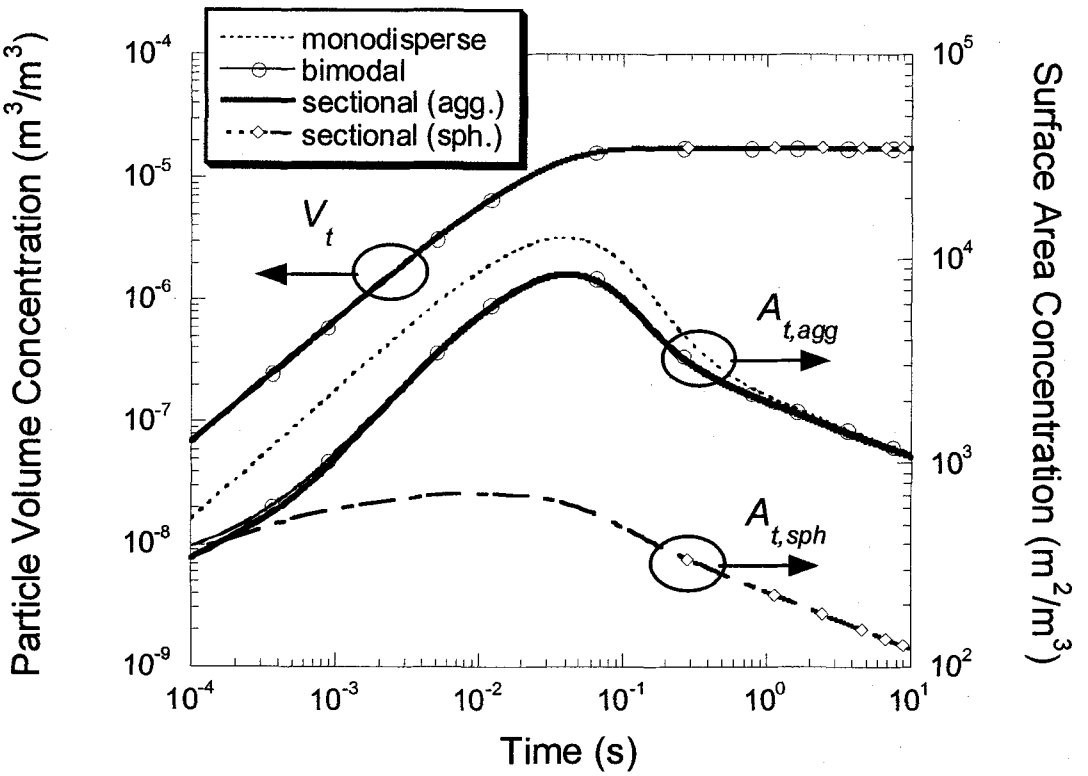

Figure 3.2.2.7. Comparison of evolution of titania particle: total volume concentrations, and surface area concentrations predicted by the non-spherical monodisperse model, the present bimodal model and the sectional model. The results of the spherical sectional model are also shown.

3.2.3. *In-situ* optical diagnostics for determining aggregate evolution in a flame

● Introduction

Laser light scattering technique based on Rayleigh-Debye-Gans scattering theory (Kerker, 1969) has been previously used to measure the morphological parameters of non-spherical nanoparticles such as the fractal dimension and radius of gyration (Sorensen *et al*, 1992, Koylu,1997). The fractal approximation for aggregates implies the following relationship between the number of primary particles in an aggregate, N_p, and the radius of gyration of the aggregate, R_g (Jullien and Botet, 1987):

$$N_p = k_f \left(\frac{R_g}{d_p}\right)^{D_f} \tag{3.2.3.1}$$

where D_f is the fractal dimension and k_f is the fractal prefactor. The scattering intensity, $I_{vv}(\theta)$, can be expressed as follows (van der Hulst, 1981)

$$I_{vv}(\theta) = Q_{vv}(\theta) SR \tag{3.2.3.2}$$

where $Q_{vv}(\theta)$ is the scattering coefficient and SR is the system response. For fractal aggregates $Q_{vv}(\theta)$ can be written as

$$Q_{vv}(\theta) = \int C_{vv}^{a}(\theta) n(N_p) dN_p \tag{3.2.3.3}$$

where $n(N_p)$ is the distribution function of N_p, that is, the number of primary particles per an aggregate. From Rayleigh-Debye-Gans(RDG) theory (Bohren and Huffman, 1983), the differential scattering cross section of a fractal aggregate, $C_{vv}^{a}(\theta)$ can be expressed as

$$C_{vv}^{a}(\theta) = N_p^2 C_{vv}^{p}(\theta) f(qR_g) \tag{3.2.3.4}$$

where the structure factor, $f(qR_g)$, is expressed as follows in the Guinier (small angle) and power law (large angle) regimes, respectively (Martin and Hurd, 1987; Dobbins and Megaridis, 1991):

$$f(qR_g) = \exp(-(qR_g)^2/3) \approx \left(1 - \left(\frac{q^2 R_g^2}{3}\right)\right) \quad \text{Guinier regime} \tag{3.2.3.5}$$

$$= (qR_g)^{-D_f} \quad \text{Power law regime} \tag{3.2.3.6}$$

here $q = (4\pi/\lambda)\sin(\theta/2)$ and λ is the wavelength. The average scattering coefficient can be found by integration of Eq. 3 over the entire distribution.(Xing *et al*, 1999)

$$Q_{vv}(\theta) = Q_{vv}(0)\left(1 - q^2 \overline{R_g^2}/3\right) \quad \text{Guinier regime} \tag{3.2.3.7}$$

where $\overline{R_g^2}$ is the N^2-weighted mean-square radius of gyration that can be determined from the

linear slope of a $Q_{vv}(\theta)$-versus-q^2 plot.

$$Q_{vv}(\theta) = n_p k_f C_{vv}^p (q d_p / 2)^{-D_f} \qquad \text{Power law regime} \qquad (3.2.3.8)$$

where n_p is the number density of primary particles and d_p is the primary particle diameter. D_f can be obtained from the linear slope of $\log(Q_{vv}(\theta))$-versus-$\log(q)$ plot.

In previous studies having used light scattering, only point measurement method has been applied. However, point measurement is very inconvenient and much time is needed in case that measuring area is large and adjusting of a measuring position is difficult. In order to resolve this problem, we used a sheet beam and an intensified charge coupled device (ICCD) camera for one dimensional measurement. We applied this method to the premixed methane flat flame that produces nonspherical silica nanoparticles to evaluate a potential of the method as a new diagnostic technique for nonspherical particle diagnostics.

● Methods

The new scattering method was applied to the measurement of nonspherical silica nanopariticles produced in a premixed methane flat flame. A schematic diagram of the experimental apparatus is shown in Fig. 3.2.3.1. We used a laminar premixed flame burner to synthesize silica nanoparticles. The burner consists of a stainless steel tube of 25mm inside diameter in which a ceramic honeycomb is packed and a flame stabilizer surrounding the tube. Silicon tetrachloride ($SiCl_4$) was used for the generation of silica particles in flames. $SiCl_4$ vapor was carried into the burner by bubbling $SiCl_4$ liquid with high purity nitrogen. The bubbler containing $SiCl_4$ liquid was maintained at 27.5°C.The gas flow rates were 0.3 slpm of methane, 0.84 slpm of oxygen, and 3.16 slpm of nitrogen, corresponding to an equivalence ratio of 0.75. The flow rate of carrier gas, N_2, was 30 sccm and air of 80 slpm flowed into the flame stabilizer. Methane, air, and $SiCl_4$ vapor were mixed prior to introduction into the burner. The gas flows were regulated with a mass flow controller (MKS). The scattering experiment was employed with an Ar-ion laser (Coherent Innova 90) having 1.2W output power operating at 514.5 nm wavelength as a light source. The vertically polarized laser beam was transformed into a sheet with one concave and one convexcylindrical lenses. The scatted light passed through an interference filter centered at 514.5nm and a polarizer and detected by an intensified charge coupled device (ICCD) camera (Princeton Instruments). Scattering angles in the range of 10-150° were adjusted with a rotator. The flame temperatures were measured using a B type thermocouple in the absence of silica particles. The thermocouple output was corrected for radiative heat transfer loss, which basically included a radiation/convection heat transfer balance assuming negligible lead loss by conduction. The particles were extracted at several positions in the flame using a local thermophoretic sampling device and observed with a transmission electron microscope (TEM). The measured flame temperature distribution is shown in Fig. 3.2.3.2. The temperature is 1790K at z=1.5 mm and the temperature decreases to 1470K at z=30mm. A flat temperature distribution with radial distance is obtained at low positions of flame in which entrainment of ambient air is small. Under this condition, it is expected that a particle distribution across the radial distance is uniform at a given axial distance.

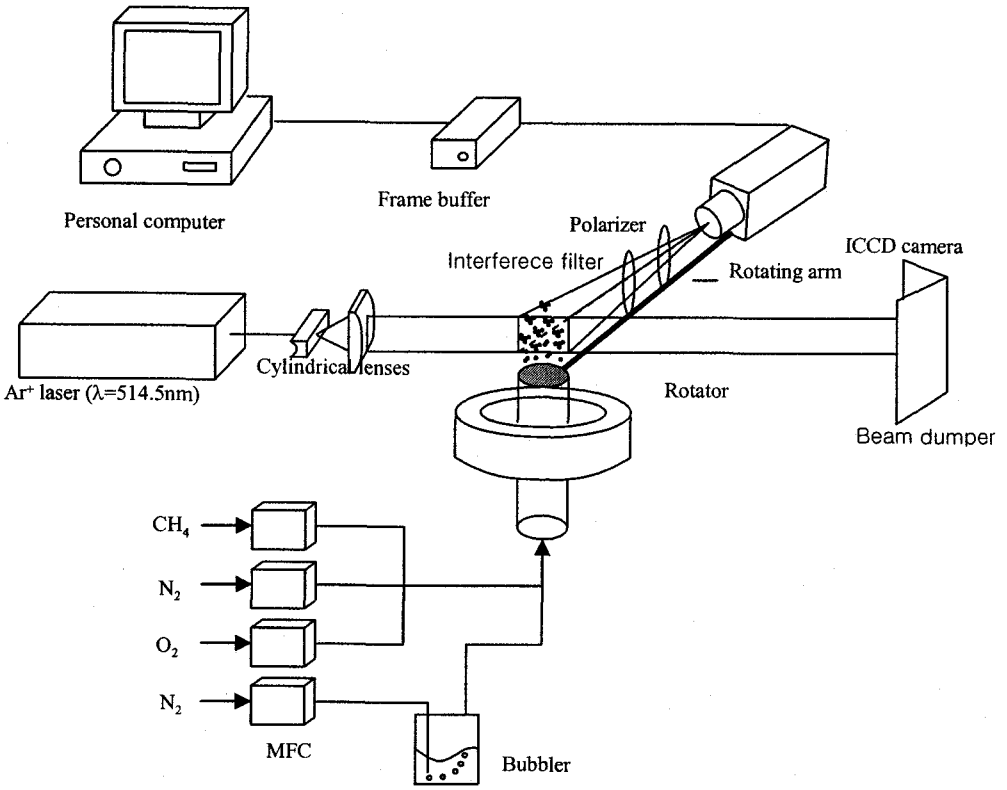

Fig. 3.2.3.1. Schematic diagram of the laser light scattering apparatus.

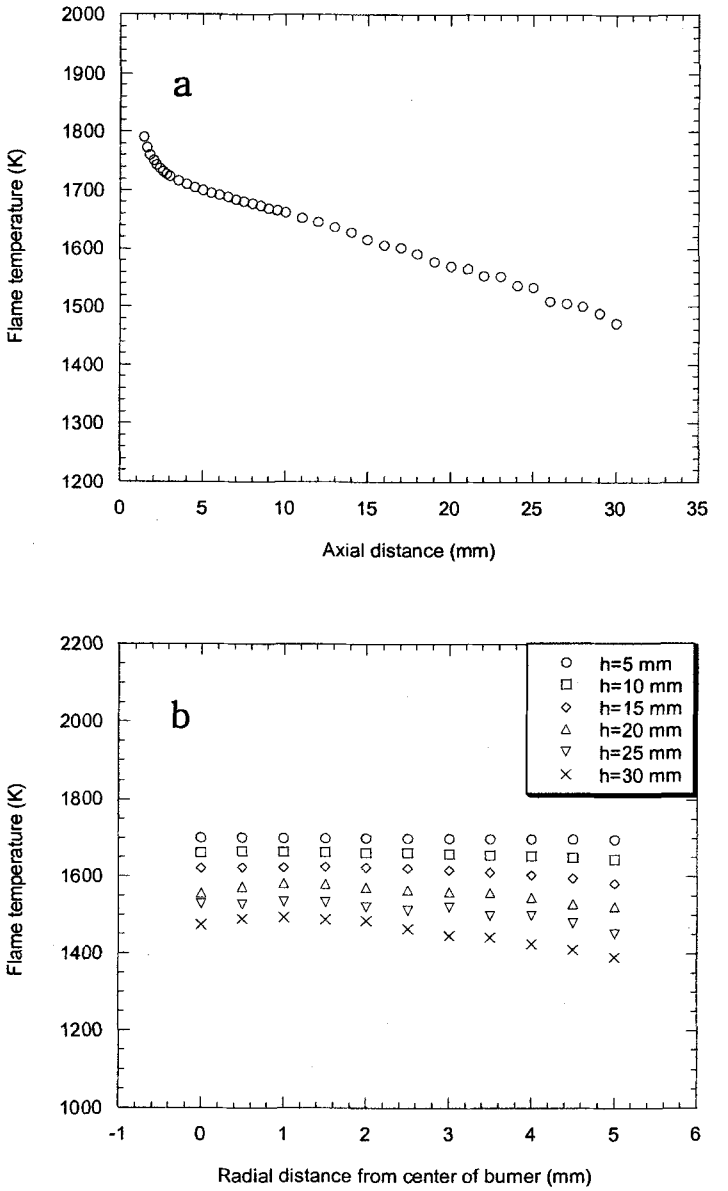

Fig. 3.2.3.2. Measured temperatures:

(a) temperature distribution along the axial position at r=0 mm;

(b) radial temperature distribution at different axial positions.

● Results and discussion

Fig. 3.2.3.3. shows the TEM image of the silica particles extracted from the flame at the axial distance of r=0mm. All particles are aggregates and the primary particle size is almost constant with axial distance. This indicates that the silica particles were almost not sintered and underwent coagulation mainly because the flame temperature was not high enough. This condition enabled the laser scattering technique based on Rayleigh-Debye-Gans scattering theory to be applied to this system. Fig. 3.2.3.4.(a) shows the images of scattered signals measured with ICCD camera. The width of the image is maximum at a scattering angle, $\theta=90^{\circ}$ and decreases as scattering angles get larger or smaller than 90° since they are proportional to sin θ. As can be seen from Fig. 3.2.3.4.(b), the scattered signal intensity distribution is very flat, which explains that the particle distribution is uniform with the radial distance at a given axial position. The angular scattering coefficient patterns are shown in Fig. 3.2.3.5. Scattering coefficient in the forward direction (small q) was always larger than the one in the backward direction (large q). This is clear evidence that the silica particles in our reactor departed from the Rayleigh scattering common for particles much smaller than the wavelength of light source. Fig. 3.2.3.6. shows the measured mean radius of gyration that was obtained from the slope of least square linear fit of a $Q_w(\theta)$-versus-q^2 plot at angles from $\theta=10^{\circ}$ to $\theta=20^{\circ}$. We can see in Fig. 3.2.3.6. that the radius of gyration obtained by one dimensional measurement technique is in good agreement with that given by the point measurement. The silica particles exhibit rapid growth at low heights, which tends to slow down with increasing distance. This behavior takes place because many particles are generated by chemical reaction close to the flame front and coagulation of particles by collision occurs briskly due to the high temperature at low heights. Fig. 3.2.3.7. shows the measured fractal dimension. As suggested by Eq. 8, the scattering coefficient varies inversely with q^{D_f} in the power law regime. Therefore, the fractal dimension of the silica aggregates can be determined from the slope of $\log(Q_w(\theta))$-versus-$\log(q)$ plot. To ensure that a scattering behavior is consistent with Eq. 8, we inferred D_f from least squares fits at angles from $\theta=110^{\circ}$ to $\theta=150^{\circ}$. The fractal dimension by new technique is also in a good agreement with the results obtained with the point measurement method. The increase of D_f with axial distance was an indication of aggregate restructuring; i.e., the structure became more compact as the residence time in flame increased.

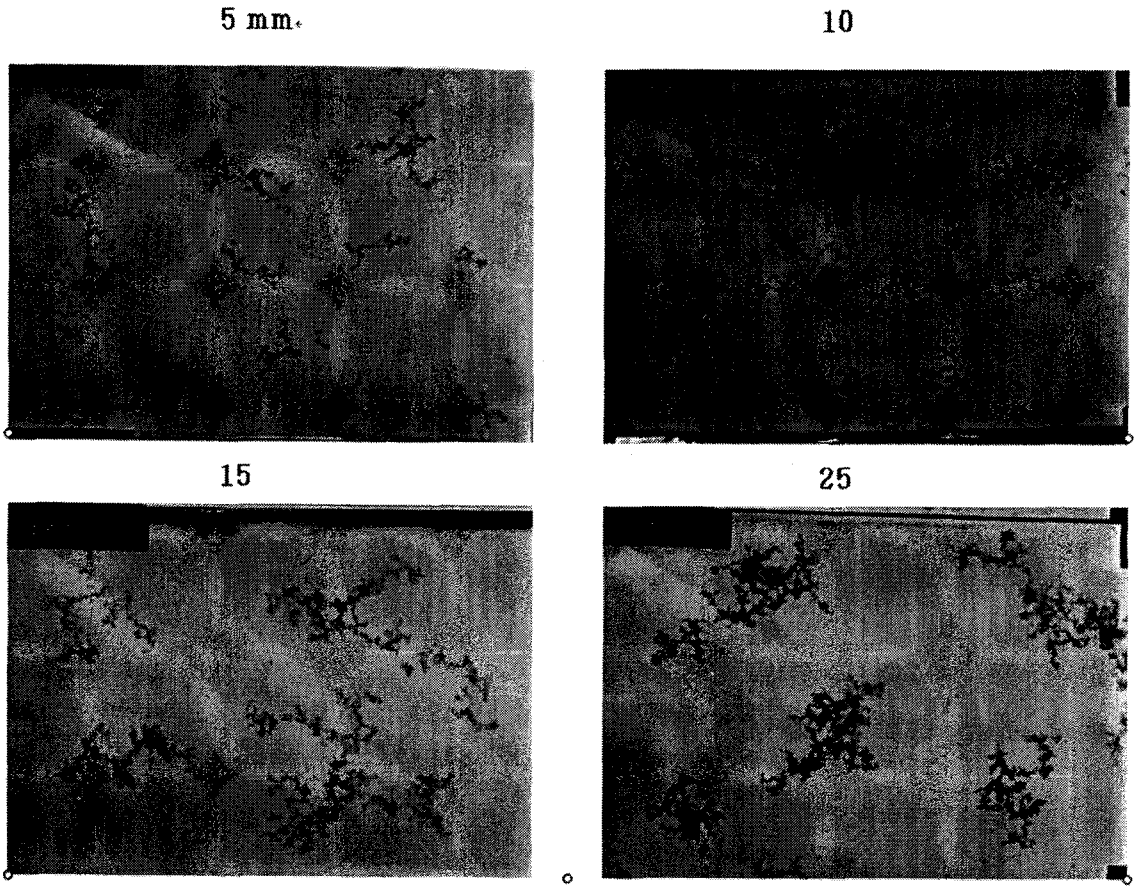

Fig. 3.2.3.3. TEM images of silica particles at different axial positions at r=0 mm.

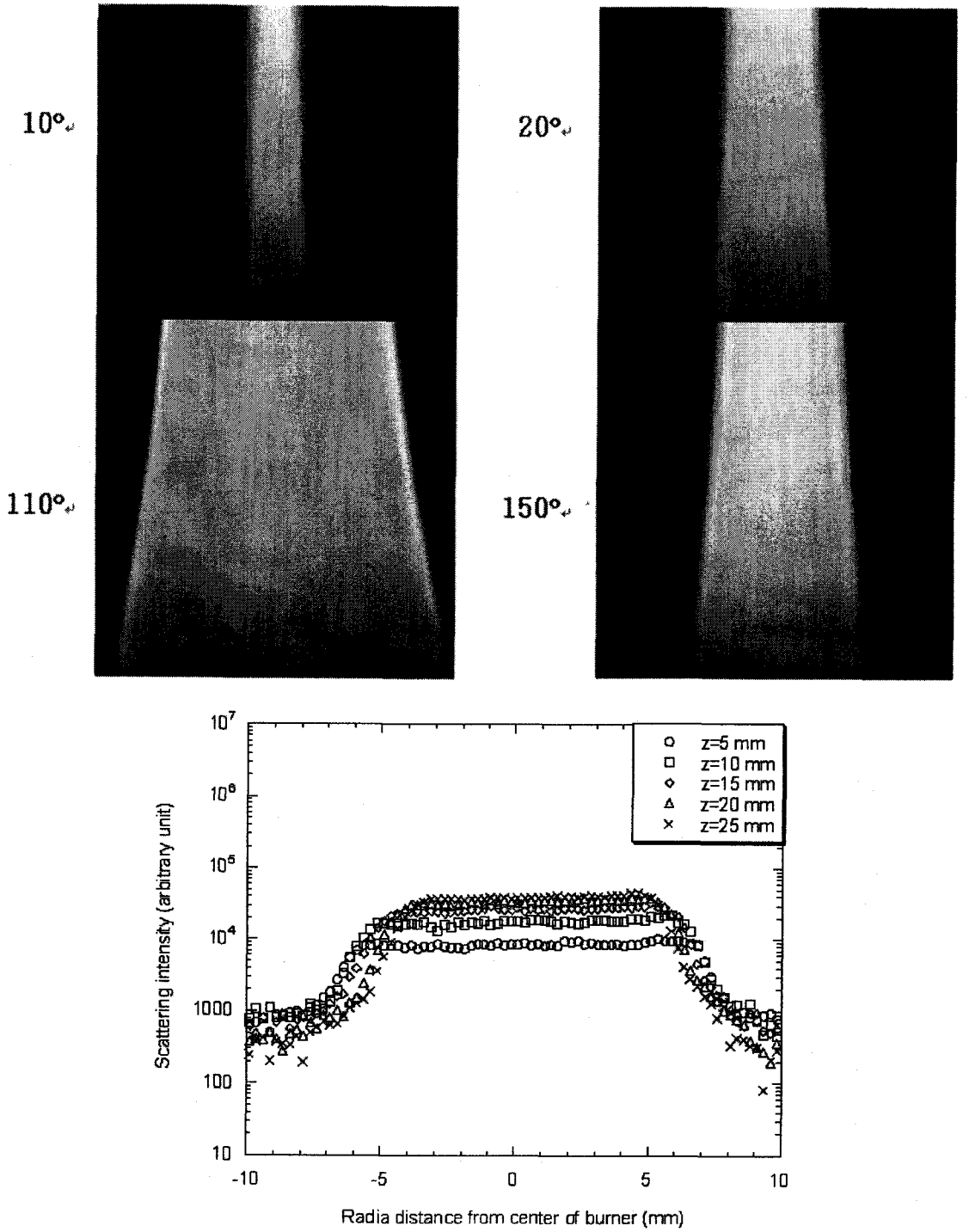

Fig. 3.2.3.4. Flame scattering.

(a) image of scattered signal measured with ICCD camera at different scattering angles

(b) radial scattering intensity distribution measured =150°.

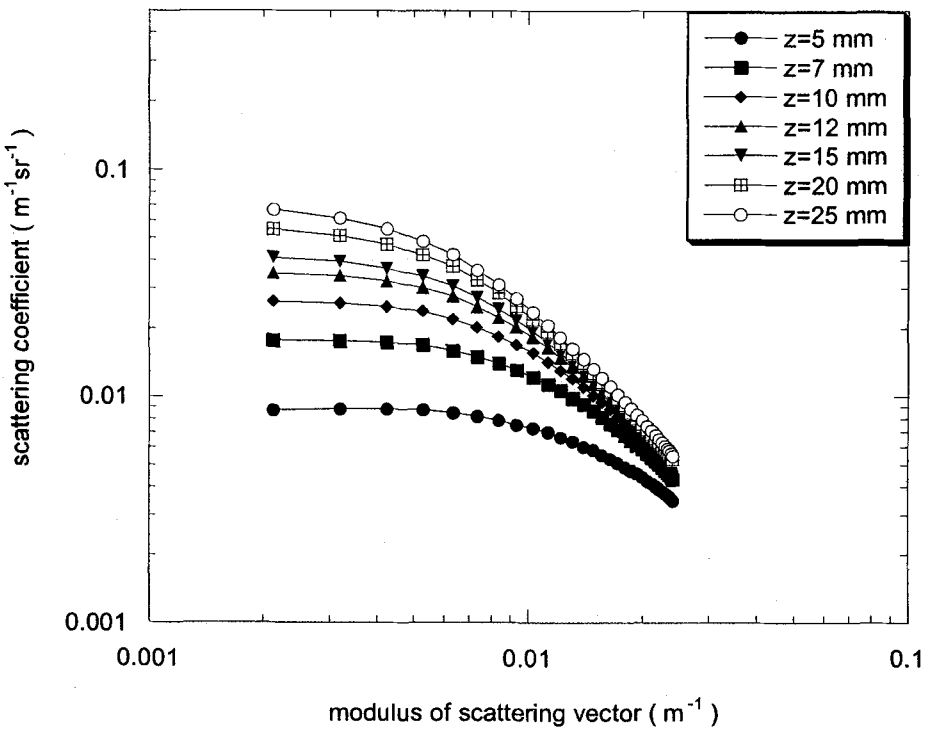

Fig. 3.2.3.5. Scattering coefficient patterns as functions of modulus of scattering vector at different axial positions.

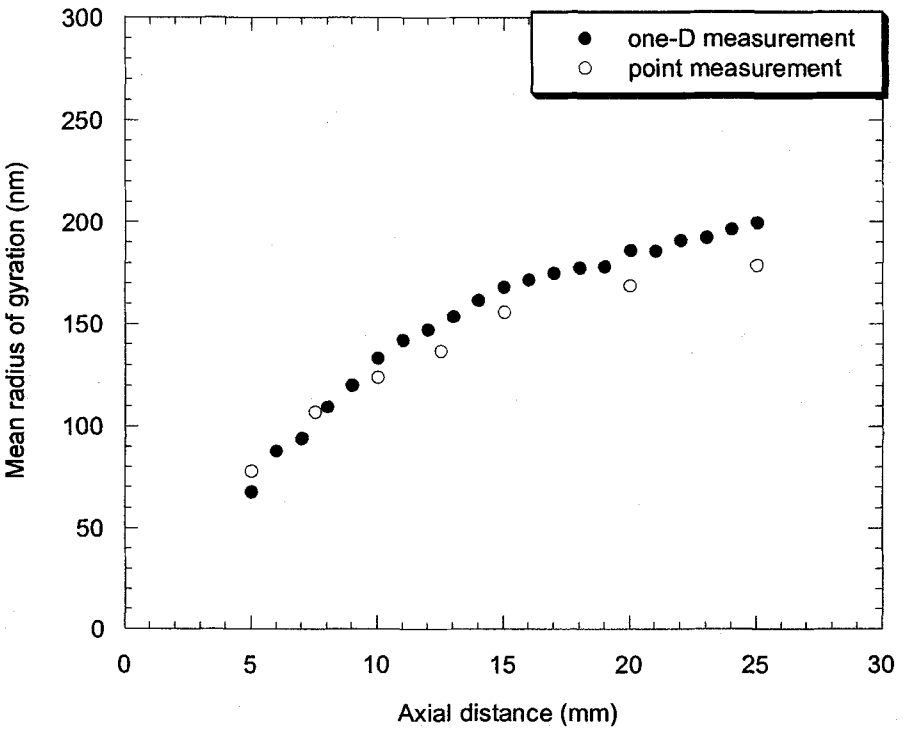

Fig. 3.2.3.6. Mean radius of gyration determined by one-dimensional measurement and by point measurement method along the axial position.

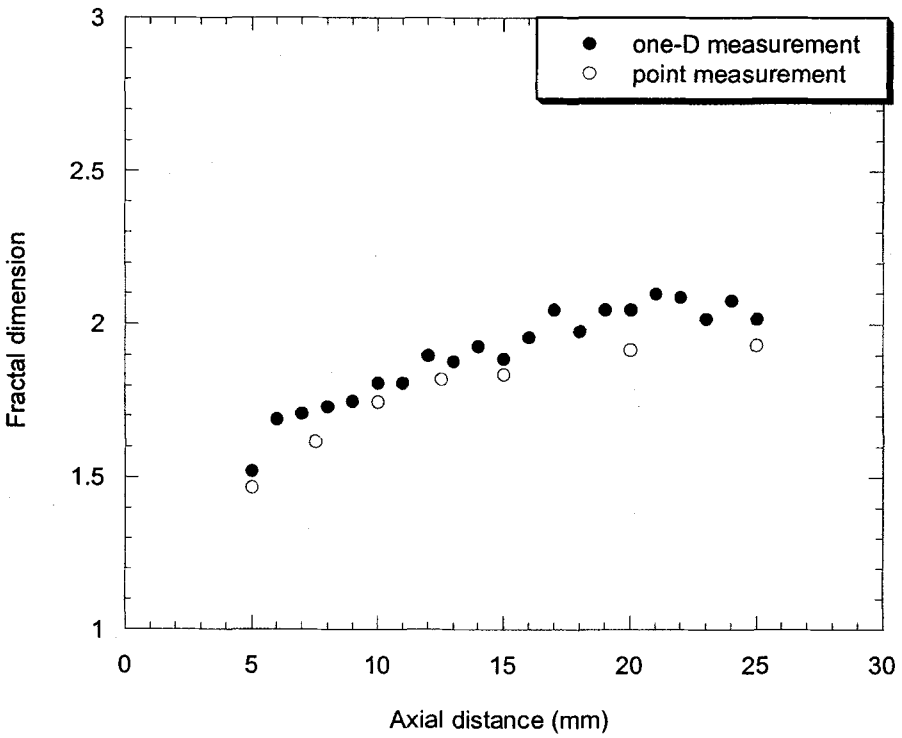

Fig. 3.2.3.7. Fractal dimension determined by one-dimensional measurement and by point measurement method along the axial position.

3.3. Elucidation of unknown fundamental phenomena

3.3.1 Measurement and calculation of flame temperatures and particle size distributions in a counter-flow diffusion flame

● Introduction

A counter-flow flame burner used in this study is similar in the configuration to that made by Chung and Katz (1985). The schematic of the counter-flow-type burner is shown in Fig. 3.3.3.1.. Two symmetric ducts with a rectangular channel stand in vertical opposite directions. The dimension of the main channel is 63.5 mm 12.7 mm. Fuel (H_2) and precursor ($SiCl_4$) are mixed and diluted with N2before they are injected upward through the lower channel. Similarly, the oxidizer (O_2) is diluted with N_2 before it is supplied downward through the upper channel. The separation distance between lower channel and upper channel is 15 mm. To keep a stabilized and steady flame configuration, a honeycomb was installed inside channels. Two pairs of cases having different flame temperatures are tested to investigate temperature effect on particle generation and, in each case, flame characteristics with $SiCl_4$ addition in fuel stream is compared with those without $SiCl_4$. The flow conditions for the cases tested are shown in Table 3.3.1.1.

Case	Lower channel			Upper channel	
	H_2	N_2	$SiCl_4$	O_2	N_2
I	1000	3000	0	700	3000
II	1000	2900	100	700	3000
III	2000	2000	0	1400	1100
IV	2000	1900	100	1400	1100
Flame#1	1350	978	10 or 19	1227	250
Hung	2263	1168	4.6	1818	167

Table 3.3.1.1. Flow rates for the tested cases (units in cc per minute at 298 K and 1 bar).

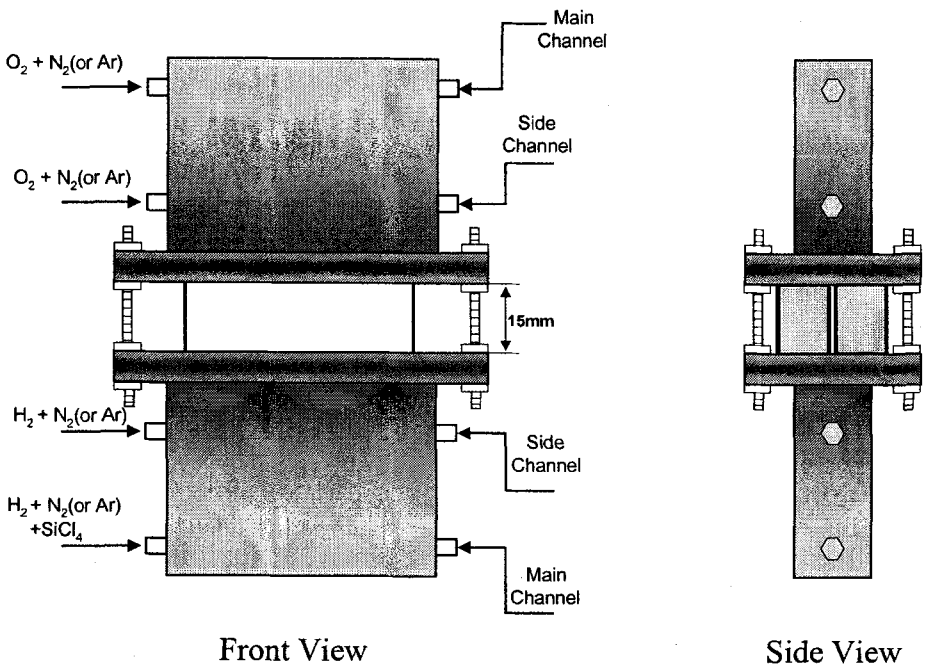

Fig. 3.3.1.1. The counter-flow diffusion burner used as a tool for generating fine silica particles in hydrogen-oxygen flames.

● Methods

The present study adopts a broadband coherent anti-Stokes Raman spectroscopy (CARS) from nitrogen to measure temperature (Hwang *et al.*, 2001), which is appropriate for measuring temperatures in silica generating flames since the signal efficiency is high and the corresponding Raman shift of nitrogen can be effectively isolated from those of other species and silica particles (Stolen and Walrafen, 1976; Eckbreth, 1988). The CARS system adopts a folded box-type optical geometry (Eckbreth *et al.*, 1984) and corresponding measuring volume has about 25 mm diameter and 0.5 mm length. A Q-switched Nd:YAG laser (Spectra Physics, GCR-150) is used as a pump laser which emits a 10 Hz pulsed laser beam with 532 nm wavelength, 7 ns duration, 1 cm-1line width, and 250 mJ energy per pulse. A modeless dye laser emits Stokes beam having 100 cm^{-1}bandwidth, 607 nm mean wavelength, and 15 mJ energy per pulse. The signal detection part consists ofa monochromator (Acton, AM510; 1200 gv/mm) and an optical multi-channel analyzer (OMA; Princeton Instruments, IRY-700G/RB), having 1 cm^{-1} resolution. Experimental detail for the CARS measurement is described in Hwang *et al.* (2001).

Concentrations of OH radicals have been measured qualitatively by using a PLIF technique (Alden *et al.*, 1982). For the excitation of OH radical, $Q_1(6)$ line of 282.95 nm with $A^2\Sigma^+ - X^2\Pi$ (1, 0) transition is adopted since this has been reported to result in the weakest temperature dependence of the fluorescence signal across the flame field of view, (Kychakoff *et al.*, 1984; Allen and Hanson, 1986). An optical system comprising a Nd:YAG laser (Continuum, PL8000), a dye laser (Continuum, ND6000), and a frequency doubler (Continuum, UVT) generates a incident laser sheet beam of 15 mm 300 mm size having 10 ns duration, 1 cm^{-1} line width, and 107 $W/cm^2/cm^{-1}$ spectral intensity which is relatively high compared to the saturation intensity for OH excitation (Eckbreth, 1988). An ICCD camera (Princeton Instrument, ICCD-576) with 576 X 384 pixels equipped with WG 305 and UG 11 filters detects fluorescence signals. Light scattering from silica particles has been monitored to visualize silica particles by using 532 nm planar laser sheet beam from the Nd:YAG laser and the ICCD camera as a light source and a detector, respectively.

Numerical calculations were conducted to model silica generation and possible changes in flame structure with the silica generation. The reaction mechanism consists of 19 species and 43 reaction steps including 19 oxy-hydrogen reactions (Mass and Warnatz, 1988) and 19 reactions related to chlorinated species (Ho *et al.*, 1992) as well as silica formation reactions via oxidation (Powers, 1978) and hydrolysis (Kochubei, 1997) of $SiCl_4$. Phase changes of SiO_2 from vapor to solid and vice versa are also included. Governing equations and numerical schemes have been presented in Lee and Chung (1994) and Smooke (1982). Thermodynamic and transport properties are calculated using CHEMKIN II (Kee *et al.*, 1989) and TRANSPORT PACKAGES (Kee *et al.*, 1983).

A localized thermophoretic sampling technique is known to collect the particles at a certain place. Such a technique was successfully applied in the case of co-flow flames (Cho and Choi, 2000). Counter-flow non-premixed flame produces a more narrow and flat reaction zone compared with co-flow non-premixed flame. Therefore it is inappropriate to insert the usual thermophoretic sampling

probe into a thin flame structure. To minimize the perturbation of flame, we modified a sampling probe into a thinner one than that used by Cho and Choi (2000). A 0.1 mm-thickness sheath was installed to protect TEM grid from being exposed to the deposition of particles while being inserted into the flames and subtracted from the flames. The sheath acts forward and backward by a 15 mm-double-acting pneumatic cylinder. The total thickness of the sampling probe assembly is 0.9 mm. The collected silica particles were observed with a transmission electron microscope (TEM, JEM-200CX). From the analysis of TEM images, we measured projected area equivalent diameter (PAED) and surface area mean diameter (SAMD). The measuring procedure is as follows.

The number of primary particles in an agglomerate can be determined by the primary particle diameter and projected area measured directly from TEM images. The following formula gives the relationship between the number of primary particles in an agglomerate and projected area (Kyl et al., 1995; Sorensen et al, 1992)

$$N_p = 1.15\left(\frac{A_{proj}}{A_{pri}}\right)^{1.09} = 1.15\left(\frac{A_{proj}}{\pi d_p^2/4}\right)^{1.09} \tag{3.3.1.9}$$

In Eq (9), N_p is the number of primary particles in an agglomerate, d_p is the primary particle diameter, A_{pri} is the area of the primary particle, A_{proj} is the projected area of an agglomerate. PAED can be obtained from the measurement of projected area. PAED is the diameter of a spherical particle having the same projected area as an agglomerate, and hence defined as

$$PAED = \sqrt{\frac{4A_{proj}}{\pi}} \tag{3.3.1.10}$$

Assuming that primary particles comprising an agglomerate are spherical, of a constant diameter in an agglomerate and touched at point, we can define the surface area per an agglomerate(SA) as

$$SA = N_p \pi d_p^2 \tag{3.3.1.11}$$

Taking into consideration of an imaginary spherical particle having the same surface area as SA, we can define SAED as

$$SAED = \sqrt{\frac{SA}{\pi}} \tag{3.3.1.12}$$

And then we can define SAMD, which is a SAED weighted with SA.

$$SAMD = \frac{\sum_i SA_i \square SAED_i}{\sum_i SA_i} \tag{3.3.1.13}$$

The aggregate number density can be determined using the light scattering technique together with localized thermophoretic sampling (see Cho and Choi, 2000). This method enables us to obtain aggregate number density by using the Rayleigh-Debye-Gans light scattering theory with the information of aggregate properties measured from TEM image.

● Results and discussion

In order to study systematically the effect of $SiCl_4$ addition and silica generation on flame structure, numerical analysis has been conducted. The present calculation adopted the detailed chemical mechanism based on oxy-hydrogen reactions of Mass and Warnatz (1988). Reactions for silica formation via oxidation (Powers, 1978) and hydrolysis (Kochubei, 1997) of $SiCl_4$ are included in the calculation where the rate of reactions for the intermediate species and phase transition of silicon dioxides between gas and solid are assumed sufficiently fast such that the phase transition maintains equilibrium state controlled by temperature. Reactions related to chlorinated species suggested by Ho *et al.*(1992) are also added to the scheme. Calculated temperatures and OH concentrations for cases I and II are compared to the experimental results in Fig. 3.3.1.2., demonstrating that the present model successfully predicts temperatures and OH concentrations for both flames with and without $SiCl_4$. Numerical analysis reveals that the temperature decrease with $SiCl_4$addition in the preheated zone is mainly due to the increase in specific heat of the gas mixture. On the other hand, the increase of the temperature gradient in the particle formation zone results from the exothermic reactions where the release of latent heat during phase transition of SiO_2vapor to the particle is the most important considering that the temperature of the particle zone is sufficiently small compared to the boiling temperature of SiO_2. Also, a sensitivity analysis demonstrated that the decrease of OH concentration is owing to HCl generated during hydrolysis of $SiCl_4$ which depletes OH radicals. Other flames are also investigated both experimentally and numerically in order to verify temperature dependency of the present model. Fig 3.3.1.3 shows the profiles of measured and calculated temperatures and OH concentrations for cases III and IV. The result demonstrates that these cases have extremely high flame temperature over 2700 K and that the present model underestimates the decrease in OH concentration with $SiCl_4$ addition. The disagreement for the high temperature flames implies possible OH consumption via direct reactions between OH radicals and silicon chlorides, which is expected to be highly sensitive to temperature.

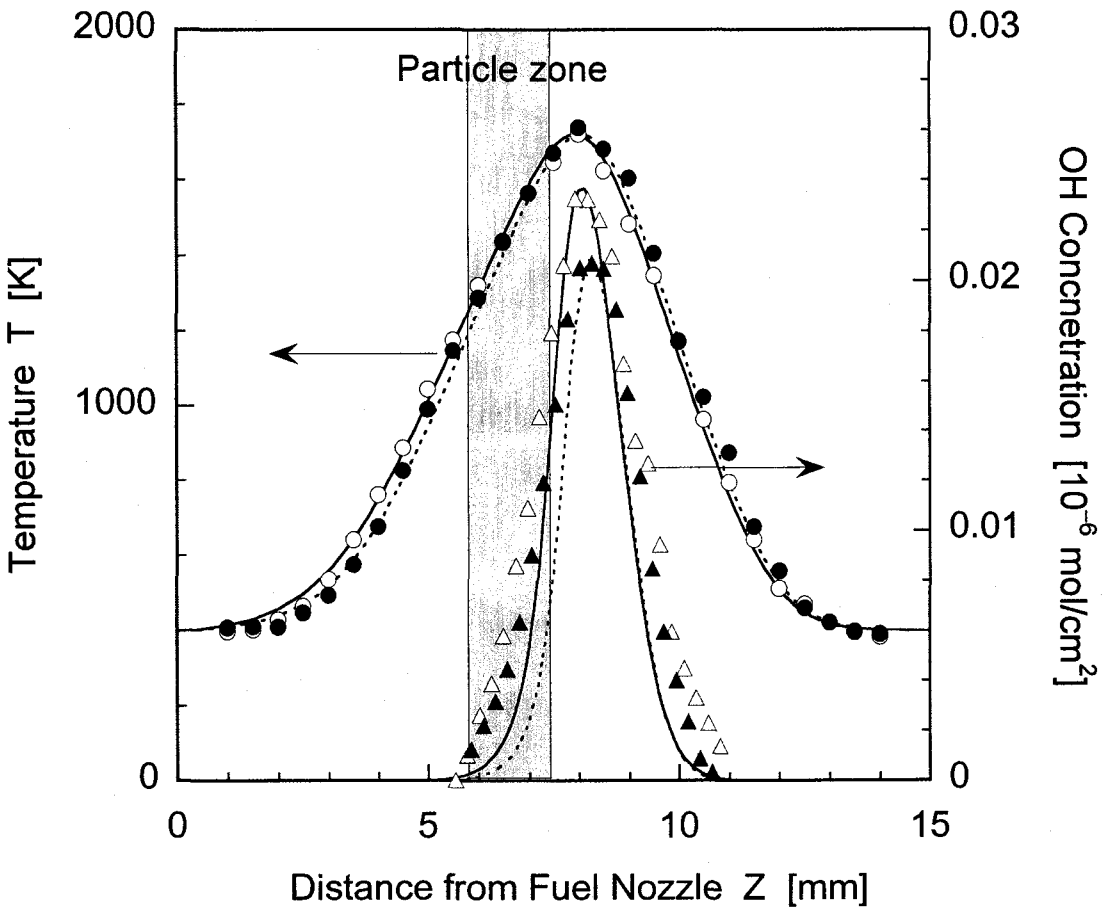

Fig. 3.3.1.2. Measured (symbols) and calculated (lines) profiles of temperatures and OH concentrations. Hollow symbols and solid lines represent case I and solid symbols and dotted lines represent case II.

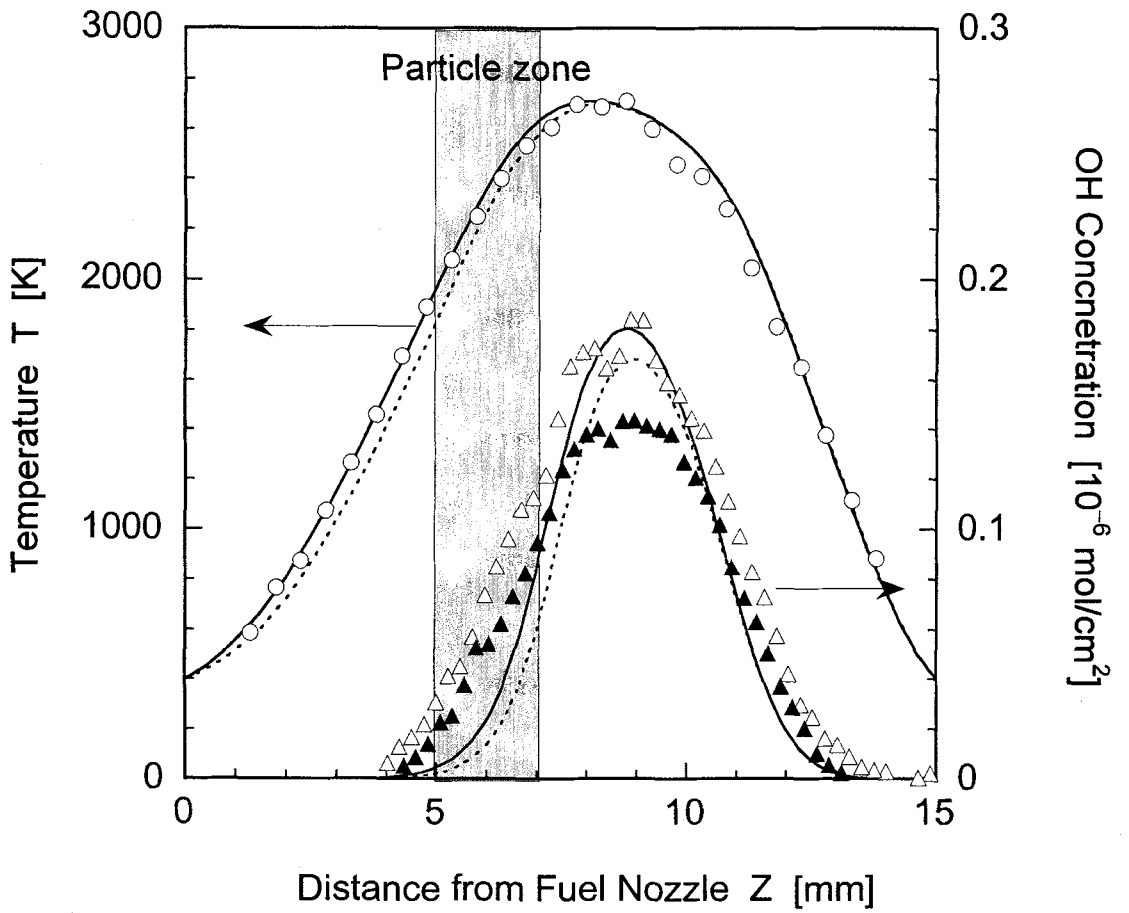

Fig. 3.3.1.3. Measured (symbols) and calculated (lines) profiles of temperatures and OH concentrations. Hollow symbols and solid lines represent case III and solid symbols and dotted lines represent case IV.

In order to study characteristics of silica generation with respect to flame structure, calculated profiles of temperature, T, particle velocity, U_p, SiO_2 scattering signal, Q_{VV}, and calculated formation rate of SiO_2(S), R_{SiO2}, for case II are shown in Fig. 3.3.1.4. Here particle velocity is determined from gas velocity and thermophoretic velocity assuming free molecular regime for particles (Wang *et al.*, 1996; Kang *et al.*, 1997). Fig. 3.3.1.4(a) shows flame structure in case II. The particle stagnation plane is located at Z=6.3 mm and flame is located in the oxidizer side of the stagnation plane near Z≈8 mm. As shown in Fig. 3.3.1.4(b), formation of SiO_2 mainly occurs between flame and the stagnation plane (6<Z<8.5 mm) where temperature ranges from 1200 K to 1750 K. Generated SiO_2 monomers coagulate moving tostagnation plane so that both mass concentration and average sizes of aggregates increase approaching the stagnation plane. Therefore, a scattering signal of silica particles shows skewed aspects from flame to stagnation having maximum value at the particle stagnation plane. Fig. 3.3.1.5. shows the flame structure and characteristics of particle formation for the high temperature flame (case IV), which are quite different from those of the low temperature flame (case II). Even though locations of the particle stagnation plane (Z=6.4 mm) and flame (Z≈8 mm) are nearly the same as in case II, temperatures at the stagnation and flame are over 1000 K higher than those in case II.

More drastic difference appears in characteristics of silica formation. Silica formation occurs in fuel side of the stagnation plane due to elevated temperature in the preheated zone. Consequently, generated particles are transported towards high temperature region undergoing particle growth so that the profile of scattering signal is inversely skewed compared to case II. Moreover, the formation rate has double peaks; the low temperature peak represent the silica formation by hydrolysis of $SiCl_4$ and the high temperature peak is resulted from oxidation of $SiCl_4$. Interestingly, the scattering signal decreases before particles reach the stagnation plane at Z=6.2 mm where temperature is about 2300 K. This is consistent with the numerical result considering that the calculated silica formation rate decreases rapidly at Z=5.9 and has negative values at Z=6.2 where the scattering signal starts to decrease. Reduction of silica formation rate at the extremely high temperature region over 2200 K is due to the phase transition of silica particles by vaporization. The decrease of scattering signal can be partly responsible for the decrease of scattering cross sections of silica aggregates by sintering process since the rate of sintering process increases fast with temperature.

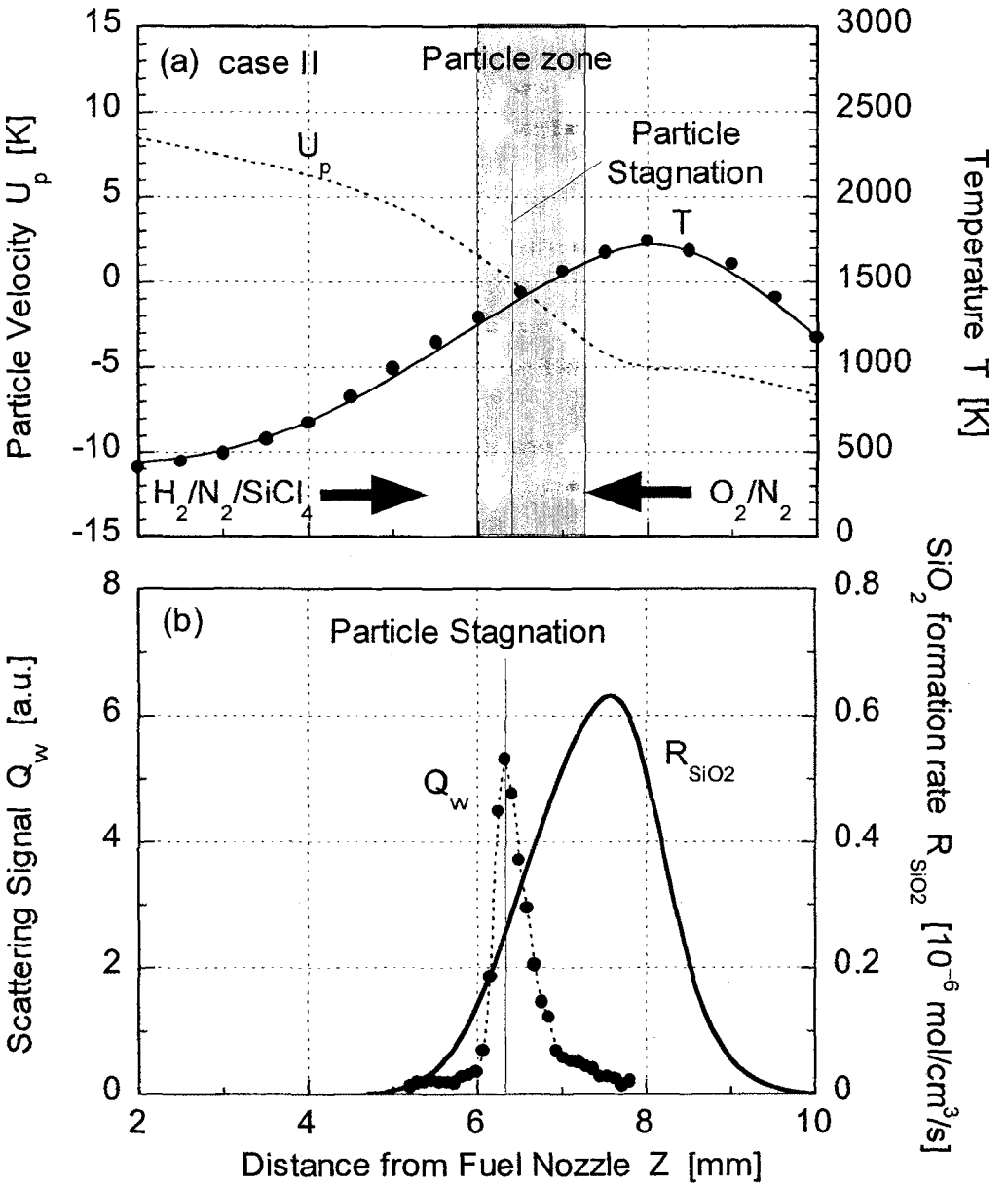

Fig. 3.3.1.4. Distributions of (a) particle velocity and temperature and (b) SiO_2 scattering signal and silica formation rate for case II.

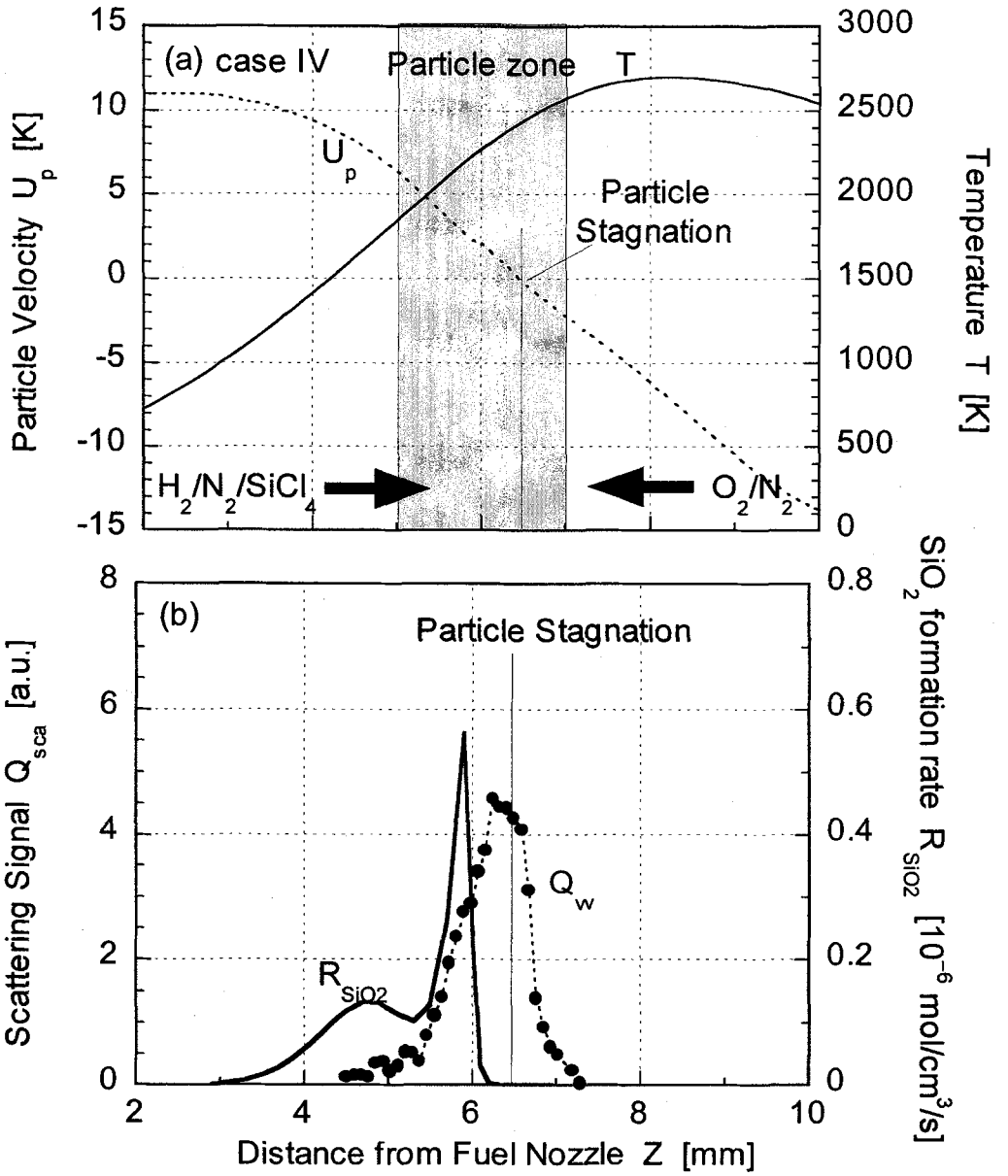

Fig. 3.3.1.5. Distributions of (a) particle velocity and temperature and (b) SiO2 scattering signal and silica formation rate for case IV.

To examine useful particle diameters to be used as a proper tool for two-dimensional microscope images of fine particles, we performed the localized thermophoretic sampling on condition of Hung and Katz's (1985) experiment (the flame condition is listed in Table 1.). PAED, SAED and SAMD were compared with hydrodynamic diameter (HD) obtained using dynamic light scattering by Hung and Katz (1985) and surface area mean diameters calculated numerically by Lee et al. (2001). The changes of the various diameters along the distance from the exit of fuel and $SiCl_4$ were shown in Fig. 3.3.1.6.. PAED and HD made a better agreement with the result of hybrid sintering model. On the contrary, SAMD agreed with the result of the fast sintering model accompanied by the viscous sintering model. The hybrid sintering model adopts an atomistic sintering model for small particles and a viscous flow sintering model for large particles. As the characteristic coalescence time increases, the particles have more time to grow into agglomerate. The characteristic coalescence time is known to depend on the particle size. If the particle diameter is large, the coalescence time increases, and then coalescence into a spherical particle is suppressed. It may be suggested that the atomistic diffusion sintering model suppresses a particle coagulation due to the dependence of characteristic coalescence time on dp^3, resulting in a slow increase of the surface area mean diameter. In the case where the fast sintering model is assumed, however, coalescence occurs instantaneously to create a large agglomerate of 1024 monomers which has the properties of bulk materials (Lee et al., 2001). It means that fast sintering model permits particles to coagulate into the large particles. The diameter calculated from a fast sinteringmodel increases rapidly up to 4.2 mm where it begins to decrease following the viscous sintering model. The observation of TEM images in Fig. 3.3.1.7. reveals that the agglomerate starts to appear at z=3.8mm and move to grow until z=4.2 mm. At z=4.6 mm, both spherical particles and agglomerate particles were observed and this is the result of coalescence at high temperature region. Because the dominant growth mechanism in the regime up to z=4.2 mm is the agglomeration, it is believed that SAMD is close to the diameter calculated from the fast sintering model.

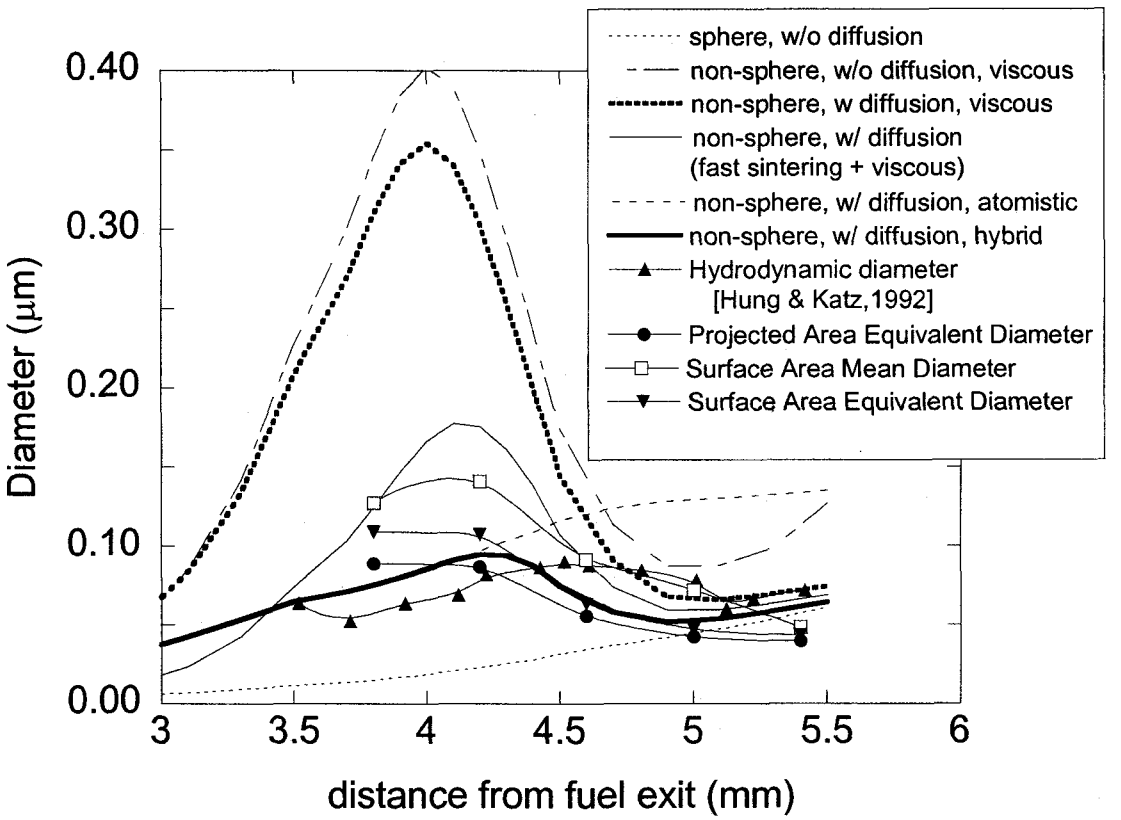

Fig. 3.3.1.6. Various diameters of silicaparticles considered in this study. Comparison between experimental data and numerical calculation by Lee et al. (2001) is also presented.

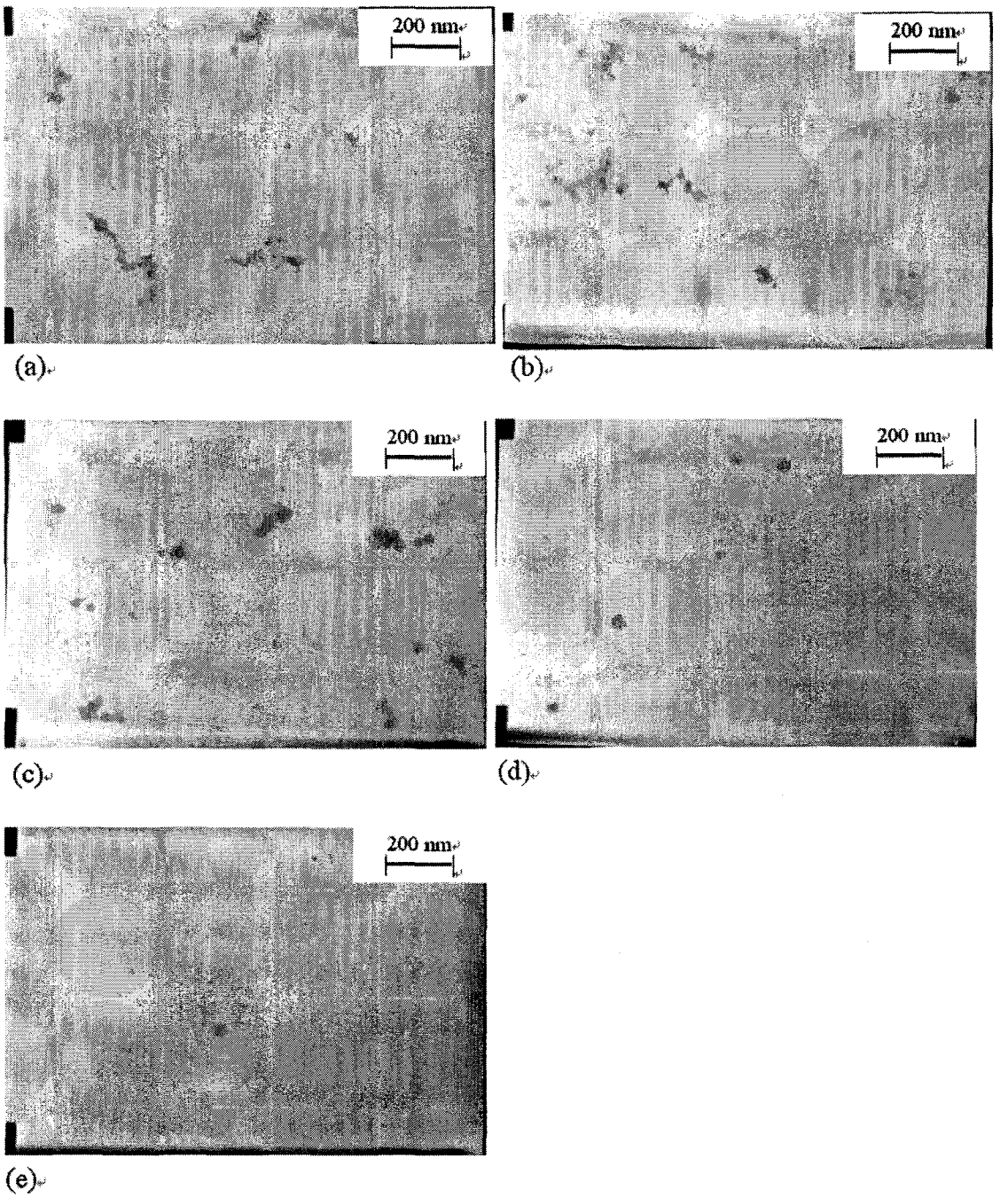

Fig. 3.3.1.7. TEM image of silica particle captured by a localized thermophoretic sampling along the exit of fuel injection. [Hung's (1992) flame condition]
(a) z=3.8 mm; (b) z=4.2 mm; (c) z=4.6 mm; (d) z = 5.0 mm; (e) z = 5.4 mm

Silica particles were collected in a different flame (Flame#1, the flow rates of gases are listed in Table 3.3.1.1) using the method of localized thermophoretic sampling at various positions for the case of 19 cc/min, 10 cc/min bubbling rates. When $SiCl_4$ was injected at the rate of 19cc/min, spherical particles were not observed, even if the particles underwent the region where temperature is above 2000 K. On the contrary, when the injection rate of $SiCl_4$ is 10 cc/min, the spherical particles started to appear at z=5.4 mm. Fig. 3.3.1.8. shows the variations of PAED and SAMD of silica particles generated in flame#1 as the distance from the exit increases. At z=4.4 mm, the ratios of PAED and SAMD for 10 cc/min bubbling rates to those for 19 cc/min bubbling rates are 0.522 and 0.612, respectively, that is, the larger particles were observed when $SiCl_4$ was supplied at the rate of 19 cc/min. Conversion energy transferred from the surrounding into the particle is proportional to the product of the surface area and coalescence time, that is, $D_{char}^{3} \sim D_{char}^{2} \cdot t_{coal}$. Consequently, the coalescence time of the particles generated at the rate of 19 cc/min bubbling was so longer than that in the case of 10 cc/min bubbling that the particles could not coalesce into spherical particles. In addition to the size effect on particle morphology, we can take into account the influence of the particle residence time. The particles started to be observed at z=3.0 mm in case of 10 cc/min bubbling, whereas the particles were not observed until z=3.6 mm when $SiCl_4$ was injectedat the rate of 19 cc/min. This means that the particles formed in the case of 10 cc/min injection pass through the flame for longer residence time than those in the case of 19 cc/min injection. Moreover, it is believed that the bubbling at the rate of 19 cc/min retarded the onset of silica particle generation, resulting in providing the growing particles an insufficient residence time to coalesce. The aggregate number density of silica aggregate particles generated in flame#1 are shown in Fig. 3.3.1.9. As one can see in Fig. 3.3.1.8. SAMD decreased about from 600 nm to 400 nm when $SiCl_4$ was injected at the rate of 19 cc/min. Besides, Fig. 3.3.1.9. shows that Naincreased about 10 times in the location from z=3.6 mm to z=5.2 mm. In the same region, SAMD decreased slightly and Naincreased about 10 times when the bubbling rate was 10 cc/min. Energy transferred from the flame by hydrogen-oxygen reaction can be used to break the osculation of loosely attached agglomerates as well as to fuse into a large spherical particle. It is conceivable that the large decrease of SAMD and the increase of Nain the case of 19 cc/min bubbling may be attributed to the fact that the combustion energy is used only to detach the weak linkage between coarse primary particles.

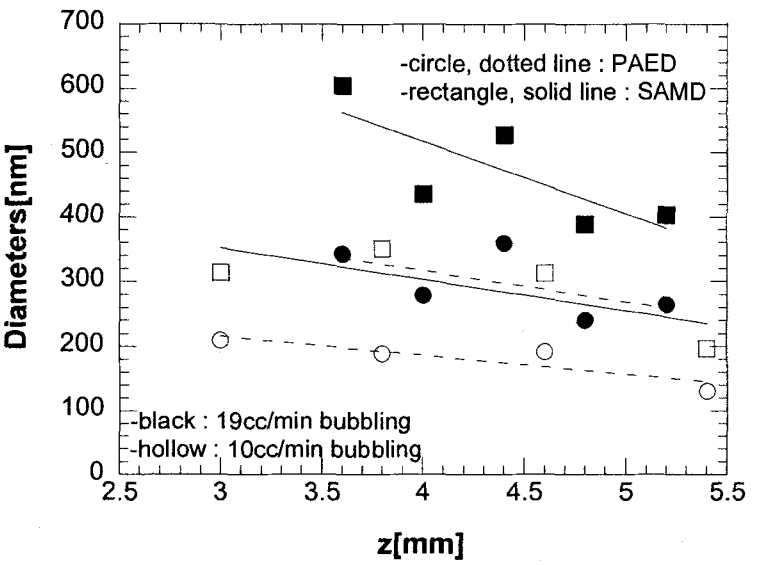

Fig. 3.3.1.8. Various sizes of silica particles measured from the TEM image in case of flame#1 for the bubbling rate of both 19cc/min and 10cc/min.

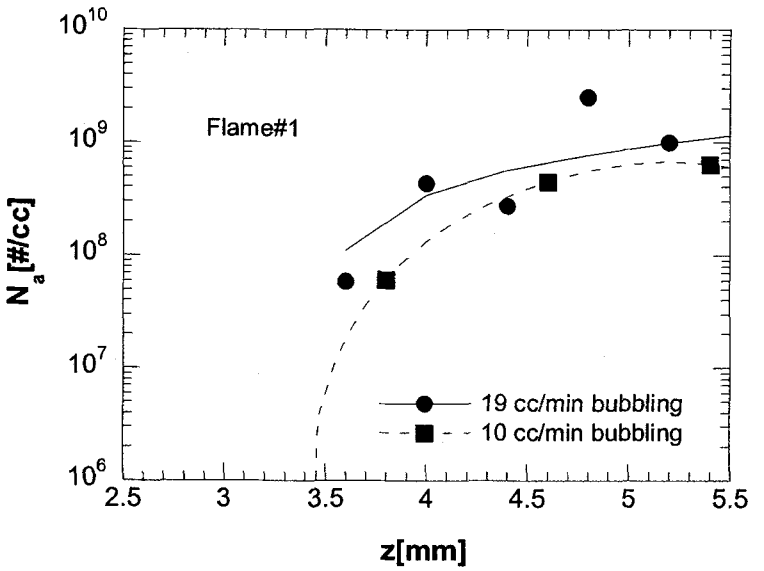

Fig. 3.3.1.9. Aggregate number density obtained using Rayleigh-Debye-Gans scattering theory on condition of flame #1.

3.3.2. Fragmentation of iron-oxide nanoparticles due to phase transformation

● Introduction

The formation and characterization of magnetic nanoparticles is the subject of intense research due to their unusual magnetic behavior compared with the corresponding bulk materials(Mørup, et al., 1994). One of the most important features of magnetic nanoparticles is their superparamagnetic property that is of great interest for potential applications including magnetocaloric refrigeration, bioprocessing and ferrofluid technology(McMichael, et al., 1992). The superparamagnetism is a unique aspect of magnetism in nanoparticles(Awschalom, et al., 1995). Reducing the size of magnetic particles and controlling their crystalline phase have greatly influenced the need for new or improved methods of nanoparticle synthesis(Martinez, et al., 1998).

Maghemite (γ-Fe_2O_3) nanoparticles have been widely studied for use in superparamagnetic applications because of their high chemical stability as well as good magnetic properties(Lin, et al., 1996, Chen, et al., 1998). Among many preparation methods for nanocrystalline γ-Fe_2O_3 particles, gas-phase routes using a flame have certain advantages, one of which is that they can produce very pure and fine nanocrystalline γ-Fe_2O_3 particles in a continuous way(Zachariah, et al., 1991). The size and crystalline phase of particles are critical factors to determine magnetic properties and their evolution in a flame is largely influenced by the flame temperature, precursor concentration and flow coordinate (i.e. residence time)(Janzen, et al., 1999, Choi, et al., 1999). The evolution of particle size and crystalline phase not only provides information on how to obtain well-controlled nanoparticles,but also understanding as to the formation and growth mechanism of nanoparticles in a flame.

In general, iron (III) oxide particles generated in a flame are known to grow continuously in size by the collision and/or coalescence of particles as most of oxide particles do(Janzen and Roth, 2001, Lee, et al., 2001, Lee and Choi, 2002). However, we found an unusual evolution of nanoparticles in a flame: initially growing iron (III) oxide nanoparticles having about 20 nm size have been abruptly transformed into ~3 nm sizes with the increasing flow coordinate i.e. the residence time of particles in the flame, which was confirmed to be accompanied by a phase transformation. This phenomenon that we found indicates that substantially different sizes and crystalline phases of Fe_2O_3 nanoparticles can be produced within a same flame depending on where to collect. These different particles (20 nm or ~3 nm) collected in a same flame obviously showed quite different magnetic properties.

● Methods

An iron (III) acetylacetonate precursor powder, $Fe(C_5H_7O_2)_3$, contained in a stainless steel chamber was maintained at 170°C in an electric furnace. The carrier gas (N_2) including vapor-phase iron (III) acetylacetonate was fed through the center of a co-axial burner. The combustion gases, hydrogen and oxygen were injected through the next two concentric annuli in that order.

The flame temperature was controlled by altering $[H_2]/[O_2]$, and was measured using a B-type thermocouple. The average bead diameter was 0.56 mm and the output data were digitized with an

A/D converter (Keithley Instruments Inc. DAS-8) and recorded in a PC. The flame temperature was measured without feeding the precursor and the thermocouple stayed in a flame for sufficient time to obtain steady data. The measured flame temperatures were corrected for radiative heat loss.

The sizes and shapes of iron (III) oxide particles were measured using a thermophoretic sampling with TEM (Jeol, JEM-3000F) image processing. For this purpose, a localized thermophoretic sampling device was used(Cho and Choi, 2000, Lee and Choi, 2000). which consists of a sampling probe holding a TEM grid (carbon-coated copper grid, 200 mesh) and a shield that covers the grid. During the sampling, the shield prevented the particles from being deposited onto the grid when the sampling probe was inserted to and subtracted from a flame. The shield was retracted to expose the grid for the sampling duration (100 - 400 ms) only after the probe was located at a desired position within the flame. To investigate the influence of the flow coordinate z (i.e. flame height from the burner exit), the particles were collected at various heights, from 15 mm to 100 mm.

The particles synthesized in the oxy-hydrogen diffusion flame were also collected using a water-cooled quartz tube for physico-chemical and magnetic analyses. The structural characterization of the iron (III) oxide nanoparticles was performed by X-ray diffraction (XRD) using a Mac Science MXP10XHF-22 diffractometer ($\theta/2\theta$, Cu Kα radiation). Magnetic properties of the iron (III) oxide nanoparticles were investigated using a superconducting quantum interference device (SQUID) magnetometer (Quantum Design, MPMS-XL).

● Results and discussion

The mean particle size increased slightly up to approximately 19 nm with the $[H_2]/[O_2]$ ratio above 0.8. Beginning with the $[H_2]/[O_2]$ ratio of 0.8 (the maximum flame temperature was around 1650°C) an unusual phenomenon was observed. Upon reaching the value of 20 nm at the flame height of $z \approx 35$ mm, the mean particle size dramatically decreased to less than 5 nm at $z \approx 45$ mm. Further increase of z did not significantly change the mean particle size. TEM imagesof iron (III) oxide particles captured at different z with the $[H_2]/[O_2]$ ratio of 0.8 are shown in Fig. 3.3.2.1. For z > 45 mm only ultrafine particles with size less than 5 nm can be observed (Fig. 3.3.2.1d).

High-resolution TEM (HRTEM) images of iron (III) oxide particles captured at different z are shown in Fig. 3.3.2.2(a,b). Lattice fringes corresponding to the (220) planes of the γ-Fe_2O_3 cubic system are seen for the particles collected at 20 mm (Fig 3.3.2.2(a)). For the 3 nm ultrafine particles (see Fig 3.3.2.2(b)) the lattice spacings of 2.70 Å as well as 2.95 Å were observed, which agreed with those of (104) planes of α-Fe_2O_3 and (220) planes of γ-Fe_2O_3, respectively. No other phase was found.

Sharp and intense x-ray diffraction (XRD) peaks shown in Fig. 3.3.2.2(c) prove that 20 nm particles at 20 mm and 30 mm were γ-Fe_2O_3 particles. However, XRD peaks of the ultrafine particles at 60 mm were broad and weak. To resolve broad peak in the XRD pattern a fitting by Pearson VII functions(Hall, et al., 1977) was performed. Four components were determined to ensure the required accuracy of the deconvolution (see the inset in Fig. 3.3.2.2c). Pearson VII peaks B ($2\theta = 33.10°$) and C ($2\theta = 35.55°$) were assigned to a (104) and a (110) reflection of α-Fe_2O_3, respectively. The Fe 2p x-ray

photoelectron spectroscopy (XPS) spectrum of the ultrafine particles revealed the ion valence state of Fe (III). Since the XPS spectrum showed no Fe_3O_4, Pearson VII peak A ($2\theta = 30.20°$) and D ($2\theta = 35.60°$) should be attributed to a (220) and (311) reflection of γ-Fe_2O_3, respectively. The width of each of four peaks corresponds to the mean particle sizes of 2.3 - 2.7 nm. Then XRD results correspond to the conclusion made from the TEM image analysis that the sudden decrease of the particle size was accompanied by a partial phase transformation from γ- into α-Fe_2O_3.

The magnetic susceptibility of nanoparticles, measured with a superconducting quantum interference device (SQUID) magnetometer, is shown in Fig. 3.3.2.3(a). Markedly different susceptibilities are obtained for particles captured from the same flame but at different heights. Note a typical superparamagnetic behavior above the blocking temperature of 45 K for ultrafine nanoparticles collected at 60 mm, which indicates a transition from ferrimagnetism to superparamagnetism. Fig. 3.3.2.3(b) shows the Mössbauer spectra for ultrafine particles. The disappearance of the 16 K sextet (originating from the internal magnetic field (Greenwood and Gibb, 1971)) and the appearance of the doublet at room temperature, confirms the superparamagnetic behavior concluded from the SQUID. There is also seen the singlet, which was not observed for γ-Fe_2O_3 nanoparticles of 3 nm coated with silica(Zhang et al., 1997). Since the singlet line could also appear when ferric ion is in an ideal cubic environment16, then the appearance of the singlet along with the doublet in our case can be interpreted as an additional ferric ion singlet, givingthe reasonable parameters of the doublet with the splitting of 1.1 mm/s (to be compared with the previously reported values of 0.9 mm/s and 1.19 mm/s(Xu et al., 2002)) and the isomer shift of about 0.25 mm/s for both the doublet and the singlet.

It is well known that the maghemite phase is metastable in the bulk though its stability can considerably improve in nanoscale(Ye, et al., 1998). At a sufficiently high temperature T_g, the energy barrier $\Delta \approx 270$ kJ/mol(Schimanke and Martin, 2000) separating γ- and α-phases can be overcome within the short residence time of a nanoparticle in flame (about 1 ms) as far as the rate of the transformation is thermally activated(Boer and Dekkers, 2001). The heat release due to the enthalpy difference(Laberty and Navrotsky, 1998), $H_{tr} = 15$ kJ/mol, between γ- and α- phases during the fast transformation heats up the maghemite nanoparticle, which leads to the further acceleration of the increase in its temperature, T_p. This feedback results in instability of the initial phase leading to the explosive fragmentation of the maghemite nanoparticle into much smaller components, part of which has been converted into the α-phase.

To locate this structural instability we use the heat balance equation that determines the particle temperature:

$$Q_{heat} - Q_{cool} = 0, \qquad (3.3.2.1)$$

where the heat gain from the phase transformation in a particle of the radius $r = 10$ nm and the mass density $\rho \sim 5$ g/cm^3 can be written as

$$Q_{heat} = H_{tr} \frac{\frac{4\pi r^3}{3}\rho N_A}{\mu}\frac{1}{\tau}, \qquad \tau = \tau_0 \exp(\Delta / T_p), \qquad (3.3.2.2)$$

The heat loss due to the cooling by the surrounding gas of the temperature T_g is

$$Q_{cool} = \frac{1}{2}\frac{\gamma+1}{\gamma-1}\frac{\alpha P_g k_B (T_p - T_g)}{\sqrt{2\pi(\mu_g / N_A)k_B T_g}} 4\pi r^2. \qquad (3.3.2.3)$$

In Eqs. (3.3.2.2) and (3.3.2.3) the molar weight is $\mu = 160$ g/mol for the iron oxide and $\mu_g = 29$ g/mol for air; N_A is the Avogadro number; $\gamma = 1.4$ is the Poisson ratio for air; k_B is the Boltzmann constant; P_g is the atmosphere pressure; α is the energy accommodation coefficient(Goodman and Wachman, 1976), τ is the characteristic time of the phase transition and τ_0 is the characteristic attempt time (about 10^{-12} s in our case). For simplicity, we neglected any other contributions affecting heat balance, which do not alter the results significantly.

Fig. 3.3.2.4 provides a principal scenario (calculated with α=0.01) for the critical behavior of the particle temperature according to Eq. (3.3.2.1). Note that there is an evidence(Altman, et al., 2001) that α can be very small at high temperatures. One can see that for the flame temperature exceeding 1750 K there are no appropriate particle temperatures for the system to be stable at a given particle radius of 10 nm while they still exist for the smaller particle radius of 2 nm. Thus on approaching the critical temperature the particle should experience a sudden transition into some other stable state which can be followed by the abrupt reduction of the characteristic particle size through the particle fragmentation. Since the fast high temperature transformation towards the α-phase produces mechanical strains, the natural way for the particle to keep the heat balance is to be fragmented into considerably smaller particles. Such an explosion-like (or maybe peeling-like) transformation can not be complete and we observe the mixture of both γ- and α- phases in ultrafine nanoparticles of 3 nm. This novel fragmentation phenomenon can be used to obtain substantially different sizes and phases of nanoparticles having different properties from the same flame. We believe that the fragmentation phenomenon revealed is general and applicable for other complex oxides.

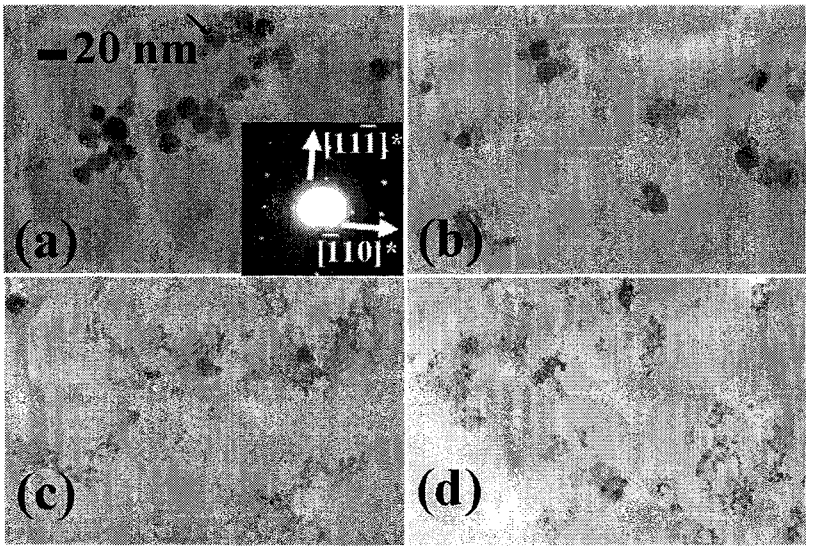

Fig. 3.3.2.1. TEM images of Fe_2O_3 nanoparticles captured at (a) 35 mm, (b) 40 mm, (c) 43 mm, and (d) 45 mm. The $[H_2]/[O_2]$ ratio was 0.8. The selected area diffraction (SAD) pattern for a 20 nm particle (indicated by the black arrow) shows that this particle is a single crystal maghemite. Particles captured at 40 mm show a distinct bimodal size distribution (the mean particle sizes of 20 nm and 3-4) As z increases, the number of large particles decreases while the number of small particles increases.

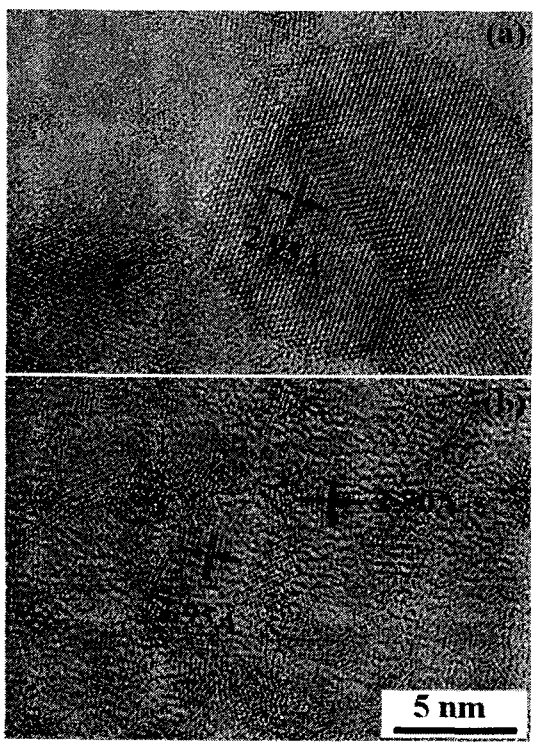
(a)
(b)
5 nm

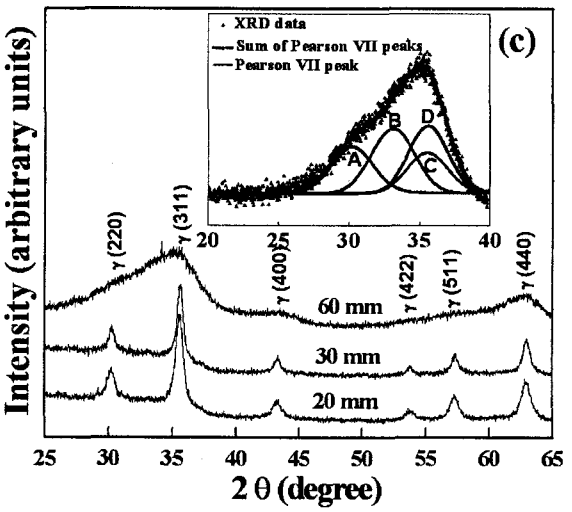

Fig. 3.3.2.2. Structural characterization of Fe_2O_3 nanoparticles. (a) High resolution TEM image of Fe_2O_3 nanoparticles collected at 20 mm, (b) The same at 60 mm, (c) XRD patterns of Fe_2O_3 nanoparticles for different z ($[H_2]/[O_2]$ = 0.8). The inset shows a fitting for the combined peak profile of the 25°-40°(2θ) range to four Pearson VII functions for ultrafine particles

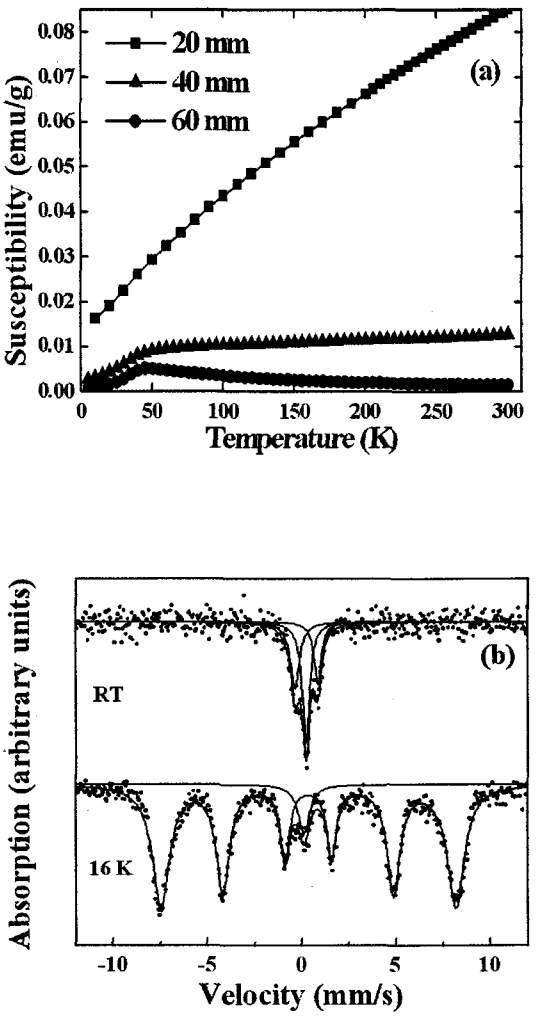

Fig. 3.3.2.3. Magnetic properties of Fe_2O_3 nanoparticles. (a) Susceptibility measured at 30 G for particles collected at different z, (b) Mössbauer spectra of ultrafine particles at room temperature and at 16 K. The solid lines are the least square fits to the experimental data.

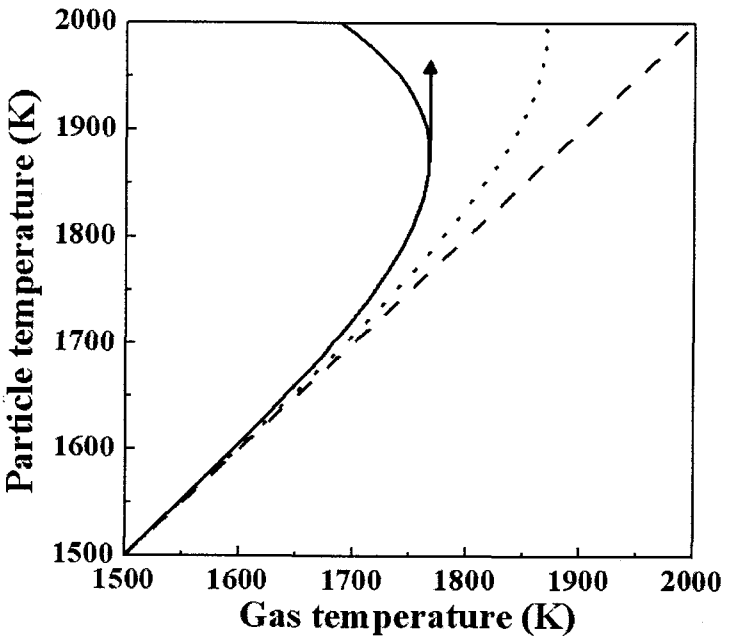

Fig. 3.3.2.4. The diagram of the particle temperature stability according to Eq. (3.3.2.1). The vertical arrow indicates the location of losing stability and the onset of the fragmentation for 20 nm particles. The dot line corresponds to 4 nm particles. The dashed line is the gas temperature shown for comparison.

3.3.3. Magnetism of oxygen adsorbed on carbon-shell particles

● Introduction

The study of magnetic properties of oxygen adsorbed on a surface has a long history. The interest particularly is caused by the ability of oxygen to create a magnetic phase at low temperatures cite (Tague, 1976; Nielsen, 1979, DeFotis,1981; Murakami,1996; Shibata,1998, Murakami1998). Being adsorbed on different substrates oxygen can form amorphous layers which are a convenient ground to test theoretical models describing magnetic systems. At the same time, despite many years of study of oxygen magnetism, many important aspects of its behavior remain open. So, for low oxygen coverage the careful measurements of oxygen magnetization are lacking. Note, that in the papers devoted to the study of magnetism of oxygen adsorbed on different substrates the main attention was paid to the study of the *M-T*curves (Gregory, 1977; Gregory, 1978; Gregory, 1981; Kbler, 1987; Kanoh, 1995; Kaneko, 1998; Tohdoh, 2001), which may bring only the general information on magnetic behavior. Such details as the characteristics of the oxygen spin-spin interaction and its interaction with the substrate could be extracted from peculiarities of the *M-H* curves at low temperatures appearing against paramagnetic saturation. However, such experiments have not been done yet. It isworth mentioning that for the analysis of the oxygen magnetization measurements the reliable information on the orientation distribution of oxygen molecular axes is needed. The best case for the analysis is the one when all the axes are parallel. However,such a case is unlikely achieved in the experiment due to the usual non-perfect parallelism of the adsorbing surfaces (Nielsen, 1979; Murakami, 1998). The possible tilt angle (as well as its distribution) of the oxygen molecule on the surface also leads to a lack of the oxygen axis parallelism. Another possible case, which can be analyzed, is realized at the random orientation distribution of the oxygen molecular axes. This is easily achieved at the random orientation distribution of the adsorbing surfaces.

In the present research we carefully investigate the magnetization of oxygen adsorbed on the surface of onion-like carbon nanoparticles at low oxygen coverage. These particles consist of contiguous graphitic shells (which are the ideal substrate for oxygen adsorption). The choice of the onion-like carbon nanoparticles for this research is caused by the particle purity and uniformity that is crucial for an analysis of the experimental results. Let us emphasize that the randomness of the graphitic shells orientations yields the randomness of the oxygen molecular axis orientations.

The onion-like carbon nanoparticles are synthesized utilizing the same experimental setup as we used to control the size, morphology, and crystalline phase of silica and titania nanoparticles during their formation in flames (Lee, 2000; Altman, 2001; Lee, 2001; Lee, 2002). The particles were generated as a result of the acetylene conversion in a co-flow oxy-hydrogen diffusion flame that is irradiated by the laser beam. The detail description of the particle synthesis is done in the other chapters. The transmission electron microscope (TEM) images of the particles are shown in Figure 3.3.3.1. As one can see in Fig. 3.3.3.1 the synthesized particles are identical in structure and do not have any impurities.

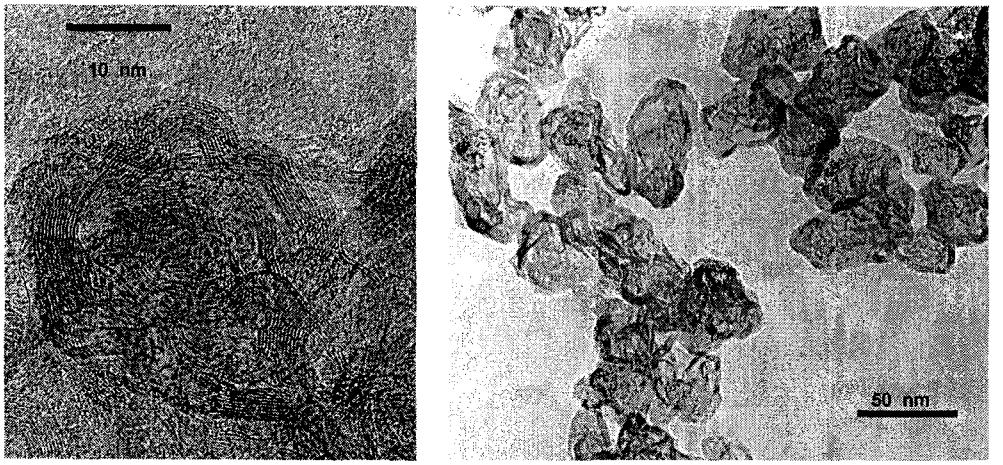

Figure 3.3.3.1. TEM images of the onion-like carbon nanoparticles.

● Methods

The magnetization of oxygen adsorbed on a substrate can be derived from the experimental data as follows. First, the magnetization of the substrate is measured in an applied magnetic field. Then it is subtracted from the magnetization of the same substrate having been exposed to some oxygen dose. The obtained difference is ascribed to the magnetization of adsorbed oxygen. In order to succeed such a procedure the accuracy of measurements should be very high, especially when low oxygen coverage is studied. However, if the sample is sealed in a container for the measurements (as is usually done), an imperfection of making the exactly same sealing for both cases (with and without oxygen) does not allow one to extract the oxygen magnetization unambiguously at least at low coverage. At the same time if the substrate is exposed to oxygen adsorption just inside the measuring system, then the problem related to the magnetization variation from a sealing substance disappears, and therefore, the additional magnetization coming from the adsorbed oxygen can be measured very precisely. Although the described method does not allow one to know the exact amount of oxygen adsorbed, the experimental data on oxygen magnetization at low coverage can be treated in a proper way described below.

Let us describe our experiment in detail. The magnetization measurements were carried out with a commercial SQUID (superconducting quantuminterference device) magnetometer (Quantum Design, MPMS 7). In order to adsorb oxygen on the surface of particles we utilized a device peculiarity of the SQUID system containing a little amount of oxygen inside the sample chamber due to a leakage. The carbon nanoparticles were put in a gelatin capsule attached to the transport rod by a straw. The mass of carbon nanoparticles in the experiment we report was m=16.22 mg. We found out that if such a sample is kept inside the SQUID at a fixed temperature rangedfrom about 55 K to about 100 K its magnetic moment at an applied magnetic field increases with time. At temperatures below 55 K the magnetic moment did not change with time. No change of the sample magnetic moment was found in the case when the gelatin capsule did not contain any carbon nanoparticles. We concluded that oxygen

precipitated on the capsule being a liquid at temperatures above 55 K could penetrate the gelatin capsule and be adsorbed on the surface of the carbon nanoparticles leading to the increase of the magnetic moment. At temperatures below 55 K the adsorption does not occur likely due to oxygen freezing. Then if the sample is maintained at a temperature above 55 K and then cooled down, the additional magnetic moment at low temperatures comes from the adsorbed oxygen. Since the magnetic moment before and after oxygen adsorption is measured for the same sample, the high precision in determination of the additional magnetic moment is easily achieved that allows one to study low oxygen coverage accurately.

We introduced the sample into the SQUID at about 5 K and measured its magnetic moment at the temperatures not exceeding 55 K, which was used as a reference value. Then the sample was heated up to 60 K and was maintained at this temperature for a different time to provide different oxygen doses adsorbed. After this the sample was cooled down and its magnetization was measured again. Subtracting the data we obtained *M-T* (magnetic moment vs. temperature) curves and *M-H*(magnetic moment vs. applied magnetic field) curves at the different temperatures for the magnetization coming from the adsorbed oxygen at different coverage values. Since we do not know the actual amount of oxygen adsorbed hereinafter we present data with the magnetic moment instead of the magnetization of adsorbed oxygen commonly used.

● Results and discussion

In order to demonstrate the occurrence of paramagnetic saturation we plotted in Figure 3.3.3.2 the *M-T* curves measured for the same oxygen dose at different magnetic fields (0.05 T and 7 T). The *M-T*curve at the low magnetic field is scaled for a comparison. As one can see at the low temperatures the magnetic moment at the high magnetic field is much smaller than that (being scaled) at the low magnetic field. It certainly comes from the paramagnetic saturation. Note that the low temperature part of the *M-T*curve at a low magnetic field can be represented by the Curie-Weiss law [$M=C/(T-\theta)$] with the Weiss temperature, -3 K, which is extracted from the linear *M-1-T* dependence (see theinset in Fig. 3.3.3.2). As one can see the Curie-Weiss dependence is violated at temperatures above about 12 K. The latter temperature is the same as that for the magnetic transition recently reported for mono- bilayer oxygen adsorbed on the graphite (Murakami, 1996).

For a careful analysis of the paramagnetic saturation we studied *M-H*curves measured at different temperatures for the same oxygen dose. The typical *M-H*curve at 2 K is shown in Figure 3.3.3.3. As we mentioned earlier we could not control the exact amount of oxygen coverage. At the same time it is clear, that, for instance, the value of the magnetic moment, M_0, at the maximal magnetic field H_0 (7 T in our experiment) increases with coverage increase. Then it can characterize the coverage. Moreover, we found out a scaling of the *M-H* curves, which means that after multiplication of the magnetic moment by a corresponding factor all *M-H* curves exactly coincide (see the inset in Fig. 3.3.3.3 where the data for minimal and maximal coverage are presented). It allows one to claim that $M(\xi)$ is proportional to the oxygen coverage. Since M_0 was varied in about 44 times in our experiment (from

0.00064 emu to 0.028 emu), then the oxygen coverage was also changed in the same manner. The absolute value of the coverage will be discussed below. The *M-H*curve shown in Fig. 3.3.3.3 exhibits a saturating trend at high magnetic field conventional for paramagnetic systems. Such a behavior might be described by the Brillouin (B_S) function as Vonsovskii, 1974

$$M=NgS\mu_B B_S(\xi), \qquad (3.3.3.1)$$

where N is the number of paramagnetic centers, g is their g-factor and S is the value of the spin; $\xi = gS\mu_B H/(k_B T)$, and k_B are the Bohr magneton and the Boltzmann constant. Hereinafter we use the value of g=2. The best fit to the experimental data (see Fig. 3.3.3.3) corresponds to S=0.032. So small a spin value of an oxygen molecule (which has unity spin in the ground state) is unrealistic even taking into account the spin reduction for a 2D oxygen system discussed elsewhere (Murakami, 1998). The fit with the value of S=1 is also presented in Fig. 3.3.3.3 for a comparison. The impossibility to fit the data with a realistic value of spin might be related to the occurrence of antiferromagnetic interaction in the system. In this case instead of the applied magnetic field H in Eq. (3.3.3.1) the effective one H_{eff} should be substituted in the expression for . Usually it is written as $H_{eff}=H-H_{int}$ with the interaction field (in the mean-field approximation) $H_{int}=\alpha M$.

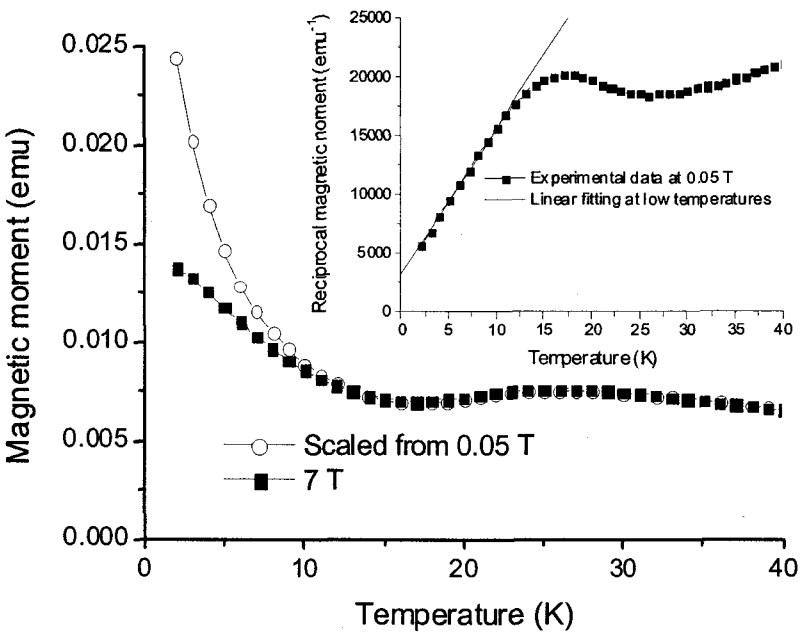

Figure 3.3.3.2. The *M-T* curves measured for the same oxygen dose adsorbed on carbon nanoparticles at different magnetic fields. The magnetic moment at 0.05 T is multiplied by 140 for an easy comparison. The inset shows the Curie plot for the magnetic moment at 0.05 T

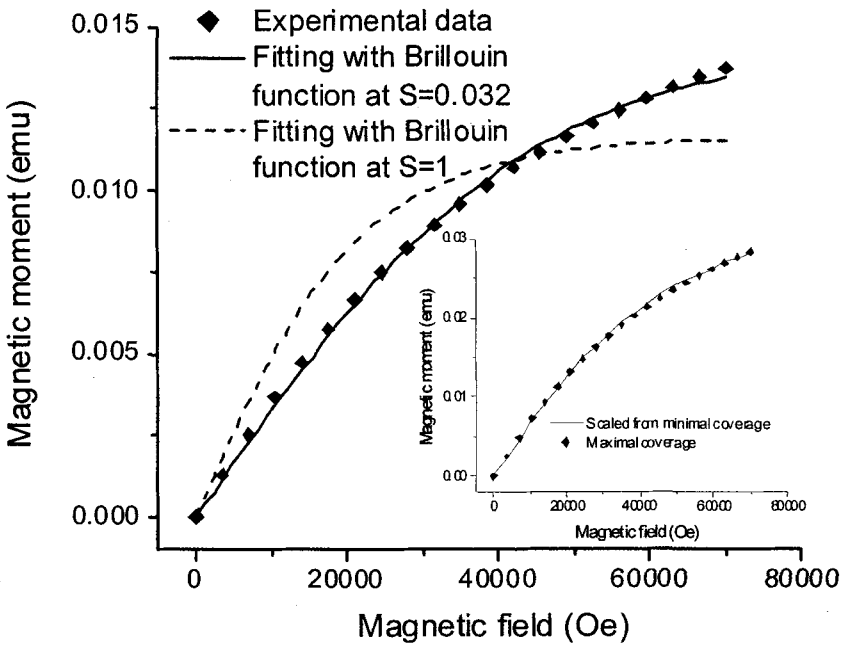

Figure 3.3.3.3. The typical M-H curve measured at 2 K for oxygen adsorbed on carbon nanoparticles. The different fittings are also presented. The inset demonstrates the scaling of the magnetic moment. The magnetic moment at minimal coverage is multiplied by the factor of 44 for a comparison.

Instead of finding out the constant that gives the best fit, we extracted the actual $H_{int}(M)$ dependence, which would lead to the *M-H*curves observed in the experiment. The idea we applied is very simple. It is illustrated in Figure 3.3.3.4 where the M-H curves at different temperatures are given. If Eq. (3.3.3.1) with H_{eff} works then the points with the same M but at the different temperatures correspond to the same values of H_{eff}/T. From the experimental data we can derive the values of H yielding the same magnitudes of the magnetic moment M at the different temperatures. Then due to the perfect linearity of H against T (see the inset in Fig. 4), the intercept of the $H(T)$ dependence at a certain value of $M$with Y-axis gives the value of $Hint$ at this value of the moment, while the slope of the dependence gives the value of H_{eff}/T. The $H_{int}(M)$dependence extracted in this way is presented in Figure 3.3.3.5. We are not aware of any model being able to give such a dependence of the antiferromagnetic exchange field upon the magnetic moment. We claim that the dependence in Fig. 3.3.3.5 is rather apparent than the real one. It likely comes from the incorrect consideration of the oxygen spin behavior made above.

Indeed, using Eq. (3.3.3.1) to fit the experimental data we implicitly assume that all oxygen molecules contributing to the magnetic moment have spins parallel to the magnetic field. It may be correct only in the case of free molecules. However, it is undoubtedly wrong in the case of oxygen molecules attached to the surface since the spin direction of an oxygen molecule is determined by its

molecular axis. Let us find out more realistic expression of magnetic moment.

In the case of the random distribution of the molecular axis directions the expression

$$\overline{B_S(\xi)} = \frac{\int_0^{\frac{\pi}{2}} B_S[\xi\cos(\theta)]\cos(\theta)\sin(\theta)d\theta}{\int_0^{\frac{\pi}{2}} \sin(\theta)d\theta} \qquad (3.3.3.2)$$

should be used in Eq. (3.3.3.1) instead of $BS(\xi)$. As one can easily see the averaging according to Eq. (3.3.3.2) leads to the reduction of the magnitude of the magnetic moment compared to that given by Eq. (3.3.3.1) at the same values of all the parameters. The reduction at a low magnetic field is 3 times while at a high magnetic field it is 2 times. We will discuss these numbers below. The fit using the $\overline{B_S(\xi)}$ function is given in Figure 3.3.3.6 showing much better agreement with the experimental data than the fit with the $B_S(\xi)$function.

Although the idea about the random spin distribution for non-interacting adsorbed oxygen molecules might explain the straightening of the experimental *M-H* curve compared with that for the free spins described by the $B_S(\xi)$ function, it does not fit the *M-H*curve in detail. Furthermore, the M-T dependence at the low magnetic field calculated using the expression $M=NgS\mu_B\overline{B_S(\xi)}$obeys the Curie law but not the Curie-Weiss one. It means that some additional assumptions are needed to match the experimental data (it would be possible if the fitting function is more straightened than the one with S=1).

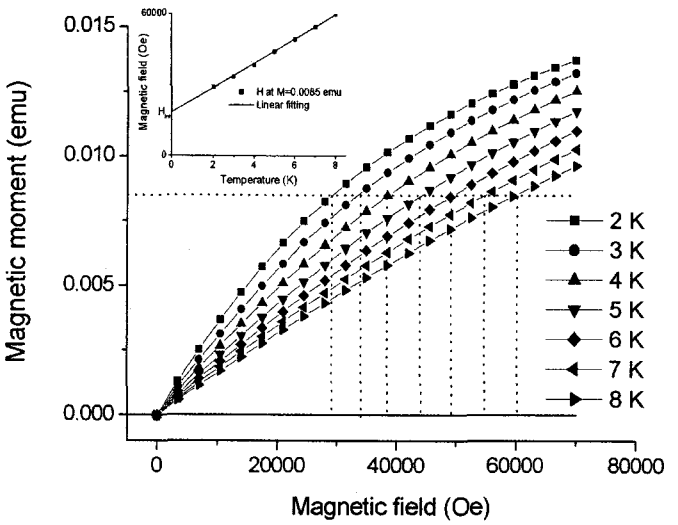

Figure 3.3.3.4. The *M-H* curves measured at different temperatures for oxygen adsorbed on the carbon nanoparticles. The procedure of the extraction of the $H_{int}(M)$ dependence with the assumption of the strong antiferromagnetic interaction in the system (see text) is illustrated. The inset demonstrates a possibility of the procedure suggested.

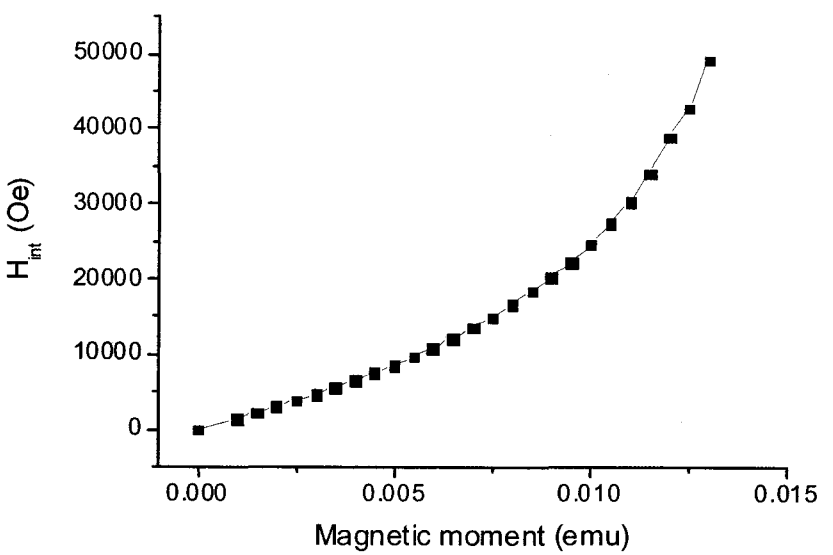

Figure 3.3.3.5. The $H_{int}(M)$dependence extracted from the experimental *M-H*curves at different temperatures for oxygen adsorbed on the carbon nanoparticles with the assumption of the strong antiferromagnetic interaction in the system (see text).

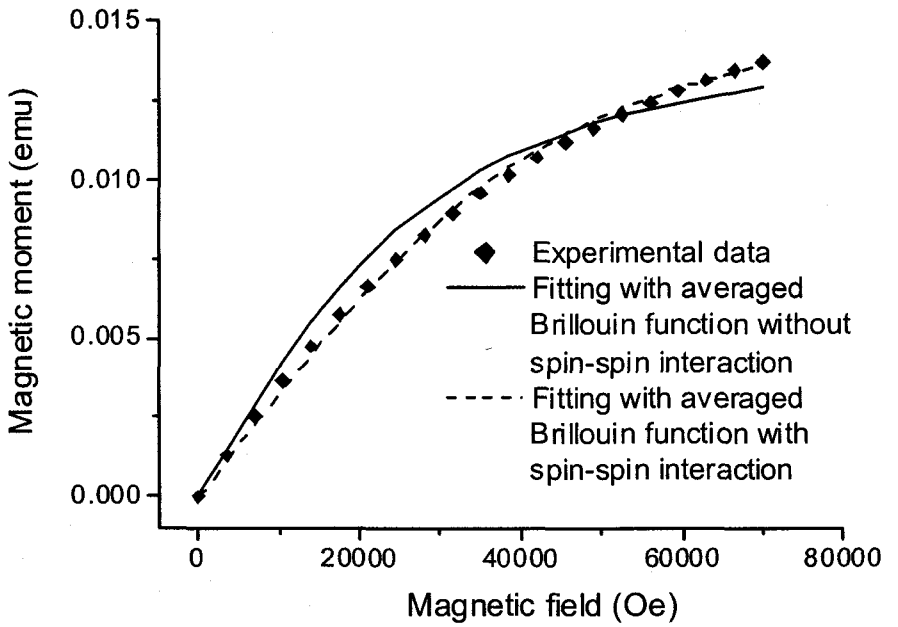

Figure 3.3.3.6. The typical *M-H* curve measured at 2 K for oxygen adsorbed on the carbon nanoparticles. The fittings using the averaged Brillouin function with and without spin-spin interaction are also shown.

In order to improve the fitting we may introduce a spin-spin interaction. The spin Hamiltonian can be expressed as

$$\hat{H}_{\text{int}} = -2\sum_{i>j} J_{ij}\overrightarrow{S_i}\overrightarrow{S_j} \qquad (3.3.3.3)$$

It is worth noting that in the system like ours the rigorous description of the spin-spin interaction is clumsy even for neighbor spins. The latter comes from the non-parallelism ofthe oxygen molecules due to the tilt angle on the surface. Since we want only to check the influence of the spin-spin interaction on the fitting but not to fit the experimental data precisely we can limit ourselves by the simplest case of the interaction of the nearest neighbor spins considering them as the parallel ones. In the latter case the product can be easily calculated. Then taking into account $\hat{H}_{\text{int}}$ for the system with S=1 we obtain the following expression for the magnetic moment at the random spin

$$M(H,T) = NgS\mu_B \frac{\int_0^{\pi/2} M_\theta(H,T)\sin(\theta)d\theta}{\int_0^{\pi/2}\sin(\theta)d\theta}, \qquad (4)$$

distribution choosing J_{ij}=J=const:

where,

$$M_{\theta}(H,T)=\frac{2\left[\sinh\left(\frac{4\mu_B H\cos(\theta)}{k_B T}\right)\exp\left(\frac{-A}{T}\right)+\sinh\left(\frac{2\mu_B H\cos(\theta)}{k_B T}\right)\cosh\left(\frac{A}{T}\right)\right]\cos(\theta)}{2\cosh\left(\frac{4\mu_B H\cos(\theta)}{k_B T}\right)\exp\left(\frac{-A}{T}\right)+4\cosh\left(\frac{2\mu_B H\cos(\theta)}{k_B T}\right)\cosh\left(\frac{A}{T}\right)+2\cosh\left(\frac{A}{T}\right)+\exp\left(\frac{2A}{T}\right)} \quad (5)$$

and A=$-2J/k_B$.

As one can see at A=0 the magnetic moment given by Eq. (3.3.3.4) exactly coincides with that following from Eq. (3.3.3.1) using the $\overline{B_S(\xi)}$ function instead of the $B_S(\xi)$ one at S=1. The use of Eq. (3.3.3.4) at A=0.9 K allows one to improve the fit of *M-H* curve significantly (see Fig. 3.3.3.6). The sign of A corresponds to the antiferromagnetic interaction. Then the introduction of the antiferromagnetism explains the observed Curie-Weiss temperature dependence of the magnetic moment. It is worth noting finally that the straightening of the *M-H*curves due to the random distribution of the spin directions is much stronger than that coming from the spin-spin interaction.

The specific surface area of the carbon nanoparticles, a_S, estimated from the TEM image is about 100 m^2/g. Using Eq. (3.3.3.4), which fits the experimental *M-H* curves we can extract the number of the oxygen molecules, N, contributing to the magnetic moment. Then the oxygen coverage, (ρ) represented as

$$\rho=\frac{N}{ma_S\times 6.36\cdot 10^{18}} \quad (3.3.3.6)$$

can be easily calculated. The factor 6.36×10^{18} (molecules/m^2) in the denominator in Eq. (3.3.3.6) characterizes the density of $\sqrt{3}\times\sqrt{3}$ oxygen structure. We found out that in our experiment the oxygen coverage calculated according to Eq. (3.3.3.6) varied from about 0.0077 to about 0.34 while its value at the state shown in Figs. 3.3.3.2-4,6 was about 0.165. We have to reiterate that at the low temperatures both *M-H* curves and *M-T* curves exhibited scaling at different coverage.

Our experiment undoubtedly demonstrates the randomness of the spin directions of the oxygen molecules adsorbed on the surface. Then the geometrical averaging reduces the Curie constant of such a system compared to that for the free spins. The reduction is about 3 for not very high magnitude of the applied magnetic field. Such a reduction could be distinguished even in the previous papers devoted to the study of the magnetization of adsorbed oxygen (Gregory, 1977; Kanoh, 1995) if the low temperature susceptibility were {carefully examined. Then a comparison of the Curie constant for adsorbed oxygen with that for free spin oxygen (but not with the reduced value) that had been done in the recent papers on the oxygen magnetization has no sense.

The found scaling of the *M-H*curves (which means an independence of their shape on the

coverage) comes from an independence of spin-spin interaction on the coverage, i.e. on the distance between the oxygen molecules. It leads us to infer that the spin-spin interaction between the oxygen molecules does not occur directly but is likely realized via a substrate. The weakness of the constant A needed in order to match the experimental dependence supports this suppose. In this case the constant of the spin-spin interactionshould depend on the substrate substance. In order to check such a hypothesis we additionally examined two substrates, namely, multi-walled carbon nanotubes (MWNT) and MgO nanoparticles, which also may provide the randomness of the oxygen molecular axis orientations. The magnetization of oxygen adsorbed on MWNT did not show any difference from that for the carbon nanoparticles while some dissimilarity was found in the case of oxygen adsorbed on the MgO nanoparticles confirming our assumption.

The Weiss temperature for oxygen adsorbed on the MgO nanoparticles was found from the *M-T* curve to be about -2 K unlike the value of -3 K for oxygen on the carbon nanoparticles. The $M-H$ curves for both cases (oxygen on carbon and oxygen on MgO) are shown together in Figure 7 clearly exhibiting the difference. The magnetization curve described by the expression $M=NgS\mu_B\overline{B_S(\xi)}$ is also plotted in Fig. 3.3.3.7 for a comparison. All the curves are scaled to the same value of M_0. The fitting of the *M-H* curves for the MgO case (see Fig. 7) gave us the value of A=0.5 K unlike the value of A=0.9 K for carbon. We have to remind that the curve $M=NgS\mu_B\overline{B_S(\xi)}$ corresponds to zero value of the constant A. It is worth noting that the absolute values of the constant of the spin-spin interaction are in agreement with the values of the Weiss temperatures, i.e. the absolute value of the Weiss temperature increases with the A increase.

Although Eq. (3.3.3.4) perfectly fits the experimental *M-H* dependence at a given temperature it fails to fit the *M-T*dependence at a given applied magnetic field in detail. So, the ratio M_0(2 K)/M_0(8 K) extracted from the experiment with oxygen on the carbon nanoparticles is about 1.42 while its value obtained using Eq. (3.3.3.4) is about 1.97. We believe that this discrepancy likely comes from the spin reduction effect known for the 2D oxygen system (Murakami, 1998).

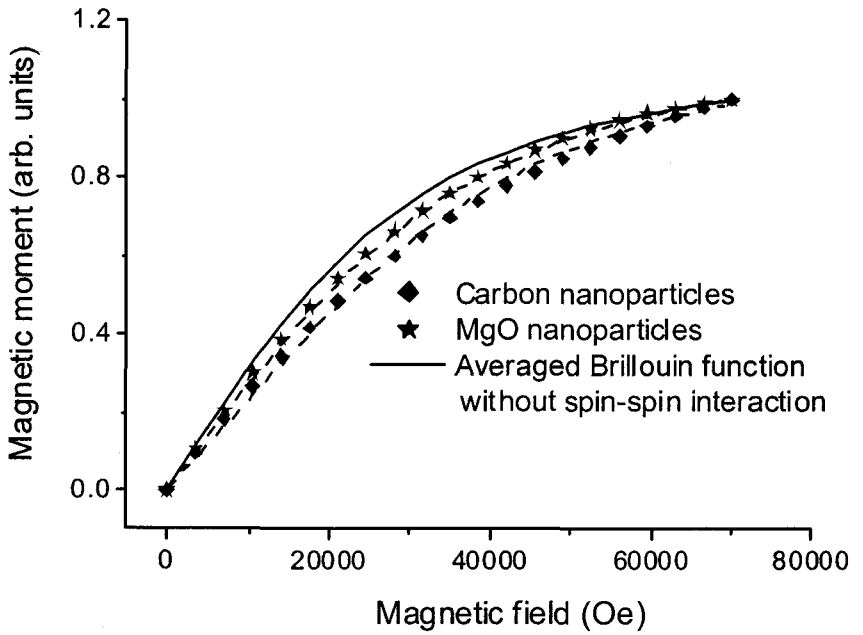

Figure 3.3.3.7. The typical *M-H* curves measured at 2 K for oxygen adsorbed on the carbon nanoparticles and on the MgO nanoparticles. The dashed lines fit the *M-H*curves using the averaged Brillouin function with spin-spin interaction. The averaged Brillouin function without spin-spin interaction is plotted for a comparison.

Indeed, the magnitude of the spin reduction (and therefore the spin itself) may depend on the temperature yielding some temperature dependence of the value considering as the constant in Eq. (3.3.3.4). However, the analysis of this spin reduction lies beyond the scope of the present research.

Summarizing, we found an intriguing behavior of the magnetic moment of oxygen adsorbed on different substrates at very low coverage. The analysis of corresponding *M-H* and *M-T*curves led to a conclusion that it is an interplay between the substrate orientation of the oxygenmolecules and a weak antiferromagnetism of unit spins occurring via the substrate that shows such a behavior. This conclusion brings in the idea that the interaction of the oxygen molecules with the substrate (being neglected in previous work) plays a crucial role (at least at low coverage) on the physical properties of the system.

3.3.4. Defect formation in SiO_2 nanoparticles

● Introduction

Silica nanoparticles are interesting due to their important technical applications in electronic and optical nanodevices. Structural defects formed on the surface of nanoparticles are particularly important since the surface defects influence the performance of the devices.

In bulk SiO_2 based material, the surface defects are well known and already extensively studied. In particular, the surface defects are mainly determined by the content and properties of hydroxyl groups (silanols) on the surface. The EPR spectrums on the surface of activated silica or -quartz have been observed to be similar but not identical to those in the bulk crystal. It has been shown that the electronic and optical properties of silica nanoparticles are different from those of the surface in bulk materials, through experiments on lightabsorption. The mechanism of defect formation was proposed from the experimental studies of the photoluminescence from hydrogen-related defects in silica nanopaticles and the laser-induced defects in silica glasses. However, the defect states of silica nanoparticles are rarely studied in theoretical side and are not clear. The characterization and control of the intrinsic and laser-induced defects should be theoretically studied to show how topological disorder and defects influence the properties of silica nanoparticles. The introduction of hydrogen has strong effects on the electronic structure. Because of the technical importance, to understand the role of hydrogen in silica nanoparticles is interesting. The optical excitation of materials leads to a change of electronic structure in the ground state. The study of the exciton-induced relaxation could provide the proper understanding of the ground states. The defects formed due to electronic excitation are also of profound importance for various silica-based applications. It is interesting to analyze the spatial localization of the defect states, whether they can be attributed to dangling bonds on the surface and structural defects in the core of the nanoparticles. In the present research, we explored defect states of SiO_2 nanoparticles using plane-wave density functional theory. The different types of defects, which are dangling bonds, high-fold coordinates, hydrogen atoms, and vacancy of O atom, were studied. The structural defects lead to narrowing of band gap and formation of localized states within band tail (Urbach tail), which were experimentally measured in light absorption of silica nanoparticles. We discuss the effects due to size, morphology, and different types of defects of nanoparticles on the minimum energies and electronic and optical properties. The introduction of hydrogen atoms removes the defect states near the Fermi level and increases the width of the gap energy. The relaxation under the O atom vacancy also leads to removing the defect states near the Fermi level and increasing the gap energy. We study the way in which hydrogen content and different types of defects influence the band tail and the morphology. These defects formed in nanoparticles are compared with the mechanism of defect states proposed from the experimental studies of the photoluminescence from hydrogen-related defects in SiO_2 nanoparticles and the laser-induced defects in silica glasses. The defect states of nanoparticles are also compared with those in the bulk and on the surface. The study of defect states formed in nanoparticles can provide possible mechanism for chemical processes to occur

on the surface of nanoparticles during formation. The characterization and control of the defects in nanoparticles are thus important for the generation of nanoparticles.

● Methods

The DFT calculations were carried out using VASP. VASP is a plane-wave DFT code based on the local-density approximation (LDA) and generalized gradient corrections (GGC) using the Perdew-Wang 91 (PW91) functional. In addition, the ultrasoft Vanderbilt pseudopotential (USPP) and spin polarization were used. The energy cutoffs were 20 Ry for the wave functions and 41 Ry for the augmented electron density. Our calculations were done on 12-46 molecule cells with a 10 Åvacuum size. The effects of an increased thickness of the vacuum have been tested and found to be small. The Brillouin zone of the cell was sampled only at the point. Additional k-points were found to have an insignificant effect on both the structure and the relative energy. Optimization of the structures was carried out using an iterative conjugate gradient minimization scheme. The DFT calculations underestimate the band gap energies when compared with experimental estimates. However, spin polarized DFT calculations have been studied to satisfactorily represent both the geometrical structures and relative energy of different configurations for localized states by comparing DFT, HF, MP2, and CAS-SCF calculations.

In order to find fully reconstructed structures for silica nanoparticles, we used a combination of empirical and DFT-GGC techniques. For the compact type of structures, we start with perfect and amorphous bulk systems and cut the systems to get nanoparticles of three different sizes including 12-, 24-, and 45-molecules with 10 Åvacuum size in three dimension for an annealing procedure. We melted the nanoparticle by heating it up to 3000 K, 2700 K, 2500 K, 2300 K, 2000 K, and 1000 K for 10000 ps using classical molecular dynamics with a BKS potential, independently. The temperature was then slowly decreased to 0 K. The final structures were then fully relaxed within the DFT-GGC. The nanoparticles were allowed to relax until the interatomic forces were smaller than 0.001 eV/Å. For each nanoparticle size, the different configurations are ordered by their energies per molecule and the low energy isomers are considered. On the other hand, the elongated type of structures are obtained by sintering of nanoparticles. As starting point configuration, we use the lowest energy structures of spherical type of nanoparticles, 6-, 12-, and 24-molecules, for the different sizes, respectively. The replicate nanoparticles are placed in contact with one another, i.e., at a distance of approach equal to the nearest-neighbor distance and melted at 3000 K, 2000 K, and 1000 K for 60000 ps using classical molecular dynamics with a BKS potential, independently. The temperature was then slowly decreased to 0 K. The final structures were then fully relaxed within the DFT-GGC until the interatomic forces were smaller than 0.001 eV/Å. The different configurations are ordered by their energies per molecule and the low energy isomers are considered for each nanoparticle size, respectively.

● Results and discussion

The geometrical structures of low energy isomers of SiO_2 containing 12 molecules formed by different types of defects are shown in Figure 3.3.4.1. The elongated type of structure, given by Figure 3.3.4.1(a), is the most energetically stable one we found. It was found that the structural transition from elongated to spherical types of structures occur at a size of around 38 molecules. As indicated in Table 3.3.4.1, Figure 3.3.4.1(a) consists of three dangling bonds of O atoms, one dangling bond of Si atom, four overcoordinated Si atoms, and two overcoordinated O atoms. Figure 3.3.4.1(b) consists of two dangling bonds of O atoms, eight overcoordinated Si atoms, and two overcoordinated O atoms. The defects of Figure 3.3.4.1(c) are four dangling bonds of O atoms, one dangling bond of Si atom, seven overcoordinated Si atoms, and two overcoordinated O atoms, while those of Figure 3.3.4.1(d) are only four overcoordinated Si atoms. The band gap energies are 2.5, 1.0, 1.4, and 2.9 eV, respectively. The presence of overcoordinated atoms leads to the formation of defects around the Fermi energy. As can be seen, the number of these localized defect states around the Fermi energy increases with increasing defect concentration due to the overcoordinated atoms, leading to the narrowing of the band gap energy. Note that DFT cannot be expected to give accurate band gap energies, but it can clarify their trends. The structures are minimized by forming double bonds from the dangling bonds so the introduction of dangling bonds causes little change in the localized states in the vicinity of the Fermi energy.

The double bond is shorter bond length (approximately 1.48 Å) than that of single bond (approximately 1.61 Å). These defects could react with atomic or molecular hydrogen, leading to the hydrogen-associated defect centers observed in EPR and IR spectra. Figures. 3.3.4.1(b), (c), and (d), which are spherical type of structures, have energies approximately 0.1, 0.25, and 0.28 eV per molecule higher than that of the most stable structure (Fig. 3.3.4.1(a)), respectively. It was found that for the spherical type of structures the more spherical and compact the nanoparticles, the more stable the structure. Most defects formed in SiO_2 isomers containing 12 molecules consist of dangling bonds on O/Si atom and high-fold coordination due to Si-Si bonds and overcoordinated O atoms. These defects are the main intrinsic structural defects formed in high-purity silica.

The density of states (DOS)characterizes the electronic and optical properties, in particular, the defect states locate around the Fermi level. Figure 3.3.4.2 displays the DOS of the spherical type of SiO_2 containing 12 molecules (Figure 3.3.4.1(b)) with different hydrogen concentrations. The introduction of hydrogen atoms removes the defect states near the Fermi level in both the valence and conduction bands. The defect concentration in hydrogenated silica nanoparticles is drastically reduced according to the concentration of hydrogen atoms. The width of the gap energy is increased with an increasing hydrogen concentration. The hydrogen atoms form hydrogen-associated species on the surface of the nanoparticles such as Si-H and/or Si-OH in order to block the surface defects with respect to the adsorption-desorption process. In particular, the introduction of the hydrogen atoms removes Si-Si bonds as the structure is reconstructed. Our results indicate that hydrogen adsorption significantly alters the electronic structures and modifies the properties of the nanoparticles. In

particular, passivation of the dangling bonds associated with the surface states of nanoparticles could strongly influence the electronic and optical properties of nanoparticles. The different types of defects including vacancy of O atom have also been studied in Figure 3.3.4.2. As can be seen, the relaxation under the O atom vacancy also leads to removing the defect states near the Fermi level and increasing the gap energy. The remove of O atom from the system leads to the structure fully reconstructed. The ground state (singlet state) structure of the Figure 3.3.4.1(b) was relaxed under the triplet state of electronic excitation. The exciton-induced relaxation leads to two self-trapped exciton states (STEs) shown in Figure 3.3.4.1. In Figure 3.3.4.3(a), the triplet state of exciton is localized at O atom by stretching the Si-O double bond with the displaced O-atom, leading to a dangling bond from the double bond.

The Figure 3.3.4.3(b) shows that the exciton is localized at Si atom by forming dangling bond with the displaced Si-atom. These exciton-induced structures of SiO_2 nanoparticles are very similar to those in the bulk. It has been shown that the relative energy of different structures and the singlet/triplet splitting for the STEs in silica clusters are represented quite well by the spin polarized DFT calculations. The Si displaced structure has an energy lower by 1.3 eV than theO displaced one, while the Si displaced structure has a similar energy with the O displaced one in the bulk. The excess spin density is localized mainly on the one dangling bond and one double bond of O atoms and on the two double bonds of O atoms and one dangling bond of Si atom, respectively.

If an electron is removed or added, the positively or negatively charged system is obtained. The fully reconstructed structures with the positively and negatively charged states are shown in Figures 3.3.4.4(a) and (b), respectively. Compared to the exciton-induced structures, the geometrical configuration with the positively charged state is very similar to the O-displaced structure formed under exciton-induced relaxation. A valence hole is trapped at O atom by forming a dangling bond from the double bond. On the other hand, the configuration with the negatively charged state is very similar to the Si-displaced one formed under exciton-induced relaxation. An excess electron is trapped at the Si atom, leading to Si dangling bond.

The size of nanoparticles plays an important role in the electronic and optical properties because of the large surface area via the volume. Here it would be interesting to see how the size of nanoparticles influences on the geometrical structures and the bonding energy per molecule. Figures 3.3.4.5(a), (b), and (c) show the local minimum structures of SiO_2containing 12 molecules, 24 molecules, and 45 molecules, respectively. The bonding energy per molecule in 45 molecules of SiO_2 is lower by 0.8 eV than that of 12 molecules and lower by 0.4 eV than that of 24 molecules of SiO_2. The size of silica nanoparticles, in which the bonding energy per molecule in the nanoparticles is close to that of the bulk materials, can be obtained from the trends of the bonding energy as a function of the size. This estimation leads to the critical size of nanoparticles to present the electronic and optical properties different with those of bulk materials. We analyse the spatial localization of the defect states of the spherical and elongated types in 45- and 46-molecules of SiO_2, respectively, whether they can be attributed to dangling bonds on the surface and structural defects in the core of the

nanoparticles. For the spherical case, in order to remove the structural defects in the core of the nanoparticles, we start with perfect bulk system containing 45 molecules. We melted the nanoparticle by heating it up to 2000 K for 20000 ps using classical molecular dynamics with a BKS potential. The temperature was then slowly decreased to zero keeping freezing the core atoms. The structure was fully relaxed within DFT, all of the atoms being allowed to relax. The core region is a crystalline bulk like structure and the surface atoms are reconstructed. The comparison of different types of defects between the spherical without and with the crystalline core are listed in Table 3.3.4.2.

For the crystalline core structure, the high-fold coordination defects due to Si-Si bonds in the core structure decrease, whiles the dangling bonds on the surface increase. Figures 3.3.4.6 demonstrates how different types of defects influences the electronic properties only in the vicinity of the Fermi level. For the spherical type of 45-SiO_2, the introduction of two hydrogen atoms removes the dangling bonds, leading to removal of localized states near the Fermi level. Due to the increase of the dangling bonds on the crystalline core structure, the defect states near the Fermi level increase despite of the decrease of high-fole coordinate defects. All remove of the dangling bonds in the crystalline core structure leads to increasing of the gap energy and decreasing of the defect states near the Fermi level. For the elongated case, the introduction of two hydrogen atoms reconstruct the edge sites, top and bottom of the structure, leading to decreasing of high-fold coordinates and removal of dangling bonds. This results in increasing of the gap energy and decreasing of the defect states near the Fermi level (see Figure 3.3.4.7).

Defect states of SiO_2 nanoparticles were presented using plane-wave density functional theory. The different types of defects such as coordination defects, hydrogen atoms, and vacancy of O atom were studied. The exciton-induced defects were also investigated. The structural defects lead to narrowing of the band gap and formation of localized states within band tail (Urbach tail), which were experimentally measured in light absorption of silica nanoparticles. We investigated the effects due to size, morphology, and different types of defects of nanoparticles on the minimum energies and the electronic and optical properties.The density of states characterizes the electronic and optical properties, in particular, the defect states located around the Fermi level. The introduction of hydrogen atoms removes the defect states near the Fermi level and increases the width of the gap energy. The relaxation under the O atom vacancy also leads to removing the defect states near the Fermi level and increasing the gap energy. We discuss how hydrogen content and different types of defects influence the band tail and the morphology.

Table 3.3.4.1. Properties of low energy isomers of SiO_2 containing 12 molecules

	(a)	(b)	(c)	(d)
Total energy (eV)	0.00	0.10	0.25	0.28
Gap energy (eV)	2.5	1.0	1.4	2.9
Dangling bonds of O atom	3	2	4	0
Dangling bonds of Si atom	1	0	1	0
Overcoordinated O atom	2	2	2	0
Overcoordinated Si atom	4	8	7	7

Table 3.3.4.2. Properties geometrical structures containing 45 molecules

	spherical	spherical with frozen core
Total energy (eV)	0.0	0.2
Dangling bonds of O atom	2	7
Dangling bonds of Si atom	0	2
Overcoordinated O atom	3	3
Overcoordinated Si atom	17	14

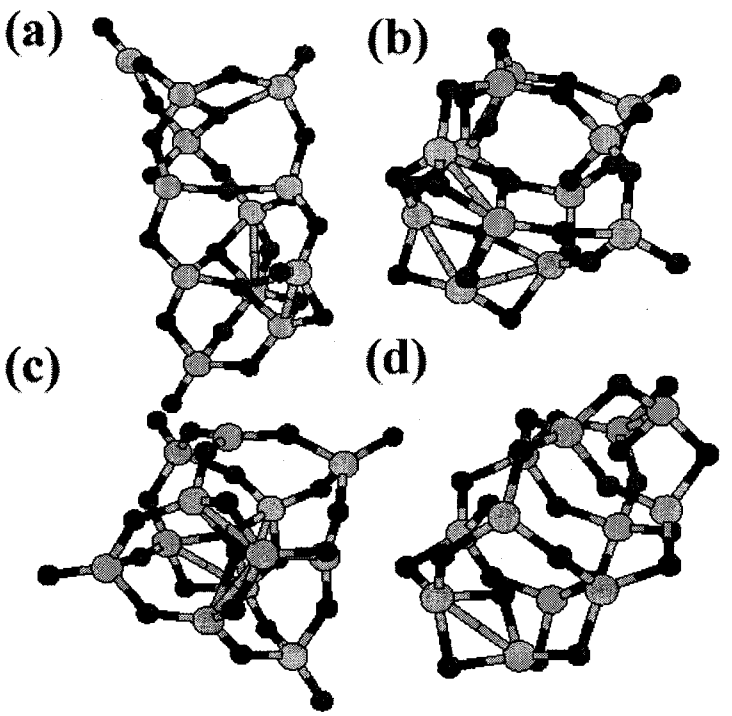

Figure 3.3.4.1 Geometrical structures of low energy isomers of SiO_2 containing 12 molecules;(a) is the elongated type of structure and (b), (c), and (d) are the spherical type of structures f ormed by different types of defects.

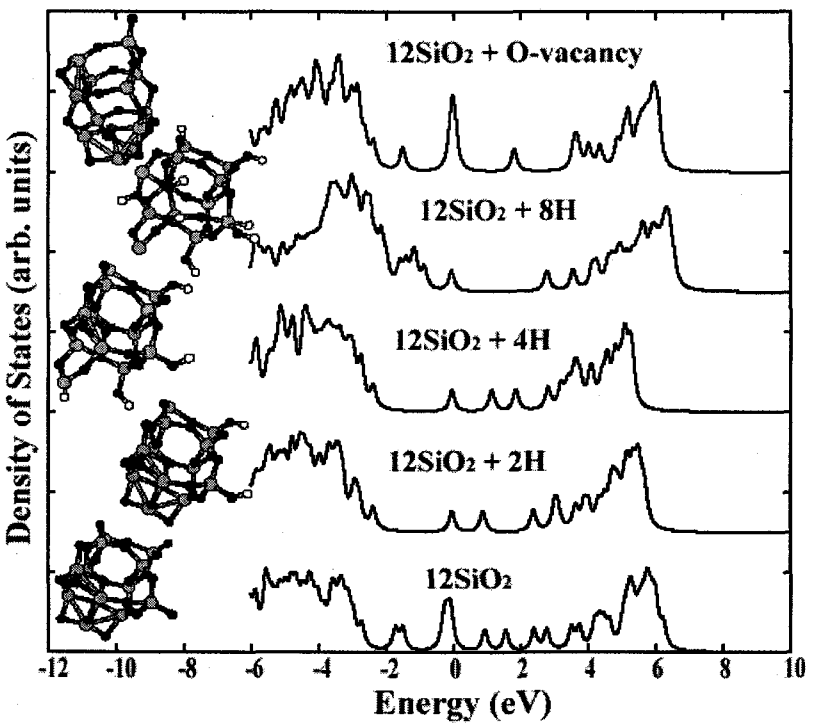

Figure 3.3.4.2. DOS of the spherical type of SiO_2 containing 12 molecules (Figure 3.3.4.1(b)) with different hydrogen concentrations.

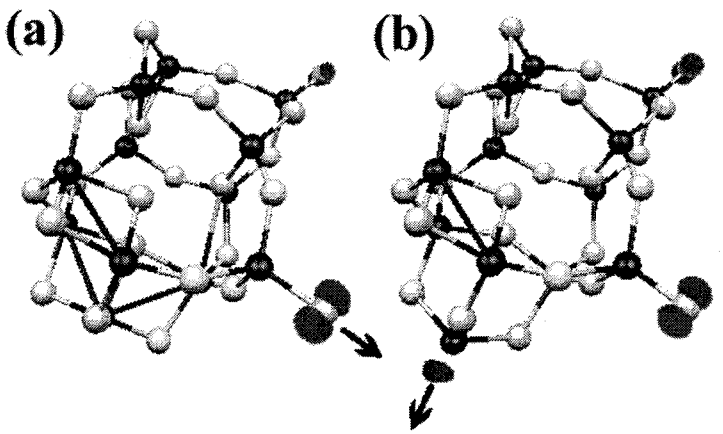

Figure 3.3.4.3 Exciton-induced relaxation; (a) triplet state of exciton is localized at O atom by stretching the Si-O double bond with the displaced O-atom;
(b) the exciton is localized at Si atom by forming dangling bond with the displaced Si-atom.

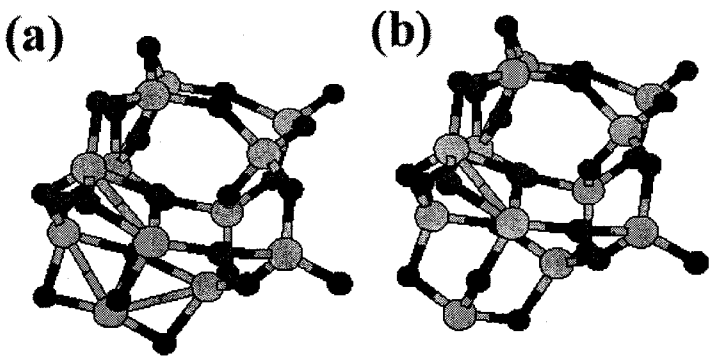

Figure 3.3.4.4. Fully reconstructed structures with (a) positively and (b) negatively charged states.

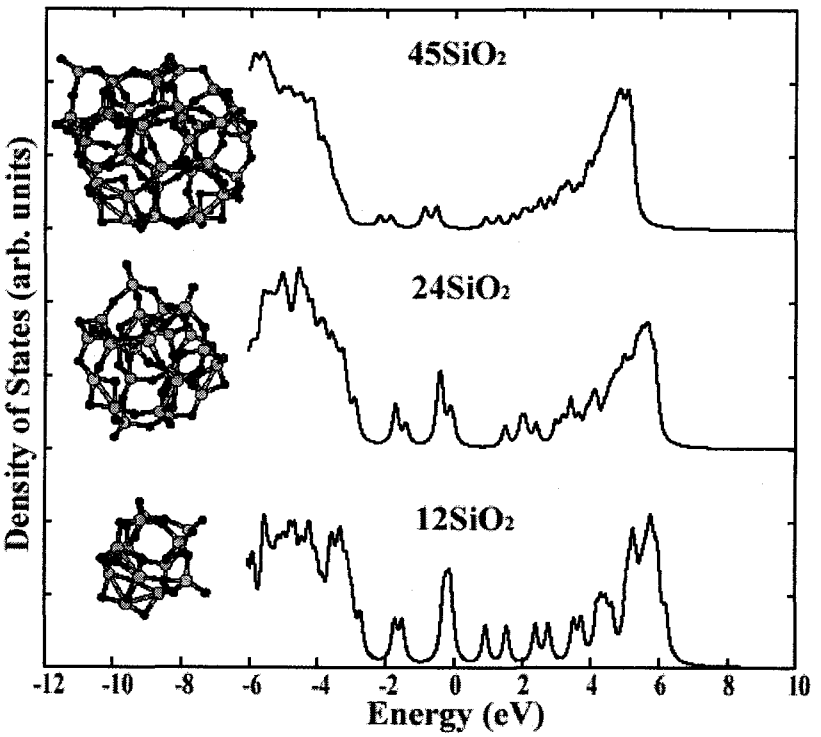

Figure 3.3.4.5. Local minimum structures of SiO_2 containing (a) 12; (b) 24 and (c) 45 molecules

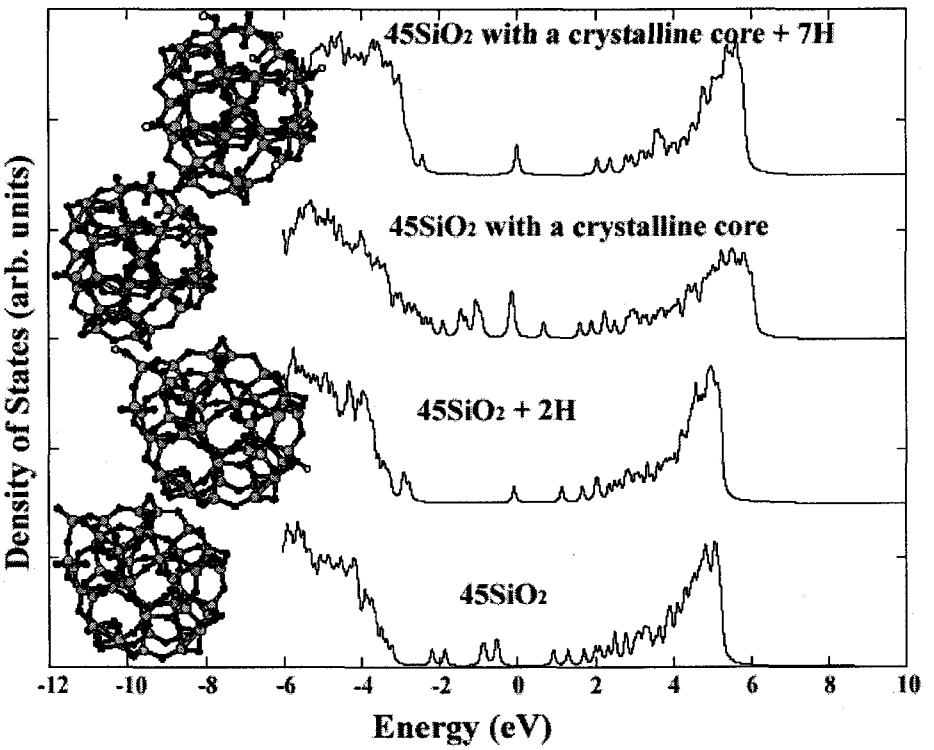

Figure 3.3.4.6. Electronic properties of different types of defects.

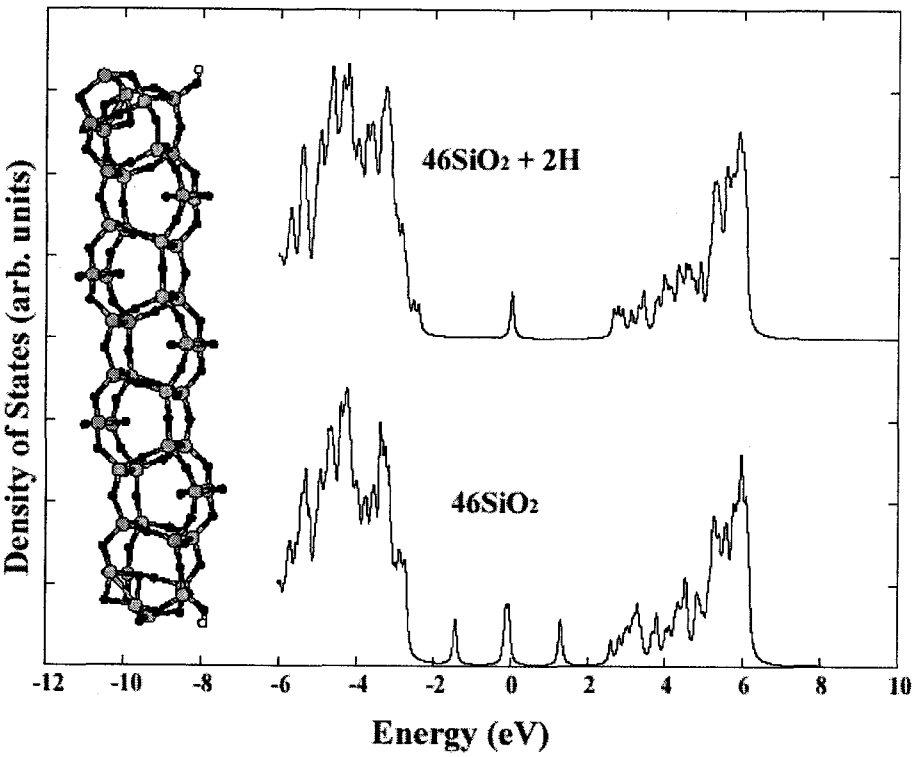

Figure 3.3.4.7. Defect influence on the gap energy.

Chapter 4. Conclusions

We have established new control strategies for nanoparticle generation and growth, developed new theoretical and experimental methods for non-spherical nanoparticle growth, and explored unknown fundamental phenomena related to particle generation, growth, and relevant heat/mass transfer.

● Development of new control strategy for nanoparticle generation and growth

Coalescence Enhanced Synthesis using CO_2 laser beam irradiation was applied to SiO_2/TiO_2 composite nanoparticles in flame. We found that the size and morphology of SiO_2/TiO_2 particles can be successfully controlled by the present method. SiO_2/TiO_2 nanoparticles with non-uniform morphology were transformed to uniform, spherical and small-sized particles by irradiating CO_2 laser at the early stage of particle formation. In addition, we showed that crystallization of SiO_2/TiO_2 nanoparticles can be controlled by the present method. X-ray diffraction spectroscopy, TEM, FT-IR spectroscopy and Raman spectroscopy confirmed that crystallization occurs with CO_2 laser irradiation. Several possible reasons are investigated and the coordination of TiO_2 domain by CO_2 laser irradiation is considered to be the reason for the crystallization. There has been no report so far on the *in-situ* controllability of the structural properties of nano-sized SiO_2/TiO_2 particles in flame and this finding may imply that continuous acquisition of multi-component nano-particles with changing structural property could be possible.

We observed a new, unknown pathway of acetylene conversion into carbonaceous particulate that is totally different from a conventional mechanism of amorphous soot formation. The distinctive feature of this pathway is a direct graphitization occurring on the surface of a growing particle within acetylene instead of conventional "mechanical" addition of acetylene and polycyclic aromatic hydrocarbons (PAHs) leading to generation of amorphous soot. It is the CO_2 laser irradiation that switches the regimes of particle generation. Unlike the usual process of the industrial synthesis of nanocarbons the shell-shaped carbon nanoparticles generated in our system with sufficiently high rate (about 100 mg/min according to our estimate) have no need in any additional purification. This determines a possible industrial interest to the process we described besides the pure scientific interest related to the critical phenomenon observed in the present research.

We extended our earlier work of a novel jet assisted aerosol chemical vapor deposition (CVD) method to multi-component deposition of SiO_2/GeO_2. It was found that the deposition efficiency of present method was enhanced with increasing jet temperature and jet flow rates compared to that of conventional method.

Isolated and non-agglomerated nanoparticles (SiO_2, TiO_2 and ZrO_2) were successfully generated using an electrospray assisted CVD method. The present ES-CVD method is believed to be a useful method for the synthesis of non-agglomerated and unipolarly charged nanoparticles for further

applications.

We report for the first time the observation of zero-phonon lines (ZPLs) originating from electron transitions of Mn^{2+} ion in MgO matrix. These lines were observed in macroscopic photoluminescence (PL) from nanocrystals synthesized by combustion. To our best knowledge this is the first observation of extremely sharp emission lines from nanocrystals. We believe that the combustion of nanocrystals can be utilized in optical nanodevices due to extraordinary discreteness of the system energy levels with the performance better than that of QDs. It can be a breakthrough in optical nanoelectronics taking into account the recently reported carbon nanotubes-MgO circuitry that can provide a local access to optical elements of nanoscale.

We fabricated considerably uniformly structured stamps, and thus, achieved robust nanoparticle patterns with the resolution of 500 nm, through a parallel deposition process. Charge patterns were transferred on an electret film of the substrate by contacting a metal-coated PDMS stamp, and then, charged monodisperse nanoparticles in gas phase were deposited on the substrate. To reduce cracks produced during the metallization of the stamp, metal coating of the stamp were carried out by a sputter method.

- **Development of new theoretical and experimental method for non-spherical nanoparticle growth**

We developed the sectional model coupled with detailed fluid dynamics calculations for analyzing the growth of non-spherical, polydispersed particles in the two-dimensional tubular furnace reactor. The spatially two-dimensional approach was found to produce detailed local information on the size distributions of polydisperse non-spherical particles in a tubular reactor. Non-uniform temperature and flow fields were found to cause significant non-uniform distributions of aggregate particle sizes inside the reactor. We also analyzed the generation and growth of polydisperse non-spherical particles in a spatially two-dimensional co-flow diffusion flame. The evolution of the size distribution for non-spherical particle undergoing generation, convection, diffusion, coagulation and coalescence was successfully predicted by the efficient sectional model.

A bimodal model is developed to describe aerosol systems where new particle formation coexists with coagulation and coalescence. The bimodal model appears as an attractive tool when the aerosol dynamics is interfaced with the detailed calculations of fluid dynamics for multi-dimensional geometry or complex flows and chemical reactions. Also it can be a good choice for the simulation of the non-spherical particle growth where surface growth mechanism plays an important role.

We developed a new *in-situ* optical diagnostics for determining aggregate evolution in two dimensional plane through one-measurement. Previous works for aggregate measurement were based on point measurement, but we used a sheet beam and Rayleigh-Debye-Gans Scattering theory to determine radius of gyration and fractal dimensions of aggregates. Due to this method, fast evaluation on the aggregate characteristics should be possible made on a large area per one measurement.

● **Elucidation of unknown fundamental phemomena**

We calculated the number density of non-spherical particles generated in counter-flow diffusion flame successfully. To complete the calculation, we measured the temperature and OH radical concentration in silica generating counter-flow diffusion flame using broadband CARS and PLIF techniques and conducted the numerical analysis on the chemical reaction of silica synthesis.

We investigated the size and crystalline phase changes of Fe_2O_3 nanoparticles formed in a H_2/O_2 flame. It is interesting to note that the mean particle size increased monotonously with the distance from the burner edge; but in high-temperature flames above 1650 °C, it suddenly decreased from 20 to 3 nm with the distance from the burner edge. We suggest the structural instability due to g- to a-phase transformation as a mechanism for a rapid fragmentation of 20 nm particles into 3 nm ones.

Defect states of SiO_2 nanoparticles such as coordination defects, hydrogen atoms, and vacancy of O atom were successfully presented for the first time using plane-wave density functional theory. It was successfully shown that three structural defects lead to narrowing of the band gap and formation of localized states with band tail. The introduction of hydrogen atoms was shown to remove the defect states near the Fermi level.

In conclusion, we have successfully established the Coalescence Enhanced Synthesis method to generate the nano-composite materials with controlled segregation of crystalline phase. We utilize the laser irradiation method to yield the carbonaceous shell-shaped nanoparticles and electrospryay assisted CVD method enables us to produce the highly charged single nanoparticles. The zero-phonon lines are observed in MgO matrix for the first time and the high resolution nanoparticle arrays were achieved through a parallel deposition process. We also developed the theoretical models for describing the population behavior of non-spherical, polydispersed nanoparticles and developed new *in-situ* optical diagnostics for aggregate evolution.

Finally, we have elucidated the novel phenomena related to particle generation and growth that have not been explored yet.

Chapter 5. Major Contributions

Size, morphology, crystalline phase, composition of nanoparticles and their patterned deposition determine the properties and quality of nanostructured materials and nanodevices. Our novel inventions covering gas phase synthesis of single component and composite nanoparticles with controlled properties, nanoparticle patterning, and nanocoating should be breakthroughs in the field of nanoparticle research and applications. We believe these achievements give broad impacts on nanotechnology field since nanoparticles are fundamental building blocks for nanostructured materials and nanodevices. Developments of new measurement and theoretical methods for the growth of nanoparticles have been already considered to be significant contributions in the field of aerosol science.

5.1. Controlled synthesis of nanoparticles

We believe that our novel control strategies to control important characteristics of nanoparticles are to be major advance of nanoparticle research field towards the practical synthesis of nanophase materials. Our new control strategy, "Coalescence Enhanced Synthesis", is successfully applied to the generation of nano-composite particles and the size, morphology and crystallinity can be controlled by adjusting the parameters of laser irradiation. One significant contribution is to present a clear solution for agglomeration problem of nanoparticles mostly occurred at high concentration environment.

All the research results what we have presented are closely related to the controlled production method for nanoparticles and nanocrystilline materials which will support the basic algorithm not only for precisely controlled functional nanoparticles in scientific field but also for the mass production of commercial nanoparticles in industrial field. For example, the enhanced jet-assisted CVD method increases the deposition efficiency by 53% compared to the conventional CVD method and unlike the conventional process of the industrial synthesis of nanocarbons, the shell-shaped carbon nanoparticles in our system can be produced with sufficiently high yield rate (about 100 mg/min according to our estimation) without any further purification process. In addition, the extremely charged unagglomerated nanoparticles generated from the electrospray assisted CVD method are believed to be a good candidate for high resolution nanoparticle patterning and for introducing bio-materials into cells. We also believe that the combustion nanocrystals can be utilized in optical nanodevices due to extraordinary discreteness of the system energy levels with the performance better than that of QDs. It can be a breakthrough in optical nanoelectronics taking into account the recently reported carbon nanotubes-MgO circuitry that can provide a local access to optical elements of nanoscale.

5.2. Novel theoretical and experimental methods for nanoparticle growth

We developed a new theoretical model for describing the population behavior of non-spherical, polydispersed nanoparticles and developed new *in-situ* optical diagnostics for aggregate evolution. The present model successfully predicts the bi-modal polydisperse size distributions of non-spherical particles and morphological evolutions even in the presence of particle generation due to chemical reactions. Computation time for the present method was approximately 1/1000 of that needed for the conventional two-dimensional sectional model. All the results allowed us to reveal the generation and growth mechanism of nanoparitcles in tubular furnace reactor and co-flow diffusion flame and they will provide a detailed picture of nanoparticle synthesis and an efficient method for industrial mass production also. Due to the in-situ optical diagnostics that we developed, fast evaluation on the aggregate characteristics could be possible made on a large area per one measurement.

5.3. Elucidation of new phenomena related to nanoparticle formation

We have elucidated the novel phenomena related to particle generation and growth that have not been explored yet. We discovered a surprising phenomenon of the fragmentation of nanoparticles due to phase transformation. 20 nm Fe_2O_3 and 40 nm SnO_2 nanoparticles were transformed into 3-5 nm Fe_2O_3 and 10 nm SnO_2 nanoparticles both in a flame and in an electron beam irradiating microscope under vacuum. For the first time, we observed extremely sharp line spectra from Mn or Cr doped MgO nanocrystals made from metal combustion. Furthermore, we observed the defect states of SiO_2 nanoparticles for the first time and we found that the introduction of hydrogen atoms can remove the defect states near the Fermi level. Newly observed phenomena are still under further investigation and they will provide insights to nanoparticle research field to understand the fundamental mechanism of nanoparticle behavior.

References

Adachi, M., Fujimoto, T., Nakaso, K., Okuyama, K., Shi, F. G., Sato, H., Ando, T. and Tomioka, H. (1999) Film formation by motion control of ionized precursors in electric field, *Appl. Phys. Lett.*, 75, 1973-1975.

Adachi, M., Okuyama, K., and Fujimoto T. (1995) Film formation by a new chemical vapor deposition process using ionization of tetraethylorthosilicate, *Jpn. Appl. Phys.*, 34, 1148-1150.

Ahn, K. H., Yoon, J. U., and Kim, Y. W. (2001) Corona Ion Assisted Nano Particle Morphology Control in an Atmospheric Pressure Furnace Reactor. *2nd Asian Aerosol Conference*, 203-204.

Ahn, K. H., Yoon, J. U., Yang, T. H., and Choi, M. (2001) Nano SiO_2 particle agglomeration control in a furnace reactor with electro-spray assisted synthesis. *International Symposium on Nanoparticles : Aerosols and Materials, Busan, Korea*, 64-67.

Ahonen, P. P., Moisala, A., Tapper, U., Brown, D. P., Jokiniemi, J. K., and Kauppinen, E. I. (2002) Gas-phase Crystallization of Titanium Dioxide Nanoparticles. *J. Nanoparticle Res.*, 4, 43-52.

Akamatsu, T., Okamura, K., and Ueda Y. (1977) Fabrication of long fibers by an improved Chemical Vapor Deposition Method (HCVD method), *Appl. Phys. Lett.*, 31, 174-176.

Akhtar, M. K., Xiong, Y., and Pratsinis, S. E. (1991) Vapor Synthesis of Titania Powder by Titanium Tetrachloride Oxidation, *AIChE J.*, 37, 1561-1570

Alden, M., Edner, H., Hdmstedt, G., Svanberg, S., and Hoegberg, T. (1982) Single-Pulse Laser-Induced OH Fluorescence in an Atmospheric Flame, Spatially Resolved with a Diode Array Detector. *Appl. Opt.*, 21,1236-1240.

Allen, M. G., Hanson, R. K., (1986) Planar Laser-Induced-Fluorescence Monitoring Of OH In A Spray Flame, *Opt. Eng,*. 25, 12, 1309-1311

Allendorf, M. D., Bautista, J. R., and Potkay, E. (1989) Temperature measurements in a vapor axial deposition flame by spontaneous Raman spectroscopy, *J. Appl. Phys.*, 66, 5046-5051.

Altman I. S., Lee D., Song J., Choi M. (2001) Experimental estimate of energy accommodation coefficient at high temperatures, *Phys. Rev. E*, 64, 052202 (4 pages).

Altman, I. S. (2000) On condensation growth of oxide particles during gas-phase combustion of metals, *Combust. Sci. Technol.*, 160, 221-230.

Altman, I. S., Pikhitsa, P. V., Choi, M. (2004) *Appl. Phys. Lett.* to appear on Feb 17.

Altman, I. S., Lee, D., Chung, J. D., Song, J., Choi, M. (2001) Light absorption of silica nanoparticles *Phys. Rev. B* , 63, 161402.

Altman, I. S., Pikhitsa, P. V., Kim, Y. J., Choi, M. (2003) Magnetism of adsorbed oxygen at low coverage, *Phys. Rev. B*, 67, 144410 (6 pages).

Andersson, O. E., Prasad B. L. V., Sato H., Enoki T., Hishiyama Y., Kaburagi Y., Yoshikawa M., Bandow, S. (1998) Structure and electronic properties of graphite nanoparticles, *Phys. Rev. B*, 58, 16387-16395.

Awschalom, D. D., and DiVincenzo, D. P. (1995) Complex Dynamics of Mesoscopic Magnet, *Phys. Today,* 48, 43-48.

Boer, C. B. and Dekkers, M. J. (2001) Unusual thermomagnetic behaviour of haematites: neoformation of a highly magnetic spinel phase on heating in air, *Geophys. J. Int.* 144, 481-494.

Bonard, J. M., Croci, M., Klinke, C., Kurt, R., Noury, O., Weiss, N. (2002) Carbon nanotube films as electron field emitters, *Carbon*, 40, 1715-1728.

Bowden, N., Brittain, S., Evans, A. G., Hutchinson, J. W., Whitesides, G. M. (1998) Spontaneous formation of ordered structures in thin films of metals supported on an elastomeric polymers, *Nature*, 393, 146-149.

Chen, Q. and Zhang, Z.J. (1998) Size-dependent superparamagnetic properties of $MgFe_2O_4$ spinel ferrite nanocrystallites, *Appl. Phys. Lett.*, 73, 3156-3158.

Cho, J., and Choi, M. (1995) An experimental study of heat transfer and particle deposition for the modified chemical deposition, *ASME J. Heat Transfer,* 117, 1036-1041.

Cho, J., Choi, M. (2000) Determination of number density, size and morphology of aggregates in coflow diffusion flames using light scattering and local sampling, *J. Aerosol Sci.*, 31, 1077-1095.

Choi, J. Y. (1997). Superdetonative mode starting process of supersonic combustion ram accelerator, *Ph.D. dissertation, Seoul National University* .

Choi, M, Cho, J, Lee, J., Kim, H.W. (1999) Measurements of Silica Aggregate Particle Growth Using Light Scattering and Thermophoretic Sampling in a Coflow Diffusion Flam, *J. Nanoparticle Res.*1, 169-183.

Choi, M., Hong, C. K., Lee, K. H. (2002) Jet Assisted Aerosol Chemical Vapor Deposition for Optical Fiber Synthesis, *Aerosol Science and Technology*, 36(3), 300-307.

Choi, W. B., Chung, D. S., Kang, J. H., Kim, H. Y., Jin, Y. W., Han, I. T., Lee, Y. H., Jung, J. E., Lee, N. S., Park, G. S., Kim, J. M. (1999), Fully sealed, high-brightness carbon-nanotube field-emission display, *Appl. Phys. Lett.*, 75, 3129-3131.

Choi, Y. H., and Merkle C. L. (1993) The application of preconditioning in viscous flows, *Journal of Computational Physics*, 105, 207-223.

Chung , S. L. and Katz , J. L. (1985) The counterflow diffusion flame burner: A new tool for the study of the nucleation of refractory compounds, *Combustion and Flame,* 61, 271-284.

Chung, S. L., Tsai, M.S., and Lin, H. D. (1991) Formation of particles in a H_2-O_2 counterflow diffusion flame doped with SiH_4 or $SiCl_4$, *Combustion and Flame*, 85, 134-142.

Dekkers, P. J. and Friedlander, S. K. (2002) The Self-Preserving Size Distribution Theory: I. Effects of the Knudsen Number on Aerosol Agglomerate Growth, *J. Colloid Interf. Sci.*, 248, 295-305.

Dobbins, R. A., Megaridis, C. M. (1987) Morphology of flame-generated soot as determined by thermophoretic sampling, *Langmuir*, 3, 254-259.

Dole, M., Mach, L. L., Hines, R. L., Mobley, R. C., Ferguson, L. P., and Alice, M. B. (1968)

Molecular beams of macroions, *J. Chem. Phys.*, 49, 2240-2249.

Dresselhaus, M. S., Dresselhaus, G., Eklund, P. C. (1996) *Science of Fullerenes and Carbon Nanotubes, Academic Press, San Diego.*

Dutoit, D. C. M., Schneider, M., Baiker A. (1995) Titania-silica mixed oxides: I. Influence of sol-gel and drying conditions on structural properties, *J. Catal.*, 153 165-176.

Eckbreth, A. C. (1988) Laser Diagnostics for Combustion Temperature and Species, *Abacus Press, Tunbridge Well, UK.*

Eckbreth, A. C., Dobbs, G. M., Stufflebeam, J. H., and Tellex, P. A. (1984) CARS Temperature and Species Measurements in Augmented Jet Engine Exhausts, *Appl. Opt.* 23, 1328-1339.

Efendiev,Y. and Zachariah, M. R. (2003) Hierarchical Hybrid Monte-Carlo Methods for Simulation of Two-Component Aerosol Nucleation, Coagulation and Phase Segregation, *J. Aerosol Sci.*, 34, 169.

Ehrman, S. H. (1998) Effect of internal pressure on nanoparticle coalescence, *J. Aerosol Sci.*, 29, 531-532.

Ehrman, S.H.(1999) Effect of particle size on rate of coalescence of silica nanoparticles, *J. Colloid and Int. Sci.*, 213,258-261.

Galvez, A., Herlin-Boime, N. Reynaud, C., Clinard, C., Rouzaud, J. N. (2002) Carbon nanoparticles from laser pyrosis, *Carbon*, 40, 2775-2789.

Gelbard, F., Tambour, Y., and Seinfeld, J. H. (1980) Sectional Representations for Simulating Aerosol Dynamics, *J. Colloid Int. Sci.*, 76, 541-556.

Goodman, F. O. and Wachman, H. Y. (1976) *Dynamics of Gas-Surface Scattering, Acad. Press, New York,* 260.

Greenwood N. M., and Gibb, T.C. (1971) *Mössbauer Spectroscopy, Chapman and Hall, London*, 250.

Gurav, A., Kodas, T., Pluym, T., and Xiong, Y. (1993) Aerosol Processing of Materials, A*erosol Sci. and Technol.*, 19, 411-452.

Hall, M. M., veeraraghavan, V. G., Rubin, .H., Winchell, P. G. (1977) The approximation of symmetric X-ray peaks by Pearson type VII distribution, *J. Appl. Phys.*, 10, 66-68.

Hinds, W. C. (1999) Aerosol Technology, *New York, Wiley-Interscience.*

Ho, W., Yu, Q. R. and Bozzelli, J. W. (1992) Kinetic study on pyrolysis and oxidation of CH_3Cl in $Ar/H_2/O_2$ mixtures, *Combustion Science and Technology*, 85, 23-63.

Hung, C. H. and Katz, J. L. (1992) Formation of mixed oxide powders in flames: Part I. TiO_2-SiO_2, *Journal of Materials Research*, 7, 1861-1869.

Hwang, J. Y., Gil, Y. S., Kim, J. I., Choi, M.,a nd Chung, S. H.(2001) Measurements of temperature and OH radical distributions in a silica generating flame using CARS and PLIF, *J. Aerosol Sci.*, 32, 601-613.

Incropera, F. P., DeWitt D. P. (1990) Fundamentals of Heat and Mass Transfer, *3rd Ed., John Wiley & Sons.*

Iribarne, J. V. and Thomson, B. A. (1976) On the evaporation of small ions from charged droplets. *J. Chem. Phys.*, 64, 2287-2294.

Jacobs, H. O., Campbell, S. A., Steward, M. G. (2002) Approaching nanoxerography: the use of electrostatic forces to position nanoparticles with 100 nm scale resolution, *Adv. Mater.* 14, 1553-1557.

Jacobs, H. O., Whitesides, G. M. (2001) Submicrometer patterning of charge in thin-film electrets, *Science,* 291, 1763-1766.

Jang, H. D. and Kim, S. K. (2001) Controlled Synthesis of Titanium Dioxide Nanoparticles in a Modified Diffusion Flame Reactor, *Mater. Bull.*, 36, 627-637.

Janzen, C. and Roth, P. (2001) Formation and Characteristics of Fe_2O_3 Nano-Particles in Doped Low Pressure H_2/O_2/Ar Flames, *Combustion and Flame* 125, 1150-1161.

Janzen, C., Roth, P., Rellinghaus, B. (1999) Characteristics of Fe_2O_3 Nano-Particles from Doped Low Pressure H_2/O_2/Ar Flames *J. Nanoparticle Res.* 1, 163-167.

Jeong, J. I., and Choi, M. (2001) A Sectional Method for the Analysis of Growth of Polydisperse Non-Spherical Particles Undergoing Coagulation and Coalescence. *J. Aerosol Sci.*, 32, 565-582.

Jeong, J. I., and Choi, M., (2003) Analysis of Non-spherical Polydisperse Particle Growth in a Two-dimensional Tubular Reactor, *J. Aerosol Sci.*, accepted for publication.

Ji, J. H., Pae, Y. I., Hwang, J. H., and Bae, G. W. (2002) Characteristics of Nano Particles Generated from Electrically Heated Tube Furnace with Air/Water Cooling, *6th International Aerosol Conference*, 445-446.

Johannessen, T., Pratsinis, S. E., Livbjerg, H. (2000) Computational Fluid-Particle Dynamics for the Flame Synthesis of Alumina Particles, *Chem. Engineer. Sci.*, 55, 177-191.

Johannessen, T., Pratsinis, S. E., Livbjerg, H. (2001) Computational Analysis of Coagulation and Coalescence in the Flame Synthesis of Titania Particles, *Powder Technol.*, 118, 242-250.

Jullien, R., and Botet, R. (1987), Aggregation and Fractal Aggregates, *World Scientific Publishing, Singapore.*

Kang, Y. C., Roh, H. S., Park, H. D. and Park, S. B. (2003) Optimization of VUV Characteristics and Morphology of $BaMgAl_{10}O_{17}:Eu^{2+}$ Phosphor Particles in Spray Pyrolysis, *Ceram. Int.*, 29, 41-47.

Katta, V. R., and Roquemore, W.M. (1995) Numerical studies on the structure of two-dimensional H_2/air premixed jet flame, *Combustion and Flame*, 102, 21-40.

Kee, R. J., Warnatz, J., and Miller, J. A. (1983) *Sandia National Laboratories Report No. SAND* 83-8209.

Kerker, M. 1969, The Scattering of Light, *Academic Press, New York*, 414-486.

Kim, D. J., and Kim, K. S. (2002) Analysis on Nanoparticle Growth by Coagulation in Silane Plasma Reactor, *AIChE J.*, 48, 2499-2509.

Kim, H. J. (2002). Numerical Analysis of Combustion and Growth of Non-spherical Silica Particles in a H_2/O_2 Co-flow Diffusion Flame, *Ph.D. Dissertation, Seoul National University.*

Kim, K. S., and Pratsinis, S. E. (1988). Manufacture of optical waveguide performs by modified chemical vapor deposition, *AIChE. J.*, 34, 912-921.

Klein, S., thorimbert, S., Maier, W. F. (1996) Amorphous microphois titania-silica mixed oxides:

preparation, characterization, and catalytic redox properties., *J. Catal.*, 163, 476-488.

Kobata, A., Kusakabe, K., and Morooka, S. (1991) Growth and Transformation of TiO_2 Crystallites in Aerosol Reactor, *AIChE J.*, 37, 347-359.

Koch, W. and Friedlander, S. K. (1990) The Effect of Particle Coalescence on the Surface Area of a Coagulating Aerosol, *J. Colloid Int. Sci.*, 140, 419-427.

Kochubei, V.F.(1997) Kinetics of the gas-phase hydrolysis of silicon tetrachloride, Kinetics and Catalysis, 38, 212-214.

Kousaka, Y., Niida, T., Okuyama, K., Tanaka, H. (1982) Development of a mixing type condensation nucleus counter, *J. Aerosol. Sci.*, 13, 231-240.

Koylu, U. O.(1997), Quantitative Analysis of In Situ Optical Diagnostics for Inferring Particle/Aggregate Parameters in Flames: Implication for Soot Growth and Total Emissivity. *Combustion and Flame*, 109, 488-500.

Koylu, U. O., Xing,Y., Rosner, D. E. (1995), Fractal morphology analysis of combustion-generated aggregates using angular light scattering and electron microscope images, *Langmuir*, 11, 4848-4854.

Krinke, T. J., Deppert, K., Magnusson, M. H., Fissan, H. (2002) Nanostructured deposition of nanoparticles from the gas phase, *Part. Part. Syst. Charact.*, 19, 321-326.

Krinke, T. J., Deppert, K., Magnusson, M. H., Schmidt, F. and Fissan, H. (2002) Microscopic Aspects of the Deposition of Nanoparticles from the Gas Phase, *J. Aerosol Sci.*, 33, 1341-1359.

Krinke, T. J., Fissan, H., Deppert, K., Magnusson, M. H. and Samuelson, L. (2001) Positioning of nanometer-sized particles on flat surface by direct deposition from the gas phase, *Appl. Phys. Lett.*, 78, 3708-3710.

Krinke, T. J., Fissan, H., Deppert, K., Magnusson, M. H., Samuelson, L. (2001) Positioning of nanometer-sized particles on flat surfaces by direct deposition from the gas phase, *Appl. Phys. Lett.*, 78, 3708-3710.

Kruis, F. E, Kusters, K. A., and Pratsinis, S. E. (1993) A simple model for the evolution of the characteristics of aggregate particles undergoing coagulation and sintering, *Aerosol Sci. and Technol.*, 19, 514-526.

Ku, B. K., and Kim, S. S. (2002) Electrohydrodynamic Spraying Characteristics of Glycerol Solution in Vacuum, *J. Electrostat*, 57, 109-128.

Kychakoff, G., Howe, R. D., and Hason, R. K. (1984) Quantitative Flow Visualization Technique for Measurements in Combustion Gases, *Appl. Opt.*, 23, 704-712.

Laberty, C., and Navrotsky, A. (1998) Energetics of stable and metastable low-temperature iron oxides and oxyhydroxide, *Geochimica et Cosmochimica Acta*, 62, 2905-2913.

Landgrebe, J. D. and Pratsinis, S. E (1990) A Discrete-Sectional Model for Particulate Production by Gas-Phase Chemical Reaction and Aerosol Coagulation in the Free-Molecular Regime, *J. Colloid Int. Sci.*, 139, 63-86.

Lee, B. W., Jeong, J. I., Hwang, J. Y., Choi, M., and Chung, S. H. (2001a) Analysis of Growth of Non-spherical Silica Particles in a Counterflow Diffusion Flame Considering Chemical Reactions,

Coagulation and Coalescence, *J. Aerosol Sci.*, 32, 165-185.

Lee, B. W., Oh, S., and Choi, M. (2001b) Simulation of Growth of Non-spherical Silica Nanoparticles in a Premixed Flat Flame. *Aerosol Sci. and Technol.*, 35, 978-989.

Lee, D. and Choi, M. (2000) Control of Size and Morphology of Nano Particles Using CO_2 Laser During Flame Synthesi, *J. Aerosol Sci.*, 31, 1145-1163.

Lee, D. and Choi, M. (2002) Coalescence enhanced synthesis of nanoparticles to control size, morphology and crystalline phase at high concentration, *J. Aerosol Sci.*, 33, 1-16.

Lee, D. Yang S., Choi, M. (2001) Cintrolled formation of nanoparticles utilzing laser irradiation in a flame and their characteristics, *Appl. Phys. Lett.*, 79, 2459-2461.

Lee, S, An Experimental Study on Control of Carbon Particle Growth in Diffusion Flame (2001), *M. S. Dissertation; Seoul National University: February.*

Lee, S. D. and Chung, S. H.(1994) *Combust. Flame* 98, 80-92 Smooke, M. D. (1982) *J. Comput. Phys.* 48, 72-105.

Lenggoro, I. W., Xia, B., Mizushima, H., Okuyama K. and Kijima, N. (2001) Synthesis of $LaPO_4$:Eu, Tb Phosphor Particles by Spray Pyrolysis, *Mater. Lett.*, 50, 92-96.

Lin, S.Y., Ferg, J., Biswas, P., Enzweiler, R., Boolchand, P. (1996) Characterization of maghemite ferric oxide crystals processed by an aerosol technique, *J. Magn. Magn. Mater.*, 159, 147-158.

Load Reyleigh (1882) On the equilibrium of liquid conducting masses charged with electricity, *Phil. Mag.*, 14, 184-186.

Madler, L., Kammler, H. K., Mueller, R., Pratsinis, S. E. (2002) Controlled synthesis of nanostructured particles by flame spray pyrolysis, *J. Aerosol Sci.* 33, 369-389.

Martinez, B., Roig, A., Molins, E. (1998) Magnetic characterization of γ-Fe_2O_3 nanoparticles fabricated by aerosol pyrolysi, *J. Appl. Phys.* 83, 3256-3262.

Mass, U., and Warnatz, J. (1988) Ignition processes in hydrogen oxygen mixtures, *Combustion and Flame*, 74, 53-69.

McMichael, R. D., Shull, R. D., Swartzendruber, L. J., Bennett, L. H. (1992) Magnetocaloric Effect in Superparamagnet, *J. Magn. Magn. Mater.*, 111, 29-33.

Mädler, L., Kammler, H., Mueller, R. and Pratsinis, S. E. (2002). Controlled Synthesis of Nanostructured Particles by Flame Spray Pyrolysis, *J. Aerosol Sci.*, 33, 369-389.

Megaridis, C. M., Dobbins, R. A. (1990) A Bimodal Integral Solution of the Dynamic Equation for an Aerosol Undergoing Simultaneous Particle Inception and Coagulation. *Aerosol Sci. Technol.*, 12, 240-255.

Mesquida, P., Stemmer, A. (2001) Attaching silica nanoparticles from suspension onto surface charge patterns generated by a conductive atomic force microscopy tip, *Adv. Mater.*, 13, 1395-1398.

Mesquida, P., Stemmer, A. (2002) Maskless nanofabrication using the electrostatic attachment of gold particles to electrically patterned surfaces, *Microelectron. Eng.* 61-62, 671-674.

Miller C. R., Biswas, P. and Leikauf, G. (2001) Combustion Generated Nickel Species Aerosols: Role

of Chemical and Morphological Properties on Lung Injury, *Aerosol Sci. Technol.*, 35, 829-839.

Mohamed, M. M., Salama, T. M., Yamaguchi, Y. (2002) Synthesis, characterization and catalytic properties or titania-silica catalysts, *Colloids and surfaces A : Physicochemical and Engineering Aspects,* 207, 25-32.

Mørup, S. and Tronc, E. (1994) Superparamagnetic relaxation of weakly interacting particle, *Phys. Rev. Lett.* 72, 3278-3281.

Mueller, R. Mdler, L., and Pratsinis, S. E. (2003) Nanoparticle Synthesis at High Production Rates by Flame Spray Pyrolysis, *Chem. Eng. Sci.*, 58, 1969-1976.

Nakaso, K., Fujimoto, T., Seto, T., Shimada, M., Okuyama, K., and Lunden, M. (2001) Size Distribution Change of Titania Nano-Particle Agglomerates Generated by Gas Phase Reaction, Agglomeration, and Sintering, *Aerosol Sci. Technol.*, 35, 929-947.

O'Connor, P. B., MacChesney, J. B., and Melliar-Smith, C. M. (1977) Large Core High NA Fibers for Data Link Applications, *Electron. Lett.,* 13, 170-171.

Okuyama, K., and Lenggoro, I. W. (2003) Preparation of Nanoparticle via Spray Route, *Chem. Eng. Sci.*, 58, 537-547.

Park, K. S., Lee, B. W., and Choi, M. (1999) An Analysis of Aerosol Dynamics in the Modified Chemical Vapor Deposition. *Aerosol Sci. Technol.*, 31, 258-274.

Park, S. H., Lee, K. W., Shimada, M. and Okuyama, K. (2002) Change in Particle Size Distribution of Aerosol undergoing Condensational Growth: Alternative Analytical Solution for the Entire Particle Size Range, *J. Aerosol Sci.*, 33, 1297-1308.

Patankar, S. V. (1980) Numerical Heat Transfer and Fluid Flow, *McGraw-Hill, New York.*

Powers, D. R. (1978) Kinetics of $SiCl_4$ oxidation, *Journal of the American Ceramic Society*, 61, 295-297.

Pratsinis, S. E., Bai, H. and Biswas, P. (1990) Kinetics of Titanium(Ⅳ) Chloride Oxidation, *J. Am. Ceram. Soc.*, 73, 2158-2162.

Pratsinis, S.E. (1998) Flame Aerosol Synthesis of Ceramic Powders, *Prog. Energy Combust. Sci.*, 24, 197-219.

Reichl, G. P. (1991). Measurement of ambient aerosols by the differential mobility analyzer method: concepts and realization criteria for the size range between 2 to 500 nm, *Aerosol Sci. and Technol.,* 14, 5-24.

Schild, A., Gutsch, A, Mühlenweg, H., and Pratsinis, S. E. (1999) Simulation of Nanoparticle Production in Premixed Aerosol Flow Reactors by Interfacing Fluid Mechanics and Particle Dynamics, *J. Nanoparticle Res.*, 1, 305-315

Schimanke, G., and Martin, M. (2000) *In situ* XRD study of the phase transition of nanocrystalline maghemite to hematit, *Solid State Ionics,* 136-137, 1235-1240.

Schraml, S., Dankers S., Bader, K., Will, S., Leipertz, A., Soot temperature measurements and implications for time-resolved laser-induced incandescence (TIRE-LII) (2000), *Comb. and Flame*, 120, 439-450.

Seinfeld, J. H. (1986) Atmosphere Chemistry and Physics of Air Pollution. N. Y., *John Wiley & Sons.*

SetSeto, T., Hirota, A., Fujimoto, T., Shimada, M., and Okuyama, K. (1997) Sintering of Polydisperse Nanometer-Sized Agglomerates. *Aerosol Sci. and Technol.*, 27, 422-438.

Shuen, J.S., Chen, K.H., and Choi, Y.(1993). A coupled implicit method for chemical non-equilibrium flows at all speeds, *Journal of Computational Physics*, 106, 306-318.

Sorensen, C. M. Cai, J.and Lu, N. (1992), Light-Scattering Measurements of Monomer size, Monomers per Aggregate, and Fractal dimension for Soot Aggregates in Flames, *Applied Optics*, 30, 6547-6557

Stolen, R. H. and Walrafen, G. E. (1976) Water and its Relation to Broken Bond defects in Fused Silica. *J. Chem. Phys.*, 64, 2623-2631.

Su, B. and Choy, K. L. (2000) Microstructure and properties of the CdS thin films prepared by electrostatic spray assisted vapour deposition (ESVAD) method, *Thin Solid Films,* 359, 160-164.

Tsantilis, S and Pratsinis, S. E. (2000) Evolution of Primary and Aggregate Particle size Distributions by Coagulation and Sintering, *AIChE J.*, 46, 407-415.

Ulrich, G. D., (1971) Theory of Particle Formation and Growth in Oxide Synthesis Flames, *Comubustion. Sci. and Tech.*, 4, 47-57.

Van der Hulst, H. C. 1957, Light Scattering by Small Particles, *Dover Publications, New York.*

Vander Wal R. L. Tomasek, A. J. Ticich, Th. M. (2003) Synthesis laser processing and flame purification of nanostructured carbon, *Nano Lett.*, 3, 223-229.

Venkateswaran, S., Deshpande, M.,and Mekle, C. L. (1995) The application of preconditioning to reacting flow computations, *AIAA Paper,* 95-1673, 306-313.

Wei, M. and Choy, K. L. (2002) Deposition of highly oriented ZnS thin films on Si(100) substrate using electrostatic spray assisted vapor deposition, *Chem. Vap. Deposition,* 8, 15-17.

Wooldridge, M.S.(1998) gas-phase combustion systhesis of particles, *Prog.Energy.*

Wu, C. Y., and Biswas, P. (1998) Study of Numerical Diffusion in a Discrete-Sectional Model and Its Application to Aerosol Dynamics Simulation. *Aerosol Sci. and Technol.*, 29, 359-378.

Wu, J. J., and Flagan, R. C. (1988) A Discrete-Sectional Solution to the Aerosol Dynamics Equation. *J. Colloid Int. Sci.*, 123, 339-352.

Xiong, Y., Akhtar, M.K.,and Pratsinis, S.E.(1993). Formation of agglomerates particles by coagulaton and sintering - Part II. the evolution of the morphology of aerosol -made titania, silica and silica-doped titania powders, *J. Aerosol Sci.*, 24, 301-313.

Xiong, Y., and Pratsinis, S. E. (1991) Gas Phase Production of Particles in Reactive Turbulent Flows. *J. Aerosol Sci.*, 22, 637-655.

Xiong, Y., and Pratsinis, S. E. (1993) Formation of Agglomerate Particles by Coagulation and Sintering Part 2: A Two-Dimensional Solution of the Population Balance Equation. *J. Aerosol Sci.*, 24, 283-300.

Xiong, Y., Pratsinis, S. E. and Mastrangelo, S. V. R. (1992) The effect of ionic additives on aerosol coagulation, *J. Colloid Interface Sci.,* 153, 106-117.

Xu, X.N., Wolfus,Y., Shaulov, A., Yeshurun, Y., Felner, I., Nowik, I., Koltypin, Y. and Gedanken, A. (2002) Annealing study of Fe_2O_3 nanoparticles: Magnetic size effects and phase transformation, *J. Appl. Phys.*, 91, 4611-4616.

Ye, X., Lin, D., Jiao, Z., Zhang, L. (1998) The thermal stability of nanocrystalline maghemite Fe_2O_3, *J. Phys., D* 31, 2739-2744.

Yu, S., Yoon, Y., Muller-Roosen, M.,and Kennedy, I.M.(1998) A two-dimensional discrete-sectional method for metal aerosol dynamics in a flame, *Aerosol Sci. and Technol.*, 28, 185-196.

Zachariah, M. R. and Huzarewicz, S. (1991) Aerosol Processing of YBaCuO Superconductors in a Flame Reacto, *J. Mater. Res.*, 6, 264-269.

Zachariah, M. R., Chin, D., Semerjian, H. G., and Katz, J. L. (1989) Dynamic light scattering and angular dissymmetry for the in-situ measurement of silicon dioxide particle synthesis in flames, *Applied Optics*, 28, 530-536.

Zhang, L., Papaefthymiou, G.C., Ying, J.Y. (1997) Size quantization and interfacial effects on a novel γ-Fe_2O_3/SiO_2 magnetic nanocomposite via sol-gel matrix-mediated synthesis, *J. Appl. Phys.* 81, 6892-6900.

Zhao, H., Ladommatos, N. (1998) Optical diagnostics for soot and temperature measurement in diesel engines, *Prog. Energy Combust. Sci.*, 24, 221-255.

특정연구개발사업 연구결과 활용계획서

<table>
<tr><td rowspan="2">사업명</td><td>중사업명</td><td colspan="4">특정연구개발사업</td></tr>
<tr><td>세부사업명</td><td colspan="4">창의적 연구진흥사업</td></tr>
<tr><td colspan="2">과제명</td><td colspan="4">물질제조를 위한 나노 입자생성 및 제어기술연구</td></tr>
<tr><td colspan="2">연구기관</td><td colspan="2">서울대학교</td><td>연구책임자</td><td>최 만 수</td></tr>
<tr><td colspan="2">총연구기간</td><td colspan="4">2000 년. 10 월. 1 일. ~ 2003 년. 9 월. 30 일. (36 개월)</td></tr>
<tr><td colspan="2" rowspan="2">총 연구비
(단위 : 천원)</td><td>정부출연금</td><td>민간부담금</td><td>합계</td></tr>
<tr><td>1,900,000</td><td>-</td><td>1,900,000</td></tr>
<tr><td colspan="2">기술분야</td><td colspan="4">나노 기술</td></tr>
<tr><td colspan="2">참여기업</td><td colspan="4">-</td></tr>
<tr><td colspan="2">공동연구기관</td><td colspan="4">-</td></tr>
<tr><td colspan="2">위탁연구기관</td><td colspan="4">-</td></tr>
<tr><td colspan="2" rowspan="2">연구결과활용
(해당항목에(∨)
표시)</td><td>1. 기업화 ( )</td><td>2. 기술이전( )</td><td>3. 후속연구추진(∨)</td><td>4.타사업에 활용 ( )</td></tr>
<tr><td>5. 선행 및 기초연구( )</td><td>6. 기타목적활용 (교육,연구)( )</td><td>7. 활용중단(미활용)( )</td><td>8. 기타( )</td></tr>
</table>

특정연구개발사업 처리규정 제 31조(연구개발결과의 보고) 제 2항에 의거 연구결과 활용계획서를 제출합니다.

첨부 : 1. 연구결과 활용계획서 1부.
2. 기술요약서 1부

2004 년 2 월 24 일

연구책임자 : 최 만 수 (인)
연구기관장 : 정 운 찬 (직인)

과학기술부장관 귀하

[첨부1]

연구결과 활용계획서

1. 연구목표 및 내용

기상 중의 단성분 혹은 복합체 나노입자의 발생과 성장, 그리고 나노입자의 패턴 방법을 제어하는 기술의 개발과 확립을 목표로 한다. 구체적으로 나노 입자의 크기, 형상, 결정상 및 성분을 제어하기 위한 새로운 이론을 확립하고, 새로운 나노 입자 패턴 방법을 고안하며, 나노 입자의 성장을 관찰하기 위한 새로운 이론적, 실험적 방법들을 개발하고, 나아가 현재까지 밝혀지지 않은 입자의 생성과 성장에 관한 신규한 현상들을 규명하는데 그 목표를 두고 있다 .

2. 연구수행결과 현황(연구종료시점까지)

가. 특허(실용신안) 등 자료목록 (별지첨부)

발명명칭	특허공고번호 출원(등록)번호	공고일자 출원(등록)일자	발명자 (출원인)	출원국	비고
계: 국외 8건/ 국내 10건					

나. 프로그램 등록목록

프로그램 명칭	등록번호	등록일자	개발자	비고

다. 노하우 내역

-

라. 발생품 및 시작품 내역

-

마. 논문게재 및 발표 실적

○논문게재 실적 (별지 첨부)

학술지 명칭	제 목	게재연월일	호	발 행 기 관	국 명	SCI게재 여부
		년 월 일				
계: 32건						

○학술회의 발표 실적 (별지 첨부)

학술회의 명칭	제 목	게재연월일	호	발 행 기 관	국 명
		년 월 일			
계: 국외 33건 /국내 17건					

3. 연구성과

4. 기술이전 및 연구결과 활용계획

가. 당해연도 활용계획(6하원칙에 따라 구체적으로 작성)

· 개발된 새로운 나노입자제어기술은 탄소나노입자를 비롯한 다양한 다성분 나노입자의 성장제어 기술의 개발에 활용
· 개발된 나노패터닝 기술의 확립을 위한 반복실험
· 개발된 나노입자 성장 모델링 기술은 이중 모멘트 방법으로 확장

나. 활용방법

-

다. 차년도이후 활용계획(6하원칙에 따라 구체적으로 작성)

3단계 연구사업에서 확장발전 시키기 위하여 다성분계 나노입자의 제조와 성장제어기술에 적용하며, 다성분계 나노입자의 성장을 모사할 수 있는 기술로 발전시킨다. 코로나 이온, 전기수력학 분사를 병행하는 나노패터닝 기술로 발전시킨다.

5. 기대효과

21세기의 핵심기술로 평가받는 나노테크놀러지의 근간을 이루는 새로운 나노입자의 제어기술의 확립으로 말미암아 나노물질제조에 있어서 세계적 수준을 확보할 수 있으며 나노입자 패터닝 기술의 확립으로 나노소자 제조에 있어서 근간기술을 제공한다. 나노기술분야에 고급 두뇌 인력양성과 세계적 수준의 학문적 센터로 자리잡는다.

6. 문제점 및 건의사항

* 특허(실용신안) 등 자료목록 (별지)

발명명칭	특허공고번호 출원(등록)번호	공고일자 출원(등록)일자	발명자 (출원인)	출원국	비고
MCVD Method and Apparatus Using an Elongated Gas Feeding Device	*6,363,754*	*April 2, 2002*	*M. Choi and D. Lee*	U.S.A.	
Methods for Manufacturing and Depositing Fine Particles Combining Flame and Laser Beam	*0308795*	*Sep.1, 2001*	*M.Choi and D. Lee*	Korea	
Method for Manufacturing Shell Shaped Fine Carbon Particles	*0385574*	*May 15, 2003*	*M.Choi, S.Lee and J.Hwang,*	Korea	
Apparatus for Diluting and Sampling Particles	*10-0339787*	*May 24, 2002*	*K.H. Ahn and M. Choi*	Korea	
Methods for Manufacturing and Depositing Fine Particles Combining Flame and Laser Beam	*09/890,366*	*July 26, 2001*	*M.Choi and D. Lee*	U.S.A.	
Methods for Manufacturing and Depositing Fine Particles Combining Flame and Laser Beam	*2000-595941*	*July 27, 2001*	*M.Choi and D. Lee*	Japan	
Methods for Manufacturing and Depositing Fine Particles Combining Flame and Laser Beam	*10083901.0*	*July 27, 2001*	*M.Choi and D. Lee*	Germany	
Apparatus and Method for Manufacturing Optical Fibers Using Inner Jet	*0263729*	*May 19, 2000*	*M.Choi and D.Lee*	Korea	
Method for manufacturing	*2001-9951*	*Feb. 27, 2001*	*K.H.Ahn and M.Choi*	Korea	

unagglomerated fine particles using electro-hydrodynamic spray in flame or furnace					
Carbon Nano Particles Having Novel Structure and Properties	*2002-11015*	*Feb. 28, 2002*	*M.Choi, Y.Kim, J.Lee, Igor Altman and Petro Pikhitsa*	Korea	
Carbon Nano Particles Having Novel Structure and Properties	*10/376,823*	*Feb. 28, 2003*	*M.Choi, Y.Kim, J.Lee, Igor Altman and Petro Pikhitsa*	U.S.A.	
Method for Patterning Nano-Sized Structure Using Electrospray of Nanoparticle	*10-2003-004 4625*	*July 2, 2003*	*M.Choi, B.Han, J.Suh*	Korea	
Process for Nanoparticle Patterning and Preparation Process of Patterning Sintered Body	*2003-44610*	*July 2, 2003*	*M.Choi, H.C.Kim*	Korea	
Process for preparing composite nano particles by gas phase coating using flame	*2003-50219*	*July 22, 2003*	*M.Choi, S.W.Shin*	Korea	
Process for field-emission using shell-shaped carbon nanoparticles	2003-58653	Oct. 25, 2003	*M.Choi, Y.Kim, Igor Altman and Petro Pikhitsa*	Korea	
Method for Manufacturing Shell Shaped Fine Carbon Particles	2002-565897	Oct. 7, 2003	*M.Choi, S.Lee and J.Hwang*	Japan	
Method for Manufacturing Shell Shaped Fine Carbon Particles	10296273.1	Oct. 8, 2003	*M.Choi, S.Lee and J.Hwang*	Germany	
Method for Manufacturing Shell Shaped Fine Carbon Particles	10/638,131	Oct. 8, 2003	*M.Choi, S.Lee and J.Hwang*	U.S.A.	
계: 국외 8건/ 국내 10건					

* 논문게재 실적(별지)

학술지 명칭	제목	게재 연월일	호	발행 기관	국명	SCI 게재 여부
Journal of Aerosol Science	Control of Size and Morphology of Nano Particles Using CO_2 Laser During Flame Synthesis	2000.10	Vol.31, No.10, pp.1145-1163	PERGAMON-ELSEVIER SCIENCE	UK	Yes
Journal of Aerosol Science	Determination of Number Density, Size and Morphology of Aggregates in Coflow Diffusion Flames Using Light Scattering and Local Sampling	2000.9	Vol. 31, No.9, pp.1077-1095	PERGAMON-ELSEVIER SCIENCE	UK	Yes
Journal of Electrochemical Society	Analysis of Radiative Heat Transfer and Mass Transfer During Multi-wafer Low Pressure Chemical Vapor Deposition Process	2000.12	Vol.147, No.12,pp.4554-4561	ELECTROCHEMICAL SOC INC	DE	Yes
International Journal of Heat and Mass Transfer	Unsteady Heat and Mass Transfer on the Codeposition of SiO2/GeO2 During the Modified Chemical Vapor Deposition Process	2000.9	Vol.43, No.17, pp.3209-3217	PERGAMON-ELSEVIER SCIENCE	UK	Yes
Numerical Heat Transfer	Effect of Radiative Transfer on the Thermophoretic Particle Deposition around a Circular Cylinder in a Uniform Cross Flow	2000.1	Part A, 37(1):19-35	HEMISPHERE PUBL CORP	US	No
International Journal of Heat and Mass Transfer	Measurements of Impinging Jet Flow and Heat Transfer on a Semi-Circular Concave Surface	2000.5	Vol.43, No. 10, pp.1811-1822	PERGAMON-ELSEVIER SCIENCE	UK	Yes
Journal of Aerosol Science	Analysis of Growth of Non-spherical silica Particles in a Counterflow Diffusion Flame Considering Chemical Reactions	2001.2	Vol.32, No. 2, pp.165-185	PERGAMON-ELSEVIER SCIENCE	UK	Yes

Journal of Aerosol Science	A Sectional Method for Analysis of Growth of Polydisperse Non-spherical Particles Undergoing Coagulation and Coalescence	2001.5	Vol. 32, No.5, pp.565-582	PERGAMON-ELSEVIER SCIENCE	UK	Yes
Applied Physics Letters	Controlled formation of nanoparticles utilizing laser irradiation in a flame and their characteristics	2001.10	Vol. 79, No. 15, pp.2459-2461	AMER INST PHYSICS	US	Yes
Physical Review B	Light Absorption of SilicaNanoparticles Generated in Flame	2001.4	Vol. 63, 161402	AMERICAN PHYSICAL SOC	US	Yes
Journal of Aerosol Science	Measurements of Temperature and OH Radical Distributions in Silica Generating Flames Using CARS and PLIF	2001.5	Vol. 32, No.5 pp.601-613	PERGAMON-ELSEVIER SCIENCE	UK	Yes
Scripta Materialia	In Situ Measurement of Nano Particle Size Distribution and Charge Characteristics in H2/O2/TEOS Diffusion Flame	2001.5	Vol. 44, No.8-9, pp.1889-1892	PERGAMON-ELSEVIER SCIENCE	UK	Yes
J. of Nanoparticle Research	Researches in Korea Gas Phase Synthesis and Control of Nanoparticles	2001.6	Vol. 3, No. 2-3, pp.201-211	KLUWER ACADEMIC PUBL	NL	Yes
J. of Nanoparticle Research	Particle Sampling and Real Time Size Distribution Measurement in H2/O2/TEOS Diffusion Flame	2001.6	Vol. 3, No. 2-3, pp.161-170	KLUWER ACADEMIC PUBL	NL	Yes
International Journal of Heat and Mass Transfer	A Refined Similarity Solution for the Multicomponent Alloy Solidification	2001.7	Vol. 44, No. 13, pp.2483-2492	PERGAMON-ELSEVIER SCIENCE	UK	Yes
Phys. Rev. E	Experimental estimate of energy accommodation coefficient at high temperatures	2001.11	Vol. 64, No.052202	AMERICAN PHYSICAL SOC	US	Yes

Aerosol Science and Technology	Simulation of Growth of Non-spherical Silica Nanoparticles in a Premixed Flat Flame	2001.12	Vol. 35, No. 6, pp.978-989	TAYLOR & FRANCIS INC	US	Yes
J. of Aerosol Science	Coalescence enhanced synthesis of nanoparticles to control size, morphology and crystalline phase at high concentrations	2002.1	Vol. 33, No. 1, pp.1-16	PERGAM ON-ELSEV IER SCIENCE	UK	Yes
J. of Materials Research	Preparation and Characterization of SiO2-B2O3-P2O5 Particles and Films Generated by Flame Hydrolysis Deposition for Planar Light-Wave Circuits	2002.2	Vol. 17, No. 2, pp.315-322	MATERIA LS RESEARC H SOCIETY	US	Yes
Aerosol Science and Technology	Jet Assisted Aerosol Chemical Vapor Deposition for Optical Fiber Synthesis	2002.3	Vol. 36 No. 3, pp.300-307	TAYLOR & FRANCIS INC	US	Yes
Key Engineering Materials	Superparamagnetic Iron (III) Oxide Nanoparticles Synthesized by Combustion Flame Process	2002.3	Vol. 206-213, pp 135-138	TRANS TECH PUBLICA-TIONS LTD	CH	Yes
Physical Review B	Stability of Elongated and Compact Types of Structures in SiO2 Nanoparticles	2002.6	Vol. 65,24, pp 241-302	AMERICA-N PHYSICAL SOC	US	Yes
Aerosol Science and Technology	Unipolar charging of nanosized aerosol particles using soft X-ray photoionization	2003.4	Vol.37, No.4, pp.330-341	TAYLOR & FRANCIS INC	US	Yes
Physical Review B	Magnetism of adsorbed oxygen at low coverage	2003.4	Vol.67, No. 14, 144410	AMERIC-A N PHYSICAL SOC	US	Yes
J. of Aerosol Science	Analysis of Non-Spherical Polydisperse Particle Growth in a Two-dimensional Tubular Reactor	2003.6	Vol. 34, No. 6, pp 713-732	PERGAM ON-ELSEV IER SCIENCE	UK	Yes

J. of Aerosol Science	Synthesis of non-agglomerated nanoparticles by an Electrospray Assisted Chemical Vapor Deposition Method	2003.6	Vol. 34, No. 7, pp 869-881	PERGAMON-ELSEVIER SCIENCE	UK	Yes
Chemical Physics Letter	Semiempirical dynamic phase diagrams of nanocrystalline products during copper(II) acetylacetonate vapor decomposition	2003.1	Vol.367, No.5-6, pp 771-777	ELSEVIER SCIENCE BV	NL	Yes
J. Aerosol Science	A Simple Bimodal Model for the Evolution of non-spherical particles Undergoing Nucleation, Coagulation and Coalescence	2003.8	Vol. 34, No. 8, pp 965-976	PERGAMON-ELSEVIER SCIENCE	UK	Yes
Powder Technology	Classification of Monodisperse aerosol Particles Using an Adjustable Soft X-ray Charger	2003.10	Vol. 135-136, pp. 336-344	ELSEVIER SCIENCE SA	US	Yes
Analytical Sciences	Measurement of Cluster Ions and Residue Nanoparticles from Water Samples with an Electrospray/Differential Mobility Analyzer	2003.6	Vol. 19, No.6, pp 843-851	JAPAN SOC ANALYTICAL CHEMIS-TRY	JP	Yes
Journal of Nanoparticle Research	Modeling of generation and growth of non-spherical nanoparticles in a co-flow flame	2003.8	Vol. 5 No.3-4, pp 237-246	KLUWER ACADE-MIC PUBL	NL	Yes
J. of Applied Physics	Nano fluids containing multi-walled carbon nanotubes and their enhanced thermal conductivities	2003.10	vol. 94, No. 8, pp 4967-4971	PERGAMON-ELSEVIER SCIENCE	UK	Yes
계: 국외 32건						

* 학술회의 발표 실적 (별지)

학술회의 명칭	제목	게재연월일	호	발 행 기 관	국 명
European Aerosol Conference 2003	Preparation of Nanosized TiO2 and Pt/TiO2 Composite Particles by CW CO_2 Laser Ablation	2003년 8월 31일-9월 5일			Spain
The 6th International Aerosol Conference	Jet-Assisted Aerosol CVD Method for the Synthesis of Multi-Component Optical Fiber	2002년 9월 8일-13일			Taiwan
The 6th International Aerosol Conference	Analysis of Heat, Mass Transfer and Particle Dynamics in a Coflow Silica Generating Flame	2002년 9월 8일-13일			Taiwan
The 6th International Aerosol Conference	Control and Modeling of Nanoparticle Growth in Flame	2002년 9월 8일-13일			Taiwan
10th Nisshin Engineering Particle Technology International Symposium	Control of Size Morphology and Crystalline Phase of Nanoparticles in a Flame	2001년 12월 17일-19일			Japan
AAAR 2001 Annual Conference	Synthesis of Shell Shaped Carbon Nanoparticles in a Flame and Their Characteristics	2001년 10월 15일-19일			U.S.A.
AAAR 2001 Annual Conference	Optical Properties of Silica Nanoparticles Generated in a Flame	2001년 10월 15일			U.S.A.
AAAR 2001 Annual Conference	Experimental and Numerical Study on Silica Generating Counterflow Diffusion Flames	2001년 10월 15일-19일			U.S.A.
European Aerosol Conference 2001	A Numerical Analysis of Growth of Non-Spherical Particles in a Spatially Two-Dimensional Furnace Reactor	2001년 9월 3일-7일			Germany

European Aerosol Conference 2001	Formation of Shell Shaped Carbonaceous Nano Particles by in Situ Laser Irradiation to Soot Precursor in a Flame	2001년 9월 3일-7일			Germany
European Aerosol Conference 2001	Size and Phase Evolution of Fe2O3 Nanoparticles during Flame Synthesis	2001년 9월 3일-7일			Germany
European Aerosol Conference 2001	On Physical Fundamentals of Laser-Induced incandescence	2001년 9월 3일-7일			Germany
7th Conference & Exhibition of the European Ceramic Society	Superparamagnetic Iron (III) Oxide Nanoparticles Synthesized by Combustion Flame Process	2001년 9월 9일-13일			Belgium
International Symposium on Nanoparticles: Aerosol and Materials	CO_2 Laser Irradiation to Sooting Diffusion Flames: Formation of Shell Shaped Carbon Nano Particles	2001년 7월 5일-6일			Korea
International Symposium on Nanoparticles: Aerosol and Materials	Nano SiO_2 Particle Agglomeration Control in a Furnace Reactor with Electro-Spray Assisted Synthesis	2001년 7월 5일-6일			Korea
2nd Asian Aerosol Conference	Anomalous Light Absorption of Silica Nanoparticles Generated Within a Flame	2001년 7월 1일-4일			Korea
2nd Asian Aerosol Conference	A Two-Dimensional Analysis of Aggregate Aerosol Dynamics in a Tubular Furnace Reactor	2001년 7월 1일-4일			Korea
2nd Asian Aerosol Conference	An Experimental Study on Composition Characteristics of SiO_2/TiO_2 Multicomponent Particle Generated in H_2/O_2 Coflow Diffusion Flame	2001년 7월 1일-4일			Korea
2nd Asian Aerosol Conference	Infrared Spectroscopic Study of Water-Related Species in Silica Nanoparticles by Flame Hydrolysis Deposition	2001년 7월 1일			Korea

2nd Asian Aerosol Conference	A Critical Temperature Behavior of Sooting Acetylene Flame Irradiated by a CO_2 Laser	2001년 7월 1일-4일			Korea
2nd Asian Aerosol Conference	Stability of Elongated and Compact Types of Structures in SiO_2 Nanoparticles	2001년 7월 1일-4일			Korea
2nd Asian Aerosol Conference	Sudden Change of Size and Phase of Iron(III) Oxide Nanoparticles in O_2/H_2 Flames	2001년 7월 1일-4일			Korea
2nd Asian Aerosol Conference	Soot Formation in Counterflow Diffusion Flames of Ethylene/Propane/Benzene Mixtures	2001년 7월 1일-4일			Korea
2nd Asian Aerosol Conference	Temperature and OH Radical Distributions in Silica Generating Counterflow Diffusion Flames	2001년 7월 1일-4일			Korea
International Congress for Particle Technology (PARTEC 2001)	Coalescence Enhanced Synthesis to Control Size, Morphology and Crystalline Phase of Nanoparticles	2001년 3월 27일-29일			Germany
First Asian Particle Technology Symposium	Flame Aerosol Synthesis of Nanopartkcles and Growth Control	2000년 12월 13일-15일			Thailand
AAAR 2000 Annual Conference	An Aerosol CVD Method Using Internal Jet for Optical Fiber Symthesis	2000년 11월 6일			U.S.A.
AAAR 2000 Annual Conference	Measurements of Temperature and Hydoxyl Radical Distributions Using CARS and PLIF in a Silica Generating Flame	2000년 11월 6일-10일			U.S.A.
AAAR 2000 Annual Conference	Control of Size, Morphology and Phase of Nano Particles Using CO2 Laser Irradiation	2000년 11월 6일-10일			U.S.A.
AAAR 2000 Annual Conference	A New Sectional Model for Simulating Non-spherical Polydisperse Particles Growth	2000년 11월 6일-10일			U.S.A.

2000 IAMS International Seminar	Heat and Mass Transfer in Aerosol Chemical Vapor Deposition for Synthesis of Thin Films and nanoparticles	2000년 10월 10일-11일			Japan
4th JSME-KSME Thermal Engineering Conference	Control of Size, Morphology and Phase of Nano Particles Using CO2 Laser Irradiation	2000년 10월 1일-6일			Japan
The 4th Korean Conference on Aerosol and Particle Technology	카본 나노튜브유체와 열전도 증가	2003년 7월 3일-5일			Korea
The 4th Korean Conference on Aerosol and Particle Technology	입자의 발생을 고려한 바이모달 모멘트 해석 방법	2003년 7월 3일-5일			Korea
The 4th Korean Conference on Aerosol and Particle Technology	화염에서 발생되는 나노입자의 절대농도 계산을 위한 희석장치의 희석비 연구	2003년 7월 3일-5일			Korea
The 4th Korean Conference on Aerosol and Particle Technology	CO2 레이저 빔을 이용한 화염 중에서 생성되는 SiO2/TiO2 복합 나노입자의 제어	2003년 7월 3일-5일			Korea
The 4th Korean Conference on Aerosol and Particle Technology	Generation of Hollow Carbon Onions from Acetylene and Their Field Emission Property	2003년 7월 3일-5일			Korea
The 4th Korean Conference on Aerosol and Particle Technology	광화학 반응에 의한 입자의 생성 및 성장 현상의 모사	2003년 7월 3일-5일			Korea
The 3rd Korean Conference on Aerosol and Particle Technology	화염 에어로졸 합성으로 SiO_2 입자에 함유된 OH/H_2O의 정량적 연구	2002년 7월 11일-13일			Korea

The 3rd Korean Conference on Aerosol and Particle Technology	A Simple Bimodal Model for the Description of Non-spherical Particles Undergoing Nucleation, Coagulation, Surface Growth and Coagulation	2002년 7월 11일-13일			Korea
The 3rd Korean Conference on Aerosol and Particle Technology	입자의 발생을 고려한 바이모달 모멘트 해석 방법	2002년 7월 11일-13일			Korea
The 3rd Korean Conference on Aerosol and Particle Technology	Jet-Assisted Aerosol CVD Method for Multi-Component Doped Optical Fiber	2002년 7월 11일-13일			Korea
The 3rd Korean Conference on Aerosol and Particle Technology	Analysis of Heat, Mass transfer and Particle Dynamics in a Coflow Silica Generating Flame	2002년 7월 11일-13일			Korea
대한기계학회 2001년도 열공학부문 추계학술대회논문집	화염 중 CO_2 레이저 조사를 이용한 탄소 나노입자 제조	2001년 9월 14일-15일			Korea
한국세라믹학회 2001년도 춘계총회	Size and Phase Evolution of Fe2O3 Nanoparticles Synthesized by Flame Aerosol Precess	2001년 4월 27일-28일			Korea
대한기계학회 2001년도 열공학부문 춘계학술대회	화염 에어로졸 공정을 이용한 산화철 나노입자의 제조 및 특성 연구	2001년 3월 23일-24일			Korea
대한기계학회 2000년도 추계학술대회	CO_2 레이저 조사를 이용한 나노 입자의 크기, 형상과 결정상의 제어	2000년 11월 2일-4일			Korea
대한기계학회 2000년도 추계학술대회	전기-수력학적 분사에 의해 합성된 초미세 SiO_2 입자의 특성	2000년 11월 2일-4일			Korea
대한기계학회 2000년도 추계학술대회	H_2/O_2확산화염에서 전기수력학적 방법과 증발기에 의해 발생된 입자의 성장 비교에 관한 실험적 연구	2000년 11월 2일-4일			Korea
계: 국외 33건/ 국내 17건					

[첨부2]

기술 요약서

■ 기술의 명칭

나노입자 성장제어 기술, 나노입자 패터닝 기술

■ 기술을 도출한 과제현황

과제관리번호				
과제명	물질제조를 위한 나노입자 생성 및 제어기술 연구			
사업명	특정연구개발사업			
세부사업명	창의적연구진흥사업			
연구기관	서울대학교		기관유형	대학
참여기관(기업)	-			
총연구기간	2000.10.1 ~ 2003.9.30			
총연구비	정부(1,900,000)천원 민간(-)천원 합계(1,900,000)천원			
연구책임자 1	성명	최 만 수	주민번호	571129-1031112
	근무기관 부서	서울대학교 기계항공공학부	E-mail	mchoi@plaza.snu.ac.kr
	직위/직급	교수	전화번호	02-880-7128
연구책임자 2	성명		주민번호	
	근무기관 부서		E-mail	
	직위/직급		전화번호	
실무연락책임자	성명	진 기 정	소속/부서	정밀기계설계공동연구소 나노입자제어기술연구단
	직위/직급	행정원	E-mail	jin2495@snu.ac.kr
	전화번호	02-880-1659	FAX	02-878-2465
	주소	(151 -742) 서울 관악구 신림동 산 56-1		

■ 기술의 주요내용

[기술의 개요]

본 연구단에서는 나노 입자의 크기, 형상, 결정상 및 성분을 제어하기 위한 새로운 이론적, 실험적인 기술들을 개발, 확립하고, 나노 입자의 위치제어를 위한 새로운 나노 입자 패턴 방법을 고안하고 있다. 새롭게 개발한 레이저를 이용한 에어로졸 제어기술은, 기상 중에서 생성되는 나노 입자들에 CO_2 레이저를 조사하여 단성분 혹은 복합체 나노 입자의 크기와 모양, 결정상, 조성까지도 제어할 수 있으며, 나노튜브의 전계방출 특성에 필적할 만한 새로운 탄소 나노 입자를 제조할 수 있다. 또한 본 연구단은 코팅된 나노 복합재료의 합성을 위한 새로운 기상 코팅 기술을 고안하였으며, 새로운 나노 입자 패터닝 방법을 개발하였다. 이론적으로 다분산 비구형 나노 입자의 성장을 예측할 수 있는 효율적인 모델링 기술들과 실험적으로 비구형 나노 입자의 성장 측정하는 광산란 기법들이 개발하였다. 금속 연소를 통해 특이한 발광특성을 나타내는 산화마그네슘 입자를 제조하였고, 또한 응집되지 않은 나노입자의 합성을 위해 정전분무 기술, 입자의 균일한 증착을 위해 내부제트를 이용한 화학 증착기술을 개발하였다.

<기술적 특징>

(1) CO_2 레이저를 이용한 나노 입자 제어기술은 나노 입자의 크기, 형상, 결정상 제어가 가능하다. 단일 성분의 나노 입자 뿐 아니라 나노 복합체의 조성 제어도 가능하며, 실리카 기지에 분포한 타이타니아 결정립의 크기와 결정상의 형태를 레이저 파워에 따라 조절할 수 있다. 또한 아세틸렌 화염에서 레이저를 조사할 때 임계 전이를 통한 결정성이 뛰어난 속이 빈 탄소 나노 입자를 연속적으로 생성할 수 있다. 이 방법에 의해 생성된 속이 빈 탄소 오니온은 탄소 나노튜브에 필적할만한 전계 방출 특성을 나타낸다.

(2) 본 연구단에서 개발된 새로운 나노 입자 패터닝 기술은, 기존의 리소그래피 방법과, DMA를 통해 전기장과 입자대전 특성을 이용한 단분산 입자의 수송 현상을 결합한 것이며, 노이즈 없이 정교한 나노 입자 패턴을 병행방법으로 만들어 낼 수 있다.

(3) 산업적으로 매우 유용한 코팅된 나노 복합체의 제조를 위해, 외부 코팅 노즐과 핵심 물질과 연료를 공급하는 내부노즐로 구성된 슬라이딩 버너를 이용하여, 단일공정으로 다양한 나노 입자에 나노미터 두께의 산화막을 균일하게 코팅할 수 있는 기술을 개발하였다.

(4) 기상 중에서의 나노입자 성장을 이론적으로 예측하는 기술로 효율적인 구간해석 방법과 바이모달 방법을 개발하였다. 이를 통해 기존에는 과도한 계산량으로 인해 예측과 모사가 제한되었던 비구형 입자의 성장 해석과 다성분 입자의 성장, 그리고 실제 공정과 같이 공간적으로 불균일한 반응기들 내에서의 복잡한 나노 입자의 성장을 해석할

수 있다. 또한 비구형 나노 입자의 성장 측정을 위해 개발된 평면 광산란 기술은 프랙탈 형태의 응집체를 *in-situ* 한 방법으로 선 측정이 가능하다.

(5) 그 외, 망간과 크롬이 소량 함유된 마그네슘 금속 분말의 연소를 통해, 기존의 벌크와 나노 구조체에서 발견되지 않은 다중의 매우 예리한 광발광 특성이 나타나는 산화마그네슘 나노 입자를 제조할 수 있었다. 또한 정전 분무를 통해 높은 양의 하전을 부과하여 응집되지 아니한 나노 입자를 합성하는 기술을 개발하였고, 수정된 화학 증착 방법을 이용한 광섬유 제조 공정에서 내부제트를 이용하여 균일한 입자 증착과 증착율의 증가 효과를 낼 수 있었다.

[용도·이용분야]

(1) CO_2 레이저를 조사하는 새로운 제어 기술은 나노 입자의 크기와 모양을 제어할 수 있을 뿐만 아니라 고농도 상태에서 나노 입자의 결정상까지도 성공적으로 제어할 수 있으며, 또한 나노 복합재료의 상분리를 제어할 수 있다. TiO_2/SiO_2 나노복합입자는 TiO_2의 광활성을 배가시킴으로 광촉매 분야를 비롯한 촉매분야, TiO_2의 유전특성을 이용한 유전체 분야 및 SiO_2 와 TiO_2의 굴절율 변화를 이용한 광학 분야에 요긴하게 사용될 수 있다

(2) CO_2 레이저를 이용하여 새롭게 제조된 탄소 입자의 경우 탄소 나노튜브에 필적하는 전계 방출특성을 보유하여 앞으로 항공우주, 생명공학, 환경에너지, 재료산업, 의약의료, 전자컴퓨터 등 거의 모든 분야에서의 활약이 기대된다.

(3) 새롭게 개발된 나노 패터닝 기술의 경우, 기존의 top-down 방식의 리소그라피 공정과는 다른, 입자를 이용한 bottom-up 방식으로, 나노입자의 실제적인 이용에 필수적인 나노 입자의 위치제어가 용이하며, 기존 방법보다 더 작은 패턴의 제조에 사용될 수 있다.

(4) 새롭게 개발된 나노입자 성장 모델링 기술은 열유동 해석을 동반하여 실제 나노 입자가 제조되는 화염과 고온 반응기내에서의 효율적인 나노 입자 성장 예측 및 모사에 사용될 수 있으며, FLUENT 와 상용적인 코드에의 적용이 가능하다. 또한 평면 광산란 방법을 통해 효율적으로 넓은 범위의 비구형 입자의 성장 과정을 측정할 수 있다.

(5) 초산자성을 갖는 나노입자는 자기 열적효과와 거대 자기저항의 특성을 갖게 된다. 자기 열적 효과를 이용하여 냉매를 사용하지 않는 환경친화적인 냉각 시스템을 구성할 수 있다. 거대 자기저항을 이용해서는 높은 기록밀도를 갖는 저장 매체를 제조할 수 있다. 또한 ferrofluid technology, biomedicine과 같은 바이오/ 생명과학 분야에 이용될 수 있다

(6) 망간과 크롬이 도핑된 산화마그네슘 나노 입자의 경우, 다수의 매우 예리한 발광 피크가 나타나는 현상을 통해 나노 레이저와 같은 광학 기기의 응용이 가능하다. 내부 제트를 이용하여 증착율을 높이고 균일하게 입자를 부착할 수 있는 광섬유 제조 방법은 산업적으로도 그 활용가치가 높다.

■ 기술의 분류

[기술코드] 215 (3 Digit)

[기술분야] (1개만 선택(∨로 표시)하여 주십시오)

☐ 정보산업 ☐ 기계설비 ☑ 소재 ☐ 정밀화학·공정 ☐ 생명과학
☐ 원자력 ☐ 자원 ☐ 에너지 ☐ 항공·우주 ☐ 해양
☐ 교통 ☐ 보건·의료 ☐ 환경 ☐ 기초·원천 ☐ 기타

[기술의 활용유형] (1개만 선택(∨로 표시)하여 주십시오)

신제품개발 ☑ 신공정개발 ☐ 기존제품개선 ☐ 기존공정개선
☐ 기 타 ( )

[기술의 용도] (복수 선택(∨로 표시)가능합니다)

☑ 기계설비 ☑ 부품소자 ☑ 원료재료 ☐ 소프트웨어
☐ 가공처리기술 ☐ 자동화기술 ☐ 불량률 감소 등 현장애로기술
☐ 제품설계기술 ☐ 공정설계기술 ☐ 기 타 ( )

■ 산업재산권 보유현황(기술과 관련한)

권리유형	명칭	국가명	출원 단계	일자	등록번호
특허	MCVD Method and Apparatus Using an Elongated Gas Feeding Device	미국	등록	*April 2, 2002*	*6,363,754*
특허	Methods for Manufacturing and Depositing Fine Particles Combining Flame and Laser Beam	대한민국	등록	*Sep.1, 2001*	*0308795*
특허	Method for Manufacturing Shell Shaped Fine Carbon Particles	대한민국	등록	*May 15, 2003*	*0385574*

특허	Apparatus for Diluting and Sampling Particles	대한민국	출원	*May 24, 2002*	*10-0339787*
특허	Methods for Manufacturing and Depositing Fine Particles Combining Flame and Laser Beam	미국	출원	*July 26, 2001*	*09/890,366*
특허	Methods for Manufacturing and Depositing Fine Particles Combining Flame and Laser Beam	일본	출원	*July 27, 2001*	*2000-595941*
특허	Methods for Manufacturing and Depositing Fine Particles Combining Flame and Laser Beam	독일	출원	*July 27, 2001*	*10083901.0*
특허	Apparatus and Method for Manufacturing Optical Fibers Using Inner Jet	대한민국	등록	*May 19, 2000*	*0263729*
특허	Method for manufacturing unagglomerated fine particles using electro-hydrodynamic spray in flame or furnace	대한민국	출원	*Feb. 27, 2001*	*2001-9951*
특허	Carbon Nano Particles Having Novel Structure and Properties	대한민국	출원	*Feb. 28, 2002*	*2002-11015*
특허	Carbon Nano Particles Having Novel Structure and Properties	미국	출원	*Feb. 28, 2003*	*10/376,823*
특허	Method for Patterning Nano-Sized Structure Using Electrospray of Nanoparticle	대한민국	출원	*July 2, 2003*	*10-2003-0044625*

특허	Process for Nanoparticle Patterning and Preparation Process of Patterning Sintered Body	대한민국	출원	*July 2, 2003*	*2003-44610*
특허	Process for preparing composite nano particles by gas phase coating using flame	대한민국	출원	*July 22, 2003*	*2003-50219*
특허	Process for field-emission using shell-shaped carbon nanoparticles	대한민국	출원	Aug. 25, 2003	2003-58653
특허	Method for Manufacturing Shell Shaped Fine Carbon Particles	일본	출원	Oct. 7, 2003	2002-565897
특허	Method for Manufacturing Shell Shaped Fine Carbon Particles	독일	출원	Oct. 8, 2003	10296273.1
특허	Method for Manufacturing Shell Shaped Fine Carbon Particles	미국	출원	Oct. 8, 2003	10/638,131

■ 기술이전 조건

이전형태	□ 유상 □무상	최저기술료	천원
이전방식	□ 소유권이전 □ 전용실시권 □ 통상실시권 □ 협의결정 □ 기타( )		
이전 소요기간	년 개월	실용화예상시기	년도
기술이전시 선행요건			

* 기술이전시 선행요건 : 기술이전을 위한 사전준비사항(필수 설비 및 장비, 전문가 확보 등)을 기술
* 실용화예상시기 : 기술을 활용한 대표적인 제품이 최초로 생산이 시작되는 시기를 기재

■ 기술의 개발단계 및 수준

[기술의 완성도]

V	① **기초, 탐색연구단계** : 특정용도를 위해 필요한 신 지식을 얻거나 기술적 가능성을 탐색하는 단계
	② **응용연구단계** : 기술적 가능성의 실증, 잠재적 실용화 가능성의 입증 등 실험실적 확인 단계
	③ **개발연구단계** : Prototype의 제작, Pilot Plant Test 등을 행하는 단계
	④ **기업화 준비단계** : 기업화에 필요한 양산화 기술 및 주변 기술까지도 확보하는 단계
	⑤ **상품화 완료단계**

[기술의 수명주기]

	① **기술개념 정립기** : 기술의 잠재적 가능성만 있는 단계
V	② **기술실험기** : 기술개발에 성공했으나 아직 실용성, 경제성 등이 확실치 않은 단계
	③ **기술적용 시작기**: 최초의 기술개발국에서만 활용되고 있는 단계
	④ **기술적용 성장기**: 기술개발국 및 일부 선진국에서 활용되고 있는단계
	⑤ **기술적용 성숙기**: 선진국사이에서 활발한 기술이전이 일어나며, 기술의 표준화가 되어가는 단계
	⑥ **기술적용 쇠퇴기**: 선진국에서 개도국으로 기술이전이 활발하게 일어나고, 선진국에서는 기술의 가치가 저하되나, 개도국에서는 아직 시장의 가치가 높은 기술

[기술발전 과정상의 기술수준]

	① **외국기술의 모방단계** : 이미 외국에서 개발된 기술의 복제, reverse Eng.
	② **외국기술의 소화·흡수단계** : 국내시장구조나 특성에 적합하게 적응시킴
	③ **외국기술의 개선·개량단계** : 성능이나 기능을 개선시킴
V	④ **신기술의 혁신·발명단계** : 국내 최초로 개발

■ 본 기술과 관련하여 추가로 확보되었거나 개발중인 기술

해당 없음